

INVESTIGATION OF ELECTROMIGRATION AND STRESS INDUCED SURFACE
DYNAMICS ON THE INTERCONNECT BY COMPUTER SIMULATION

A THESIS SUBMITTED TO
THE GRADUATE SCHOOL OF NATURAL AND APPLIED SCIENCES
OF
MIDDLE EAST TECHNICAL UNIVERSITY

BY

AYTAÇ ÇELİK

IN PARTIAL FULFILLMENT OF THE REQUIREMENTS
FOR
THE DEGREE OF DOCTOR OF PHILOSOPHY
IN
METALLURGICAL AND MATERIALS ENGINEERING

MARCH 2011

Approval of the thesis:

INVESTIGATION OF ELECTROMIGRATION AND STRESS INDUCED SURFACE DYNAMICS ON THE INTERCONNECT BY COMPUTER SIMULATION

submitted by **AYTAÇ ÇELİK** in partial fulfillment of the requirements for the degree of **Doctor of Philosophy in Metallurgical and Materials Engineering Department, Middle East Technical University** by,

Prof. Dr. Canan Özgen
Dean, Graduate School of **Natural and Applied Sciences**

Prof. Dr. Tayfur ÖZTÜRK
Head of Department, **Metallurgical and Materials Engineering**

Prof. Dr. Tarık Ömer OĞURTANI
Supervisor, **Metallurgical and Materials Eng. Dept., METU**

Prof. Dr. Mehmet Kadri AYDINOL
Co-supervisor, **Metallurgical and Materials Eng. Dept., METU**

Examining Committee Members:

Prof. Dr. Ahmet Macit ÖZENBAŞ
Metallurgical and Materials Engineering, METU

Prof. Dr. Tarık Ömer OĞURTANI
Metallurgical and Materials Engineering, METU

Prof. Dr. Salim ÇIRACI
Physics Department, Bilkent University

Prof. Dr. Güngör GÜNDÜZ
Chemical Engineering, METU

Prof. Dr. Ali Şakir BOR
Metallurgical and Materials Engineering, METU

Date:

I hereby declare that all information in this document has been obtained and presented in accordance with academic rules and ethical conduct. I also declare that, as required by these rules and conduct, I have fully cited and referenced all material and results that are not original to this work.

Name, Last Name: AYTAÇ ÇELİK

Signature :

ABSTRACT

INVESTIGATION OF ELECTROMIGRATION AND STRESS INDUCED SURFACE DYNAMICS ON THE INTERCONNECT BY COMPUTER SIMULATION

ÇELİK, Aytaç

Ph.D., Department of Metallurgical and Materials Engineering

Supervisor : Prof. Dr. Tarık Ömer OĞURTANI

Co-Supervisor : Prof. Dr. Mehmet Kadri AYDINOL

March 2011, 179 pages

Purpose of this work is to provide a comprehensive picture of thin film (interconnect) and solid droplet surface evolution under the several external applied forces with anisotropic physical properties so that one can eventually be able to predict main reasons and conditions under which stability of surface is defined.

A systematic study based on the self-consistent dynamical simulations is presented for the spontaneous surface evolution of an thin film and isolated thin solid droplet on a rigid substrate, which is driven by the surface drift diffusion induced by the anisotropic diffusivity, the anisotropic capillary forces (surface stiffness) and mismatch stresses under electron winding. The effect of surface free energy anisotropies (weak and strong (anomalous)) on the development kinetics of the Stranski-Krastanow island type morphology are studied. Although, various tilt angles and anisotropy constants were considered during simulations, the main emphasis was given on the effect of rotational symmetries associated with the surface Helmholtz free energy topography in 2D space.

The investigations of dynamics of surface roughness on concurrent actions of the applied

elasto- and electro- static fields clearly indicate that applied misfit stress level is highly important effect on resultant surface form which may be smooth wave like or crack like. The droplet simulations revealed the formation of an extremely thin wetting layer during the development of the bell-shaped Stranski-Krastanow island through the mass accumulation at the central region of the droplet via surface drift-diffusion. The developments in the peak height, in the extension of in the wetting layer beyond the domain boundaries, and the change in triple junction contact angle, one clearly observes that these quantities are reaching certain saturation limits or plateaus, when the growth mode turned-off. Islanding differences for weak anisotropy constant levels and the strong (anomalous) anisotropy constant domains are discussed.

Keywords: Interfaces and surfaces, Instability of surface morphology, Non-equilibrium thermodynamics, Electromigration, Continuum mechanics

ÖZ

ARABAĞLANTI ELEMANLARININ ELEKTROGÖÇ VE STRESS NEDENLİ YÜZEY DİNAMİĞİNİN BİLGİSAYAR SİMÜLASYONU ARACILIĞI İLE ARAŞTIRILMASI

ÇELİK, Aytaç

Doktora, Metalurji ve Malzeme Mühendisliği Bölümü

Tez Yöneticisi : Prof. Dr. Tarık Ömer OĞURTANI

Ortak Tez Yöneticisi : Prof. Dr. Mehmet Kadri AYDINOL

Mart 2011, 179 sayfa

Bu çalışmanın amacı, ince filmlerin ve ince katı damlacıkların elektron rüzgarı, uyumsuzluk gerilimi, eşyönsüz yüzey kayma difüzyonu, yüzey kararlılığı eşyönsüzlüğü altında yüzey evriminin kapsamlı bir tablosunun ortaya koymaktır, böylece kişi yüzey kararlılığının bağlı olduğu ana nedenleri ve koşulları tahmin edilmesini sağlayacaktır.

Katı altlık üstündeki ince filmlerin ve ince katı damlacıkların yüzeylerinin elektron rüzgarı, uyumsuzluk gerilimi, eşyönsüz yüzey kayma difüzyonu, yüzey kararlılığı eşyönsüzlüğü altında evrimi dinamik modelleme ile araştırılmıştır. Stranski-Krastanow adacıklarının oluşumunda eşyönsüz serbest yüzey enerjisinin etkisi gözlemlenmiştir. Örgü yapı ile altlık arasındaki birçok açı ve farklı eşyönsüzlük şiddeti göz önünde bulundurulmuştur.

Yüzey pürüzlüğünün elektrostatik ve elastostatik alanlar altındaki dinamikleri göstermiştir ki; ince filmin maruz kaldığı uyumsuzluk stress miktarı oldukça önemlidir ve bu gerilimin basınç yada çekme kuvveti olması düzgün dalga şeklinde yada çatlak benzeri formda olan sonuç morfolojini derinden etkilemektedir. Damlacık deneylerinde, damlacık kenarlarından madde transferi ile damlacık ortasında çan şekilli Stranski-Krastanow adacıklarının oluşumu

sırasında oldukça ince ıslanma katmanı oluşumu gözlemlenmiştir. Buhar yağunlaşması devre dışı bırakıldığında, adacık yüksekliği, ıslanma açısı ve ıslanma katmanı uzunluğu belli değerlerde sabitlendiği gözlemlenmiştir. Adacık şekillenmelerindeki fark düşük eşyönsüzlük sabiti değerleri ile yüksek eşyönsüzlük sabiti değerlerinden nasıl etkilendiği tartışılmış.

Anahtar Sözcükler: Yüzeyler, Yüzey morfolojisi kararsızlığı, Denge dışı termodinamik, Elektrogöç, Sürekli medya

To my family

ACKNOWLEDGMENTS

First of all, I would like to thank to my supervisor Prof. Dr. Tarık Ömer Oğurtanı for giving me the opportunity to fulfill this research and for his support, guidance, and motivation. I would also like to thank to Dr. Ersin Emre Ören for his help and guidance. I also acknowledge my thesis examining committee members for evaluating the work of this thesis. I would also like to specially thank to Prof. Dr. Ahmet Macit ÖZENBAŞ, Prof. Dr. Güngör GÜNDÜZ and Prof. Dr. Mehmet Kadri AYDINOL for their guidance and helpful discussions.

I would like to express my gratitude to Sadi Uçkun EMEL, Kamil Devrim ÇANACIK, Mehmet Can AVAR, Gökalp ULUCAN, Mustafa Serhan DEMIREL, Sencer TURUNÇ, Dr. Şener YILMAZ and Dr. Umut ADEM for their support, friendship and help for conducting and completing this study. Special thanks go also to Cem ÇELİK for his endless support. An-neme, babama ve kardeşime her zaman yanımda oldukları için tesekkür ederim.

Many years have passed during these studies. So, please forgive me if I missed someone to mention here, as I appreciate even the slightest help and courage from anyone who love me and believe in me...

TABLE OF CONTENTS

ABSTRACT	iv
ÖZ	vi
ACKNOWLEDGMENTS	ix
TABLE OF CONTENTS	x
LIST OF FIGURES	xiii
NOMENCLATURE	xxv
CHAPTERS	
1 INTRODUCTION AND LITERATURE REVIEW	1
1.1 Motivation	1
1.2 Epitaxial growth of thin films	2
1.2.1 Heteroepitaxy	4
1.3 Role of stress on thin film morphology	7
1.3.1 Morphology and surface stability of a stressed body	7
1.3.2 Elastic interactions of elastic defects	8
1.3.3 Effects on diffusion constant	10
1.4 Role of electromigration on thin film morphology	10
1.5 Thermodynamics of surface stress	15
1.6 Thermodynamics of Irreversible Processes	17
1.6.1 The fundamental principles of irreversible thermodynamics	18
1.7 Fluxes and driving forces for diffusion	21
1.7.1 Diffusional mass transport by capillarity	21
1.7.2 Diffusional mass transport in an electrical potential gradient	22
1.7.2.1 Charged ions in ionic conductors	22
1.7.2.2 Electromigration in metals	23

1.7.3	Diffusional mass transport in the presence of stress	24
1.7.3.1	Stress effect on mobility	24
1.8	Literature review	25
1.8.1	Theoretical works	25
1.8.2	Experimental observations	32
1.9	Outline of the thesis	39
2	IRREVERSIBLE THERMOKINETIC THEORY OF INTERFACES	40
2.1	Introduction	40
2.2	Irreversible thermo-kinetics of micro-discrete open composite systems with interfaces	41
2.3	Ordinary point motion along the surface normal	46
2.3.1	Internal entropy production	47
2.3.2	Rate of entropy flow	51
2.3.3	The local rate of change in the entropy density	52
3	MATHEMATICAL MODEL AND NUMERICAL PROCEDURES	59
3.1	Introduction	59
3.2	Mathematical model	59
3.3	Fundamental solutions of potential and elastic problems	62
3.3.1	Steady state potential solution	62
3.3.2	Static elastic solution	63
3.4	Numerical procedures	66
	Calculation of node curvatures:	66
	Anisotropic surface diffusivity:	67
	Anisotropic surface stiffness:	68
	Wetting potential:	70
	Adaptive remeshing:	71
	Explicit euler's method:	72
4	THE ORIENTATION DEPENDENT INTERACTION OF ELECTROMIGRATION AND THE UNIAXIAL COMPRESSIVE STRESSES IN SINGLE CRYSTAL METALLIC THIN FILMS	73
4.1	Physical model	73

4.2	Linear stability analysis	74
4.3	Results and discussion	80
4.3.1	Epitaxially strained thin film with isotropic texture on rigid substrates	81
4.3.2	Epitaxially strained thin film with anisotropic texture on rigid substrates	90
4.3.2.1	Two-fold rotational symmetry in cubic structures: Zone axis $\langle 1\bar{1}0 \rangle$	90
4.3.2.2	Four-fold rotational symmetry in cubic structures: Zone axis $\langle 001 \rangle$	93
4.3.2.3	Six-fold rotational symmetry in cubic structures: Zone axis $\langle 111 \rangle$	94
4.3.3	Epitaxially strained thin film with anisotropic texture under electromigration on rigid substrates	96
5	SURFACE DYNAMICS IN EPITAXIALLY STRAINED FLAT DROPLETS	101
5.1	Physical model	101
5.2	Results and discussion	102
5.2.1	Island formation in epitaxially strained flat droplets with isotropic texture on rigid substrates	102
5.2.1.1	Morphological evolution of droplet without growth:	103
5.2.1.2	Morphological evolution of droplet with growth:	114
5.2.2	Island formation in epitaxially strained flat droplets with anisotropic texture on rigid substrates	116
5.2.2.1	Two-fold rotational symmetry in cubic structures: Zone axis $\langle 1\bar{1}0 \rangle$	116
5.2.2.2	Four-fold rotational symmetry in cubic structures: Zone axis $\langle 001 \rangle$	120
5.2.2.3	Six-fold rotational symmetry in cubic structures: Zone axis $\langle 111 \rangle$	124
6	CONCLUSION	128
	REFERENCES	133
	APPENDICES	
A	PROGRAM CODE	143
	CURRICULUM VITAE	178

LIST OF FIGURES

FIGURES

Figure 1.1 Schematic evolution of the (a) Frank-van der Merwe, (b) Volmer-Weber, and (c) Stranski-Krastanov growth morphologies [3].	3
Figure 1.2 Cross-section micrograph of an uncapped InP island on GaInP grown by MOVPE at 580 °C along the (a) $[1\bar{1}0]$ and (b) $[110]$ directions (Georgsson et al. [8]).	4
Figure 1.3 STM image (1600 Å x 1600 Å) of Ge hut clusters grown in Si(001) at 575 K (B Voigtländer [17]).	6
Figure 1.4 Elastic interaction in between: a) 2 adatoms considered as elastic dipoles ($\mathbf{D}=0, \mathbf{m}=1$), b) 2 steps bearing dipoles ($\mathbf{D}=1, \mathbf{m}=1$) of same sign or (and) monopoles ($\mathbf{D}=1, \mathbf{m}=0$) of same sign when the solid is stressed, c) 2 steps of opposite sign [19].	9
Figure 1.5 The driving force for electromigration.	11
Figure 1.6 The diffusion paths of electromigration.	12
Figure 1.7 Schematic illustrations of several sites at which flux divergence is expected in metallization systems: (a) triple points in conductor layers; (b) regions where the conductor changes in width; (c) a gold wire/aluminum film contact; (d) at defects in an interconnect.	14
Figure 1.8 Increasing ratio of w/d	14
Figure 1.9 Left: Gibbs definition of the two phases α and β are separated by an ideal interface σ Right: Guggenheim defined interface as an extended interphase with a volume.	15
Figure 1.10 Interface among three phases.	17
Figure 1.11 Positive and negative surface curvature. The curvature differences cause diffusion potential gradients that cause surface smoothing by mass transport. . . .	21

Figure 1.12 An AFM image of undulations elongated along $\langle 100 \rangle$ and $\langle 010 \rangle$ directions obtained in regime II for $Si_{0.85}Ge_{0.15}$ [67].	33
Figure 1.13 (a) An AFM image of the bimodal size distribution of islands due to the coexistence of square-based hut and round-shaped dome islands for $Si_{0.6}Ge_{0.4}$ ($h = 5$ nm). TEM cross-section images of (b) huts and (c) domes. The enlargement of (c) presented in (d) evidences the presence of (113) and (111) facets [67].	34
Figure 1.14 (a) Hut form of Ge on a pseudomorphic Ge layer on Si(100). (b) Multifacet dome [17].	34
Figure 1.15 Ni clusters in the TiN metallic matrix: (a) low-magnification TEM image and (b) STEM Z-contrast image [68].	35
Figure 1.16 Evolution of the quantum fortress surface morphology for growth of $Ge_{0.3}Si_{0.7}/Si(100)$ at a growth temperature of 550 °C and a growth rate of 0.9 \AA s^{-1} . AFM scans are $5 \mu m \times 5 \mu m$ in area. $Ge_{0.3}Si_{0.7}$ film thicknesses are (a) 0 nm; (b) 15 nm; (c) 30 nm; (d) 53 nm; (e) 100 nm [69].	36
Figure 1.17 InAs dot shape evolution from pyramid to dome transition on Si (001) [70].	37
Figure 1.18 Cu(21 21 23) surface with meandering instability after 600 monolayer of copper at 313 K ($400nm \times 400nm$) [74].	37
Figure 1.19 STEM image of Cu(1 1 17) surface ($200 \times 200 - nm^2$) after deposition of 80 ML at $F = 1.8 \times 10^{-2}$ ML/s and $T = 285$ K sample temperature [75, 76].	38
Figure 1.20 AFM image of a Si (118) surface heated by a direct current during 150 h at 1373 K. Faceted structure of period $\lambda = 6 \mu m$ and height $0.6 \mu m$ created by electromigration due to the ascending current. (001) and (113) are the so-formed facets. The period gives access to the difference $s_{\tau}^{(001)} - s_{\tau}^{(113)}$ with τ the common edge shared by the (001) and (113) facets [77].	39
Figure 2.1 Ordinary point motion along surface normal. a) Macro-structure, b) Micro-structure. ABC: interfacial layer and $\delta\eta$: virtual displacement of the ordinary point along surface normal [84].	47
Figure 2.2 Structure of micro-composite system [84].	51
Figure 3.1 Notation for two-dimensional Kelvin solution [86].	65
Figure 3.2 The unique circle that pass from the three successive void nodes [84].	67

Figure 3.3	Diffusion anisotropy: a) $\{110\}$ Two-fold rotational symmetry in cubic structures with parameters $D_{\sigma}^0 = 1, A = 5, m = 1, \theta = 3.93\pi/10$. b) $\{100\}$ Four-fold rotational symmetry in cubic structures with parameters $D_{\sigma}^0 = 1, A = 7, m = 2, \theta = \pi/4$. c) $\{111\}$ Six-fold rotational symmetry in cubic structures with parameters $D_{\sigma}^0 = 1, A = 3, m = 3, \theta = \pi/6$	68
Figure 3.4	Typical behavior of the surface specific Gibbs free energy and the surface stiffness for the set of four fold symmetry planes $\{0\bar{\mp}10\}$ and $\{\bar{\mp}100\}$ in a fcc crystal having $[001]$ zone axis normal to the thin film surface. The anisotropy constant: $B = 0.2$. The negative spikes of the surface stiffness are clearly seen along the $\langle 1\bar{\mp}10 \rangle$ directions, which indicates inherent instability.	70
Figure 4.1	Side view of metallic thin film with sinewave perturbation.	74
Figure 4.2	Growth rate vs. wavenumber in the absence of electrostatic force.	77
Figure 4.3	The instability growth rate Γ is plotted for isotropic diffusion with respect to the wave number $k = 0 - 4$ and applied misfit stress $\Xi = \pm 6$. The elastostatic data for copper used: $E_0 = 130G Pa$, $\nu = 0.34$, $g_{\sigma}^0 = 1.6JM^{-2}$, and $ Tr\lambda_{\sigma}^{Cu} = 0.4$	77
Figure 4.4	Growth rate constant Γ is plotted with respect to the tilt angle ϕ and wave number k for the sidewall surface morphological evolution of thin film having (110) plane which has 2 fold symmetry.	78
Figure 4.5	Growth rate constant Γ is plotted with respect to the tilt angle ϕ and EDTI Ξ for the sidewall surface morphological evolution of thin film having (110) plane which has 2 fold symmetry with and without electromigration ($\chi = 0$ and $\chi = 150$) for constant wave number $k = 25$	79
Figure 4.6	Neutral stability plot for (110) plane at different angles between texture and substrate. Uniform state is stable below the plane and above the plane pattern formation is possible.	80
Figure 4.7	Side wall morphological evolution of single crystal copper thin film with isotropic diffusivity, wave number $k = 1.7$ and amplitude of $Amp = 0.05$, which is subjected to misfit tensile $\Xi = 0.56$ along the longitudinal axis. (a) shows morphological evolution in 3D plot. (b) shows the normalized displacement of trough and crest tips as a function of normalized time in logarithmic scale.	81

Figure 4.8 Side wall morphological evolution of single crystal copper thin film with isotropic diffusivity, wave number $k = 5.14$ and amplitude of $Amp = 0.05$, which is subjected to misfit tensile $\Xi = -0.11$ along the longitudinal axis. (a) shows morphological evolution in 3D plot. (b) shows the normalized displacement of trough and crest tips as a function of normalized time in logarithmic scale.	82
Figure 4.9 Side wall morphological evolution of single crystal copper thin film with isotropic diffusivity, wave number $k = 5.14$ and amplitude of $Amp = 0.01$, which is subjected to misfit tensile $\Xi = -11.16$ along the longitudinal axis. (a) shows morphological evolution in 3D plot. (b) shows normalized the displacement of trough and crest tips as a function of normalized time in logarithmic scale.	83
Figure 4.10 Side wall morphological evolution of single crystal copper thin film with isotropic diffusivity, wave number $k = 1.7$ and amplitude of $Amp = 0.1$, which is subjected to misfit tensile $\Xi = -5.58$ along the longitudinal axis. (a) Morphological evolution in 3D plot. (b) Normalized the displacement of trough and crest tips as a function of normalized time in logarithmic scale. (c) Instantaneous hoop stress and surface profile along the thin film at the on set of trough tip splitting ($\tau = 0.0019$).	84
Figure 4.11 Side wall morphological evolution of single crystal copper thin film with isotropic diffusivity, wave number $k = 3.99$ and amplitude of $Amp = 0.01$, which is subjected to misfit tensile $\Xi = -3.35$ along the longitudinal axis. (a) Morphological evolution in 3D plot. (b) Normalized displacement of trough and crest tips as a function of normalized time in logarithmic scale. (c) Instantaneous hoop stress and surface profile along the thin film at the on set of trough tip splitting ($\tau = 0.052$).	84
Figure 4.12 Growth rate Γ versus EDTI (Ξ) values represented for different values of amplitude and wave numbers. (a) Trough growth rate for wave number $k = 1.71$. (b) Crest growth rate for wave number $k = 1.71$. (c) Trough growth rate for wave number $k = 5.14$. (d) Crest growth rate for wave number $k = 5.14$	85
Figure 4.13 Growth rate Γ versus Amp/λ plot for $\Xi = -0.5558$ for different amplitudes and their power series fittings.	86
Figure 4.14 Experiment normalized failure and equilibrium reach time plot with respect to amplitude and surface wave number for different misfit stress values Ξ	86

Figure 4.15 Normalized time plot with respect to misfit stress values $\Xi < -1$ (EDTI) for different amplitudes and their power series fittings at wave number $k = 1.7136$.	87
Figure 4.16 Experiment normalized failure time plot with respect to amplitude and surface wave number for $11.16 \geq \Xi \geq -3.35$ misfit stress values and its fitting surface.	88
Figure 4.17 Normalized time plot with respect to misfit stress values $\Xi > 0$ (EDTI) for different amplitudes and their power series fittings.	89
Figure 4.18 Normalized time plot with respect to misfit stress values $-1.116 \geq \Xi \geq 0$ (EDTI) for different amplitudes and their power series fittings.	90
Figure 4.19 The evolution of side wall surface of thin film with (110) plane as a top plane with a tilt angle $\phi = 0^\circ$ and $A = 5$, subjected to a compression $\Xi = -5.58$ misfit, without electromigration ($\chi = 0$, $Amp = 0.05$, $k = 2.85$). (a) Morphological evolution in 3D plot. (b) Normalized displacement of trough and crest tips as a function of normalized time in logarithmic scale. (c) Hoop stress and surface profile on the evolving surface.	91
Figure 4.20 The evolution of side wall surface of thin film with (110) plane as a top plane with a tilt angle $\phi = 90^\circ$ and $A = 5$, subjected to a compression $\Xi = -5.58$ misfit, without electromigration ($\chi = 0$, $Amp = 0.01$, $k = 5.1$). (a) Morphological evolution in 3D plot. (b) Normalized displacement of trough and crest tips as a function of normalized time in logarithmic scale.	92
Figure 4.21 The evolution of side wall surface of thin film with (110) plane as a top plane with a tilt angle $\phi = 77^\circ$ and $A = 5$, subjected to a compression $\Xi = -3.35$ misfit, without electromigration ($\chi = 0$, $Amp = 0.1$, $k = 1.71$). (a) Morphological evolution in 3D plot. (b) Normalized displacement of trough and crest tips as a function of normalized time in logarithmic scale. (c) Hoop stress and surface profile on the evolving surface.	92
Figure 4.22 The evolution of side wall surface of thin film with (001) plane as a top plane with a tilt angle $\phi = 0^\circ$ and $A = 5$, subjected to a compression $\Xi = -11.16$ misfit, without electromigration ($\chi = 0$, $Amp = 0.05$, $k = 2.85$). (a) Normalized displacement of trough and crest tips as a function of normalized time in logarithmic scale. (b) Morphological evolution in 3D plot. (c) Hoop stress and surface profile on the evolving surface.	93

- Figure 4.23 The evolution of side wall surface of thin film with (001) plane as a top plane with a tilt angle $\phi = 45^\circ$ and $A = 5$, subjected to a compression $\Xi = -1.116$ misfit, without electromigration ($\chi = 0$, $Amp = 0.01$, $k = 1.71$). (a) Morphological evolution in 3D plot. (b) Normalized displacement of trough and crest tips as a function of normalized time in logarithmic scale. 94
- Figure 4.24 The evolution of side wall surface of thin film with (111) plane as a top plane with a tilt angle $\phi = 0^\circ$ and $A = 5$, subjected to a compression $\Xi = -11.16$ misfit, without electromigration ($\chi = 0$, $Amp = 0.01$, $k = 1.71$). (a) Morphological evolution in 3D plot. (b) Normalized displacement of trough and crest tips as a function of normalized time in logarithmic scale. (c) Surface profile and hoop stress along the thin film surface. 95
- Figure 4.25 The evolution of side wall surface of thin film with (111) plane as a top plane with a tilt angle $\phi = 30^\circ$ and $A = 5$, subjected to a compression $\Xi = -3.35$ misfit, without electromigration ($\chi = 0$, $Amp = 0.01$, $k = 1.71$). (a) Morphological evolution in 3D plot. (b) Normalized displacement of trough and crest tips as a function of normalized time in logarithmic scale. (c) Instantaneous hoop stress and surface profile along the thin film at the on set of trough tip splitting ($\tau = 0.003$). 95
- Figure 4.26 The evolution of side wall surface of thin film with (110) plane as a top plane with a tilt angle $\phi = -10^\circ$ and $A = 10$, subjected to a compression $\Xi = -1.11$ due to misfit, with electromigration $\chi = 20$. ($Amp = 0.05$, $k = 4$). (a) Normalized displacement of trough and crest tips as a function of normalized time in logarithmic scale. (b) Morphological evolution in 3D plot. 96
- Figure 4.27 The evolution of side wall surface of thin film with (110) plane as a top plane with a tilt angle $\phi = 50^\circ$ and $A = 10$, subjected to a compression $\Xi = -1.11$ due to misfit, with electromigration $\chi = 20$. ($Amp = 0.05$, $k = 4$). (a) Normalized displacement of trough and crest tips as a function of normalized time in logarithmic scale. (b) Morphological evolution in 3D plot. 97
- Figure 4.28 The evolution of side wall surface of thin film with (100) plane as a top plane with a tilt angle $\phi = 62^\circ$ and $A = 10$, subjected to a compression $\Xi = -3.35$ due to misfit, with electromigration $\chi = 6$. ($Amp = 0.27$, $k = 1.71$). (a) Normalized displacement of trough and crest tips as a function of normalized time in logarithmic scale. (b) Morphological evolution in 3D plot. 97

Figure 4.29 The evolution of side wall surface of thin film with (111) plane as a top plane with a tilt angle $\phi = 37.8^\circ$ and $A = 10$, subjected to a compression $\Xi = -5.58$ due to misfit, with electromigration $\chi = 46$ ($Amp = 0.37$, $k = 1.71$). (a) Normalized displacement of trough and crest tips as a function of normalized time in logarithmic scale. (b) Morphological evolution in 3D plot. (c) Final configuration. 98

Figure 4.30 The evolution of side wall surface of thin film with (111) plane as a top plane with a tilt angle $\phi = 37.8^\circ$ and $A = 10$, subjected to a compression $\Xi = -5.58$ due to misfit, with electromigration $\chi = 46$ ($Amp = 0.37$, $k = 1.71$). (a) Normalized displacement of trough and crest tips as a function of normalized time in logarithmic scale. (b) Morphological evolution in 3D plot. (c) Final configuration. 99

Figure 4.31 The evolution of side wall surface of thin film with (111) plane as a top plane with a tilt angle $\phi = 40^\circ$ and $A = 10$, (a) subjected to a compression $\Xi = -1.165$ due to misfit, with electromigration $\chi = 50$ which is applied from $\tau = 0.37$. (b) subjected to a compression $\Xi = -1.56$ due to misfit, with electromigration $\chi = 50$ which is applied from $\tau = 0.1$ 100

Figure 5.1 Side view of metallic droplet. 101

Figure 5.2 (a) The island profile change with transition stage just before the onset of the SK islands formation regime. The final profile is fitted by a Gaussian bell-shape curve having following parameters: $\bar{h}_p = 2.30$, $\bar{w} = 3.25$, which corresponds to the peak height-to-peak width ratio of $\xi = 0.354$. (b) Instantaneous velocity and the hoop stress distributions along the final droplet profile. (c) Evolution of the contact angle is shown on the left y-axis. On the right y-axis, the strain energy and surface free energy changes are given for Ge/Si(100) system, and scaled by $nm^2 \rightarrow 10^{-18}$. (d) Time evolution of peak height and TJ displacement. Simulation Data: $\Sigma = 0.25$, $\bar{h}_p = 1$, $\beta = 28$, $\nu = 0.273$, $\bar{M}_{TJ} = 2$, $\lambda_{TJ} = 1$, $\bar{\delta} = 0.005$, $\gamma_s = 1.2$ and $\gamma_f = 1$ 104

Figure 5.3 (a) Spontaneous formation of the SK island with an almost perfect flat wetting layer from a single crystal droplet on a stiff substrate by the isotropic surface drift diffusion driven by the combined actions of the misfit strain (isochoric) and the capillary forces. The inset details the structure of the wetting layer at the TJ. Gaussian bell-shape curve representing the final profile has the following parameters: $\bar{h}_p = 3.15$, $\bar{w} = 2.90$ and thus the peak height-to-peak width ratio of $\xi = 0.543$. (b) Instantaneous velocity and the hoop stress distributions along the final droplet profile. (c) Evolution of the contact angle is shown on the left y-axis. On the right y-axis, the strain energy and surface free energy changes are given for Ge/Si(100) system. (d) Time evolution of peak height and TJ displacement. Simulation Data: $\Sigma = 0.40$, $\bar{h}_p = 1$, $\beta = 28$, $\nu = 0.273$, $\bar{M}_{TJ} = 2$, $\lambda_{TJ} = 1$, $\bar{\delta} = 0.005$, $\gamma_s = 1.2$ and $\gamma_f = 1$ 106

Figure 5.4 (a) Spontaneous formation of the SK doublets with an almost perfect flat wetting layer from a single crystal droplet. The inset details the structure of the wetting layer between the individual peaks. The fourth degree Gaussian fitting have the following parameters: $\bar{h}_p = 2.07$, $\bar{w} = 2.06$ and thus the peak height-to-peak width ratio of $\xi = 0.502$. (b) 3D time evolution of island profile. (c) Evolution of the contact angle is shown on the left y-axis. On the right y-axis, the strain energy and surface free energy changes are given for Ge/Si(100) system. (d) Time evolution of peak height and TJ displacement. Simulation Data: $\Sigma = 0.45$, $\bar{h}_p = 1$, $\beta = 28$, $\nu = 0.273$, $\bar{M}_{TJ} = 2$, $\lambda_{TJ} = 1$, $\bar{\delta} = 0.005$, $\gamma_s = 1.2$ and $\gamma_f = 1$ 108

Figure 5.5 (a) The stationary island profile at the transient stage just before the onset of the SK island formation regime. Gaussian bell-shape curve representing the final profile has the following parameters: $\bar{h}_p = 1.47$, $\bar{w} = 2.20$ and thus the peak height-to-peak width ratio of $\xi = 0.334$. (b) 3D time evolution of island profile. (c) Evolution of the contact angle is shown on the left y-axis. On the right y-axis, the strain energy and surface free energy changes are given for Ge/Si(100) system. (d) Time evolution of peak height and TJ displacement. Simulation Data: $\Sigma = 0.4$, $\bar{h}_p = 1$, $\beta = 10$, $\nu = 0.273$, $\bar{M}_{TJ} = 2$, $\lambda_{TJ} = 1$, $\bar{\delta} = 0.005$, $\gamma_s = 1.2$ and $\gamma_f = 1$ 109

Figure 5.6 (a) Spontaneous formation of the SK island with an almost perfect flat wetting layer from a single crystal. The inset details the structure of the wetting layer at the TJ. The singlet has fourth degree Gaussian bell-shape curve having the following parameters: $\bar{h}_p = 1.76$, $\bar{w} = 1.80$ and thus the peak height-to-peak width ratio of $\xi = 0.489$. (b) 3D time evolution of island profile. (c) Evolution of the contact angle is shown on the left y-axis. On the right y-axis, the strain energy and surface free energy changes are given for Ge/Si(100) system. (d) Time evolution of peak height and TJ displacement. Simulation Data: $\Sigma = 0.50$, $\bar{h}_p = 1$, $\beta = 10$, $\nu = 0.273$, $\bar{M}_{TJ} = 2$, $\lambda_{TJ} = 1$, $\bar{\delta} = 0.005$, $\gamma_s = 1.2$ and $\gamma_f = 1$ 111

Figure 5.7 (a) Evolution of the Cosine-shape droplets towards the stationary equilibrium state by readjustment of the base length through the TJ motion. Gaussian bell-shape curve representing the final profile has the following parameters: $\bar{h}_p = 1.10$, $\bar{w} = 8.00$ and thus the peak height-to-peak width ratio of $\xi = 0.069$. (b) Instantaneous velocity and the hoop stress distributions along the final droplet profile. (c) Evolution of the contact angle is shown on the left y-axis. On the right y-axis, the strain energy and surface free energy changes are given for Ge/Si(100) system. (d) Time evolution of peak height and TJ displacement. Simulation Data: $\Sigma = 0.175$, $\bar{h}_p = 1$, $\beta = 10$, $\nu = 0.273$, $\bar{M}_{TJ} = 2$, $\lambda_{TJ} = 1$, $\bar{\delta} = 0.005$, $\gamma_s = 1.2$ and $\gamma_f = 1$ 113

Figure 5.8 (a) The effect of the growth on the SK island morphology: formation of two satellites shouldering the primary pea, and separated by almost perfectly flat wetting layers. Gaussian bell-shape curve representing the final profile has the following parameters: $\bar{h}_p = 1.10$, $\bar{w} = 8.00$ and thus the peak height-to-peak width ratio of $\xi = 0.069$. (b) Instantaneous velocity and the hoop stress distributions along the final droplet profile. (c) Evolution of the contact angle is shown on the left y-axis. On the right y-axis, the strain energy and surface free energy changes are given for Ge/Si(100) system. (d) Time evolution of peak height and TJ displacement. Simulation Data: $\Sigma = 0.40$, $\bar{h}_p = 1$, $\beta = 28$, $\nu = 0.273$, $\bar{M}_{TJ} = 2$, $\lambda_{TJ} = 1$, $\bar{\delta} = 0.005$, $\gamma_s = 1.2$ and $\gamma_f = 1$ and the growth parameters $\bar{M}_b = 1$, $\Delta\bar{F}_{vf}^o = 2$ 115

Figure 5.9 (a) Spontaneous formation of the SK island from a single crystal droplet on a stiff substrate via the surface drift diffusion driven by the combined actions of the misfit strain (isochoric) and the anisotropic capillary forces. (b) Instantaneous velocity and the hoop stress distributions along the final droplet profile. (c) Evolution of the contact angle is shown on the left y-axis. On the right y-axis, the strain energy and surface free energy changes are given for the Ge/Si(111) system. (d) Time evolution of peak height and TJ displacement. Data: $\Sigma = 0.40$, $B = 0.05$, $B = 0.05$, $\bar{h}_p = 1$, $\beta = 28$, $\nu = 0.273$, $\bar{M}_{TJ} = 2$, $\lambda_{TJ} = 1$, $\bar{\delta} = 0.005$, $\gamma_s = 1.2$ and $\gamma_f = 1$ 117

Figure 5.10 Spontaneous formations of the right- and left- shifted SK islands from single crystal droplets for (a and b) very low, $B = 0.05$, and (d and c) very high, $B = 1.0$, surface free energy anisotropy constants at $\pm 45^\circ$ tilt angles. At the threshold level of the anomalous instability regime, very sharp faceting at the right and left edges may be easily seen. Data: $\Sigma = 0.40$, $\bar{h}_p = 1$, $\beta = 28$, $\nu = 0.273$, $\bar{M}_{TJ} = 2$, $\lambda_{TJ} = 1$, $\bar{\delta} = 0.005$, $\gamma_s = 1.2$ and $\gamma_f = 1$ 118

Figure 5.11 (a) Spontaneous formation of the SK doublets with an almost perfect flat wetting layer from a single crystal droplet having exposed to the anisotropic surface stiffness with a tilt angle of $\phi = 90^\circ$. (b) Evolution of the contact angle is shown on the left y-axis. On the right y-axis, the strain energy and surface free energy changes are given for Ge/Si ($11\bar{2}$) system. Data: $\Sigma = 0.40$, $B = 0.05$, $\phi = 90^\circ$, $\bar{h}_p = 1$, $\beta = 28$, $\nu = 0.273$, $\bar{M}_{TJ} = 2$, $\lambda_{TJ} = 1$, $\bar{\delta} = 0.005$, $\gamma_s = 1.2$ and $\gamma_f = 1$ 119

Figure 5.12 Side view of a metallic droplet. This configuration corresponds to the four-fold rotation symmetry designated by $[100]$ zone axis. Where $n = 2m = 4$ and the tilt angle $\phi = 45^\circ$ if one takes the $\{1\bar{1}0\}$ form has lower free energy than the form of planes $\{100\}$, as far as the diffusion and the specific surface Helmholtz free energy dyadics are concerned. 120

Figure 5.13 (a) Spontaneous formation of a tilted SK singlet towards the right edge with an almost perfect flat wetting layer from a single crystal droplet having exposed to the anisotropic surface stiffness with tilt angle of $\phi = 22.5^\circ$. (b) Where the same droplet is exposed to a tilt angle $\phi = -22.5^\circ$ by keeping all other system parameters same. Data: $\Sigma = 0.40$, $B = 0.05$, $\bar{h}_p = 1$, $\beta = 28$, $\nu = 0.273$, $\bar{M}_{TJ} = 2$, $\lambda_{TJ} = 1$, $\bar{\delta} = 0.005$, $\gamma_s = 1.2$ and $\gamma_f = 1$ 121

Figure 5.14 (a,b) Spontaneous formation of the SK doublets with an almost perfect flat wetting layer from a single crystal droplet having exposed to the anisotropic surface stiffness with tilt angle of $\phi = 45^\circ$. (c) Evolution of the contact angle is shown on the left y-axis. On the right y-axis, the strain energy and surface free energy changes are given for Ge/Si(100) system. (d) Time evolution of peak height and TJ displacement. Data: $\Sigma = 0.40$, $B = 0.05$, $\bar{h}_p = 1$, $\beta = 28$, $\nu = 0.273$, $\bar{M}_{TJ} = 2$, $\lambda_{TJ} = 1$, $\bar{\delta} = 0.005$, $\gamma_s = 1.2$ and $\gamma_f = 1$ 122

Figure 5.15 (a-c) Spontaneous formation of the SK singlets with an almost perfect flat wetting layer from a single crystal droplet having exposed to the anisotropic surface free energies having various intensities below the threshold level with the tilt angle of $\phi = 0^\circ \Rightarrow (1\bar{1}0)$. d) The formation of the pyramidal shape faceted islanding just above the onset of the anomalous instability regime without the wetting layer. Data: $\Sigma = 0.40$, $B = \{0.01 - 0.25\}$, $\bar{h}_p = 1$, $\beta = 28$, $\nu = 0.273$, $\bar{M}_{TJ} = 2$, $\lambda_{TJ} = 1$, $\bar{\delta} = 0.005$, $\gamma_s = 1.2$ and $\gamma_f = 1$ 123

Figure 5.16 (a) The droplet at the zero tilt angle designated as $\phi = 0^\circ \Rightarrow 1\bar{1}0$ shows no shape change even for the very large values of the anisotropy constant other than the slight spreading. (b) Surface free energy and stiffness are illustrated in polar plot, which shows $\langle 100 \rangle$ spikes having rather strong negative intensities that indicates the anomalous regime. (c) Evolution of the contact angle is shown on the left y-axis. On the right y-axis, the strain energy and surface free energy changes are given for Ge/Si($1\bar{1}0$) system. (d) Monotonic decrease in the peak height followed up by the substantial increase in the base length. Data: $\Sigma = 0.40$, $B = 2.0$, $\bar{h}_p = 1$, $\beta = 28$, $\nu = 0.273$, $\bar{M}_{TJ} = 2$, $\lambda_{TJ} = 1$, $\bar{\delta} = 0.005$, $\gamma_s = 1.2$ and $\gamma_f = 1$ 124

Figure 5.17 (a-d) Spontaneous formations of the SK singlets having different morphological appearances depending upon the tilt angles are presented for an anisotropy constant, , which is just below the anomalous threshold level of $B_{th} = 1/17$. Data: $\Sigma = 0.40$, $\bar{h}_p = 1$, $\beta = 28$, $\nu = 0.273$, $\bar{M}_{TJ} = 2$, $\lambda_{TJ} = 1$, $\bar{\delta} = 0.005$, $\gamma_s = 1.2$ and $\gamma_f = 1$ 125

Figure 5.18 (a) The droplet at the zero tilt angle shows no shape change even for the very large values of the anisotropy constant in the anomalous regime. (b) Instantaneous velocity and the hoop stress distributions along the final droplet profile. (c) Evolution of the contact angle is shown on the left y-axis. On the right y-axis, the strain energy and surface free energy changes are given for the Ge/Si(100) system. (d) Time evolution of peak height and TJ displacement, which indicates the monotonic decrease in the peak height, and the steady increase in the base length, followed by some erratic variations in the wetting angles at the triple junctions. . . 126

NOMENCLATURE

Latin letters

A	: Area
<i>A</i>	: Surface diffusion anisotropy intensity
A_k^j	: Affinity of the <i>j</i> th chemical reaction taking place in <i>k</i> phase
<i>AFM</i>	: Atomic force microscopy
<i>BEM</i>	: Boundary element method
<i>c</i>	: Atomic volumetric concentration
<i>d</i>	: Distance
d_a	: Inter-atomic distance
D	: Dimension
<i>D</i>	: Diffusion constant
\tilde{D}_σ	: Self diffusivity
D_σ^0	: Minimum surface diffusivity corresponding to a specific surface orientation
<i>e</i>	: Unit electric charge
E	: Elastic modulus
<i>E</i>	: Electrostatic field
E	: Activation energy
<i>EDTI</i>	: Elastic dipole tensor interaction

EM	: Electromigration
$ESED$: Elastic strain energy density
EWI	: Electron wind intensity
F	: Helmholtz free energy
f	: Specific Helmholtz free energy
f_{ij}	: Surface stress tensor
\mathbf{F}	: Driving force
F_i	: Generalized force
FEM	: Finite element method
g	: Specific Gibbs free energy density
\check{g}	: Volumetric Gibbs free energy density
g_{vb}	: Specific Gibbs free energy of formation
\check{g}_{vb}	: Volumetric density of Gibbs free energy of formation
G	: Shear modulus
G^*	: Volumetric density of Gibbs free energy of formation
$GFEDoT$: Volumetric density of Gibbs free energy of formation
$GIEP$: Global internal entropy production
h_p	: Peak height
$IBEM$: Indirect boundary element method
IC	: Integrated circuit
IEP	: Internal entropy production
J_i	: Generalized conjugated flux

k	: Boltzmann constant
ℓ	: Curvilinear coordinate along the surface (arc length)
ℓ_0	: Arbitrary scaling length
L	: Half film length
L_{ij}	: Kinetic coefficients
<i>LISA</i>	: Linear stability analysis
m	: Dimensionless parameter that determine the crystal symmetry through the number of crystallographic directions corresponding to fast diffusion paths (half fold number)
m^*	: Effective mass of electrons
m	: Multiple order
M	: Mobility
<i>MEMS</i>	: Micro electromechanical systems
n	: Number of chemical species
\hat{n}	: Surface normal vector
N	: Density of moving species
N	: Density of conduction electrons
N_d	: Defect density
<i>NEMS</i>	: Nano electromechanical systems
<i>NSTS</i>	: Normalized and scaled time and space
\bar{P}	: Mean isotropic pressure in the layer
<i>PDE</i>	: Partial differential equation
q	: Heat received by the system

q^*	: Surface effective charge
Q	: Deviatoric part of the stress tensor
QD	: Quantum dot
\vec{r}	: Position vector
REF	: Rate of entropy flow
S	: Entropy
SK	: Stranski-Krastanov
SEM	: Scanning electron microscope
$STEM$: Scanning transmission electron microscope
\hat{t}	: Surface tangent
T	: Temperature
\vec{T}, \vec{t}	: Traction vector
TEM	: Transmission electron microscope
Tr	: Trace operator
TJ	: Triple junction
U	: Internal energy
u	: Displacement normal to the surface
$ULSI$: Ultra large scale integration
V	: Volume
v	: Velocity
$VLSI$: Very large scale integration
w, W	: Work

\bar{w}	: Film half width
WP	: Wetting parameter
Z	: Effective charge
Z^*	: Effective charge
x_i	: Atomic fractions

Greek letters

γ	: Helmholtz free energy density in NSTS
γ_f	: Normalized Helmholtz free energy of the film
γ_s	: Normalized Helmholtz free energy of the substrate
γ_{fs}	: Interfacial normalized Helmholtz free energy between the film and the substrate
$\gamma_{ij}, \gamma(\theta)$: Surface tension
$\tilde{\gamma}$: Surface stiffness
δ	: Variational operator
δ_{area}	: Fractional change in the area
ε	: Strain
η	: Infinitesimal longitudinal displacement along the TJ
θ	: Angle formed by the local surface tangent and the abscissa
κ	: Curvature
λ	: Wavelength
λ_{TJ}	: Wetting parameter
λ_c	: Critical wavelength

λ_m	: The wavelength which corresponds to highest growth rate
Γ	: Growth rate
μ	: Chemical potential
ν	: Poisson's ratio
ρ	: Resistivity
σ	: Stress
$\dot{\tau}$: Shear stress
τ	: Normalized time
τ_0	: Scaling time
τ_f	: Failure time
τ_e	: Equilibrium time
ϕ, θ	: The misorientation of the symmetry direction; tilt angle
χ	: Electron wind intensity
ω	: Reversible work done on the system
Δ	: Space-scaling operator
Ξ	: Elastic dipole tensor interaction
Σ	: Elastic strain energy density
Φ	: Energy received by the system
Ω	: Mean atomic specific volumes

Symbols

$d\xi_{\sigma}^j$: Extent of the j th chemical reaction taking place in σ phase
ϑ	: Electrostatic potential

φ : Dihedral angle

∇ : Del operator

∇^2 : Laplace operator

Subscripts

b : Bulk

em : Electromigration

ex : External

in : Internal

h : Hoop

ord : Ordinary point

\perp : Transverse

s : Surroundings

thrs : Threshold

v : Void

b : Bulk phase

σ : Interfacial layer

W : Wetting layer

Superscripts

– : Left hand side of the system

– : Right hand side of the system

i : Dummy index to denote a chemical species

j : Dummy index to denote a chemical reaction

long : Longitudinal

trans : Transverse

Signs over symbols

∨ : Denotes volumetric quantities

∧ : Denotes surface densities

∧ : Denotes normal vectors

→ : Denotes vector quantities

- : Denotes normalized quantities

Signs under symbols

- : Denote vectors

= : Denote tensors

CHAPTER 1

INTRODUCTION AND LITERATURE REVIEW

1.1 Motivation

The thin films have been inserted into engineering systems in order to accomplish a wide range of practical service functions. Among these are microelectronic devices and packages; micro-electro-mechanical systems (MEMS) or nano-electro-mechanical systems (NEMS). To a large extent, the success of this endeavor has been enabled by research leading to reliable means for estimating forces in small material systems and by establishing frameworks in which to satisfy the integrity or functionality of the systems. The material failure due to electromigration and stress continue to be a technology-limiting barrier. Due to continuing miniaturization of ultra large scale integration (ULSI) circuits, interconnects are subject to increasingly high current densities. Under these conditions, electromigration can lead to the electrical failure of interconnects in very short times by reducing the circuit lifetime to an unacceptable level. And the role of mechanical stress on the process is another important reliability issue. In systems with very small size scale and high temperature, stress of large magnitude can have a significant influence on the thin film surface evolution. Besides the reliability issues, mechanical stress has an important application in surface morphology control which provide potential opportunity for the controlled formation of patterned surfaces for many functional application. For example: evolution of nano-crystalline islands on surfaces which can be used as quantum dot. Small size, high temperature, large stress and high current densities are characteristics of interconnects, where the phenomenon of surface evolution is considerable scientific and practical importance. In this study, free surface evolution dynamics in connection with the morphological evaluation is investigated under the applied capillary force, electromigration force, and elastostatic force with anisotropic surface energy

and anisotropic diffusion by the use of unified theory of linear instability (LISA theory). The central question is the stability of the free surface under sinusoidal perturbations of its shape resulting from mass rearrangement and its evolution kinetics under the several combination of system variable (such as anisotropic surface energy, anisotropic diffusion coefficient, crystal structure texture, and initial sinusoidal wave amplitude-to-wavelength ratio, etc.). For this purpose, free surface morphology evolution and the sinusoidal perturbation drift and decay behaviors are tracked.

1.2 Epitaxial growth of thin films

Epitaxial growth process is a deposition of new material as a crystal on an underlying crystalline surface. The first study of this process was 150 years ago, but systematics of epitaxial growth was revealed by the work of Louis Royer in the 1920s. Royer used the term 'epitaxy' to define the notion of growing a new crystal whose orientation is determined by a crystalline substrate and to separate epitaxial growth from noncrystalline and amorphous growth.

Morphology of the film depends on a number of factors, including the deposition rates of the species, the surface temperature, the surface material, and its crystallographic orientation. The dependence of the morphology on the deposition rate of new material means that epitaxial growth is inherently nonequilibrium process. So it has an important distinction from crystal growth with solution, and is therefore a near-equilibrium process. Growth near equilibrium is almost governed by thermodynamics. For epitaxial growth process, the overall driving force for the morphological evolution of the surface is also provided by thermodynamics, but equilibrium is attained by kinetics.

Numerous experiments (Kern et al. [1], Venables et al. [2]) have showed that the epitaxial growth morphology shows the three distinct growth types for small amounts of one material deposited onto the surface of another material. These are referred to as: Frank-van der Merwe morphology, with flat single crystal films consisting of successive complete layers; Volmer-Weber morphology, with three-dimensional island that leave part of the substrate exposed; and Stranski-Krastanov morphology, with 3D island atop a thin flat 'wetting' film that completely covers the substrate (Fig.1.1).

For lattice-matched systems, Frank-van der Merwe and Volmer-Weber morphologies can be

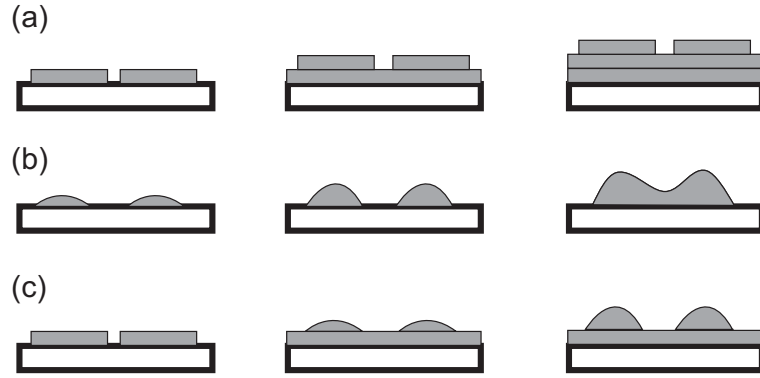


Figure 1.1: Schematic evolution of the (a) Frank-van der Merwe, (b) Volmer-Weber, and (c) Stranski-Krastanov growth morphologies [3].

understood from thermodynamic wetting arguments based on interfacial free energies. The Frank-van der Merwe growth mode is seen if $\gamma_f + \gamma_{fs} < \gamma_s$. Here, the free energy of epitaxial layer/vacuum interface denoted by γ_f , epitaxial layer/substrate interface denoted by γ_{fs} and substrate/vacuum interface denoted by γ_s . In The Frank-van der Merwe growth mode, the free energy decreases initially as the epilayers are formed before attaining a steady-state value for thicker films. Alternatively, if $\gamma_f + \gamma_{fs} > \gamma_s$ then Volmer-Weber growth is observed. Here, the free energy increases if epilayers are formed on the substrate. The Stranski-Krastanov morphology is observed in systems where there is appreciable lattice mismatch between the epilayer and the substrate. The Stranski-Krastanov growth mode is seen to be related to misfit strain, which changes the balance between interfacial free energies and the surface as the strain energy increases due to the film thickness. Therefore, although the growth of wetting layers is favored initially, the increasing of strain energy eventually makes subsequent layer growth undesirable. The deposition of additional material leads to the appearance of 3D islands within which strain is relaxed by the formation of misfit dislocations. However, there is another scenario within the Stranski-Krastanov morphology: the formation of islands without dislocations -called coherent islands (Fig. 1.2)- one or more wetting layers (Eaglesham and Cerullo [4], Madhukar and Rajkumar [5]). This phenomenon has been observed for a number of systems (Petroff and DenBaars [6], Seifert et al. [7]) and has the potential for many applications.

Although wetting arguments based on interfacial free energies provide a useful classification scheme for the equilibrium morphology of thin films, the inherently kinetic nature of epitaxial

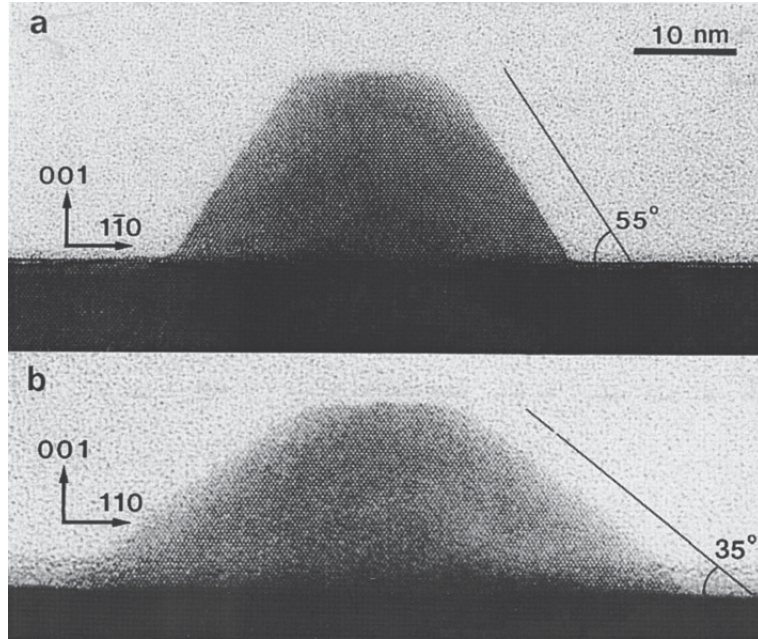


Figure 1.2: Cross-section micrograph of an uncapped InP island on GaInP grown by MOVPE at 580 °C along the (a) $[1\bar{1}0]$ and (b) $[110]$ directions (Georgsson et al. [8]).

growth means that fundamental issues are left open. Foremost among there is the competition between different strain relaxation mechanisms. For example, the growth of InAs on the three low-index surfaces of GaAs. The Stranski-Krastanov morphology is observed only on the (001) surface; on the other two orientations strain relaxation involves misfit dislocation formation and a two-dimensional (2D) growth mode (Belk et al. [9], Yamaguchi et al. [10]). For the growth of Ge and SiGe alloys on Si(001), strain relaxation can occur by several mechanisms of dislocation formation whose relative effects are determined by the morphology of the epilayer which, in turn, depends on the magnitude of the strain (Tersoff and LeGoues [11], LeGoues [12]). These observations suggest that heteroepitaxial phenomena particularly those involving materials with appreciable lattice mismatch occupy a far richer and much more complex arena than arguments based solely on thermodynamics would suggest.

1.2.1 Heteroepitaxy

The fabrication of heterostructures requires growing crystalline materials on the surfaces of different materials, a process called as heteroepitaxy. The morphology is central to the production of all quantum heterostructures. This morphology is determined by the interface

energies of the materials and the surface, strain is formed if the materials have different lattice constants, and any effects of segregation and alloying. Controlling the morphology during heteroepitaxy need understanding the atomistic mechanisms.

Kinetics of atomic processes on the surfaces of strained systems are not determined simply by the local environment of the atoms, as in the case of homoepitaxy, but may incorporate non-local information, such as the height of a terrace above the initial substrate or the size and shape of 2D and 3D islands. Then there is the issue of lattice relaxation at heterogeneous interfaces has relied largely on the minimization of energy functionals with various degrees of sophistication to determine equilibrium atomic positions near the interface as a function of the lattice mismatch.

Quantum dots formed from 3D islands during Stranski-Krastanov growth of InAs on GaAs (001) with 7% misfit have a number of fascinating and potentially useful characteristics (Leornard et al. [13], Moison et al. [14]). They are small enough to exhibit quantum effects in confined carriers. The dispersion about the size averages is between $\pm 10\%$ and $\pm 20\%$. The dot shapes are elongated truncated pyramids with well oriented sidewalls along one direction. This suggests that the structures of the individual dots are strongly influenced by thermodynamics, though the appearance of different facets suggests that kinetic factors cannot be neglected. Most important properties of these quantum dots is that they are coherent. The growth of InAs on GaAs(001) starts by nucleation of 2D islands which coalesce into coherently strained layers. These are the wetting layers in the conventional SK formation. An important property of the growth of the 3D islands is that at low temperatures, the material within the 3D islands can be accounted for simply from the accumulation of deposited material, but at high temperatures the volume of the island far exceeds the volume of InAs actually deposited. The conclusion is that the additional material comes from the wetting layers, so the 3D islands are InGaAs alloys. This demonstrates the active role of wetting layers in the final stage of SK growth (Joyse et al. [15]).

The tendency of 3D islands to form near atomic steps suggests that their positions may be influenced by an appropriately modified substrate. The controlled positioning of individual quantum dots reveal new opportunities for utilizing their properties, for example, as the active components in single-electron and resonant tunneling devices. Two strategies that have been used to manipulate the position of 3D islands are the strain-induced nucleation, and the local

large modification of substrate by etching.

Strain-induced nucleation provides a natural way of ordering 3D islands in the vertical growth direction. If two or more layers of 3D islands are grown sufficiently close to each other, then the islands on successive layers align with the extent of the alignment decreasing with increasing interlayer separation (Xie et al. [16]). When vertical separation increased alignment diminishes and the positioning of the islands becomes more statistical. Reason for this observation might be that the strain relaxation of 3D island is greatest in a region where the strain energy is a maximum. Thus just as the formation of 3D islands appears to be favored near steps of the wetting layer, so the strain relaxation caused by underlying 3D islands creates preferred regions for island formation on subsequent layers.

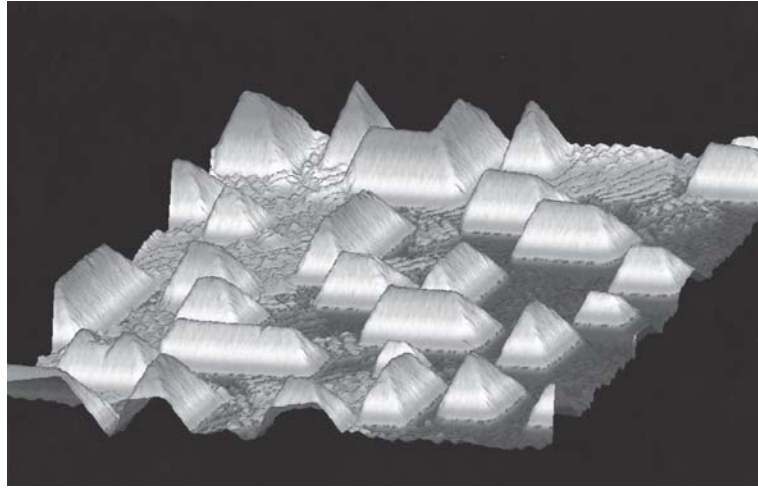


Figure 1.3: STM image ($1600 \text{ \AA} \times 1600 \text{ \AA}$) of Ge hut clusters grown in Si(001) at 575 K (B Voigtländer [17]).

The strain-induced 2D to 3D transformation during growth in the SiGe system with 4% misfit is manifested in a variety of surface morphologies whose characteristic feature size depends on the lattice misfit between the epilayer and the substrate. The growth of pure Ge on Si(001) follows SK growth with hut clusters (Mo et al. [18]) which appears quickly after the wetting layer formed. Structurally, they exhibit {105} facets and they are elongated along the $\langle 100 \rangle$ directions, with rectangular bases having up to 8:1 aspect ratio, therefore they show hut-like morphology. Their kinetics include metastability, since they dissolve during annealing, and self-limiting growth mechanism which causes larger islands to grow more slowly than small islands. Thus, smaller islands catch up to bigger ones, this cause uniform island size.

Therefore hut clusters natural candidates for producing arrays of quantum dots.

1.3 Role of stress on thin film morphology

Force per unit area is the definition of stress. Its unit is pressure, and in reality pressure is one variety of stress. However, it varies both with direction and with the surface it acts on so stress is a much more complex quantity than pressure. Mechanical stress in thin films is known as one of the most important issues when it comes to the application and reliability of thin film devices. The basic theory that accounts for the elastic-plastic changes in the bilayer was introduced by Frank and van der Merwe. It attempts to account for the accommodation of misfit between two lattices rather than being a theory of epitaxy per se. The theory predicts that any epitaxial layer having a lattice parameter mismatch with the substrate of less than $\sim 9\%$ would grow pseudomorphically, i.e., for very thin films the deposit would be elastically strained to have the same interatomic spacing as the substrate. The interface would, therefore, be coherent with atoms on either side lining up. With increasing film thickness, the total elastic strain energy increases, eventually exceeding the energy associated with a relaxed structure consisting of an array of so-called misfit dislocations separating wide regions of relatively good fit. At this point, the initially strained film would ideally decompose to this relaxed structure where the generated dislocations relieve a portion of the misfit. As the film continues to grow, more misfit is relieved until at infinite thickness the elastic strain is totally eliminated. In the case of epitaxial growth without interdiffusion, pseudomorphism exists only up to some critical film thickness h_c , beyond which misfit dislocations are introduced.

1.3.1 Morphology and surface stability of a stressed body

Two lattice planes of A and B and at least two lattice rows come in contact and in case of coherent epitaxy accommodate their two dimensional (2D) misfit. By this means the couple A/B stores a certain amount of elastic energy. The so-stored elastic energy has been recognized so far as a source of mechanical problems such as cracking, blistering, peeling. Then for many years the main problem of crystal growers was to avoid strain by choosing very low-mismatched systems. Nevertheless it has also been recognized that stress can modify some crystal properties. This is the case of the functional performance of devices such as the

possibility of band-gap engineering involving strained structures or the correlation between mechanical stress and magnetic anisotropy in ultra-thin films. These technological considerations have stimulated crystal growers to consider also crystal growth properties induced by stress. Nevertheless the problem of formation of a strained crystal on a single crystal is complex. The difficulties basically have three origins.

The first difficulty arises from the fact that since the equilibrium shape of a crystal essentially depends upon surface energy considerations, a good description of the thermodynamic state of a strained crystal needs to accurately define the role of stress and strain on specific surface energies. This can be done by properly defining surface stress and strain quantities as partially done by Gibbs, Shuttleworth, Herring and others.

The second difficulty arises from the fact that most strains are anisotropic and inhomogeneous. Because of the Poisson effect the in-plane strain due to misfit accommodation is accompanied by a vertical opposite strain. On the other hand, islands or nuclei can relax by their edges. Obviously this elastic relaxation depends on the shape of the island and therefore cannot be homogeneous. Thus a good description of the bulk elastic energy needs to calculate accurately elastic relaxation.

The third difficulty arises from the fact that, even weak, the elastic effects dominate at long range. Thus elasticity may also affect long-range behavior usually driven by surface diffusion considerations. In other words not only the energetics of crystal growth may be altered by elasticity but kinetics behavior may also be altered.

1.3.2 Elastic interactions of elastic defects

Since surface defects create a displacement field in the underlying substrate, surface defects interact by way of the underlying deformation. The interaction energy between two defects is simply the work done by the force distribution of first defect due to the displacement field generated by the other defect.

A lot of literature on elastic interactions between point defects exists for many situations. For defects at the surface, Rickman and Srolovitz have proposed a generalized approach. Each surface defect is characterized by its dimension (**D**) and its multipole order (**m**). An adatom thus is characterized by **D**=0 and **m**=1 (dipole), whereas a step (**D**=1) can be characterized by

$\mathbf{m}=1$ (dipoles) or $\mathbf{m}=0$ (monopoles) according to the nature of the step (step on a stress free surface or boundary in between two stressed domains).

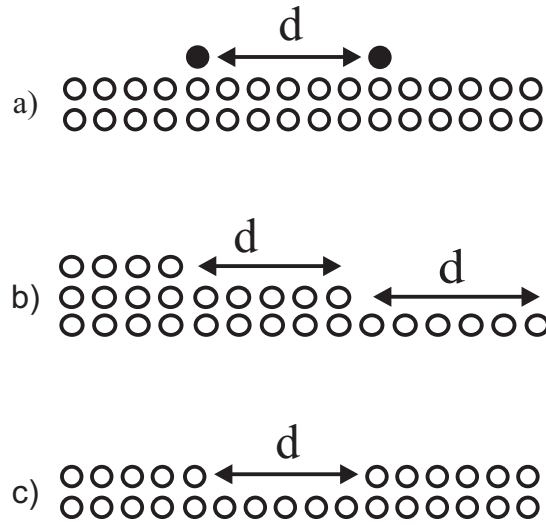


Figure 1.4: Elastic interaction in between: a) 2 adatoms considered as elastic dipoles ($\mathbf{D}=0$, $\mathbf{m}=1$), b) 2 steps bearing dipoles ($\mathbf{D}=1$, $\mathbf{m}=1$) of same sign or (and) monopoles ($\mathbf{D}=1$, $\mathbf{m}=0$) of same sign when the solid is stressed, c) 2 steps of opposite sign [19].

Integration along the line gives the interaction of a line of dipoles (step) and a dipole and result gives an interaction in d^{-2} . The elastic interaction between two steps on a stress free body is obtained by integration over the step of infinite length of the d^{-3} law then multiplied by the number of dipoles in the other step giving again a d^{-2} law. The interaction of adatoms (dipoles) with step of a stressed body (the step bears monopoles) gives an x^{-1} law interaction, so interaction changes sign with x axis. This result shows similar the interaction of a dipole and a semi-infinite sheet of dipoles. Indeed as in electrostatics a semi-infinite sheet of dipoles is equivalent to a distribution of monopoles located at the border of the sheet. Thus the interaction between a dipole and a step on a stressed body can be obtained by a supplementary integration of the d^{-2} law over the various rows of dipoles constituting the domain and thus give a x^{-1} interaction law. More recently Peyla et al showed that for very thin substrates things change too. For example identical adatoms deposited onto a true 2D isotropic layer may attract or repel each other according to the in-plane direction. The local force distribution seems to be responsible. For thicker sheets this effect goes backwards to usual d^{-3} repulsion valid for thick isotropic substrates.

1.3.3 Effects on diffusion constant

Strain also have an effect on the diffusion coefficient itself as shown by Schroeder and Wolf, they calculated the activation barriers for diffusion on strained high symmetry plane surfaces. The activation energy for diffusion is calculated by minimal energy path saddle point. They showed that for tensile stress activation energy is increased on the other hand for compressive stress cause lower activation. The diffusion barrier change is mainly due to a change of the saddle point energy whereas the minima are shifted only very little. In the same paper the authors have also studied theoretically diffusion on top of a stressed island. Since the finite size island can elastically relax by its free edge the strain along the top surface of the island becomes inhomogeneous and thus diffusion may vary from the center of the island towards its edges. For compressive strain the diffusion is faster near the island center whereas for tensile stress it is faster towards the edges. Thus it should be easier to nucleate on top of a tensile strained island than on top of a compressive strained island.

These two effects are second order effects in comparison to elastic interaction in between adatoms and steps. The simple surface diffusion change cannot modify the growth mechanism. More precisely since adatom density essentially depends upon the ratio Diffusion/Flux a strain-induced change of the surface diffusion constant (D) is exactly equivalent to an appropriate change of flux (F) and thus may only weakly shift the transition between step flow and $2D$ nucleation or change the nucleation density. At the same since the taller a crystal, the more relaxed its top face, this kind of elasticity-induced Schwoebel barrier thus can only help the first stages of the thickening of tensile islands.

1.4 Role of electromigration on thin film morphology

Electromigration is forced atomic diffusion with the driving force due to an electric field and associated electric current in metals (Arzt and Nix [20]). Electromigration is an important failure mechanism in integrated circuit metallization for two reasons. The first is that metal thin films can dissipate enormous power densities without melting and in turn can carry large current densities ($> 10 \text{ MA/cm}^2$ for aluminum). Thus, the driving force can be quite large. Second, the ratio of grain boundary/interface area to film cross-sectional area is large, leading to fast diffusion paths and high average mobility. Thus, the diffusion process itself is faster in

the interconnects which also enhance the effect.

In any transport process, the flux of material, J_e , can be described by the Nernst-Einstein diffusion relationship

$$J_e = \frac{\mathbf{NMF}}{kT} \quad (1.1)$$

Where \mathbf{N} is the density of moving species, M is their mobility and \mathbf{F} is the driving force for migration on each of these species. In electromigration, \mathbf{F} is the force exerted on a metallic atom by the passage of an electron flux and this force is made up of two contributions. The ionic core of the metal atom experiences a force due to the potential gradient across the conductor. This force is proportional to the valence of the metal and is directed in the opposite direction to the electron flux. The second contribution to \mathbf{F} comes from the electron wind force, which may be thought of as being due to collisions between the electrons and polarized vacancy-metal ion complexes. The momentum transfer between electron and ion usually results in a force directed in the same direction as the electron flux. In gold and aluminum the electron wind force is measured to be much greater than the field-ion force and so dominates the electromigration process.

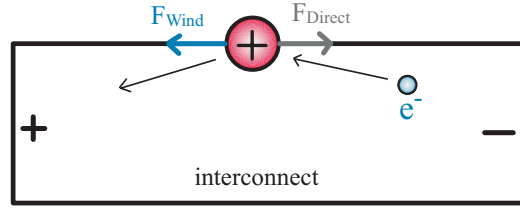


Figure 1.5: The driving force for electromigration.

$$\mathbf{F}_{total} = \mathbf{F}_{direct} + \mathbf{F}_{wind} \quad (1.2)$$

The electron wind force per atom, F , is proportional to the applied electrostatic field:

$$\mathbf{F}_{total} = Z^* eE \quad (1.3)$$

where the dimensionless number Z^* is known as the effective valance or the effective charge, e is the unit electrostatic charge and E is the electrostatic field.

The Value of Z^* has been expressed by Huntington and Grone [21], as

$$Z^* = \frac{1}{2} \left(\frac{\rho_d N}{\rho N_d} \right) \frac{m^*}{|m^*|} \quad (1.4)$$

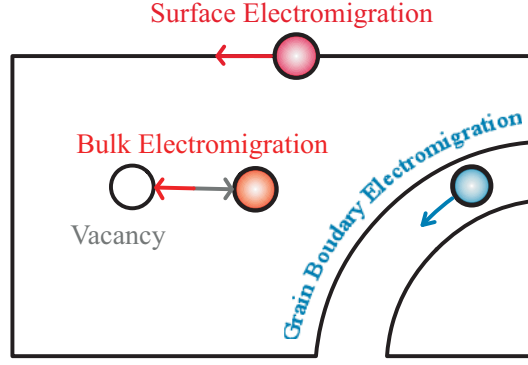


Figure 1.6: The diffusion paths of electromigration.

where \mathbf{N} is the density of conduction electrons, ρ_d is the specific defect resistivity, N_d the defect density, ρ is the metal resistivity, and m^* is the effective mass of the electrons near the Fermi surface taking part in the momentum exchange. This equation makes clear the close relationship between the fundamental process of electron scattering which contributes to electrical resistivity and the electronic scattering event that is the cause of the electron wind force. It is also clear that the vacancy-ion complex is important in electromigration just as it is in ordinary diffusion transport. Electromigration requires both a force on the metallic atom to encourage it to migrate and a mechanism for migration, in this case vacancy diffusion. The effective charge Z^* characterizes the momentum transfer, its value which is not well understood, can be inferred from experimental data. The Einstein - Nernst relation for diffusion in a potential field relates the drift velocity to the electron wind force, F :

$$v_{drift} = MF = \frac{D}{kT} F = \frac{DZ^*eE}{kT} = \frac{DZ^*e\rho j}{kT} \quad (1.5)$$

where $D = D_0 \exp\left(\frac{-Q}{kT}\right)$ is the diffusion coefficient, M is the mobility, k is Boltzman's constant, T is absolute temperature and j is the current density. In equation 1.5, electromigration induced mass flow is seen to be directly proportional to the current density and the diffusion constant D . The drift velocity, v_{drift} , will be a function of the diffusion pathway and the temperature dependence of v_{drift} will be characterized by the activation energy of the predominant diffusion mechanism, Q .

In the interconnect, atoms may diffuse along several paths: the surface of metal, the bulk crystal, and the grain boundaries. The schematic picture of these diffusion paths can be seen in Fig. 1.6. Since atoms are more loosely bonded at the grain boundaries than in the lattice,

atoms migrate along grain boundaries more easily than through the grain bulk lattice. Therefore, the grain structure is a critical factor in electromigration. But the surface diffusion is the fastest one due to the easy movement of adatoms at the surface. According to Lloyd [22], the activation energies, E , for the pathways are in general,

$$\mathbf{E}_{surface} = \frac{3}{2}\mathbf{E}_{grainboundary} = 3\mathbf{E}_{bulk} \quad (1.6)$$

Mass transport on the surface of interconnects is the sum of the electron field force and capillary forces:

$$J = \frac{D\delta}{\Omega kT} \left(-eZ^* + \Omega\gamma \frac{d\kappa}{dl} \right) \quad (1.7)$$

where J is the surface flux of atoms (the number of atoms passing per unit length per time), D is the surface diffusivity, δ is the thickness of the surface layer taking part in the diffusion process Ω is the atomic volume, γ is the surface energy, κ is the curvature of the surface (positive for a rounded void), and l is the arc length. The physical meaning of (1.7) is that atoms will diffuse in the direction of electron flow if the electric wind force dominates, but toward the position with large curvature if the capillary forces dominate.

From the above discussions it is clear that electromigration could not cause a failure unless there is a divergence in the flux somewhere in the interconnect that allows voids or hillocks to form. Flux divergence will occur whenever there are changes in F , the driving force for electromigration, or in D , the mobility of the diffusing species in the grain boundaries. F depends on Z^* and this parameter can vary both from grain boundary to grain boundary in a polycrystalline film and at contacts between two dissimilar metals. Therefore contact points of substrate and the interconnect, temperature gradient in the interconnect, grain structure, and photolithography or etch defects are some examples to the source of flux divergence (Fig. 1.7).

These weak sites lead to the nucleation of edge voids or hillocks. After the nucleation, growth and movement of the defect is highly dependent on the microstructure and applied electromigration stress. By decreasing the interconnect width, electromigration failure depends on the grain structure is partially overcome, because interconnect width is strongly related to the grain structure. As the interconnect width decreases or the grain size increases, the grain structure changes from polycrystalline to a near-bamboo structure, and finally bamboo structure (Fig. 1.8). In polycrystalline interconnect grain boundaries form a continuous network. And as discussed above diffusion on grain boundary is faster than diffusion in lattice so the

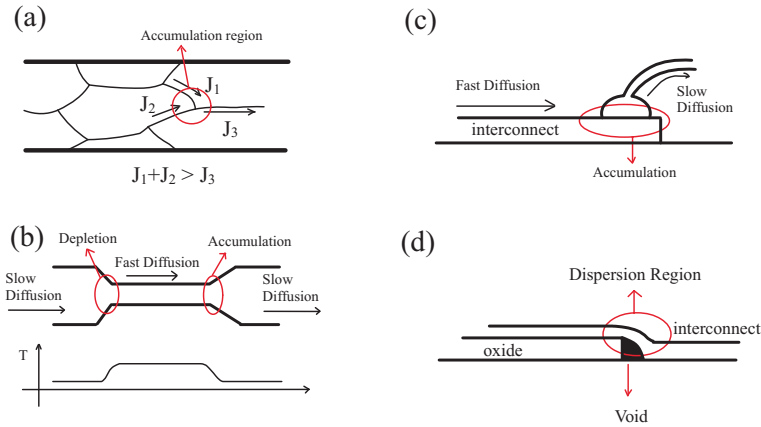


Figure 1.7: Schematic illustrations of several sites at which flux divergence is expected in metallization systems: (a) triple points in conductor layers; (b) regions where the conductor changes in width; (c) a gold wire/aluminum film contact; (d) at defects in an interconnect.

latter is negligible (Wang and Suo [23]). By contrast, a narrow interconnect has a bamboo-like grain structure, where grain boundaries are far apart and nearly perpendicular to the interconnect direction and hence do not aid in the diffusion process, thus in bamboo-like interconnects grain boundary diffusion becomes negligible. It is observed that the lifetime decreases to a minimum and then increases as the interconnect width decreases (Vaidya et al. [24]). This means that bamboo structured lines tend to show the greatest resistance to the electromigration induced damage. However, bamboo interconnects are not immortal yet. They still show

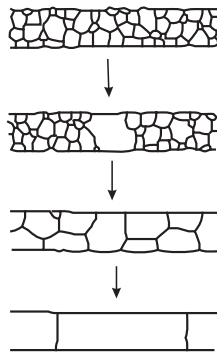


Figure 1.8: Increasing ratio of w/d .

various type failure modes. After the line is subject to an electric current, the void exhibit extra ordinarily complex dynamics: they disappear, re-form, drift, change shape, coalescence, and break up (Marieb et al. [25]). A particular behavior has captured much attention. A

void sometimes takes the shape of a slit, lying inside a single grain, severing the interconnect (Sanchez et al. [26], Rose [27]). Arzt et al. [28] reported that a void is round initially; it moves, grows, and then changes shape to become a slit.

Edge void or hillock migration may be understood in terms of surface diffusion. Atoms diffuse on the surface of the void or hillock from one portion to another, so that the void or hillock appears to translate in the grain.

1.5 Thermodynamics of surface stress

In this introduction the Gibbs convention will be used. In this convention the two phases α and β are thought to be separated by the Gibbs dividing plane, an infinitesimal thin boundary layer. The Gibbs dividing plane is an idealization, called an ideal interface. Guggenheim proposed an alternative model which defines the extended interfacial region.

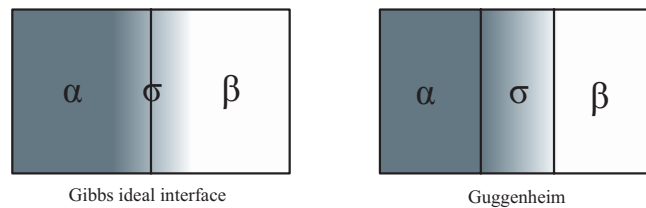


Figure 1.9: Left: Gibbs definition of the two phases α and β are separated by an ideal interface σ Right: Guggenheim defined interface as an extended interphase with a volume.

There is a quantity γ that represents the excess free energy per unit area due to the existence of a surface in the Gibbsian formulation. It can also be defined as the reversible work per unit area needed to create a new surface. The amount of reversible work dw performed to create new area $d\mathbf{A}$ of surface can be expressed as

$$dw = \gamma * d\mathbf{A} \tag{1.8}$$

The total work needed to create a planar surface of area \mathbf{A} (equivalently, the total excess free energy of the surface) is equal to $\gamma * d\mathbf{A}$.

Gibbs was the first to point out that for solids, there is another type of surface quantity, different from γ , that is associated with the reversible work per unit area needed to elastically

stretch a pre-existing surface. The elastic deformation of a solid surface can be expressed in terms of a surface elastic strain tensor ε_{ij} , where $i, j = 1, 2$. Consider a reversible process that causes a small variation in the area through an infinitesimal elastic strain $d\varepsilon_{ij}$.

One can define a surface stress tensor f_{ij} that relates the work associated with the variation in γA , the total excess free energy of the surface, owing to the strain $d\varepsilon_{ij}$:

$$d(\gamma A) = \mathbf{A} f_{ij} d\varepsilon_{ij} \quad (1.9)$$

Both f and γ can each be considered as representing a force per unit length, the former exerted by a surface during elastic deformation, and the latter exerted by a surface during plastic deformation. As a result, both f and γ have been referred to as surface tension. This has undoubtedly contributed to some of the confusion in the literature concerning the difference between them, and it is probably best not to use the term when discussing solid surfaces.

According to the thermodynamics of interfaces, γ_{ij} can be described as the area derivative of the surface free energy per unit area of an interface, either a solid-vapour, solid-liquid, liquid-liquid or liquid- vapor interface, respectively:

$$\gamma_{ij} = \left(\frac{\delta G}{\delta A_{ij}} \right)_{T,p,n} \quad (1.10)$$

or

$$\gamma_{ij} = \left(\frac{\delta F}{\delta A_{ij}} \right)_{T,V,n} \quad (1.11)$$

where G is the Gibbs free energy of the system and F the Helmholtz free energy, and A_{ij} the area of the interface between phases i and j . The subscript n denotes the assumption of adsorption equilibrium, in the case of multi-component systems. In the thermodynamics of interface-containing systems, both quantities, i.e. the Gibbs and the Helmholtz free energies, are defined as excess quantities, thus drawing an imaginary and arbitrary dividing mathematical surface (Gibbs surface) between the two phases separated by the interface.

When three phases are coexisting along an edge, we have three interfacial tensions. Assuming that one of the three phases is a vapor, we will write these as γ_β , γ_α , and $\gamma_{\alpha\beta}$. The edge of the mobile phase is at equilibrium under the tensions directed along the three interfaces. Equating the horizontal components of the forces in Fig. 1.10, we have

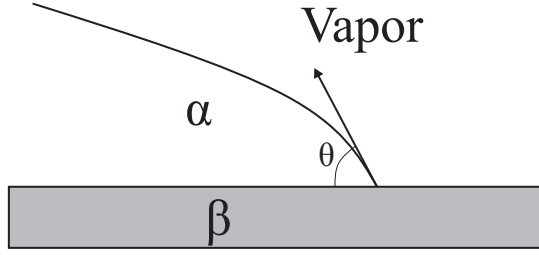


Figure 1.10: Interface among three phases.

$$\gamma_\beta = \gamma_\alpha \cos \theta + \gamma_{\alpha\beta} \quad (1.12)$$

θ is called as equilibrium angle; $\cos \theta > 1$ shows a non-equilibrium situation and seen if

$$\gamma_\beta - \gamma_{\alpha\beta} > \gamma_\alpha \quad (1.13)$$

or

$$\gamma_\alpha + \gamma_\beta - \gamma_{\alpha\beta} > 2\gamma_\alpha \quad (1.14)$$

$2\gamma_\alpha$ is called as cohesive energy, W_{coh}^α , of α phase. It is the required energy to separate the α phase and $\gamma_\alpha + \gamma_\beta - \gamma_{\alpha\beta}$ is called as adhesive energy, $W_{adh}^{\alpha\beta}$, of $\alpha\beta$ interface. Spreading coefficient, $S^{\alpha\beta}$, can be defined as

$$S^{\alpha\beta} \equiv +\gamma_\beta - \gamma_\alpha - \gamma_{\alpha\beta} = W_{adh}^{\alpha\beta} - W_{coh}^\alpha \quad (1.15)$$

If $S^{\alpha\beta} > 0$, in the horizontal case, α phase will spread over the surface β and this is called complete wetting.

1.6 Thermodynamics of Irreversible Processes

Generally, thermodynamics is divided into statistical and phenomenological description. The statistical description begins with initial events, like molecular encounters, and describes

larger systems with statistical methods. The phenomenological description of thermodynamic processes starts with experimental observations and continuum assumption, and follows a more technical perspective. The foundation of irreversible thermodynamics is the concept of entropy production. The consequences of entropy production in a dynamic system lead to a natural and general coupling of the driving forces and corresponding fluxes that are present in a non-equilibrium system.

Irreversible thermodynamics introduce the term dissipative structures to contrast such structures from the equilibrium structures. They provide an example of non-equilibrium as a source of order. They can exist in far from equilibrium conditions only through a sufficient flow of energy and matter.

1.6.1 The fundamental principles of irreversible thermodynamics

For certain processes, the fluxes at any given instant depend on the values of the forces (affinities) at that instant. These processes have no memory and are called Markoffian processes. A non-Markoffian system or process has memory in the sense that the fluxes will depend on the forces applied at previous times as well as on those applied at the present. A resistor is an example of a Markoffian system, whereas a capacitor is non-Markoffian.

Generally, the fluxes J_i can be expanded in a power series as functions of the forces with no constant terms all J_i are known to vanish as the forces F_j vanish. The results give

$$J_i = L_{ij}F_j + \frac{1}{2!}L_{ijk}F_jF_k + \frac{1}{3!}L_{ijkl}F_jF_kF_l + \dots, \quad (1.16)$$

where $L_{ij} = (\partial J_i / \partial F_j)_{F=0}$ and $L_{ijk} = (\partial^2 J_i / \partial F_j \partial F_k)_{F=0}$ are the kinetic coefficients and second-order kinetic coefficients, respectively, and so forth.

Because the applied forces are usually very small, a truncated form of the power series of Eq. 1.16 gives to a very good approximation the phenomenological relation

$$J_i^\alpha = L_{ij}^{\alpha\beta} F_j^\beta \quad (1.17)$$

which represents a linear Markoff process. Here, J_i^α and F_j^β are the fluxes and driving forces,

respectively. The $L_{ij}^{\alpha\beta}$ are the phenomenological coefficients that are related to the conductivities $K_{ij}^{\alpha\beta}$ but will not, in general, be identical to them. The phenomenological coefficients L_{ij} are mostly of empirical nature and must be determined experimentally depending on the material characteristics. This relationship may be classified by the following:

$L^{\alpha\alpha}$ Related to the conjugate or proper conductivities σ, k, D

$L^{\alpha\beta}(\alpha \neq \beta)$ Related to the cross or interference conductivities as, for example, thermoelectric, electrodiffusive, and thermodiffusive coefficients.

The gap between thermodynamic equilibrium and an irreversible (steady-state) process is bridged by considering the micro fluctuations in a system at local equilibrium. With this, we may state the principle of microscopic reversibility as follows.

For a system in thermodynamic equilibrium, every type of micro motion occurs just as often as its reverse. (Principle of microscopic reversibility)

Using fluctuation theory for the small spontaneous motions around thermodynamic equilibrium, Onsager (after Lars Onsager, 1903 – 1976) proved what is now referred to as Onsager's principle.

A simple statement of Onsager's theorem is given as follows: Provided a proper choice is made for the fluxes J_i and driving forces F_j , the matrix of phenomenological coefficients (L_{ij}) is symmetrical, that is

$$J_{ij}^{\alpha\beta} = L_{ji}^{\beta\alpha} \text{ and } J_{ij}^{\alpha\alpha} = L_{ji}^{\alpha\alpha} \text{ (} i, j = 1, 2, \dots, n \text{), but } J_{ij}^{\beta\alpha} = L_{ji}^{\alpha\beta} \quad (1.18)$$

The relationships, Eqs. 1.18, are called Onsager's reciprocal relations in the absence of a magnetic field. Note that only the $L^{\alpha\alpha}$ phenomenological coefficients have self-symmetry in the sense of $L_{ij}^{\alpha\alpha} = L_{ji}^{\alpha\alpha}$.

The criterion for Onsager's reciprocal relations is contained in the expression for entropy density production inside the system undergoing an irreversible process. This is expressed in quadratic form as

$$\dot{S} = \frac{\partial S}{\partial t} = \sum_{\alpha} J^{\alpha} F^{\alpha} = \sum_{\alpha\beta} L^{\alpha\beta} F^{\alpha} F^{\beta} > 0 \quad (s \text{ in units of energy} / l^3 t T) \quad (1.19)$$

where l is length (e.g., meter, m), t is time (e.g., second, s), and T is temperature (e.g., K) as in the SI system of units for which energy is given in joules, ($1 \text{ W} = 1 \text{ J/s}$). Thus, entropy density production is taken as the time variation of unrecoverable work per unit volume per unit temperature inside the system and whose quadratic form must be positive definite. In general, following requirements are asserted

- $S = 0$ (reversible process)
- $S > 0$ (irreversible process)
- $S < 0$ (a process that cannot occur without altering the system conditions)

The quadratic form of the entropy production is positive definite and implies that the matrix of phenomenological coefficients $L^{\alpha\beta}$ also be positive definite. Therefore determinant of the $L^{\alpha\beta}$ matrix and all of its minors be positive definite. Take, for example, a two-flow process involving a two-dimensional matrix $L^{\alpha\beta}$ given by

$$\begin{bmatrix} J^1 \\ J^2 \end{bmatrix} = \begin{bmatrix} L^{11} & L^{12} \\ L^{21} & L^{22} \end{bmatrix} \begin{bmatrix} F^1 \\ F^2 \end{bmatrix} \quad (1.20)$$

where $L^{12} = L^{21}$ according to Onsager's principle. The necessary and sufficient condition for Eq. 1.20 to be positive definite is that the 2×2 determinant of $L^{\alpha\beta}$ be positive definite. Thus,

$$\begin{vmatrix} L^{11} & L^{12} \\ L^{21} & L^{22} \end{vmatrix} = L^{11}L^{22} - (L^{12})^2 > 0 \quad (1.21)$$

Generally, the diagonal coefficients $L^{\alpha\alpha} > 0$ (i.e., are positive), but the $L^{\alpha\beta}$ coefficients can be positive or negative.

For thermoelectric coupling of electrical currents ($J^2 = I_{el}, F^2 = \Delta U_{el}$) with heat transfer ($J^1 = Q, F^1 = \Delta T$), the electrical measurement and the direct heat conduction over a thermocouple gives the conductivity values for L^{11} and L^{22} . In the case of absence of electrical current I_{el} , the voltage ΔU_{el} gives the Seebeck coefficient L^{12} in [V/K] for a given temperature difference ΔT . The temperature difference with given voltage ΔU_{el} and vanishing heat

flux gives the Peltier coefficient L_{21} . Measuring the heat flux and the voltage in the case of absence of electrical current gives additional experimental data for the coupling coefficients L^{12} and L^{21} .

1.7 Fluxes and driving forces for diffusion

Surface flux may arise from several different types of driving forces. For instance, a charged ion has tendency to flow due to an electrostatic field; a solute atom stimulates local volume dilation and tends to flow toward regions of lower hydrostatic compression. Chemical components tend to flow toward regions with lower chemical potential. All the driving forces can be collected and attributed to the generalized diffusion potential because different driving forces can arise for a chemical species.

1.7.1 Diffusional mass transport by capillarity

Capillarity is an important motivation for diffusion in many materials systems containing interfaces. The diffusion potentials of the components depend on the local interface curvature in the direct vicinity of an interface. Differences in diffusion potential will drive mass transport between these regions which have different curvatures so that the system reduces the amount of energy.

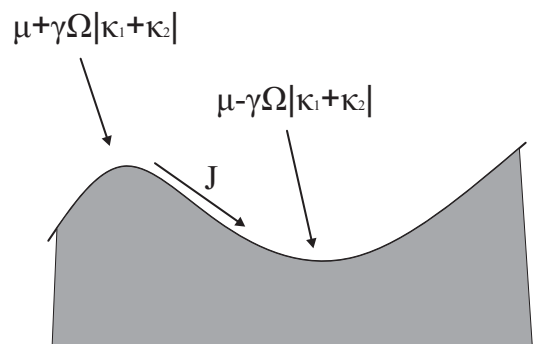


Figure 1.11: Positive and negative surface curvature. The curvature differences cause diffusion potential gradients that cause surface smoothing by mass transport.

Fig. 1.11 presents a pure crystalline material with a curved surface in which self-diffusion occurs by the vacancy exchange mechanism. Here, the diffusion potential of the atoms just

below the concave surface is lower than in the region where the surface is convex. This cause to establish a diffusion flux through the bulk from the convex area to the concave area to smooth the surface and reducing the total interfacial energy for isotropic case. Finding expressions for the atom flux and the diffusion equation in the crystal gives the rate of surface smoothing, and then solving the diffusion equation subject to the boundary conditions at the surface.

1.7.2 Diffusional mass transport in an electrical potential gradient

A gradient in electrostatic potential can produce a driving force for the mass diffusion of a species.

1.7.2.1 Charged ions in ionic conductors

The diffusion potential will be the electrochemical potential, if an electric field, $E = -\nabla\phi$, is applied :

$$J_1 = L_{11}F_1 = -L_{11}\nabla\Phi = -L_{11}\nabla(\mu_1 + q_1\phi) \quad (1.22)$$

which takes form

$$J_1 = -D_1\nabla C_1 - \frac{D_1 c_1 q_1^2}{kT} \nabla\phi \quad (1.23)$$

in the case of absence of significant concentration gradient, the resultant flux of charge is then

$$J_q = q_1 J_1 = -\frac{D_1 c_1 q_1^2}{kT} \nabla\phi \quad (1.24)$$

By the help of Ohm's law, $J_q = -\rho\nabla\phi$, the electrical conductivity, ρ , is

$$\rho = \frac{D_1 c_1 q_1^2}{kT} \quad (1.25)$$

Result shows that the diffusivity is directly proportional to the conductivity.

1.7.2.2 Electromigration in metals

Due to a cross effect between the diffusing species and the flux of conduction electrons, an applied electrical potential gradient can induce mass transport in metals. There are two fluxes in the system: a flux of conduction electrons, J_q , and a flux of the atoms, J_1 when an electric field is applied to a ionic core of the metal atoms in a metal. For a system at constant temperature with $F_q = -\nabla\phi$

$$J_1 = -L_{11}\nabla\mu + L_{1q}E \quad (1.26)$$

Evaluating the quantity L_1 , requires understanding the physical mechanism that couples the mass flux of the metallic atoms to the electron current. A force F_e on a diffusing particle which is proportional to the local current density is caused by the electron current in a metal. The force arises from the change in the self-consistent electronic charge distribution surrounding the defect. The defect scatters the current-carrying electrons and creates a dipole, which in turn creates a resistance and a voltage drop across the defect. This dipole, known as a *Landauer resistivity dipole*, exerts an electrostatic force on the nucleus of the interstitial. This current-induced force is usually described phenomenologically by ascribing an effective charge to the defect, which couples to the applied electric field to create an effective force. When this force is averaged over all jumps of a diffusing interstitial, an average force $\langle F^e \rangle$ is obtained which is proportional to E, so that

$$\langle F^e \rangle = \beta E \quad (1.27)$$

where β is a constant. This force, in turn, induces a diffusional drift flux of interstitials given by

$$J_1^e = \langle v_1 \rangle c_1 = M_1 \langle F^e \rangle c_1 = \frac{D_1 c_1 \beta}{kT} E \quad (1.28)$$

so

$$L_{1q} = \frac{D_1 c_1 \beta}{kT} \quad (1.29)$$

Consider now the interstitial flux in a material subjected to both an electrostatic driving force

and a concentration gradient.

$$J_1^e = -D_1(\nabla c_1 - \frac{c_1 \beta}{kT} E) \quad (1.30)$$

1.7.3 Diffusional mass transport in the presence of stress

Because stress affects the mobility, the diffusion potential, and the boundary conditions for diffusion, it both induces and influences diffusion. One can study the main aspects of diffusion in stressed systems by examining selected effects of stress in isolation. The elastic strain energy density can be given by

$$dw = \sigma_1 d\varepsilon_1 \quad (1.31)$$

When this work term is added to the chemical potential term, $\mu_1 dc_1$, and the procedure leading to

$$F_1 = -\nabla(\mu_1 + \sigma_m \Omega_1) \quad (1.32)$$

Therefore;

$$J_1 = L_{11} F_1 = -D_1(\nabla c_1 + \frac{c_1 \Delta \Omega}{kT} \nabla \sigma) \quad (1.33)$$

1.7.3.1 Stress effect on mobility

For the diffusion of atoms in an isothermal unstressed crystal, flux equation is given as

$$\bar{J}_1 = -L_{11} \nabla \mu_1 = -M_{11} c_1 \nabla \mu_1 \quad (1.34)$$

M_1 will be a tensor in non-uniform stress field because the stress will cause differences in the rates of atomic migration in different directions. When the jumping atom squeezes its way from one interstitial site to another there will be a distortion of the host lattice, and work must be done during the jump against any elements of the stress field that resist this distortion. Different amounts of work must be done against the stress field during these jumps because jumps in different directions will cause different distortions in the fixed stress field. So, the mobility should vary linearly with stress and be expressible as a tensor in the very general linear form

$$M_{ij} = M_{ij}^o + \sum_{kl} M_{ijkl} \sigma_{kl} \quad (1.35)$$

where the stress dependent terms in the sum are relatively small.

1.8 Literature review

1.8.1 Theoretical works

The reliability of the interconnects in integrated circuits has become a major concern for the microelectronics industry since 1966, when for the first time the failure of thin aluminum stripes on oxidized silicon due to electromigration is reported. The grainy structure of the interconnects have changed from polycrystalline to a bamboo structure with shrinking dimensions. The reduced number of grain boundaries increase the lifetime of such conductor lines. Nevertheless, these lines eventually fail because of electromigration, very often by the occurrence of slit-like transgranular voids.

The formation of the slits can be explained by several possible process. Slits may form because of stress induced grain diffusion if the void is on a grain boundary. Slits may also form due to electromigration induced surface diffusion. Suo et al. [29] have pointed out that there are two driving forces for diffusion: electromigration tends to promote the formation of slits, while surface energy tends to favor rounded voids. They suggest that a rounded void will collapse into slit if the electric current density exceeds a critical value. Detailed computations showed that if the surface diffusivity is isotropic, slits form parallel to the line and do not causes open circuits. However, if the surface diffusivity is anisotropic, Kraft and Arzt [32] and Gungor and Maroudas [35] pointed out that open circuits may form by this mechanism. They showed that slit voids will only form in grains with certain crystallographic orientations.

Kraft and Arzt [32] examined electromigration mechanism in unpassivated interconnects by both experimental and theoretical. Both theoretically and experimentally observed voids showed a typical asymmetric shape with respect to the direction of the electron flow. They conclude that shape of growing voids is largely determined by electromigration induced surface diffusion. Beside shape changes, the simulations also described void motion and growth. And also their TEM and SEM observations showed that interconnects usually contain large

number of voids, and that the behavior of voids is extremely complex. Voids continuously nucleate and heal during the life of the interconnect. Voids also migrate along the interconnect in the direction of current flow, changing their shape as they do so (Kraft and Arzt [28]).

During the theoretical studies, they applied finite difference and finite element formulations, and compared the results of numerical simulations with experimental studies. And they developed a model to predict lifetimes of interconnects and to describe the microscopic damage behavior, considering nucleation and growth of voids.

Oren and Ogurtani [78, 137] developed a mathematical model of the mass flow and accumulation on void surfaces under the action of applied electrostatic force field and capillary effects that follows from the conservation laws, and from fundamental postulates of linear irreversible thermodynamics, accounting for the effects of applied electric field, mechanical and thermal stress. Numerical simulations were run with and without the surface diffusion anisotropy, with the initial void shape critical asymmetric with respect to the direction of electron flow. These numerical experiments show that the two fold asymmetry in the anisotropic diffusion coefficient becomes a main factor in the development of a straight advancing slit, which accelerates the early open circuit failure due to a sharp slit hitting the upper edge of the interconnect.

Gungor and Maroudas [35] studied the complex problem of linear and non-linear dynamics of transgranular voids in thin films with bamboo grain structure. They simulated the formation of various morphological features: void faceting, formation of wedge-shaped voids, propagation of slit like and soliton like features. They presented the effects of anisotropy of void surface diffusivity on the stability of the interconnects. They show that morphological instabilities caused by simultaneous action of applied mechanical stress and electric field on transgranular dynamics of voids and propagation of slits (Gungor and Maroudas [36]).

Schimschak and Krug [37] proposed a continuum model of evolution of the surface that takes into account capillary driven diffusion and electromigration. They applied a one dimensional model of interface dynamics, which can be parameterized by a height function. The one dimensional geometry is convenient and relevant to the modeling of shape changes at the edge of an effectively two dimensional conductor line, but becomes inappropriate if the dynamics create overhangs. They studied numerically the motion and the shape evolution of an infinitely long isotropic interconnects.

The electromigration induced shape evolution of cylindrical voids was numerically examined in their work at 1998 with the same theoretical background in the previous work [38]. They observed two main routes. Protrusion develops at the leading end of the void, and forms a separate daughter void if the initial deformation is an elongation in the current direction. Since daughter is smaller, it moves rapidly and runs ahead of the mother void. If, on the other hand, the void is initially elongated perpendicular to the current, invagination develops which eventually splits the void horizontally.

Schimschak and Krug [39] add crystal anisotropy to their calculations in the work at 2000 and they simulate edge voids in addition to the voids in the interconnects. In this study, they allow the entire upper edge to evolve, and periodic boundary conditions are imposed along the current direction. And they observe that edge instability can lead to the formation of overhangs which subsequently pinch off and release voids into the interior of the strip.

Their calculations showed that most important parameter effecting void stability and evolution was to be founded to be the ratio of the void size to the characteristic length scale. Also crystalline anisotropy has a decisive influence both on the formation of voids at the edge of the line and on the evolution of fatal slits out of large edge voids.

Mahadevan et al. [40] studied edge instability in single crystal metal lines, applying a numerical phase field technique. They defined the critical value of the applied current when the edge perturbation grows to become a slit shaped void, and cause the circuit lifetime to an unacceptable level.

Mahadevan and Bradley [41] used a phase field method by accounting for electromigration, surface diffusion, and current crowding to simulate the time evolution of perturbation to the edge of a current carrying interconnects. They provided a fabrication criterion that guarantee the wire will not fail by formation of voids.

Also the stability of stressed solid surfaces under a variety of environmental conditions is still a challenging theoretical problem. Asaro and Tiller [42] made the first serious attempt to develop an equilibrium thermodynamic model of interfacial morphological evolutions during stress corrosion cracking by adding the elastic strain energy density (ESED) directly to the so-called chemical potential defined only at the surface layer. Like most authors, notably Srolovitz [43],[44] and Grinfeld ESED appear with a positive sign in their formula. That

means they are implicitly referring the molar Helmholtz free energy density rather than the molar Gibbs free energy density in their treatment. Therefore, their formulations are strictly valid for the isochoric systems that are bounded by the fixed rigid walls and/or the traction free surfaces in the absence of the external body forces. As shown by Ogurtani and Oren that the main reason for this apparent sign conflict between isobaric and isochoric systems, which starting with Herring in the literature is due to the fact that the interface displacement process has been treated as an isothermal reversible process by minimizing the total Helmholtz free energy function. This approach is further elaborated by Rice and Chuang in later studies. Their analysis produced an additional positive contribution such as ESED to the chemical potential as presented by Herring. The system studied by Rice and Chuang is related to the diffusive cavity growth under the uniaxial loading (i.e., grain boundary voiding), and is an isobaric system by definition since the system is exposed to the constant surface traction forces (i.e., uniaxial tension). The more realistic treatment of the isobaric problem would be the use of the dissipation function approach for the nonequilibrium processes as indicated by Fowler and Guggenheim. In such a treatment one should use the Planck criterion $[\delta F - \Delta W] < 0$ for natural isothermal changes by properly stating the necessary subsidiary conditions: the composite closed system is 1) under the constant applied stresses (dead loading); and 2) enclosed by diathermal boundaries to keep the temperature constant. Here the closed implies that no matter exchange takes place between the composite system and its surrounding. Designates the infinitesimal work done on the system. This proper nonequilibrium approach puts the generalized Gibbs free energy $[\delta F - \Delta W] \Rightarrow \delta G < 0$ back into a unique position for those thermodynamics systems so-called isobaric systems, which are exposed to the constant surface tractions and body forces, and evolving isothermally. It is strangely enough that the inner product of stress σ_{ij} and strain ε_{ij} tensors enters into the volumetric Gibbs free energy density with a negative sign. This generates a negative rather than positive contributions of the strain energy density to the thermal part of the Gibbs free energy density (i.e., by definition, it is the chemical potential for the single component systems) especially in those majority cases where the stress dependence of the entropy density is almost negligible. One should also mention here that this apparent sign conflict in the ESED also appears in other studies related to the interfaces and the triple junctions, which are all basing their work on the equilibrium treatment of Herring modified by Rice and Chuang, and dealing implicitly or explicitly with the isobaric systems exposed to the constant external stress fields through the surface tractions and body forces.

Chuang and Fuller [45] realized that the ESED contribution on the driving force is inadequate to explain the experimental findings. They postulated ad hoc reaction kinetic theory, where the activation energy depends on the applied stress system through the fictitious activation strain.

The motion of the interface between amorphous silicon (100) and crystalline under the non-hydrostatic stress were studied by Aziz et al. [46]. They have observed that SPEG growth rate on the compressive side of elastically bent wafers is lower on the tensile side. They have developed an activation strain tensor concept in connection with the kinetic expression.

The role of mechanical stress gradients as a driving force in conjunction with electromigration was first explored in a series of experimental and theoretical. It was reported (Blech [47]; Blech and Herring [48]) that a current density threshold exists below which Al mass transport is arrested. This threshold was found to be inversely proportional to the Al stripe length. Below a critical length there was no observable depletion or extrusion.

The dependence of depletion on strip length was explained by the effect of back stress. When electromigration transports Al atoms in a strip from cathode to anode, the anode will be in compression while the cathode will be in tension. On the basis of the Nabarro-Herring model of equilibrium vacancy concentration in a stressed solid, the tensile region has more, and the compressive region has fewer vacancies than the unstressed region. As a result, there exists a vacancy concentration gradient decreasing from cathode to anode. The gradient induces an atomic flux of Al diffusing from anode to cathode, and it opposes the Al flux driven by electromigration from cathode to anode.

The formation of macroscopic cracks in a stressed single crystal at elevated temperature has been discussed by Sun et al. [49]. They observed that small voids produced in the crystal during fabrication can change shape and volume as atoms migrate under various circumstances. Sun et al. [50] considered the morphological evolution of grains in a polycrystalline fiber, and applied a variational analysis to microstructure development by using mass transport mechanisms and thermodynamic forces. The free energy consist of the elastic, interfacial, chemical components and electrostatic. The rate process included grain boundary motion, creep, diffusion and interface reactions. In a later work, Sun et al. modeled the dynamics of thin film with two grain on a substrate [50]. They formulate with a finite element with bulk phase free energy density, surface tension anisotropy, and finite junction mobility. The authors formu-

lated the laws for the motion of grain boundaries and grain void interfaces. Sun and Suo study the large shape changes of solid due to matter diffusion on its surface.

Suo [51] investigate aluminum interconnects in the presence of insulator and shunts, subjected to temperature change and a direct electric current. He studied the evolution of interconnects into a segment of aluminum depleted near the cathode as a stable state with a linear pressure distribution in the rest of the line, and no further mass diffusion, and predict time for the interconnects to evolve into the stable state. He described the mechanisms for diffusive processes in solid structures of small sizes, between a few to hundreds of nanometers [52]. He applied the concept of free energy for microelectronic and photonic devices. The change of free energy creates a thermodynamic force which drives the configurational change of the structure. He made a physical description of forces of various origin that plays a role in morphological dynamics of interconnect lines, including elasticity, electrostatics, capillary, electric current.

Srolovitz [44] first investigate a stress applied to the solid in the direction nominally in the plane of the interface. The work of Herring (1950) on the stress assisted grain boundary diffusion considers only the stress normal to the surface, Srolovitz tried to adapt the chemical potential to work of Herring. Then by dropping Herring's formula Srolovitz [44] proceed along the line of Asaro and Tiller [42] by adding the elastic strain energy density to the chemical potential directly. All these models not only suffer from the sign conflict but also predict identical behavior for solids under tension and compression, because the stress enters through the elastic strain energy density quadratically.

Liniger et al. [53] studied the kinetics of void growth in unpassivated and electroplated copper lines. The effect of line-width and sample temperature on the void growth rate is studied by using the scanning electron microscope. Voids are observed to grow by consuming grains in a stepwise fashion, either by thinning out from the top down, or through a simple edge mechanism of displacement mechanism. In all cases, the primary diffusion path was surface diffusion for void growth. Grain boundaries provided a secondary diffusion path for polycrystalline lines. Hillock formation was observed to the anode end of the lines. Over time, hillock formation spread over the entire length of the line but the area just around the cathode end of the test structure. Voiding was initiated at the cathode end of the line, and start to grow along an apparent grain boundary. In the end, the void grew across the entire width of the line, leaving behind a small copper island.

Barviosa-Carter et.al. [54] in their recent publication tried to take into account the growth rate orientation anisotropy by adding a cofactor to their phenomenological mobility, without considering the additional importance of the surface tension anisotropy on the growth rate and faceting

Gungor and Maroudas, and collaborators, studied the complex linear and nonlinear dynamics and stability of transgranular voids in thin films exposed to the electromigration and external stress systems (isobaric) in a series of papers. They successfully simulated the formation of various morphological features: void faceting, formation of wedge-shape voids and propagation of slit-like and soliton-like features causing open circuit failure, and the healing effects of the electromigration on the stressed solid surfaces. Anisotropic properties are taken into account in the surface diffusion. In the stress applications, even though they employed Herring's chemical potential as modified by Rice and Chuang in their treatments. Their results are perfectly in agreement in predicting morphological instabilities caused by simultaneous action of applied mechanical stress and electric fields on transgranular dynamics of voids with the expense of the very high stresses. The main reason for their apparent success dealing with the isobaric system in their treatment of the stress induced instability is due to the fact that the strain energy density because of the sign conflict enters into the governing equation with a negative sign, which makes it effectively to behave similar to the compressive stresses and thus results in inherent instability if other subsidiary conditions are satisfied.

Spencer and Tekalign [55] have made extensive and very successful analysis on the morphological instability of growing epitaxially strained dislocation-free solid films. These analyses were based on the surface diffusion driven by the capillary forces and misfit strains by elaborating various types of wetting potentials associated with the thickness dependent surface specific free energy. In their work, similar to the simulation studies of the stability of epitaxially strained islands by Chiu and Gao [56], Zhang and Bower [57], Srolovitz [43], Krishnamurthy and Srolovitz [58], Medhekar and Shenoy [59], Golovin et al. [60], and Levine et al. [61] elastic strain energy density appears to be additive. Almost without exception, including the work on the equilibrium morphologies by Kukta and Freund [62], all numerical and analytical studies reported in the literature for the so-called steady state solutions of the nonlinear free moving boundary value problem utilized the periodic boundary conditions, and relied mostly on the instabilities initiated by the white noise or the small amplitude initial perturbations, where the film thickness is smaller than the wavelength of surface variations.

Healing phenomenon has been first reported very recently by Tomar et al. [63] who also produced very interesting linear instability analysis which reveals improved surface morphological stability over a range of misorientation angles between easy direction of surface drift diffusion and the electric field. First Averbuch et al. [64],[65] observed the healing effect of electromigration on the grain boundary grooving as a slowing down in the displacement kinetics in their rather early terminated numerical experiments.

1.8.2 Experimental observations

It is commonly reported that self-assembling of quantum dots (QD) goes through the classical stages of nucleation and growth of islands followed by a last sequence of coarsening. This part of review summarizes the current status of research in the field of nucleation, growth, and self-organization QDs. There are many theoretical and experimental works on the strain relaxation mechanisms but the influence of substrate orientations poorly investigated.

Berbezier et al. [67] made extensive work on (001) and (111) surfaces of SiGe, during their work they deposited $Si_{1-x}Ge_x$ with a thickness between just below the critical thickness of dislocation nucleation and higher than the theoretical critical thickness of island formation. They observed evolution between (001) and (111) surfaces, their observations showed on (001) surface unique formation of metastable coherent dislocation free islands. On Si (111) only two growth regimes are reported: **2D** layer-by-layer growth at low thickness and strain, and classical SK growth at high thickness and strain values. Undulations and dislocation-free islands were not observed on this substrate orientation.

On (001) the evolution of SiGe surfaces they observed four different regimes:

Regime I is characterized by a layer-by-layer growth with a gradual increase of surface roughness. This surface roughness primarily consists of dimer vacancies, kinks, and additional steps.

In regime II, ripple-like islands that show a extensive distribution in size and in shape are observed at low (h, ε) . The main feature of these is their side orientation along $\langle 100 \rangle$ directions. Furthermore, they show elongation in chains or in square patterns oriented along [100] and [010] at increasing thickness (Fig. 1.12). They state that such morphologies can be equilibrium structures of (001) surfaces when thin film is subjected to biaxial compressive

stress but it is evident that kinetic considerations cannot be ignored since kinetic instabilities observed in Si homoepitaxy which give rise to similar morphological evolution of layers.

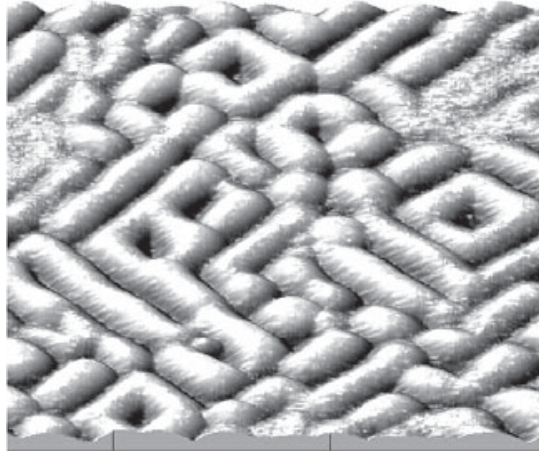


Figure 1.12: An AFM image of undulations elongated along $\langle 100 \rangle$ and $\langle 010 \rangle$ directions obtained in regime II for $Si_{0.85}Ge_{0.15}$ [67].

Starting from a ripple-like as grown surface, after 1 h 30 min annealing formation of fully strained hut islands are observed. After 18 h annealing, islands evolved towards large isolated huts with well-defined (105) facets. No further evolution occurred during the following 46 h annealing, they suggest that their morphology is stabilized by the compressive biaxial stress applied by the substrate to the islands.

In regime III, huts and domes are observed together (Fig. 1.13(a)). These island groups are characterized by various aspect ratios and shapes: pyramidal huts (Fig. 1.13(b)) and round-shaped huts (Fig. 1.13(c)) with the larger facets corresponding to $\{113\}$ and $\{111\}$ planes (Fig. 1.13(d)). Domes are favored in the higher-stress regime, while huts are favored in the lower-stress regime. Huts represent the steady-state morphology of this regime. Because stress relaxation is energetically favored, the islands are largely relaxed and the steady-state morphology consists of domes at higher misfit. So, even if the formation of huts is possible during growth, they will rapidly transform into domes, during any annealing.

In regime IV, a bimodal size distribution of domes is observed. They correspond to dislocated and coherent structures. Hut islands are never observed in this regime. The steady-state morphology consists of larger-sized relaxed islands.

They also investigate the role of step density and of stress on the onset/evolution of the

The huts are formed initially as square shaped because of the fourfold symmetry of the surface with relatively low surface energy of {105} surface (Fig. 1.14(a)). The transition to the dome is mainly because of the elastic deformation energy, the steeper sides of the dome allow better relaxation of the strain in the 4% lattice mismatched Ge cluster (Fig. 1.14(b)).

Narayan et al. [68] developed two efficient and reliable methods of creating self-assembled Ni nanodots of uniform size embedded in amorphous and crystalline matrices practically over any substrate. The method is based on pulsed laser deposition, where the size of nanoparticles and self-assembly are determined by the flux, interfacial energy, substrate temperature, and pulsed laser deposition variables. The formation of epitaxial nanodots with a large misfit over 7 to 8 pct shows a major challenge until the discovery of domain matching epitaxy. Using domain matching epitaxy, they demonstrate an epitaxial growth of nickel nanodots on TiN with a lattice misfit over 16 pct, and they showed that these epitaxial nanodots can be self-assembled to form three-dimensional nanostructures. The self-assembly of Ni nanodots is possible by controlling the kinetics of clustering in a narrow range of deposition and substrate variables to overcome thermodynamic driving forces leading to Ostwald ripening.

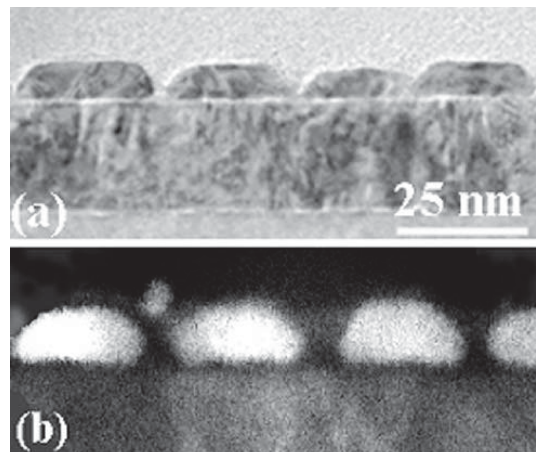


Figure 1.15: Ni clusters in the TiN metallic matrix: (a) low-magnification TEM image and (b) STEM Z-contrast image [68].

Fig. 1.15 shows the low-magnification TEM (a) and STEM Z-contrast image (b) of Ni nanodots embedded in a metallic TiN matrix. Here, nickel nanodots grow as truncated pyramids. The size of nanoparticles and separation between different monolayers can be controlled by relative fluxes of two constituents. By changing the size distribution in different layers, they can also create functionally gradient materials. They can create a smaller size near the top for

blue light via quantum confinement, intermediate size in the middle for green light, and large size for red light [68].

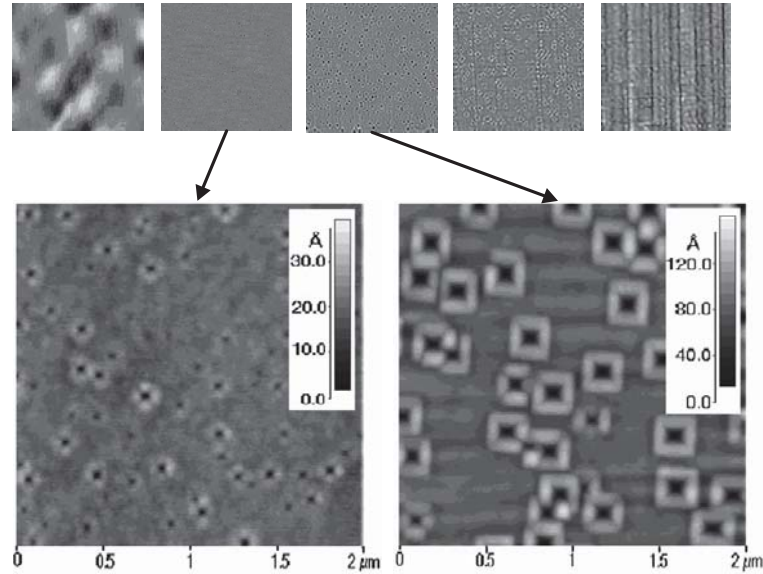


Figure 1.16: Evolution of the quantum fortress surface morphology for growth of $Ge_{0.3}Si_{0.7}/Si(100)$ at a growth temperature of $550\text{ }^{\circ}\text{C}$ and a growth rate of $0.9\text{ }\text{\AA}\text{s}^{-1}$. AFM scans are $5\text{ }\mu\text{m}\times 5\text{ }\mu\text{m}$ in area. $Ge_{0.3}Si_{0.7}$ film thicknesses are (a) 0 nm; (b) 15 nm; (c) 30 nm; d) 53 nm; (e) 100 nm [69].

Hull et al. [69] described new approach to patterning of Si(100) surfaces for controlled nucleation of heteroepitaxial Ge semiconductor clusters (Fig. 1.16). The method create self-assembly of strain-stabilized quantum quadruplet and quantum fortress structures, whereby cooperative island nucleation around shallow strain-relieving pits is observed during $Ge_xSi_{1-x}/Si(100)$ heteroepitaxy. These configurations are kinetically limited structures that exist over a range of compositions, growth temperatures, and growth rates, but they are destabilized by strain relaxation. These formations are strain-stabilized, as the strain disappears due to the introduction of misfit dislocations, so do the quantum fortresses. These configurations are meta-stable structures, they stabilized only through a relatively narrow range of kinetic pathways. For example, at a composition of $x = 0.3$ and a growth temperature of $550\text{ }^{\circ}\text{C}$, they observe the fortresses at growth rates of 0.9 and $3.0\text{ }\text{\AA}\text{s}^{-1}$, but not at $0.15\text{ }\text{\AA}\text{s}^{-1}$. These structures are not present at temperature of $650\text{ }^{\circ}\text{C}$ for a growth rate of $0.9\text{ }\text{\AA}\text{s}^{-1}$. Thus, it is clear that if surface diffusion lengths are high enough, the quadruplet fortress morphologies do not form, instead the standard hut cluster-like morphologies are observed.

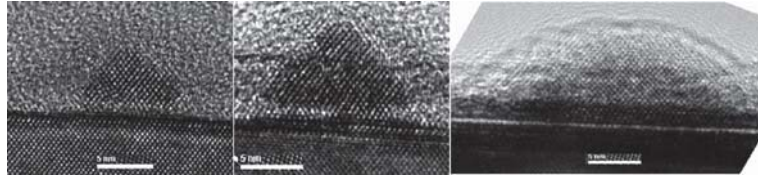


Figure 1.17: InAs dot shape evolution from pyramid to dome transition on Si (001) [70].

Zhao et al. [71, 70] used MBE for InAs quantum dots on Si (001) surface, growth proceeded with Volmer-Weber growth mode. Fig. 1.17 shows the InAs dots shape evolution. Islands go through a pyramid shape which is bordered by $\{111\}$ facets to multi faceted dome shape with increase in size.

Initially ideal vicinal surface should have a step meandering instability according to Bales and Zangwill [72]. The evidence of meandering instability was showed by Helium diffraction experiments of Schwenger et al. [73] in 1997. Later they made detailed analysis of the characteristic wavelength of meandering as a function of temperature with STEM images of copper surfaces with uniformly meandering.

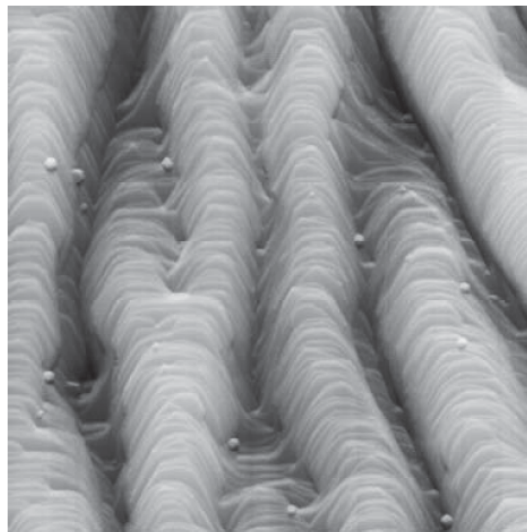


Figure 1.18: Cu(21 21 23) surface with meandering instability after 600 monolayer of copper at 313 K ($400nm \times 400nm$) [74].

Fig. 1.18 illustrates the meandering instability on Cu (21 21 23) surface which is vicinal to Cu (111) with a terrace width of $21+2/3$ atoms rows. The steps has a nearly strait segments in the dense atom packing directions at 60° angle with horizontal step orientation.

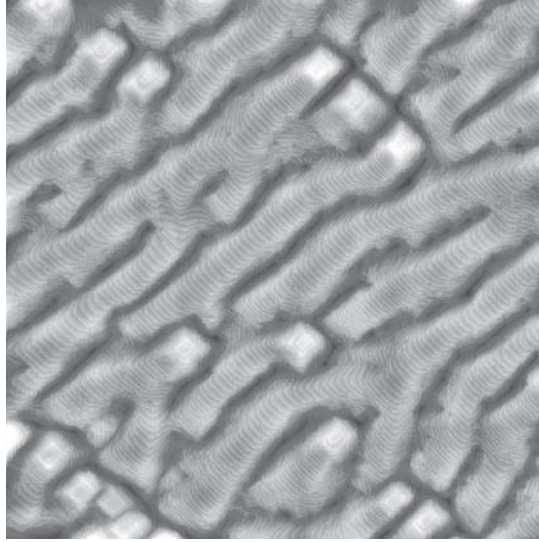


Figure 1.19: STEM image of Cu(1 1 1) surface ($200 \times 200 - nm^2$) after deposition of 80 ML at $F = 1.8 \times 10^{-2}$ ML/s and $T = 285$ K sample temperature [75, 76].

Maroutian et al. [76, 75] observed BZ instability experimentally. They showed that homoepitaxial growth of Cu surfaces develops a surface instability, causing a patterning of surface with temperature and flux dependent characteristic wavelength. Their observation showed that according to the step stiffness anisotropy level, morphology of BZ instability can be seen either smooth wave or sawtooth form. They also observed pyramidal formations.

Muller et al. [77] proposed a new method to obtain the surface stress anisotropy of silicon based on modifications of the Si equilibrium shape by means of electromigration (Fig. 1.20). To create faceting on Si surface they used electromigration. The main assumption is that though electromigration is the driving force for faceting, the period remains fixed by elasticity. They used following equation to predict surface properties.

$$\lambda = \frac{2\pi c}{\sin(\pi\delta)} \exp\left(1 + \frac{\pi E\rho}{2f^2(1-\nu^2)}\right) \quad (1.36)$$

with $f^2 = (s_\tau^\alpha - s_\tau^\beta)^2 + 4s_\tau^\alpha s_\tau^\beta \sin^2(\frac{\alpha+\beta}{2})$, α and β the angles the facets form with the original orientation, $\delta = \frac{tg\alpha}{tg\alpha+tg\beta}$ a geometrical factor and c an atomic unit. The surface-stress components s_τ^i which appear in Equation 1.36 are the surface-stress components perpendicular to the edge τ which separates the facets α and β .

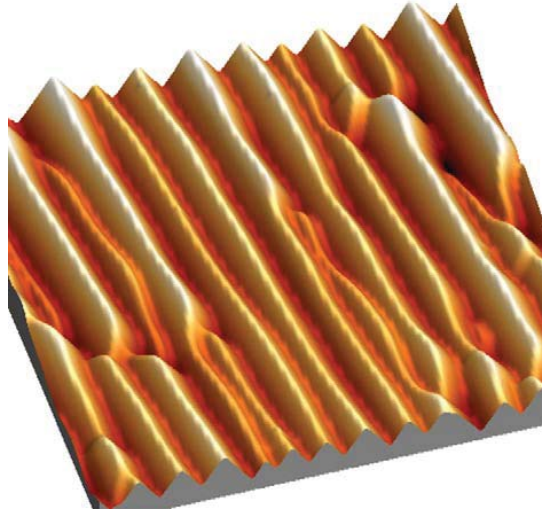


Figure 1.20: AFM image of a Si (118) surface heated by a direct current during 150 h at 1373 K. Faceted structure of period $\lambda = 6 \mu\text{m}$ and height $0.6 \mu\text{m}$ created by electromigration due to the ascending current. (001) and (113) are the so-formed facets. The period gives access to the difference $s_{\tau}^{(001)} - s_{\tau}^{(113)}$ with τ the common edge shared by the (001) and (113) facets [77].

1.9 Outline of the thesis

Chapter 1 introduces the background of current research and gives literature review to research works conducted by previous researchers. Chapter 2 introduces the theoretical basis of computational model for the surface morphology evolution with both elastostatic and electrostatic basis. Chapter 3 explains the numerical methods and some important functions used. Chapter 4 investigates the surface dynamics and stability of an thin film and interconnect which has sinewave perturbation at one surface under the applied mechanical and electrical force. And some special effects of texture, mechanical load and applied potential combinations are discussed. Chapter 5 investigates the island formation in epitaxially strained flat droplets with crystallographic texture and misfit strain. Chapter 6 concludes the thesis and suggests the future research directions.

CHAPTER 2

IRREVERSIBLE THERMOKINETIC THEORY OF INTERFACES

2.1 Introduction

To begin with, it will be useful to give a brief definition of the terms morphology and structure. The term morphology is associated with a macroscopic property of solids. The word originates from the Greek $\mu\omicron\rho\phi\eta$, which means form or shape, and here it will be used to refer to the macroscopic form or shape of a surface or interface. Structure, on the other hand, is associated more with a microscopic, atomistic picture and will be used to denote; the detailed geometrical arrangement of atoms and their relative positions in space.

The most general macroscopic approach to a problem in the physics of matter is that of thermodynamics. The specific features associated with a thermodynamic description of an interface are illustrated. This chapter focuses on the irreversible or non-equilibrium thermodynamic treatment of the morphological evolution dynamics of surfaces and interfaces composed of ordinary points (Ogurtani and Oren, [78]). By relying only on the fundamental postulates of linear irreversible thermodynamics as advocated by Prigogine [79] for the bulk phases, Ogurtani (2000) has obtained a compact and rigorous analytical theory of a network of interfaces by utilizing the more realistic monolayer model of Verschaffelt (1936) and Guggenheim [80] for the description of interfaces and surfaces. A brief summary of Ogurtani theory is reported recently by Oren and Ogurtani 2002 in connection with their computer simulation studies on the effect of various combinations of grain textures on the life time and the failure mechanisms of thin film interconnects.

2.2 Irreversible thermo-kinetics of micro-discrete open composite systems with interfaces

The term microscopic region refers to any small two or three-dimensional region containing a number of molecules sufficiently large not only for microscopic fluctuations to be negligible but also all of the intensive properties are homogeneous in space. The composite system, considered here, has at least two physico-chemically distinct domains (or phases in most general sense) separated by thin layers of interfaces, that are not only mutually interacting by the exchange of matter and energy but they are also completely open to the surroundings through the moving or immobile boundaries.

In this theory, the general view points of Guggenheim , Van Der Waals and Bakker [81] are adopted as far as the interface between any two phases or domains is concerned. Namely, the interface is autonomous, finite but a thin layer across which the physical properties and/or the structures vary continuously from those of the interior of one phase to those of the interior of the other. Since the interfacial layer is a material system with well-defined volume and material content, its thermodynamic properties do not require any special definition. One may speak of its temperature, entropy, free energy, and composition and so on just as for a homogeneous bulk phase. The only functions that call for special comment are the pressure and the interfacial (surface) tension.

The total reversible work, $\delta\Delta\omega$, done on a flat surface phase with micro-extent, indicated in terms of Δ space-scaling operator, by variations of its volume $d\Delta V_\sigma$, and area $d\Delta A_\sigma$ (keeping its material content unaltered, but stretching) is given by the following well known expression, assuming that the component of the stress tensor along the surface normal P is quasi-homogeneous in the layer and other transverse two components denoted by P-Q are equal (rotational symmetry) but heterogeneous (in the absence of electrostatic and other non-mechanical force fields),

$$\delta\Delta\omega = -\bar{P}d\Delta V_\sigma + \gamma d\Delta A_\sigma \quad (2.1)$$

where, \bar{P} is the mean isotropic pressure in the layer, and γ is called the surface tension, whose value and the location of the surface in which it acts can be uniquely determined by the knowledge of the transverse component of the stress tensor as demonstrated by Buff (1955).

Its value may be given roughly by

$$\gamma = \int_0^{h_\sigma} Q dz \quad (2.2)$$

where, Q is the deviatoric part of the stress tensor and h_σ is the thickness of the surface layer and the integration is performed along the surface normal. The above given expression for the reversible work becomes $-\bar{P}d\Delta V_\sigma$ for a homogeneous bulk phase in the formulation of the first law of thermodynamics. In the conventional theory of irreversible processes (Prigogine [79] and Glansdorff and Prigogine [82]), it has been postulated that the Gibbs formula, which is derived for the reversible changes, is also valid for irreversible processes. However in the present formulation, it is tacitly postulated that the differential form of the Helmholtz free energy in equilibrium thermodynamics has the same validity for irreversible changes. Mathematically this assumption is exactly equivalent to the Gibbs formula used extensively in standard treatment.

The local anisotropic properties of the medium are now automatically embedded in the intensive variables, which are characterized by second order tensors or dyadics. Hence the Helmholtz free energy for an open surface phase of a micro-extent may be written as,

$$d\Delta F_\sigma = -\Delta S_\sigma dT_\sigma - P_\sigma d\Delta V_\sigma + \gamma d\Delta A_\sigma + \sum_i \mu_\sigma^i d\Delta n_\sigma^i - \sum_j \Delta A_\sigma^j d\xi_\sigma^j \quad (2.3)$$

where, ΔS_σ denotes the entropy, μ_σ^i denotes the chemical potential, Δn_σ^i is the number of i^{th} chemical species in the micro-element, $d\xi_\sigma^j$ is the extent of the homogeneous j^{th} chemical reaction taking place in the phase under consideration, and ΔA_σ^j is the affinity of the homogeneous j^{th} chemical reaction and is related to the chemical potentials and the stoichiometric numbers as defined by Th. De Donder et al. (1936).

In above relationship, it is assumed that, in a single phase only the homogeneous chemical reactions take place and the phase transitions occurring at the mobile boundaries are not considered in the last term. The Helmholtz free energy change due to the passage of the substance from the phase to the surroundings is accounted by the fourth term in above expression (frozen chemical reactions). Therefore, in the case of a close system, one should subtract only

the term given by $\sum_i \mu_\sigma^i d\Delta n_\sigma^i$, which is closely related to the direct exchange of matter with the surroundings.

For the bulk phase, b , (α or β), one may rewrite very similar expression namely,

$$d\Delta F_b = -\Delta S_b dT_b - P_b d\Delta V_b + \sum_i \mu_b^i d\Delta n_b^i - \sum_j \Delta A_b^j d\xi_b^j \quad (2.4)$$

In the case of a composite system as defined previously, the total Helmholtz free energy differential can be immediately written down from Eqs. (2.3 and 2.4) by using the fact that the extensive thermodynamic quantities are additive. If there would be thermal, hydrostatic and physico-chemical equilibrium in the multi-phase system with plane interfaces there is no need to add subscripts to T , P and μ^i ; there must have values uniform throughout the various phases (bulk and surface) present in the system. For the present non-equilibrium case, first it will be assumed that no such restrictions on the system, but later a system at thermal equilibrium will be treated. For the present problem the system is an open composite system, and it is composed of two bulk phases and two surface phases (the interface between void and interconnect, or interconnect and its surrounding).

The entropy of the system is an extensive property; therefore if the system consists of several parts, the total entropy of the system is equal to the sum of the entropies of each part.

The entropy of any system whether it is close or open can change in two distinct ways, namely by the flow of entropy due to the external interactions, $d\Delta S_{ex}$, and by the internal entropy production due to the changes inside the system, $d\Delta S_{in}$. Symbolically, one may write this as,

$$d\Delta S = d\Delta S_{in} + d\Delta S_{ex} \quad (2.5)$$

The entropy increase $d\Delta S_{in}$ due to changes taking place inside the system is positive for all natural or irreversible changes, is zero for all reversible changes and is never negative. For a close system external entropy contribution has a very simple definition, and it is given by $d\Delta S_{ex} = \delta q/T$ where δq is the heat received by the system from its surroundings. Now, let us generalize the first law of thermodynamics for any infinitesimal change associated with an open system. For an open system, in which not only the energy but also the matter exchange takes place between the system and its surroundings, the conservation of energy becomes,

$$\delta\Delta\Phi = d\Delta U - \delta\Delta\omega = d[\Delta F + T\Delta S] - \delta\Delta\omega \quad (2.6)$$

where, $\delta\Delta\Phi$ is the energy received by the system, in terms of heat and matter transfer processes from the surroundings, $d\Delta U$ is the internal energy change, and $\delta\Delta\omega$ is the reversible work done on the system by the external agents, and this work is equal to $-Pd\Delta V$ or $-Pd\Delta V - \gamma d\Delta$ depending upon whether one deals with the bulk phase or the surface phase, respectively.

Eq. (2.6) and Eq. (2.3 or 2.4) results the following formula in regards to the total differential of the total entropy for the phase, k (surface or bulk phases);

$$d\Delta S = \frac{\delta\Delta\Phi}{T_k} - \sum_i \frac{\mu_k^i}{T_k} d\Delta n_k^i + \sum_j \frac{\Delta A_k^j}{T_k} d\xi_k^j \quad (Total\ Entropy\ Change) \quad (2.7)$$

where the summations with respect to i and j indicate summation over different chemical species and over different reactions taking place simultaneously in the same phase, respectively.

The Eq. (2.7) can be divided into two parts, similar to the Prigogine (1961), who applied such a splitting procedure to the systems consist of two open phases but the system is closed as a whole:

The first two terms of (2.7), correspond to the rate of external entropy flow term (REF): namely,

$$\frac{d\Delta S_{ex}}{dt} = \frac{1}{T_k} \frac{\delta\Delta\Phi}{dt} - \sum_i \frac{\mu_k^i}{T_k} \frac{d\Delta n_k^i}{dt} \quad (Rate\ of\ Entropy\ Flow\ (REF)) \quad (2.8)$$

And the last term of Eq. (2.7), on the other hand constitutes to the internal entropy production term (IEP): namely,

$$\frac{d\Delta S_{in}}{dt} = \sum_j \frac{\Delta A_k^j}{T_k} \frac{d\xi_k^j}{dt} \geq 0 \quad (Internal\ Entropy\ Production\ (IEP)) \quad (2.9)$$

As one might expect that, the IEP in a single phase directly related to the chemical reactions taking place in the region whether it is closed or open. Only the REF is affected from the matter flow through the open boundary.

One may also write down the power dissipation, ΔP , for natural changes, which is a very useful function, which is also known as Helmholtz dissipation function (Haase, 1969)[83], for the treatment of the isothermal processes taking place in multi-phase systems with uniform and continuous temperature distribution, and it is given by the following expression.

$$\Delta P = T \frac{d\Delta S_{in}}{dt} = \sum_i \Delta A^i \frac{d\xi^i}{dt} \geq 0 \quad (2.10)$$

Inequalities given by Eqs. (2.9 and 2.10) are valid for any natural change, taking place in any phase whether it is bulk or surface. Only difference between these two expressions is that the first one is valid for any type of natural changes taking place in the system but the second one is restricted only for the isothermal natural processes.

For a global composite system having discontinuous (heterogeneous) phases, there are two additional IEP terms, one is due to the internal entropy flow associated with the transfer of chemical species from one subdomain to another subdomain; and the other one is due to the energy transfer between the subdomains of the composite system.

This second IEP term for a composite system immediately drops out if the subdomains have identical temperatures. The total differential of the entropy for such a system is;

$$d\Delta S = \left\{ \begin{array}{l} - \sum_{i,k} \frac{\mu_k^i}{T_k} d\Delta n_{k \leftrightarrow s}^i + \sum_k \frac{\delta \Delta \Omega_{k \leftrightarrow s}}{T_k} \\ - \sum_{i,k} \frac{\mu_k^i}{T_k} d\Delta n_k^i + \sum_k \frac{\delta \Delta \Omega_k}{T_k} + \sum_{j,k} \frac{\Delta A_k^j}{T_k} d\xi_k^j \end{array} \right\} (Total \ Entropy \ Change) \quad (2.11)$$

where the double summations with respect to k and i or j indicate summation over various phases (bulk or surface) and over different chemical species or reactions taking place simultaneously in the same phase, respectively. $\delta \Delta \Omega_k$ is the amount of energy transported to the individual phase from the other phases present in the global system due to heat or matter exchange. In Eq. (2.11), the subscript $k \leftrightarrow s$ indicates that the matter and energy exchange takes place between the phases of the system, k , and the surrounding, s .

By performing the splitting procedure to the Eq. (2.11) similar to the single-phase systems: The REF from the surrounding to an open composite system may be written as,

$$\frac{d\Delta S_{ex}}{\delta t} = - \sum_{i,k} \frac{\mu_k^i}{T_k} \frac{d\Delta n_{k\leftrightarrow s}^i}{\delta t} + \sum_k \frac{1}{T_k} \frac{\delta\Delta\Omega_{k\leftrightarrow s}}{\delta t} \quad (REF) \quad (2.12)$$

and the IEP due to the irreversible processes:

$$\frac{d\Delta S_{in}}{\delta t} = - \sum_{i,k} \frac{\mu_k^i}{T_k} \frac{d\Delta n_k^i}{\delta t} + \sum_k \frac{1}{T_k} \frac{\delta\Delta\Omega_k}{\delta t} + \sum_{j,k} \frac{\Delta A_k^j}{T_k} \frac{d\xi_k^j}{\delta t} \quad (IEP) \quad (2.13)$$

On the other hand the first term contributes to IEP of a composite system as long as one has chemical potential differences between respective sub-domains regardless the transfer process isothermal or not.

A comparison of the IEP expressions, for the single-phase system, Eq. (2.9), and the composite system, Eq. (2.13), immediately shows us that the internal entropy production IEP is not an additive property of a thermodynamic system composed of interacting open sub-systems unless the whole system is in complete physico-chemical equilibrium state (uniform temperature and chemical potential distributions).

At the onset, it should be clearly stated that in the case of an open composite system having only homogeneous chemical reactions with inactive external boundaries (no chemical reaction or phase transition occurring there) any ordinary exchange of matter and/or energy with its surroundings only contributes to the total entropy flow term, and it is noting to do with the IEP.

2.3 Ordinary point motion along the surface normal

During the derivation of the formula for the global IEP associated with the arbitrary virtual displacement, $d\eta$, of the interfacial loop of a finite thickness, which separates the second phase, denoted by β , from the interconnect, denoted by b , having multi-components, one has to integrate the rate of local entropy density change along the curved interface in order to obtain desired connection between generalized forces and conjugate fluxes. The rate of local entropy density change is the only quantity, which has the additive property that allows to be integrated. Therefore, not only the local internal entropy production (source term), but also the external entropy flow term should be evaluated for the virtual displacement.

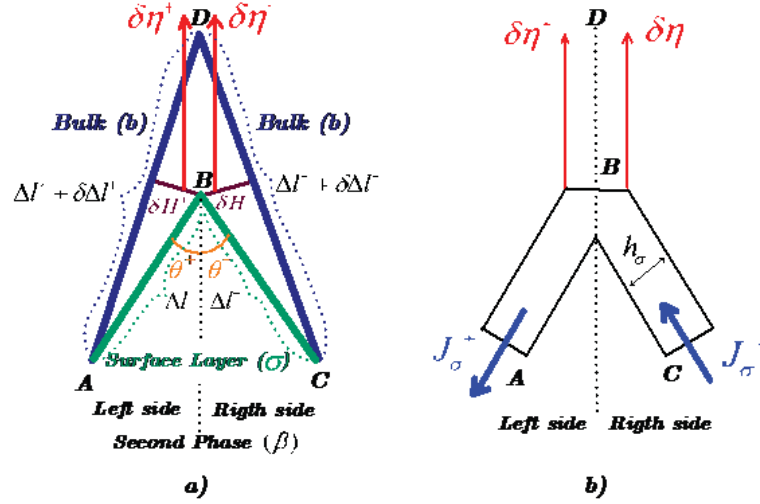


Figure 2.1: Ordinary point motion along surface normal. a) Macro-structure, b) Micro-structure. ABC: interfacial layer and $\delta\eta$: virtual displacement of the ordinary point along surface normal [84].

2.3.1 Internal entropy production

The IEP of an open composite system is given by the Eq. (2.13). As far as the second phase - interconnect surface layer is concerned, it is assumed that the whole system is in thermal equilibrium, T , and there is no insitu chemical reactions is taking place. These assumptions drop out the second and the third terms of Eq. (2.13), as discussed before. Then the only non-vanishing term of IEP, which represents an additional contribution in the composite system due to internal entropy flow associated with the transfer of chemical species from one sub-domain to another sub-domain, is given by,

$$\frac{\delta\Delta S_{in}}{\delta t} = -\frac{1}{T} \sum_{i,j} \mu_j^i \frac{\delta\Delta n_j^i}{\delta t} \quad (2.14)$$

Double summations with respect to i and j indicate summations over different chemical species and over various phases (b, β and σ), respectively.

Now, let us calculate the internal entropy variation for the left hand side sub-system when the ordinary point moves along the surface normal with a distance $\delta\eta^+$. From figure 2.1, one immediately finds the following variational relationships among various quantities by assuming that: $\Delta\ell^+ \gg \delta\eta^+$ and $\Delta\ell^- \gg \delta\eta^-$;

$$\delta\Delta\ell^+ = \delta\eta^+ \cos \theta^+ \text{ and } \delta H^+ = \delta\eta^+ \sin \theta^+ \quad (2.15)$$

$$\delta\Delta n_b^+ = -\frac{1}{2\Omega_b} \Delta\ell^+ \sin \theta^+ \delta\eta^+ \quad (2.16)$$

$$\delta\Delta n_\beta^+ = \frac{1}{2\Omega_\beta} \Delta\ell^+ \sin \theta^+ \delta\eta^+ \quad (2.17)$$

$$\delta\Delta n_\sigma^+ = \frac{h_\sigma}{\Omega_\sigma} \cos \theta^+ \delta\eta^+ \quad (2.18)$$

where Ω_σ , Ω_b and Ω_β are the mean atomic specific volumes, associated with the surface layer, bulk and second phases, respectively. $\Delta\ell^+$ and $\Delta\ell^-$ denote segment lengths of the surface layer just next to the ordinary point right and left hand sides, respectively. h_σ is the thickness of the surface layer and assumed to be invariant. $\delta\Delta n_\beta^+$ and $\delta\Delta n_b^+$ are the number of atoms gain in the reaction zones associated with the second phase - interfacial layer and the bulk - interfacial layer respectively, while the transformation processes are taking place there during the virtual displacement of the interfacial layer. $\delta\Delta n_\sigma^+$ is equal to the net atomic gain by the interfacial layer denoted by σ due to enlargement (extension without stretching) of that layer during the displacement operation. δ and Δ are variational and micro-discretization operators, respectively.

One can obtain exactly similar expressions for the other side of the ordinary point, which will be identified by a negative sign as superscript in the following formulas:

$$\delta\Delta\ell^- = \delta\eta^- \cos \theta^- \text{ and } \delta H^- = \delta\eta^- \sin \theta^- \quad (2.19)$$

$$\delta\Delta n_b^- = -\frac{1}{2\Omega_b} \Delta\ell^- \sin \theta^- \delta\eta^- \quad (2.20)$$

$$\delta\Delta n_\beta^- = \frac{1}{2\Omega_\beta} \Delta\ell^- \sin \theta^- \delta\eta^- \quad (2.21)$$

$$\delta\Delta n_\sigma^- = \frac{h_\sigma}{\Omega_\sigma} \cos \theta^- \delta\eta^- \quad (2.22)$$

Also, one should recall that in the case of multi-component system, the variations in the number of atomic species could be easily obtained by simply multiplying the total atomic number variations by the respective atomic fractions denoted by x_j^i . As an example, the number of chemical species involved in the left and right hand side bulk phases due to the virtual displacement may be given by

$$\delta\Delta n_j^{i+} = x_j^i \delta\Delta n_j^+ \quad (2.23)$$

and

$$\delta\Delta n_j^{i-} = x_j^i \delta\Delta n_j^- \quad (2.24)$$

Then, one can write down the rate of entropy production due to ordinary point virtual displacement along the surface normal for the left as well as for the right hand side domains;

$$\frac{\delta\Delta S_{in}^+}{\delta t} = \frac{1}{T} \left\{ \begin{array}{l} \left[\sum_i \left(\frac{x_b^{i+}}{\Omega_b} \mu_b^{i+} - \frac{x_\beta^{i+}}{\Omega_\beta} \mu_\beta^{i+} \right) \right] \frac{1}{2} \Delta\ell^+ \sin \theta^+ \\ -\Gamma_\sigma \cos \theta^+ \sum_i x_\sigma^{i+} \mu_\sigma^{i+} \end{array} \right\} \frac{\delta\eta^+}{\delta t} \quad (2.25)$$

and

$$\frac{\delta\Delta S_{in}^-}{\delta t} = \frac{1}{T} \left\{ \begin{array}{l} \left[\sum_i \left(\frac{x_b^{i-}}{\Omega_b} \mu_b^{i-} - \frac{x_\beta^{i-}}{\Omega_\beta} \mu_\beta^{i-} \right) \right] \frac{1}{2} \Delta\ell^- \sin \theta^- \\ -\Gamma_\sigma \cos \theta^- \sum_i x_\sigma^{i-} \mu_\sigma^{i-} \end{array} \right\} \frac{\delta\eta^-}{\delta t} \quad (2.26)$$

where, $\Gamma_\sigma = h_\sigma/\Omega_\sigma$ corresponds to the specific mean atomic density associated with the surface layer.

In above relationship, the special superscript + or - has been employed above the atomic fractions as well as the chemical potentials in order to indicate explicitly that those quantities may depend upon the orientation of the local surface normal. One should also recall that for the multi-component surface phases, $\sum \Gamma_\sigma^i \mu_\sigma^i$ is exactly equal to the specific Gibbs free energy density associated with the interfacial layer. This may be denoted by g_σ . Here, $\Gamma_\sigma^i = \Gamma_\sigma x_\sigma^i$, is by definition known as the specific surface concentration of chemical species in surface layer.

The terms appearing in the first group on the right side of Eq. (2.25) and (2.26) such as, $\sum_i x_b^i \mu_b^i / \Omega_b$ and $\sum_i x_\beta^i \mu_\beta^i / \Omega_\beta$ are the volumetric Gibbs free energy densities. These quantities are denoted by \check{g}_b and \check{g}_β , and associated with the bulk phase and void region having their own instantaneous compositions just next to the hypothetical geometric boundaries of the interfacial layer (reaction fronts or zones). Furthermore, these quantities are related to the specific Gibbs free energy densities by the relationship: $g_\sigma = h_\sigma \check{g}_\sigma$. By using these definitions the following equations are obtained,

$$\frac{\delta\Delta S_{in}^+}{\delta t} = \frac{1}{T} \left\{ \left(\check{g}_b^+ - \check{g}_\beta^+ \right) \frac{1}{2} \Delta\ell^+ \sin \theta^+ - g_\sigma^+ \cos \theta^+ \right\} \frac{\delta\eta^+}{\delta t} \quad (2.27)$$

and

$$\frac{\delta\Delta S_{in}^-}{\delta t} = \frac{1}{T} \left\{ \left(\check{g}_b^- - \check{g}_\beta^- \right) \frac{1}{2} \Delta\ell^- \sin \theta^- - g_\sigma^- \cos \theta^- \right\} \frac{\delta\eta^-}{\delta t} \quad (2.28)$$

The total internal entropy production is:

$$\frac{\delta\Delta S_{in}}{\delta t} = \frac{\delta\Delta S_{in}^+}{\delta t} + \frac{\delta\Delta S_{in}^-}{\delta t} \quad (2.29)$$

$$= \frac{1}{T} \left\{ \begin{array}{l} -\frac{\Delta\ell}{2} \left(\check{g}_{\beta b}^+ \sin \theta^+ + \check{g}_{\beta b}^- \sin \theta^- \right) \\ - \left(g_\sigma^+ \cos \theta^+ + g_\sigma^- \cos \theta^- \right) \end{array} \right\} \frac{\delta\eta}{\delta t} \quad (2.30)$$

$$(2.31)$$

where $\check{g}_{\beta b} = (\check{g}_\beta - \check{g}_b)$, and it corresponds by definition to the volumetric density of Gibbs Free Energy of Transformation (GFET) (negative of the affinity of an interfacial reaction such as condensation or adsorption, $g_{\beta b}$) associated with the transformation of the bulk phase into the realistic second phase, which contains chemical species even though they are present in a trace amount. In the case of thermostatic equilibrium between a second phase and an adjacent bulk phase, GFET becomes identically equal to zero, if the reaction front would be a flat interface. There is a very simple connection between this quantity GFET and the Specific Gibbs Free Energy of transformation between the parent phase and the second phase that may be given by $g_{\beta b} = \check{g}_{\beta b} h_\sigma$. By dividing both sides of the Eq. (2.29) by $\Delta\ell$, it is obtained that,

$$\frac{\delta\Delta S_{in}/\Delta\ell}{\delta t} = -\frac{1}{2T} \left\{ \begin{array}{l} \left(\check{g}_{\beta b}^+ \sin \theta^+ + \check{g}_{\beta b}^- \sin \theta^- \right) \\ + \left(g_\sigma^+ \frac{\cos \theta^+}{\Delta\ell/2} + g_\sigma^- \frac{\cos \theta^-}{\Delta\ell/2} \right) \end{array} \right\} \frac{\delta\eta}{\delta t} \quad (2.32)$$

Now if one applies the limiting procedures such as; first with respect to $\delta t \rightarrow 0$, and then $\Delta\ell \rightarrow 0$, and recalls the definition of the local radius of curvature, κ , which is given by;

$$\kappa = \lim_{\Delta\ell \rightarrow 0} \left(\frac{\cos \theta}{\Delta\ell/2} \right) \quad (2.33)$$

and also keeps in mind that $\lim_{\Delta\ell \rightarrow 0} \theta^\pm = \frac{\pi}{2}$, $\check{g}_{\beta b}^+ = \check{g}_{\beta b}^- = \check{g}_{\beta b}$ and $g_\sigma^+ = g_\sigma^- = g_\sigma$, one immediately obtains the following continuum relationship for the IEP,

$$\frac{d\Delta\hat{S}_{in}}{dt} = -\frac{1}{T} \left(\check{g}_{\beta b} + g_\sigma \kappa \right) \frac{d\eta}{dt} \quad (\text{erg/oK/cm/sec}) \quad (2.34)$$

where $d\Delta\hat{S}_{in}/dt$ is the surface density of IEP associated with ordinary points.

2.3.2 Rate of entropy flow

Similarly, the external entropy accumulation in the surface phase due to flow of chemical species, i , along the surface layer, J_σ^i , and the perpendicular incoming flux intensities from the bulk, \hat{J}_b^i , and the void, \hat{J}_β^i , phases, can be calculated by using the law of conservation of entropy without the source term or IEP.

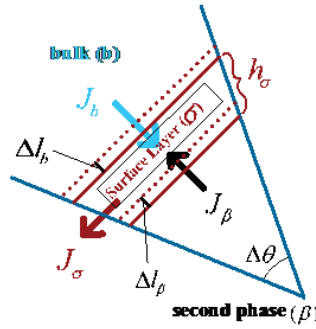


Figure 2.2: Structure of micro-composite system [84].

From figure 2.2 it can be written as,

$$\frac{d\Delta\hat{S}_{ex}}{dt} = -\frac{\partial}{\partial\ell} J_\sigma + \hat{J}_b + \hat{J}_\beta \quad (2.35)$$

$$= -\sum_i \frac{\partial}{\partial\ell} \left(\frac{\mu_\sigma^i}{T_\sigma} J_\sigma^i \right) + \sum_i \frac{\mu_b^i}{T_b} \hat{J}_b^i + \sum_i \frac{\mu_\beta^i}{T_\beta} \hat{J}_\beta^i \quad (2.36)$$

$$= -\sum_i \frac{\partial}{\partial\ell} \left(\frac{\mu_\sigma^i}{T_\sigma} x_\sigma^i J_\sigma \right) + \sum_i \frac{\mu_b^i}{T_b} x_b^i \hat{J}_b + \sum_i \frac{\mu_\beta^i}{T_\beta} x_\beta^i \hat{J}_\beta \quad (2.37)$$

$$(2.38)$$

where, \hat{J}_ν and \hat{J}_b are the total atomic flux intensities in such directions that they are perpendicular and oriented towards the interfacial layer, just at the reaction fronts between the second

phase and the interfacial layer and the bulk phase and the interfacial layer, respectively.

By remembering the definitions of the volumetric Gibbs free energy densities, \check{g}_k , given by $\sum_i x_k^i \mu_k^i / \Omega_k$, where k represents the different phases, and keeping in mind that the global system is in thermal equilibrium, Eq. (2.35) can be rewritten as:

$$\frac{d\Delta\hat{S}_{ex}}{dt} = -\frac{\Omega_\sigma}{T} \left[\frac{\partial}{\partial\ell} (\check{g}_\sigma J_\sigma) + \check{g}_\sigma (\hat{J}_b + \hat{J}_\beta) \right] \quad (2.39)$$

where $d\Delta\hat{S}_{ex}/dt$ is the surface density of REF associated with ordinary points.

In this formula it is also assumed that the mean atomic specific volumes of the bulk and the second phases are nearly equal to that of the interfacial layer.

2.3.3 The local rate of change in the entropy density

The total entropy production has to be calculated since only this term has the additive property that will be used to calculate the total entropy production of the whole surface layer under isothermal condition by a path integration procedure. By using Eqs. (2.34 and 2.39);

$$\frac{d\Delta\hat{S}}{dt} = \frac{d\Delta\hat{S}_{in}}{dt} + \frac{d\Delta\hat{S}_{ex}}{dt} \quad (2.40)$$

$$= -\frac{1}{T} \left\{ (\check{g}_{\beta b} + g_\sigma \kappa) \frac{d\eta}{dt} + \Omega_\sigma \left[\frac{\partial}{\partial\ell} (\check{g}_\sigma J_\sigma) + \check{g}_\sigma (\hat{J}_b + \hat{J}_\beta) \right] \right\} \quad (2.41)$$

In order to calculate the global rate of entropy change of the whole curved interfacial layer, which is between the second phase region and the bulk phase, let first take the line integral of Eq. (2.40) all along the closed curved interface, represented by C which may be situated at a point denoted by the open interval $(-\varepsilon, +\varepsilon)$, where $\varepsilon \rightarrow 0$. This interface is represented by C° and equal to $C - (-\varepsilon, +\varepsilon)$.

$$\oint_{C^o} d\ell \frac{d\Delta\hat{S}}{dt} = \lim_{\varepsilon \rightarrow 0} \int_{+\varepsilon}^{-\varepsilon} d\ell \frac{d\Delta\hat{S}}{dt} \quad (2.42)$$

$$= -\frac{1}{T} \lim_{\varepsilon \rightarrow 0} \int_{+\varepsilon}^{-\varepsilon} d\ell \left\{ \begin{aligned} & \left(\check{g}_{\beta b} + g_{\sigma\kappa} \right) \frac{d\eta}{dt} \\ & + \Omega_{\sigma} \left[\frac{\partial}{\partial \ell} (\check{g}_{\sigma} J_{\sigma}) + \check{g}_{\sigma} (\hat{J}_b + \hat{J}_{\beta}) \right] \end{aligned} \right\} \quad (2.43)$$

In the absence of the particle source and sink terms, the atomic flux divergence is proportional with the amount of mass accumulated or depleted on an interfacial layer, which causes the interface to move in a local normal direction. However in this formulation a more general situation, namely, the additional entropy source terms associated with the normal components of the atomic flows coming from the bulk phase, and the void region due to condensation or evaporation processes that may be summarized by, $\hat{J}_{b\beta} = \hat{J}_b + \hat{J}_{\beta}$, is considered. Hence, the following expression can be written for the conservation of atomic species during the virtual displacement of curved interface having no stretching and thickness variations:

$$\left[(c_b - c_{\beta}) - h_{\sigma} \bar{\kappa} c_{\sigma} \right] \frac{d\eta}{dt} = \sum_i \frac{\partial J_{\sigma}^i}{\partial \ell} - \sum_i (\hat{J}_b^i + \hat{J}_{\beta}^i) = \frac{\partial J_{\sigma}}{\partial \ell} - \hat{J}_{b\beta} \quad (2.44)$$

where, c_b , c_{β} and c_{σ} are the atomic volumetric concentrations associated with the bulk, second phase and surface phases, respectively. Now if one considers the following plausible and highly accurate approximations for second phase, which may be treated as polyatomic dilute gas, such as: $c_{\beta} = 0$ and $h_{\sigma} \bar{\kappa} = 0$. One would get the following results using the fact that $\Omega_b = c_b^{-1}$, which is mostly adapted in the literature (Guggenheim [80] and Ogurtani and Oren [78]):

$$\frac{d\eta}{dt} = \vec{n} \cdot \frac{d\vec{r}}{dt} = \Omega_b \left(\frac{\partial J_{\sigma}}{\partial \ell} - \hat{J}_{b\beta} \right) \quad (2.45)$$

where, \vec{n} and \vec{r} are the surface normal and the position vectors, respectively.

Now, let us substitute above identity into Eq. (2.42), and also remember that it is assumed that the mean atomic specific volume of the bulk phase is nearly equal to that of the interfacial layer.

$$\oint_{C^0} d\ell \frac{d\Delta\hat{S}}{dt} = -\frac{\Omega_\sigma}{T} \lim_{\varepsilon \rightarrow 0} \int_{+\varepsilon}^{-\varepsilon} d\ell \left\{ \begin{aligned} & \left(\check{g}_{\beta b} + g_{\sigma\kappa} \right) \left(\frac{\partial J_\sigma}{\partial \ell} - \hat{J}_{b\beta} \right) \\ & + \left[\frac{\partial}{\partial \ell} (\check{g}_\sigma J_\sigma) + \check{g}_\sigma \hat{J}_{b\beta} \right] \end{aligned} \right\} \quad (2.46)$$

In order to apply the integration by parts let us write Eq. (2.46) in the following form,

$$\oint_{C^0} d\ell \frac{d\Delta\hat{S}}{dt} = -\frac{\Omega_\sigma}{T} \lim_{\varepsilon \rightarrow 0} \left\{ \begin{aligned} & \int_{+\varepsilon}^{-\varepsilon} d\ell \left[(\check{g}_{\beta b} + g_{\sigma\kappa}) \frac{\partial J_\sigma}{\partial \ell} \right] \\ & - \int_{+\varepsilon}^{-\varepsilon} d\ell \left[(\check{g}_{\beta b} + g_{\sigma\kappa}) \hat{J}_{b\beta} \right] \\ & + \int_{+\varepsilon}^{-\varepsilon} d\ell \frac{\partial}{\partial \ell} (\check{g}_\sigma J_\sigma) + \int_{+\varepsilon}^{-\varepsilon} d\ell (\check{g}_\sigma \hat{J}_{b\beta}) \end{aligned} \right\} \quad (2.47)$$

The first group of terms on the right side of the Eq. (2.47) can be integrated by parts, as shown below; In order to save the space the left side of the equation are not shown in the following two equations.

$$= -\frac{\Omega_\sigma}{T} \lim_{\varepsilon \rightarrow 0} \left\{ \begin{aligned} & \int_{+\varepsilon}^{-\varepsilon} d\ell \frac{\partial}{\partial \ell} \left[(\check{g}_{\beta b} + g_{\sigma\kappa}) J_\sigma \right] - \int_{+\varepsilon}^{-\varepsilon} d\ell \left[J_\sigma \frac{\partial}{\partial \ell} (\check{g}_{\beta b} + g_{\sigma\kappa}) \right] \\ & - \int_{+\varepsilon}^{-\varepsilon} d\ell \left[(\check{g}_{\beta b} + g_{\sigma\kappa}) \hat{J}_{b\beta} \right] \\ & + \int_{+\varepsilon}^{-\varepsilon} d\ell \frac{\partial}{\partial \ell} (\check{g}_\sigma J_\sigma) + \int_{+\varepsilon}^{-\varepsilon} d\ell (\check{g}_\sigma \hat{J}_{b\beta}) \end{aligned} \right\} \quad (2.48)$$

After some manipulations and rearrangements,

$$= \frac{\Omega_\sigma}{T} \lim_{\varepsilon \rightarrow 0} \left\{ \begin{aligned} & \int_{+\varepsilon}^{-\varepsilon} d\ell \left[J_\sigma \frac{\partial}{\partial \ell} (\check{g}_{\beta b} + g_{\sigma\kappa}) \right] - \left[(\check{g}_{\beta b} + g_{\sigma\kappa}) J_\sigma \right]_{+\varepsilon}^{-\varepsilon} \\ & + \int_{+\varepsilon}^{-\varepsilon} d\ell \left[(\check{g}_{\beta b} + g_{\sigma\kappa}) \hat{J}_{b\beta} \right] - \left[\check{g}_\sigma J_\sigma \right]_{+\varepsilon}^{-\varepsilon} - \int_{+\varepsilon}^{-\varepsilon} d\ell (\check{g}_\sigma \hat{J}_{b\beta}) \end{aligned} \right\} \quad (2.49)$$

At the final step after the integration by parts procedure, one should carefully split the global rate of entropy change into two parts, namely the REF term and the IEP term by carefully inspecting the individual contributions in Eq. (2.49).

$$\frac{d}{dt}S_{REF} = \frac{\Omega_\sigma}{T} \lim_{\varepsilon \rightarrow 0} \left\{ - \int_{+\varepsilon}^{-\varepsilon} d\ell \left(\tilde{g}_\sigma \hat{J}_{b\beta} \right) - \left[\tilde{g}_\sigma J_\sigma \right]_{-\varepsilon} + \left[\tilde{g}_\sigma J_\sigma \right]_{+\varepsilon} \right\} \quad (2.50)$$

where, the first term is the integrated entropy flow to the interfacial layer from the embedding parent phases through the incoming matter flux, $\hat{J}_{b\beta}$.

The remaining terms of Eq. (2.49) are related to the IEP and given by,

$$\frac{d}{dt}S_{IEP} = \frac{\Omega_\sigma}{T} \lim_{\varepsilon \rightarrow 0} \left\{ \int_{+\varepsilon}^{-\varepsilon} d\ell \left[J_\sigma \frac{\partial}{\partial \ell} \left(\tilde{g}_{\beta b} + g_{\sigma\kappa} \right) \right] + \int_{+\varepsilon}^{-\varepsilon} d\ell \left[\left(\tilde{g}_{\beta b} + g_{\sigma\kappa} \right) \hat{J}_{b\beta} \right] \right. \\ \left. - \left[\left(\tilde{g}_{\beta b} + g_{\sigma\kappa} \right) J_\sigma \right]_{-\varepsilon} + \left[\left(\tilde{g}_{\beta b} + g_{\sigma\kappa} \right) J_\sigma \right]_{+\varepsilon} \right\} \quad (2.51)$$

This original result clearly confirms that the bulk flow of particles or substances for nonviscous systems appears to be a reversible phenomenon as first discovered by Prigogine [79], in another content using the velocity of the centre of gravity as a reference system in the calculation of the possible singularity. In the absence of this singularity, the last two terms of Eqs. (2.50 and 2.51), become identically zero and drop out completely.

Here it should be clearly stated that the singularities have to be treated individually as a special case, where the discrete formulation of irreversible thermodynamics as suggested and developed by Ogurtani (2000), may be a very powerful tool to handle this problem successfully, as it will be shown in the next section.

After these mentioned drop outs, the following formula obtained for the IEP

$$\frac{d}{dt}S_{IEP} = \frac{\Omega_\sigma}{T} \lim_{\varepsilon \rightarrow 0} \left\{ \int_{+\varepsilon}^{-\varepsilon} d\ell \left[J_\sigma \frac{\partial}{\partial \ell} \left(\tilde{g}_{\beta b} + g_{\sigma\kappa} \right) \right] + \int_{+\varepsilon}^{-\varepsilon} d\ell \left[\left(\tilde{g}_{\beta b} + g_{\sigma\kappa} \right) \hat{J}_{b\beta} \right] \right\} \quad (2.52)$$

Before proceeding further, let us turn back to postulates of irreversible thermodynamics: As shown by Prigogine [79], the internal entropy production of the irreversible processes can be written as a sum of the products of generalized forces or affinities and the corresponding rates or generalized fluxes,

$$\frac{d}{dt}S_{IEP} = \sum_k J_k F_k \geq 0 \quad (2.53)$$

By utilizing this postulate, which means by comparing the Eqs. (2.52 and 2.53), one obtains the following forces from the integrated IEP expression (2.52), which is valid for any arbitrary closed loop.

$$F_\sigma = \frac{\Omega_\sigma}{T} \frac{\partial}{\partial \ell} \left(\tilde{g}_{\beta b} + g_{\sigma \kappa} \right) \quad (2.54)$$

and

$$F_{\beta b} = \frac{\Omega_\sigma}{T} \left(\tilde{g}_{\beta b} + g_{\sigma \kappa} \right) \quad (2.55)$$

where, F_σ and $F_{\beta b}$ denote longitudinal and transverse generalized forces that are acting on the interfacial layer respectively.

If one considers the additional contributions due to external forces, denoted by \vec{F}_{ext} ,

$$F_\sigma = \Omega_\sigma \left[\frac{1}{T} \frac{\partial}{\partial \ell} \left(\tilde{g}_{\beta b} + g_{\sigma \kappa} \right) + \vec{t} \cdot \vec{F}_{ext} \right] \quad (2.56)$$

and

$$F_{\beta b} = \Omega_\sigma \left[\frac{1}{T} \left(\tilde{g}_{\beta b} + g_{\sigma \kappa} \right) + \vec{n} \cdot \vec{F}_{ext} \right] \quad (2.57)$$

Here \vec{t} and \vec{n} denote unit tangent and normal vectors at the surface. The external forces were discussed by Ogurtani and Oren [78] in Appendix B of that reference for various kind of external forces, such as electrostatic, and magnetic in nature.

The external generalized forces per particle, i , associated with electromigration is given by,

$$\vec{F}_{em}^i = -\frac{eZ^i}{T} \nabla \vartheta \quad (2.58)$$

Where, ϑ is the electrostatic potential and eZ^i is the effective charge of the particle i . The external generalized total force density (per unit volume) associated with electromigration and acting on particles may have the following form for a multi- component system whether it is a bulk phase or an interfacial layer,

$$\vec{F}_{em} = -\frac{1}{T\Omega_\sigma} \left(\sum_i x^i eZ^i \right) \nabla\vartheta = -\frac{1}{T\Omega_\sigma} eZ^* \nabla\vartheta \quad (2.59)$$

where, eZ^* is the effective charge in multi-component systems.

The external generalized forces per particle, i , associated with strain energy interaction is given by,

$$\vec{F}_\epsilon^i = \nabla(\bar{\lambda}^i \otimes \bar{\sigma})/T \quad (2.60)$$

where $\bar{\lambda}^i$ is the elastic dipole tensor of the individual chemical species denoted by "i".

The contribution of \vec{F}_{em} in Eq. (2.57), $\vec{n} \cdot \vec{F}_{em}$, becomes identically zero since the normal component of the electric field intensity vanish at the surface. In the same manner, The contribution of \vec{F}_ϵ in transverse flux is equal to zero if the normal component of traction at surface is zero.

Then, according to the Onsager theory (de Groot [85] and Prigogine [79]), which connects generalized forces and conjugate fluxes through generalized mobilities, the conjugate fluxes associated with the above forces can immediately be written down, by neglecting the cross-coupling terms between generalized forces and fluxes, as:

$$J_\sigma = \frac{M_\sigma}{kT} \Omega_\sigma \frac{\partial}{\partial \ell} \left[\left(\bar{g}_{\beta\beta} + g_{\sigma\kappa} \right) - \langle eZ^* \rangle \frac{\vartheta}{\Omega_\sigma} + \langle \bar{\lambda} \rangle \otimes \bar{\sigma} \right] \quad (Surface\ Flux) \quad (2.61)$$

and

$$\hat{J}_{\beta\beta} = \frac{M_{\beta\beta}}{kT} \Omega_\sigma \left(\bar{g}_{\beta\beta} + g_{\sigma\kappa} \right) \quad (Incoming\ net\ lateral\ flux\ density) \quad (2.62)$$

where, M_σ/k and $M_{\beta\beta}/k$ are the generalized phenomenological mobilities associated with the respective conjugated forces and fluxes, $\langle eZ^* \rangle$ is the mean value of the effective electromigration charge associated with the interacting species and k is the Boltzman's constant. $\langle \bar{\lambda} \rangle$ is the elastic dipole tensor associated with the interacting species.

For multi-component systems, where one is interested only in the net atomic (mass) transport regardless to the contributions of individual chemical species, the first generalized-mobility, M_σ , may not be easily connected to any combination of the intrinsic surface diffusivities of

individual chemical species in the interfacial layer or in the bulk phase. However, for one component system having minor amount of doping elements or impurities, the situation is rather simple where one can easily identify the existence of the following relationship between generalized mobility and the surface self-diffusivity of host matter denoted by \tilde{D}_σ ,

$$\hat{M}_\sigma = \frac{M_\sigma}{kT} = \frac{\tilde{D}_\sigma}{kT} \frac{h_\sigma}{\Omega_\sigma} = \frac{\tilde{D}_\sigma}{kT} \Gamma_\sigma \quad (2.63)$$

CHAPTER 3

MATHEMATICAL MODEL AND NUMERICAL PROCEDURES

3.1 Introduction

3.2 Mathematical model

According to this discrete microfinite elements method formulation of the irreversible thermodynamics of surfaces and interfaces by Ogurtani and Oren, the evolution kinetics of traction free surfaces exposed to the electrostatic and elastostatic fields in addition to the capillary forces may be described in terms of surface normal displacement velocities \bar{V}_{ord} by the following well-posed moving boundary value problem in $2\mathbf{D}$ space for ordinary points, using normalized and scaled parameters and variables, which are indicated by the bar signs over the letters.

$$\bar{V}_{ord} = \frac{\partial}{\partial \bar{\ell}} \left[\bar{D}(\theta, \phi, m) \frac{\partial}{\partial \bar{\ell}} \left(\Xi \bar{\sigma}_h + \Sigma \bar{\sigma}_h^2 + \chi \bar{\vartheta} + \bar{\gamma}_{f \leftrightarrow s}(\bar{y}) \hat{\gamma}(\theta, \phi, m) \bar{\kappa} + \bar{\omega}(\bar{y}) \right) \right] - M_{fv} \left(\Xi \bar{\sigma}_h + \Sigma \bar{\sigma}_h^2 + \bar{\gamma}_{f \leftrightarrow s}(\bar{y}) \hat{\gamma}(\theta, \phi, m) \bar{\kappa} + \bar{\omega}(\bar{y}) \right) \quad (\text{Ordinary points}) \quad (3.1)$$

$$\bar{V}_{long} = -\bar{M}_{long} \bar{\Omega}^{-1} \{ \lambda_{TJ} - \cos(\theta_W) \} \quad \forall \quad \lambda_{TJ} \geq 1 \quad (\text{Triple junction contour line}) \quad (3.2)$$

In Eq. (3.1), the first and second terms represent the elastic dipole tensor (EDTI) and elastic strain energy density (ESED) interactions, and the third and fourth terms are associated with

the electromigration, and capillary forces, respectively. In the governing equation Eq. (3.1), the normalized hoop stress is denoted by $\bar{\sigma}_h \equiv (\sigma_h/\sigma_o)$, where σ_o is the applied stress (missfit or uniaxial). The hoop stress in plane strain condition is defined by $\sigma_h = \hat{t} \cdot \underline{\sigma}_s \cdot \hat{t}$, where \hat{t} is the unit surface tangent vector, and $\underline{\sigma}_s$ is 2D-stress tensor evaluated at the region just adjacent to the surface layer. The dimensionless parameters Σ and Ξ correspond, respectively, the intensities of the ESED and the EDTI contributions on the stress-driven surface drift diffusion. χ is the electron wind intensity (EWI) parameter, $\bar{\vartheta}$ is the normalized electrostatic potential generated at the surface layer due to the applied electrostatic field intensity designated by E_0 . $\bar{\kappa}$ is the normalized local curvature and is taken to be positive for a convex void or a concave solid surface (troughs). Similarly the positive direction of the surface displacement is assumed to be towards the bulk (matrix) phase, and implies void growth. $\bar{D}(\theta, \phi, m)$ is the diffusion coefficient. In the above expression, $\bar{\ell}$ is the curvilinear coordinate along the surface (arc length) in 2D space scaled with respect to ℓ_0 . Where ℓ_0 is the arbitrary length scale, and in the present paper the line width of the thin single crystal film ω_0 is chosen as a natural scaling length, namely; $\ell_0 = \omega_0$. $\bar{\omega}(\bar{y})$ is the normalized wetting potential, which is given by $\omega(y) = \Omega_\sigma n_y \cdot \gamma'_{f \leftrightarrow s}(y)$ in particle representation. The generalized mobility, \bar{M}_{fv} , associated with the interfacial displacement reaction (adsorption or desorption) is assumed to be independent of the orientation of the interfacial layer in crystalline solids.

Eq. (3.2) defines the in-plane displacement velocity of the contour line (i.e., the TJ line shared by the droplet, substrate and vapor phases). The TJ longitudinal velocity, \bar{V}_{long} , associated with the natural motion of the film-substrate contour line may be given in terms of the wetting parameter $\lambda_{TJ} = [(\gamma_s - \gamma_{fs})/\gamma_f]$, and the temporal one-sided dihedral or wetting contact angle as a dynamical variable. Here γ_s is the Helmholtz surface free energy of the substrate, and $\gamma_{fs}(\cong 0)$ is the interfacial free energy between the film and the substrate, and γ_f is the surface free energy of the thick solid film; $\gamma_f \rightarrow \gamma_{f \leftrightarrow s}(\infty)$, where $\gamma_{f \leftrightarrow s}(y)$ is the height dependent surface Helmholtz free energy of the film.

In the present formulation of the problem, the bar sign over the letters still indicates the following scaled and normalized quantities:

$$\bar{t} = t/\tau_0, \quad \bar{\ell} = \ell/\ell_0, \quad \bar{\kappa} = \kappa\ell_0, \quad \bar{\omega}_0 = \omega_0/\ell_0, \quad \bar{L} = L/\ell_0 \quad (3.3)$$

$$\bar{\vartheta} = \frac{\vartheta}{E_0 \ell_0}, \quad \chi = \frac{e|\hat{Z}|E_0 \ell_0^2}{\Omega_s g_s}, \quad \bar{\sigma}_h = \frac{\sigma_h}{\sigma_0}, \quad \Xi = (1 + \nu) \frac{\ell_0 \sigma_0}{3g_s} |Tr \underline{\lambda}_s^V|, \quad (3.4)$$

$$\Sigma = \frac{(1 - \nu^2) \ell_0}{2E g_\sigma} \sigma_0^2, \quad \omega_0 = \frac{(1 - \nu_\sigma^2) \sigma_0^2}{2E_\sigma} \quad (3.5)$$

Where, g_s is the specific surface Gibbs free energy density.

In above expressions, E_0 denotes the electric field intensity directed along the longitudinal axis of the specimen, $e|\hat{Z}|$ is the effective charge, which may be given in terms of the atomic fractions, x^i , by $\hat{Z} = \langle |x^i \hat{Z}^i| \rangle$ for multi-component alloys. In the present study, \hat{M}_σ denotes the minimum value of the mobility of the surface diffusion and is given by: $\hat{M}_\sigma = (\bar{D}_\sigma h_\sigma / \Omega_\sigma kT)$. Here, $\bar{\Omega}_\sigma$ is the mean atomic volume of chemical species in the void surface layer, \hat{D}_σ is the isotropic part (i.e., the minimum value) of the surface diffusion coefficient. In the formulation of the problem, we adopted a convention such that the positive direction of motion is always towards the bulk material whether one deals with inner voids or outer surfaces or interfaces. We scaled the time and space variables $\{t, \ell\}$ in the following fashion: first of all, \hat{M}_σ , an atomic mobility associated with the mass flow at the surface layer, is defined, and then a new time scale is introduced by $\tau_0 = \ell_0^4 / (\Omega_\sigma^2 \hat{M}_\sigma g_\sigma)$, where the space variable ℓ is scaled with respect to the specimen (line) width denoted as $\ell_0 = \omega_0$.

According to the definitions of the time constant t and the surface mobility \hat{M}_σ introduced previously, one may write $\tau_0 \equiv [kT \ell_0^4 / (\Omega_\sigma D_\sigma h_\sigma g_\sigma^0)]$, which may be easily calculated using the published physico-chemical data available in the literature, where the following tentative atomistic structural constants might be considered without going to much into details; $\{\Omega \cong 1.66 \times 10^{-29} m^3, h_\sigma \cong 2.56 \times 10^{-10} m\}$. For the copper interconnect line, the surface diffusivity and the surface specific Gibbs free energy may be taken as equal to $D_\sigma^{Cu} = 5.85 \times 10^{-5} \exp(-0.95 eV/kT)$ and $g_\sigma^0 = 1.725 Jm^{-2}$, respectively, for the uncontaminated free surfaces, then one finds depending upon the selected scale length ℓ_0 [100nm – 1000nm] in above given range at $T = 573^\circ K$, that is standard device accelerated test temperature. At the room temperature, $T = 300^\circ K$, one obtains about seven orders of magnitudes lower values for the normalized time such as $\tau = 8.36 \times [10^9 - 10^{13}] s$.

3.3 Fundamental solutions of potential and elastic problems

3.3.1 Steady state potential solution

The electrostatic potentials at the surface is governed by Laplace equation.

$$\nabla^2 \vartheta(r) = 0 \quad (3.6)$$

With the following boundary conditions, namely Neumann boundary conditions,

$$\hat{n} \nabla \vartheta(r) = \hat{n} \frac{\partial \vartheta(r)}{\partial r} \hat{r} = 0 \quad (3.7)$$

The simplest solution we can find is that of a concentrated source at point P (source point) of magnitude one in an infinite homogeneous domain. This means that internal potential generation only occurs at one point (P) in the domain and is zero elsewhere. The function describing this variation is also referred to a Dirac Delta function which is defined as

$$\delta(P - Q) = 0 \text{ when } P \neq Q \quad (3.8)$$

$$\int_{\Omega} \delta(P - Q) d\Omega = 1 \quad (3.9)$$

where Q is a point in the domain Ω . Due to a unit point source at P, electrostatic potentials at point Q (field point) can be written for the two-dimensional case as

$$U(P, Q) = \frac{1}{2\pi} \ln \frac{1}{r} \quad (3.10)$$

where r is the distance from source point to field point. For two-dimensional isotropic problems, the flow is computed by

$$T(P, Q) = \hat{n} \nabla U(P, Q) = -\frac{1}{2\pi} \frac{\cos \theta}{|\vec{r}|} \quad (3.11)$$

where θ is defined as the angle between the normal vector n and the distance vector r, It can be seen that both solutions decay very rapidly from the value of infinity at the source. Whereas the fundamental solution for U is symmetric with respect to polar coordinates, the solution for T with the vector n pointing in x-direction (thus meaning flow in x-direction) is antisymmetric.

It can be shown that for potential problems, the following single integral equation is obtained

$$u(P) = \int_S t(Q)U(P, Q)dS(Q) - \int_S u(Q)T(P, Q)dS(Q) \quad (3.12)$$

where $u(Q)$ and $t(Q)$ are the potential and the normal derivative respectively at point Q on S , and $U(P, Q)$ and $T(P, Q)$ are the fundamental solutions at Q for a source at point P . The integration is carried out over a line S for two-dimensional problems.

3.3.2 Static elastic solution

In solid mechanics applications, a relationship between stress and strain must be established. Stresses are forces per unit area inside a solid. They can be visualized by cutting the solid on planes parallel to the axes and by showing the traction vectors acting on these planes.

The traction vectors acting on the three planes are defined as:

$$\vec{t}_1 = \begin{pmatrix} \sigma_x \\ \check{t}_{xy} \\ \check{t}_{xz} \end{pmatrix}; \quad \vec{t}_2 = \begin{pmatrix} \check{t}_{yx} \\ \sigma_y \\ \check{t}_{xz} \end{pmatrix}; \quad \vec{t}_3 = \begin{pmatrix} \check{t}_{zx} \\ \check{t}_{zy} \\ \sigma_z \end{pmatrix}; \quad (3.13)$$

The components of the traction vectors are also known as stress components.

Infinitesimal strains are defined in terms of displacement components in the x, y, z directions (u_x, u_y, u_z) by

$$\varepsilon_x = \frac{\partial u_x}{\partial x} \quad (3.14)$$

$$\varepsilon_y = \frac{\partial u_y}{\partial y} \quad (3.15)$$

$$\varepsilon_z = \frac{\partial u_z}{\partial z} \quad (3.16)$$

$$\gamma_{xy} = \frac{\partial u_x}{\partial y} + \frac{\partial u_y}{\partial x} \quad (3.17)$$

$$\gamma_{yz} = \frac{\partial u_y}{\partial z} + \frac{\partial u_z}{\partial y} \quad (3.18)$$

$$\gamma_{zx} = \frac{\partial u_z}{\partial x} + \frac{\partial u_x}{\partial z} \quad (3.19)$$

The elastic material response is governed by Hooke's law. For an isotropic material, this is in three dimensions.

$$\varepsilon_x = \frac{1}{E} [\sigma_x - \nu(\sigma_y + \sigma_z)] \quad (3.20)$$

$$\varepsilon_y = \frac{1}{E} [\sigma_y - \nu(\sigma_x + \sigma_z)] \quad (3.21)$$

$$\varepsilon_z = \frac{1}{E} [\sigma_z - \nu(\sigma_y + \sigma_x)] \quad (3.22)$$

$$\gamma_{xy} = \frac{1}{G} \ddot{\tau}_{xy}, \quad \gamma_{yz} = \frac{1}{G} \ddot{\tau}_{yz}, \quad \gamma_{zx} = \frac{1}{G} \ddot{\tau}_{zx} \quad (3.23)$$

where E is the modulus of elasticity, ν the Poisson's ratio and G the shear modulus, given by

$$G = \frac{E}{2(1 + \nu)} \quad (3.24)$$

The governing differential equations are obtained from the condition of equilibrium. For two-dimensional problems these are

$$\frac{\partial \sigma_x}{\partial x} + \frac{\partial \ddot{\tau}_{xy}}{\partial y} + b_x = 0 \quad (3.25)$$

$$\frac{\partial \sigma_y}{\partial y} + \frac{\partial \ddot{\tau}_{xy}}{\partial x} + b_y = 0 \quad (3.26)$$

where b_x and b_y are components of body force in x and y directions. Substitution of the equations for strain 3.14 and the Hooke's law for plane strain conditions gives

$$G \left(\frac{\partial^2 u_x}{\partial x^2} + \frac{\partial^2 u_x}{\partial y^2} \right) + \left(\frac{\nu E}{(1 + \nu)(1 - 2\nu)} + G \right) \left(\frac{\partial^2 u_y}{\partial x \partial y} + \frac{\partial^2 u_y}{\partial x \partial y} \right) + b_x = 0 \quad (3.27)$$

$$\left(G + \frac{\nu E}{(1 + \nu)(1 - 2\nu)} \right) \left(\frac{\partial^2 u_x}{\partial x \partial y} + \frac{\partial^2 u_x}{\partial y \partial x} \right) + G \left(\frac{\partial^2 u_y}{\partial x^2} + \frac{\partial^2 u_y}{\partial y^2} \right) + b_y = 0 \quad (3.28)$$

For the plane strain problem, the fundamental solution is obtained for point unit loads in x and y directions of magnitude 1, which are distributed to infinity in the +z and -z directions. The solution was first worked out by Lord Kelvin. The solutions for the displacements in x

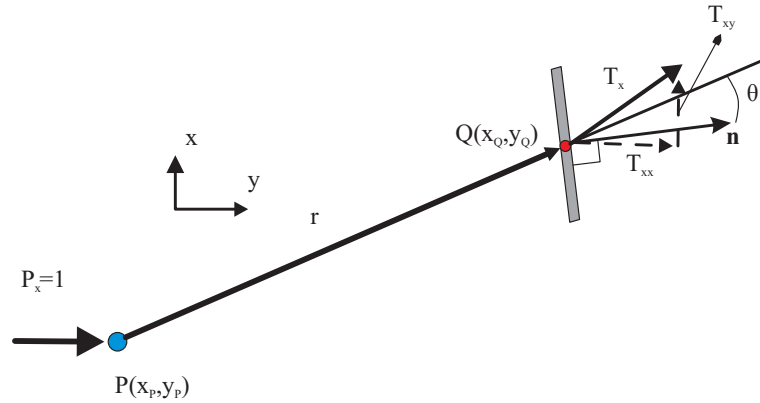


Figure 3.1: Notation for two-dimensional Kelvin solution [86].

and y directions due to a unit load in x direction can be written as

$$U_{xx}(P, Q) = C \left[C_1 \ln\left(\frac{1}{r}\right) + r_x^2 \right] \quad (3.29)$$

$$U_{xy}(P, Q) = C r_x r_y \quad (3.30)$$

$$C = 1/(8\pi G(1 - \nu)), \quad C_1 = 3 - 4\nu \quad (3.31)$$

For the boundary element method we also need the solutions for the boundary stresses (tractions) acting on a surface with an outward normal direction of n. The fundamental solutions for the tractions are obtained by first computing the fundamental solutions for the strains and then applying Hooke's law. The fundamental solutions for strains are obtained by taking the derivative of the displacement solution.

The tractions at point Q due to a unit load at P in x direction are given by

$$\vec{T}_{xx}(P, Q) = \frac{C_2}{r}(C_3 + 2r_x^2) \cos \theta \quad (3.32)$$

$$\vec{T}_{xy}(P, Q) = \frac{C_2}{r} [2r_x r_y \cos \theta + C_3 [n_y r_y - n_x r_x]] \quad (3.33)$$

$$C_2 = 1/(4\pi(1 - \nu)), \quad C_3 = 1 - 2\nu, \quad \cos \theta = \frac{1}{r} r \cdot n \quad (3.34)$$

where θ is defined in Figure 3.1 If we assume that there are no body forces acting in the domain, then integral equation becomes

$$u_x(P) = \int_S [\vec{i}_x(Q)U_{xx}(P, Q) + u_y(Q)U_{xy}(P, Q)] dS - \int_S [u_x(Q)\vec{T}_{xx}(P, Q) + u_y(Q)\vec{T}_{xy}(P, Q)] dS \quad (3.35)$$

Using matrix algebra we can combine x direction and y direction so

$$u(P) = \int_S U(P, Q)\vec{i}(Q)dS - \int_S \vec{T}(P, Q)u(Q)dS \quad (3.36)$$

Equations (3.36) represent for the two-dimensional problem discussed here a system of two integral equations which relate tractions \vec{t} and displacements u at the boundary directly, thereby removing the need to compute fictitious forces.

3.4 Numerical procedures

At the initial state, system composed of the film surface which is simulated by a finite number of nodes using predetermined segment lengths. The positions of the nodes are defined by reference to the cartesian coordinates and represented by the three dimensional vectors. After knowing the node position vectors, it is straight forward to calculate the segment lengths, s , the centroid position vectors, \vec{r}_c . Some other important system parameter calculation methods are discussed in the following subsections.

Calculation of node curvatures: The curvatures at the nodes can be evaluated at each node by using a discrete geometric relationship in connection with the fundamental definition of radius of curvature and the normal vector.

Let us define some geometric relationships; first of all the curvature of a circle with radius ρ_i (radius of curvature) is $1/\rho_i$ and furthermore three points in the plane define a unique circle

thin film line having a length designated by L , and in the direction of the applied electrostatic intensity vector. A is an anisotropy constant, which may be a few orders of magnitude. Where $n = 2m$ corresponds to the $2\pi/n$ degrees of rotational folding associated with the zone axis of a given family of planes over which diffusion takes place.

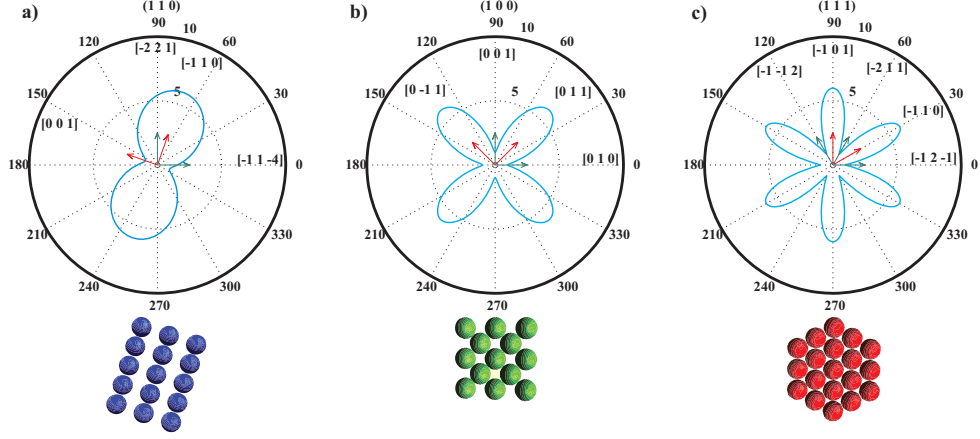


Figure 3.3: Diffusion anisotropy: a) $\{110\}$ Two-fold rotational symmetry in cubic structures with parameters $D_{\sigma}^0 = 1, A = 5, m = 1, \theta = 3.93\pi/10$. b) $\{100\}$ Four-fold rotational symmetry in cubic structures with parameters $D_{\sigma}^0 = 1, A = 7, m = 2, \theta = \pi/4$. c) $\{111\}$ Six-fold rotational symmetry in cubic structures with parameters $D_{\sigma}^0 = 1, A = 3, m = 3, \theta = \pi/6$.

Similarly, the tilt angle ϕ is the angle between the major axis of the $2\mathbf{D}$ diffusion map, along which diffusivity is maximum, and the global x-axis. The stability and instability regimes for the finite amplitude perturbations may be defined, respectively, by the following open intervals for the tilt angles: $(0 < \phi < \pi/2m)$ and $(\pi/2m < \phi < \pi/m)$, plus their periodic extensions.

Anisotropic surface stiffness: The surface energy of a rough surface can be written as

$$E_s = \int_{\mathbf{A}} \gamma(\theta) \frac{d\mathbf{A}}{\cos(\theta)} \approx \gamma(0)d\mathbf{A} + \int_{\mathbf{A}} \theta \left. \frac{\partial \gamma}{\partial \theta} \right|_{\theta=0} d\mathbf{A} + 0.5 \int_{\mathbf{A}} \theta^2 \left[\gamma(0) + \left. \frac{\partial^2 \gamma}{\partial \theta^2} \right|_{\theta=0} \right] d\mathbf{A} \quad (3.42)$$

Therefore, the energy change

$$\Delta E = 0.5 \left[\gamma + \left. \frac{\partial^2 \gamma}{\partial \theta^2} \right]_{\theta=0} \int_{\mathbf{A}} \theta^2 d\mathbf{A} \quad (3.43)$$

Sign of energy change depends on the sign of the quantity:

$$\tilde{\gamma} = \gamma + \frac{\partial^2 \gamma}{\partial \theta^2} \quad (3.44)$$

Equation 3.44 called surface stiffness. if $\tilde{\gamma} > 0$ then $\Delta E > 0$ so the surface stable against undulation, if $\tilde{\gamma} < 0$ then $\Delta E < 0$ then surface is unstable against undulation. Latter case, the surface will minimize its energy by developing facets.

In Eq. (3.1), the expression denoted by $\bar{\gamma}(\hat{\theta}, \hat{\phi}, m) = \{\tilde{\gamma}(\hat{\theta}, \hat{\phi}, m) + \tilde{\gamma}_{\theta\theta}(\hat{\theta}, \hat{\phi}, m)\}$ is the angular part of the surface stiffness, namely given by $[\hat{\gamma}(\hat{\theta}, \hat{\phi}, m)/\gamma^0]$. By following the general trend, one may introduce the trigonometric representation by defining the tilt angle $\hat{\phi}$ as such that the surface normal of a selected vicinal plane coincides with the x-axis, when theta becomes equal to zero, $\hat{\phi} = 0$;

$$\bar{\gamma}(\hat{\theta}, \hat{\phi}, m) = \gamma(\hat{\theta}, \hat{\phi}, m)/\gamma_0 = \{1 + B \sin^2 [m(\hat{\theta} - \hat{\phi})]\} \quad (3.45)$$

Where γ_0 is the minimum value of the surface Gibbs free energy density, and $B \geq 0$ is the surface stiffness anisotropy constant, which is a positive quantity. Using above relationship denoted as Eq. (3.45), one may easily deduced the surface stiffness formula as presented below;

$$\hat{\gamma}(\hat{\theta}, \hat{\phi}, m) = \gamma_0(1 + B/2) \left[1 - \frac{B(1 - 4m^2)}{B + 2} \cos [2m(\hat{\theta} - \hat{\phi})] \right] \quad (3.46)$$

Where $\hat{\theta} = \pi/2 - \theta$ is the angle between the line normal vector of the diffusion plane of a generalized cylindrical surface projected into 2-D space (surface normal in 3-D) and the x-axis of the global Cartesian reference system. In Fig.3.4, the normalized specific surface Gibbs free energy $\bar{\gamma}$ and the angular part of the surface stiffness $\bar{\gamma} = (\hat{\gamma}/\gamma^0)$ are illustrated in the polar plot for the sidewalls planes of a metallic single crystal, thin film interconnect line, having a surface texture denoted by (001) , where $\hat{m} \equiv 2m = 2$.

According to Eq. (3.46), the surface stiffness can be positive definite, regardless the orientation of the surface with respect to the EM direction, if the surface Gibbs free energy anisotropy constant satisfies the following inequality: $B \leq 2/[|(1 - 4m^2)| - 1]$. That means one should have the following set of upper limits for $B \leq \{1; 1/7; 1/17\}$ in the case of two, four and six fold symmetries, respectively. As can be seen from Fig 3.4 for the given anisotropy constant $B = 0.2 > 1/7$ for the set of planes belonging to the [001] zone axis, the imperfect faceting may occur at the cusps orientations (vicinal planes) because of the appreciable negative surface stiffness appears at the directions $\langle \mp 110 \rangle$, where one has concave topography (maxima in

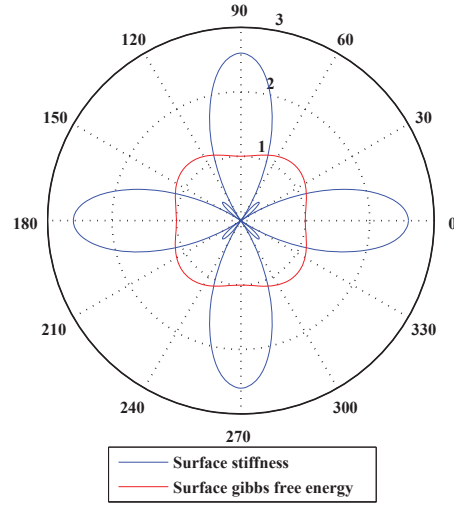


Figure 3.4: Typical behavior of the surface specific Gibbs free energy and the surface stiffness for the set of four fold symmetry planes $\{0 \neq 10\}$ and $\{\neq 100\}$ in a fcc crystal having $[001]$ zone axis normal to the thin film surface. The anisotropy constant: $B = 0.2$. The negative spikes of the surface stiffness are clearly seen along the $\langle 1 \neq 10 \rangle$ directions, which indicates inherent instability.

free energy profile), because of the relatively weak representation of the cusp regions by the trigonometric function. These negative surface stiffness spikes may cause inherent instability along those directions.

Wetting potential: Surface energy of thin film undergoes rapid transition from γ_f to γ_s , this transition depends on the film thickness.

$$\gamma_{f \leftrightarrow s}(y) = \frac{\gamma_f + \gamma_s}{2\gamma_f} + \left[\frac{\gamma_f - \gamma_s}{\gamma_f} \right] \frac{1}{\pi} \arctan y/\delta \quad (3.47)$$

To model for the wetting layer, wetting potential $\omega(y)$ is defined as

$$\omega(y) = n_y \cdot \frac{d\gamma_{f \leftrightarrow s}(y)}{dy} \quad (3.48)$$

$$\omega(y) = \frac{1}{\sqrt{1+y^2}} \frac{\gamma_f - \gamma_s}{\pi\gamma_f} \frac{\delta}{\delta^2 + y^2} \quad (3.49)$$

where $n_y = -n \cdot j$ is the projection of the surface normal along y axis. By employing this potential, surface energy change from the value of substrate to the value of film shows smooth transition. Derivation of the wetting potential formulation is done by Golovin [60].

Adaptive remeshing: For keeping the experiment time and error in an acceptable level, adaptive remeshing system employed in the simulations. For this purpose, first energy term μ^n is defined for each node in the system at given time step n . The energy term is naturally calculated in the program as a chemical potential. Then, the gradient of the energy, $\nabla\mu_i^n$, is approximated at the thin film surface by the usage of finite difference expression.

$$\nabla\mu_i^n = \frac{\mu_{i+1}^n - \mu_i^n}{S_i} \quad (3.50)$$

Where S_i is the segment length which connects the nodes. Defining thresholds ξ and ζ , segment is marked for remeshing if the following criteria are met:

$$|\nabla\mu_i^n| > \xi G^n \text{ and } |\mu_i^n| > \zeta Q^n \quad (3.51)$$

for dividing the segment and

$$|\nabla\mu_i^n| < \xi G^n \text{ and } |\mu_i^n| < \zeta Q^n \quad (3.52)$$

for erasing the segment.

Where

$$G^n = \max|\nabla\mu_i^n| \quad (3.53)$$

$$Q^n = \max|\mu_{av}^n| \quad (3.54)$$

$$\mu_{av}^m = \frac{1}{N} \sum_i |\mu_i^n| \quad (3.55)$$

The adaptive remeshing is executed in a segment when an instantaneous threshold are exceeded. Therefore, fast evolving high energy gradient surfaces will have smallest possible segment length, on the other hand slow evolving and low energy gradient surfaces will have largest possible segment length.

Explicit euler's method: Explicit Euler's method (Mathews, 1992) is used to perform the time integration of Eq. (3.1) for the surface evolution. The time step is determined from the maximum surface velocity and minimum segment length such that the displacement increment is kept constant for all time step increments. This so-called adapted time step auto-control mechanism combined with the self-recovery effect associated with the capillary term guarantees the long time numerical stability and the accuracy of the explicit algorithm even after performing several hundred to several millions steps.

CHAPTER 4

THE ORIENTATION DEPENDENT INTERACTION OF ELECTROMIGRATION AND THE UNIAXIAL COMPRESSIVE STRESSES IN SINGLE CRYSTAL METALLIC THIN FILMS

4.1 Physical model

Physically, the thin film is attached to the substrate with a coherent interface, and the top surface is subjected to the surface drift diffusion, and it is exposed to a vapor environment, whose pressure may be neglected. Since simulations are performed in $2\mathbf{D}$ space (equivalent to parallel ridges or quantum wires in three dimensions), no variation of the interface profile and the displacement fields in the film and substrate occurs in the direction (i.e., \hat{z} axis) perpendicular to the plane of the schematics in Fig.4.1. Similarly, to simplify the numerical computations it is assumed that the film/substrate interface is flat and the substrate is stiff. These assumptions guarantees that the initial displacement along the interface associated with the misfit strain ε_0 stays constant during the evolution process (i.e., Dirichlet boundary condition).

The morphology of an initially perfectly flat surface having a perturbation in the shape of a sinusoidal wave is demonstrated in Fig.4.1, where the positive direction of electric field is from the left (anode) to the right (cathode). The scaled interconnect width is denoted as \bar{h}_0 , and the wave vector and the wave length are given by \bar{k} and $\bar{\lambda}$, respectively. These are all scaled with respect to the arbitrary length denoted by ℓ_0 .

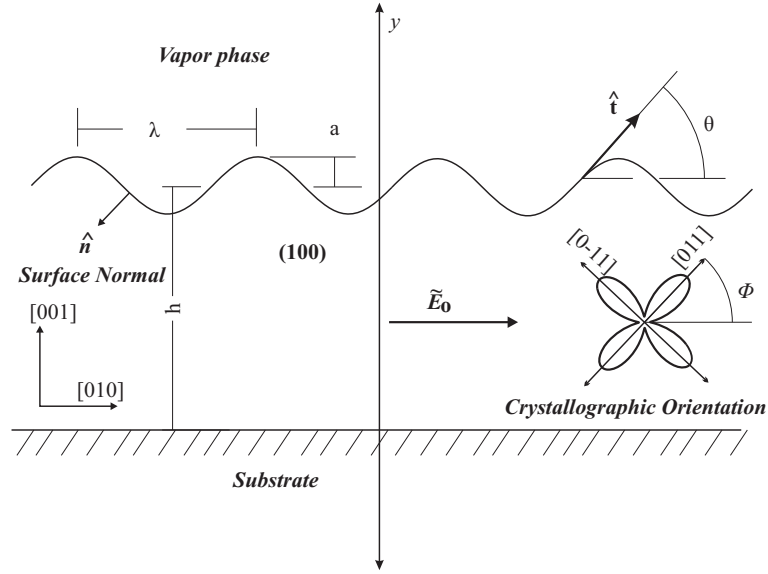


Figure 4.1: Side view of metallic thin film with sinewave perturbation.

4.2 Linear stability analysis

In this section linear stability analysis of the relevant equation (Eq. (4.2)) is presented. Traveling plane wave with complex argument is injected to the system as an initial data (Eq. (4.1)). Where the scaled thin film thickness is denoted as $h_0 = 1$, and the wave vector and the wavelength are given by $\bar{k} = k h_0$ and $\bar{\lambda} = \lambda h_0$, respectively. These are all scaled with respect to the arbitrary length chosen as $\ell_0 = h_0$ for convenience. Here h_0 is the initial uniform thickness of the metallic thin-film before it is exposed to any surface disturbances.

$$h(x, t) = 1 + \bar{M}_{vb} \Delta \bar{g}_{bv} t + \epsilon a_\epsilon \{ \exp [i k(x - v t)] + c.c. \} \quad (4.1)$$

where a_ϵ , the amplitude of the traveling wave, is $k = 2\pi/\bar{\lambda} = k h_0$, which is the normalized wave number, and $0 \leq \epsilon \leq 1$ is the perturbation order operator. v is a complex number (i.e., phase velocity), which carries the most important information concerning the dynamical behavior of the system. $\omega = k v$ is called the frequency index. The real part of the complex velocity, v_{\Re} , corresponds to the phase velocity (dispersion), and the imaginary part, v_{\Im} , deals with the dissipation or growth rate $\Gamma = k v_{\Im}$.

$$\bar{V}_{ord} = \frac{\partial}{\partial \bar{\ell}} \bar{D}(\theta, \phi, m) \left[\frac{\partial}{\partial \bar{\ell}} (\Xi \bar{\sigma}_h - \Sigma \bar{\sigma}_h^2 + \bar{k} + \chi \bar{\vartheta}) \right] \quad (\text{Ordinary points}) \quad (4.2)$$

Above equation can be converted to cartesian coordinate system with initial perturbation $h(x, t)$ as follows:

$$\bar{V}_{ord} = \frac{\partial h(x, t)}{\partial \bar{t}} = \frac{\partial}{\partial \bar{x}} \bar{D}(\theta(x, t), \phi, m) \left[\frac{\partial}{\partial \bar{x}} (\Xi \bar{\sigma}_h - \Sigma \bar{\sigma}_h^2 + \bar{k} + \chi \bar{\vartheta}) \right] \quad (\text{Ordinary points}) \quad (4.3)$$

where

$$\theta(x, t) = \arcsin \left[\frac{2}{\sqrt{1 + \left(\frac{\partial h(x, t)}{\partial x}\right)^2}} \right] \quad (4.4)$$

So following transformations must be defined:

$$\partial_x \equiv (1 + h_x^2)^{-1} h_{xx} \partial_\theta, \quad \partial_\ell \equiv (1 + h_x^2)^{-1/2} \partial_x \quad (4.5)$$

and $f(h_x)$ called structure function is defined as

$$f(h_x) = (1 + h_x^2)^{-1/2} \quad (4.6)$$

So the equation 4.2 takes the following form in cartesian coordinates.

$$-f(h_x) h_t = f(h_x) \partial_x [D(\cdot) f(h_x) \partial_x (\Xi \bar{\sigma}_h - \Sigma \bar{\sigma}_h^2 + f(h_x)^2 h_{xx} + \chi \bar{\vartheta})] \quad (4.7)$$

The quasielectrostatic potential φ satisfies the Laplace equation $\nabla^2 \varphi = 0$ in $2\mathbf{D}$ space and the Neumann boundary conditions at the inactive and active surfaces, respectively:

$$\vartheta_y(0, x; t) = 0, \quad \text{and} \quad \vartheta_y(h, x; t) = h_x(x, t) \varphi_x(h, x; t) \quad (4.8)$$

So, the normalized quasielectrostatic potential at the active sidewall (or upper surface) may be represented by the following expression, which was first presented by Schimschak and Krug and later further elaborated by Brush and Oren [87]:

$$\bar{\vartheta}(x, y : t) = -x - i\epsilon a_\epsilon \frac{\coth(ky)}{\sinh(k)} \exp[ik(x - vt)] + c.c. \quad (4.9)$$

for the upper surface $y = 1$ therefore

$$\bar{\vartheta}(x : t) = -x - i\epsilon a_\epsilon \frac{1+k}{k} \exp[ik(x - vt)] + c.c. \quad (4.10)$$

Evolution equation takes the following form :

$$h_t = \lim_{\theta \rightarrow 0} \{-\chi [D(\theta, \phi, m) \partial_{xx} + \partial_x D(\theta, \phi, m) \partial_x^C] \vartheta - D(\theta, \phi, m) h_{xxxx} + [D(\theta, \phi, m) \partial_{xx} + \partial_x D(\theta, \phi, m) \partial_x^C] [\Xi \bar{\sigma}_h - \Sigma \bar{\sigma}_h^2]\} \quad (4.11)$$

In the above relationship the superscript over the partial differential operator ∂_x^C implies the extraction of the constant term from the gradient of the operand function. In the case of homogenous fields, this term drops out automatically. In addition, if one assumes that the thermal part of the Gibbs free energy of the transformation $\Delta \bar{g}_{bv}^0$ is homogeneous along the surface layer and the transformation mobility \bar{M}_{vb}^0 is independent of the applied stress and orientation of the surface, then one may write

$$i k v - \bar{M}_{vb}^0 (\bar{g}_{bv}^0 + \bar{w}_b^0) = i \chi k^2 \coth(k) [1 + A \cos^2(m\phi)] + \chi m k^2 A \sin(2m\phi) + [1 + A \cos^2(m\phi)] k^4 + \{[1 + A \cos^2(m\phi)] \partial_{xx} + mA \sin(2m\phi) \partial_x^C\} [\Xi \bar{\sigma}_h - \Sigma \bar{\sigma}_h^2] \quad (4.12)$$

In Eq. (4.12), $\Sigma \bar{\sigma}_h^2$ represents the first-order contribution to the ESED due to the formation of surface undulations on the surfaces, otherwise flat and traction free. \bar{w}_b^0 is the elastic strain energy density for the flat surface. The above general relationship yields the following expressions, for the growth rate and the phase velocity, by separating the real and imaginary parts of the complex velocity such as $v = v_{\Re} + i v_{\Im}$, where the real part corresponds to the propagation or phase velocity and the imaginary part is related to the growth rate constant denoted by Γ . Electromigration induced disturbance drift and disturbance growth rate associated with electromigration, elastostatic forces and capillarity effects may be easily deduced as follows:

$$\Gamma \equiv k v_{\Im} \cong -\chi m k^2 A \sin(2m\phi) - [1 + A(\cos^2(m\phi))] [\Xi - 2\Sigma] 2k^3 - [1 + A \cos^2(m\phi)] k^4 \quad (4.13)$$

and

$$v_{drift} = v_{\Re} \cong \chi k^2 \coth(k) [1 + A \cos^2(m\phi)] \quad (4.14)$$

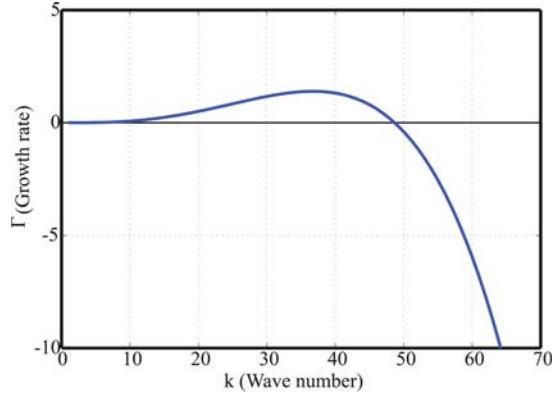


Figure 4.2: Growth rate vs. wavenumber in the absence of electrostatic force.

The sign of the growth rate depends on the sign of the applied stress system acting along the interfacial layer denoted by σ , whether it is tension $\Xi > 0$ or compression $\Xi < 0$. Equation 4.13 shows that the elastic dipole interaction always favors surface smoothing under tension, on the other hand if there is a compression, enhancement of the roughness occur regardless of the wave number or the tilt angle (Fig. 4.3). For copper under $\sigma = 100 \text{ MPa}$ ($E = 130 \text{ GPa}$, $\nu = 0.34$) compressive load growth rate constant Γ vs. wave number k is shown in Fig. 4.2 for isotropic diffusivity. Growth rate at $k=0$ is always zero, often this is the indication of conservation law.

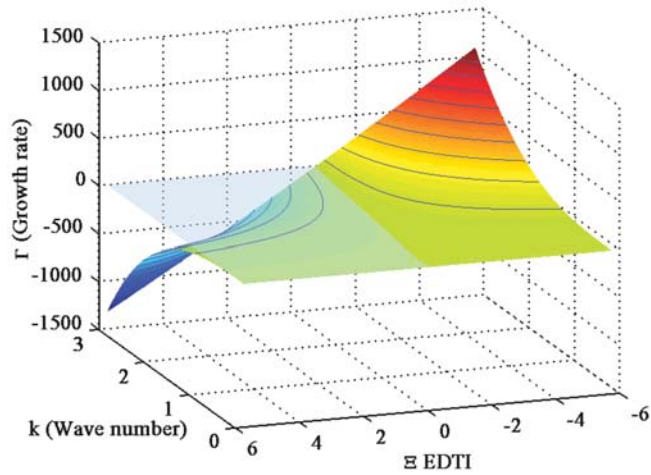


Figure 4.3: The instability growth rate Γ is plotted for isotropic diffusion with respect to the wave number $k = 0 - 4$ and applied misfit stress $\Xi = \pm 6$. The elastostatic data for copper used: $E_0 = 130 \text{ GPa}$, $\nu = 0.34$, $g_\sigma^0 = 1.6 \text{ JM}^{-2}$, and $|\text{Tr}\lambda_\sigma^{\text{Cu}}| = 0.4$.

In the absence of electromigration, Fig. 4.4 shows the stress induced growth rate of instability of hypothetical copper thin film having (110) under $\sigma = -100 \text{ MPa}$ load and range of wave numbers. Here, Diffusion anisotropy intensity $A = 10$ is selected and plot generated for $\phi = \pm\pi i$. For the high values of wave number $k > 2$, surface shows stability at given stress load $\Xi = 1.116$ with any texture angle.

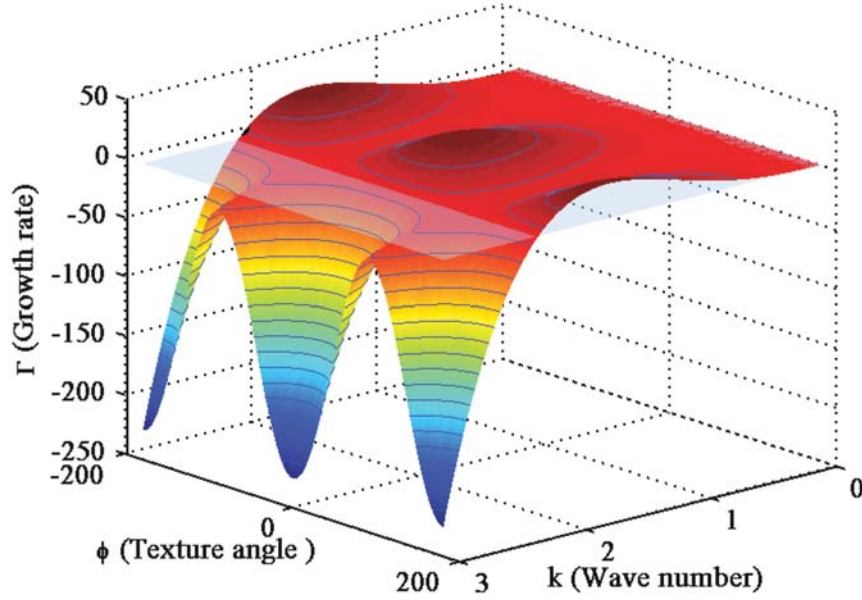


Figure 4.4: Growth rate constant Γ is plotted with respect to the tilt angle ϕ and wave number k for the sidewall surface morphological evolution of thin film having (110) plane which has 2 fold symmetry.

And the critical wavelength may be calculated with following equation in the absence of electric potential:

$$\lambda_c = \frac{\pi}{2\Sigma - \Xi} \quad (4.15)$$

$$\lambda_m = \frac{4\pi}{6\Sigma - 3\Xi} \quad (4.16)$$

Under the critical wavelength λ_c , Surface perturbation shows instability. So λ_c represents the maximum wavelength leading to growth of the perturbation. And λ_m defines the wavelength with maximum growth rate at a given stress. For the compressive stress values $\sigma_0 =$

-100 MPa – -1000 MPa , critical wavelength varies from 280 nanometer to 27 nanometer in real dimensions in the absence of electric potential. These calculated wavelengths are in good agreement with the experimental observations of Maroutian et al. [76].

Figure 4.5 shows both healing and worsening effect of the electromigration force when coupled with stress field. Healing effect of electromigration even at high EDTI $\Xi = -11.16$ values at which instability is expected is observed at $\phi = 0.25 - 1.5$ interval for wave number $k = 25$. On the other hand, at EDTI $\Xi > -7$ values at which stability is expected instability regions appears at certain tilt angle interval $\phi > 1.5$ due to the electromigration.

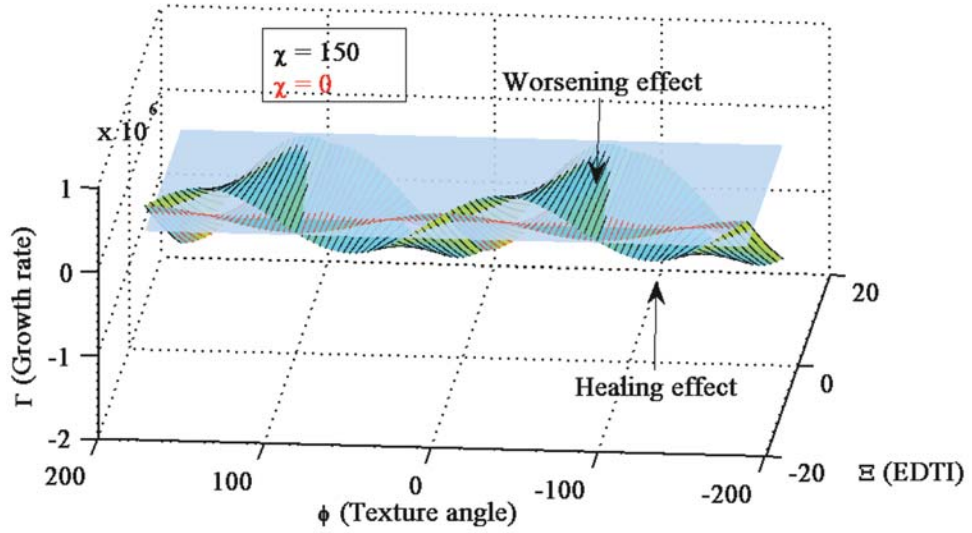


Figure 4.5: Growth rate constant Γ is plotted with respect to the tilt angle ϕ and EDTI Ξ for the sidewall surface morphological evolution of thin film having (110) plane which has 2 fold symmetry with and without electromigration ($\chi = 0$ and $\chi = 150$) for constant wave number $k = 25$.

An alternative way to summarize the information in Eq. (4.13) is to plot neutral stability curve where the real part of the growth rate is zero. Neutral stability curve does not give information about the growth rate, but it gives the picture of the range of modes that could grow from uniform state that might be available for pattern formation.

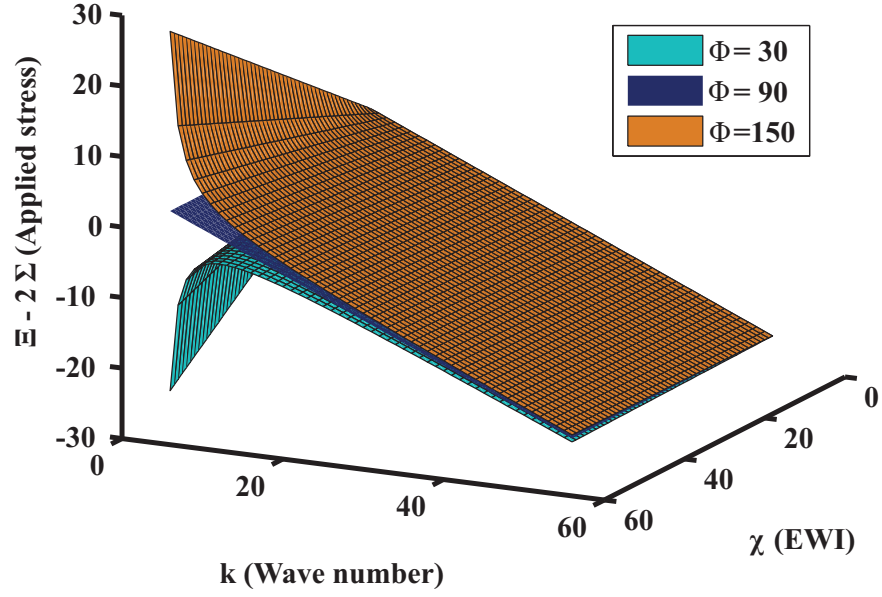


Figure 4.6: Neutral stability plot for (110) plane at different angles between texture and substrate. Uniform state is stable below the plane and above the plane pattern formation is possible.

4.3 Results and discussion

In this section, it is assumed that the sample is sandwiched between top and bottom high resistance coatings, which constitute diffusion barrier layers with the substrate. It is also assumed here that only the one edge (sidewall) of the interconnect line is subjected to the surface drift diffusion, and it is exposed to an environment whose conductivity is neglected.

Different combination of misfit stress (compression or tension) $\sigma \Rightarrow \{\Xi, \Sigma\}$, electron wind intensity χ , drift diffusion anisotropy coefficients $\{\phi, A\}$, various combination of wavelengths $\lambda = 1 - 4$ and amplitudes $Amp = 0.01 - 0.5$ are considered in this section. Electron wind intensity covers very large interval from low to high current densities by taking $\chi = 1 - 50$ which corresponds to $J = 10^9 - 10^{12} A/M^2$. Applied misfit stress taken in the range of $\sigma_0 = \pm 1 MPa - \pm 1000 MPa$ which corresponds to the following parameters for copper thin film with width of $w_0 = 10^{-6} m$; having EDTI $\Xi = \pm 0.1 - \pm 11.16$, and ESED $\Sigma = 2.12 * 10^{-9} - 0.212$ assuming that elastic dipole tensor constant for copper is given by $|Tr\lambda| = 0.4$. The specific surface Gibbs free energy of copper is taken as $g_{Cu} = 1.6J/M^2$, and Young modulus $E_{Cu} = 70 GPa$, and Poisson's ratio $\nu_{Cu} = 0.35$. In

addition to isotropic case, anisotropic structure is taken as FCC structure with three different groups of crystal planes ($\{110\}$, $\{100\}$, $\{111\}$) for the surface of single crystal thin film. Therefore, $\langle 110 \rangle$, $\langle 100 \rangle$, and $\langle 111 \rangle$ are the zone axis of perturbed sidewall where the diffusion take place.

4.3.1 Epitaxially strained thin film with isotropic texture on rigid substrates

In this section, isochoric system is considered such that no external traction applied to the evolving surface, surface diffusivity is defined as isotropic. System evolution is investigated under only applied misfit strain.

Evolution of the boundary is described in terms of displacement velocities with following formula:

$$\bar{V}_{ord} = \frac{\partial}{\partial \bar{\ell}} \left[\frac{\partial}{\partial \bar{\ell}} \left(\Xi \bar{\sigma}_h - \Sigma \bar{\sigma}_h^2 + \bar{\kappa} \right) \right] \quad (\text{Ordinary points}) \quad (4.17)$$

In Eq. 4.17, $\bar{\ell}$ is the arc length in 2D space which is scaled with respect to ℓ_o . First part of the equation describes the evolution behavior of strained thin films by surface diffusion which is driven by the gradient of ESED $\Sigma(\bar{\sigma}_h)^2$ and capillary potential $\bar{\kappa}$.

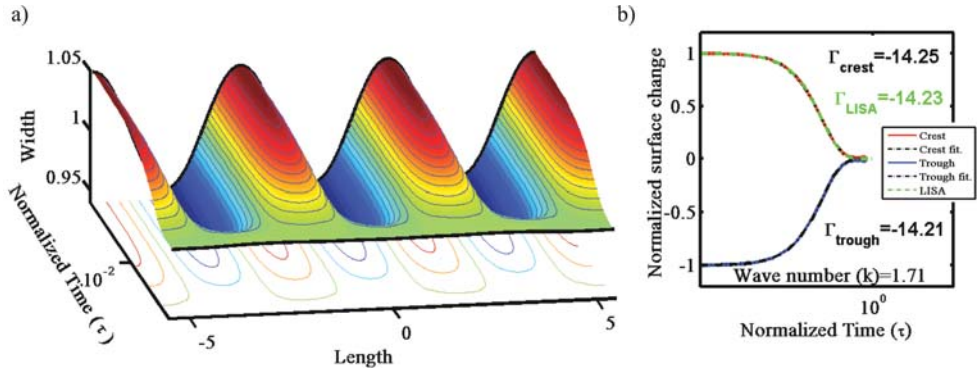


Figure 4.7: Side wall morphological evolution of single crystal copper thin film with isotropic diffusivity, wave number $k = 1.7$ and amplitude of $Amp = 0.05$, which is subjected to misfit tensile $\Xi = 0.56$ along the longitudinal axis. (a) shows morphological evolution in 3D plot. (b) shows the normalized displacement of trough and crest tips as a function of normalized time in logarithmic scale.

Fig. 4.7 demonstrates the behavior of wave patterned surface under 50MPa ($\Xi = 0.56$) tensile

load. Experimental growth rate is calculated as $\Gamma_{crest} = -14.26$ and $\Gamma_{trough} = -14.21$, which are excellent agreement with the LISA value $\Gamma_{LISA} = -14.23$. Negative growth rate term indicate that surface roughness decay. Surface roughness slowly decay off in due time and finally perfect flat surface is formed.

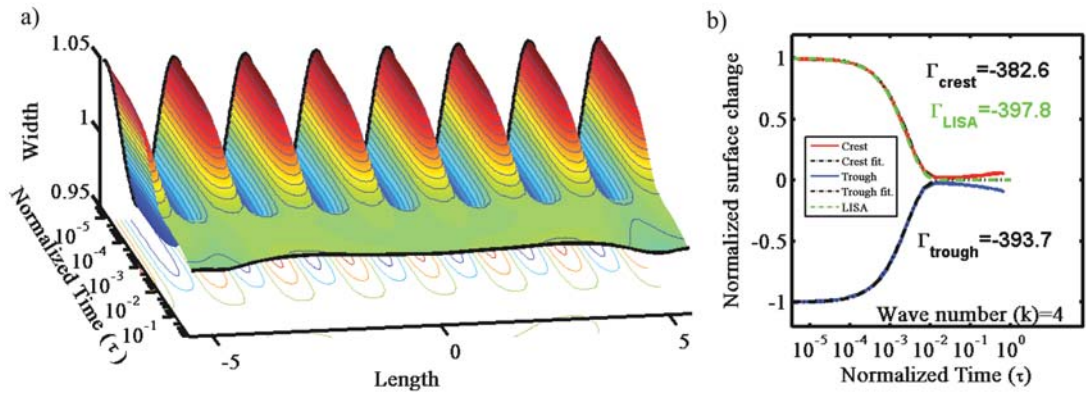


Figure 4.8: Side wall morphological evolution of single crystal copper thin film with isotropic diffusivity, wave number $k = 5.14$ and amplitude of $Amp = 0.05$, which is subjected to misfit tensile $\Xi = -0.11$ along the longitudinal axis. (a) shows morphological evolution in 3D plot. (b) shows the normalized displacement of trough and crest tips as a function of normalized time in logarithmic scale.

Even at higher wave number $k = 5.14$ and compressive stress $10MPa$ ($\Xi = -0.11$) LISA successfully predict the behavior of the surface evolution (Fig. 4.8) which is $\Gamma_{crest} = -382.6$ and $\Gamma_{trough} = -393.7$ and theoretical value is $\Gamma_{LISA} = -397.8$. In both case surface evolution takes place under the dominant effect of capillary forces. Increase in wave number (k) increase the tendency to stability, so perturbed surface with large wave number has tendency to decay. Isotropic thin film experiments shows that decay rate of the surface can be precisely predicted by LISA for $-0.56 \leq \Xi \leq 11.16$ stress range and wave amplitudes $Amp \leq 0.1$.

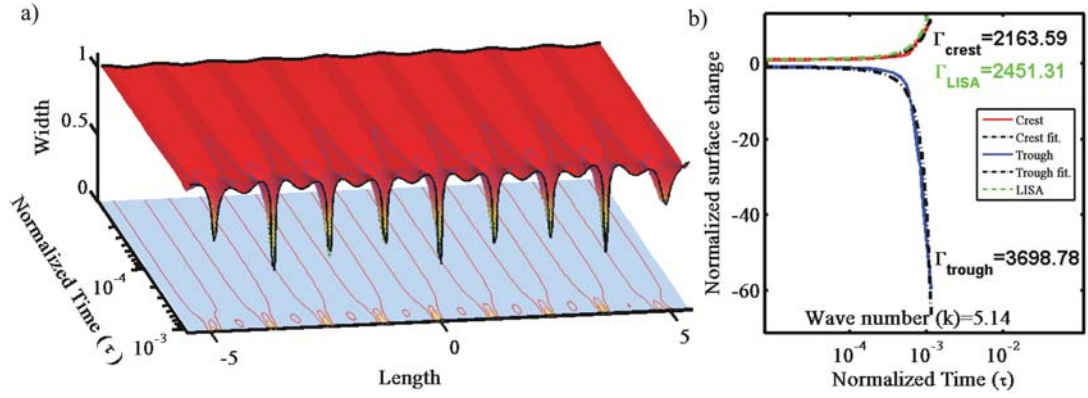


Figure 4.9: Side wall morphological evolution of single crystal copper thin film with isotropic diffusivity, wave number $k = 5.14$ and amplitude of $Amp = 0.01$, which is subjected to misfit tensile $\Xi = -11.16$ along the longitudinal axis. (a) shows morphological evolution in 3D plot. (b) shows normalized the displacement of trough and crest tips as a function of normalized time in logarithmic scale.

In Fig. 4.9(a) surface crack like formation can be seen under the high misfit stress $\Xi = -11.16$ with the grooving at the sides of crack. These crack like formations appear with different forms for high compressive forces $\sigma < -100 \text{ MPa}$ ($\approx \Xi < -1.1$). Due to the fast growth of grooving with respect to initial crest tip after the sharp elbow formed at crest height change, Fig. 4.9(b) defines the growth rate of the grooving. This phenomenon is called as "tip splitting" in literature. The sharp elbow on the normalized crest height plot is closely related to the onset of tip-splitting regime ($\tau = 5.8 \cdot 10^{-4}$), which also shows accelerated displacement kinetics of crack and grooving. After that point, trough tips transform into crack like form and deviates from the LISA, which predicts growth rate as $\Gamma_{LISA} = 2451$, with growth rate $\Gamma_{trough} = 3698.78$.

In Fig. 4.10 summarize the trough splitting of the surface at $\sigma_0 = 500 \text{ MPa}$ misfit stress. Fig. 4.10(c) the surface profile, which shows no sign of tip splitting at trough, is plotted. On the other hand, in same figure sign of tip splitting of trough can be seen at hoop stress plot. Here, crest growth rate ($\Gamma_{crest} = 68.97$) fits to LISA with some deviation after tip splitting, trough growth rate ($\Gamma_{trough} = 218.8$) show large deviation from the calculated growth rare of LISA $\Gamma_{LISA} = 48.63$. Again formation of elbow can be seen at normalized surface displacement graph (Fig. 4.10). Under high compressive stress values surface perturbation with low wave number tends to multiple crack form which may be called as trough splitting. Concentration

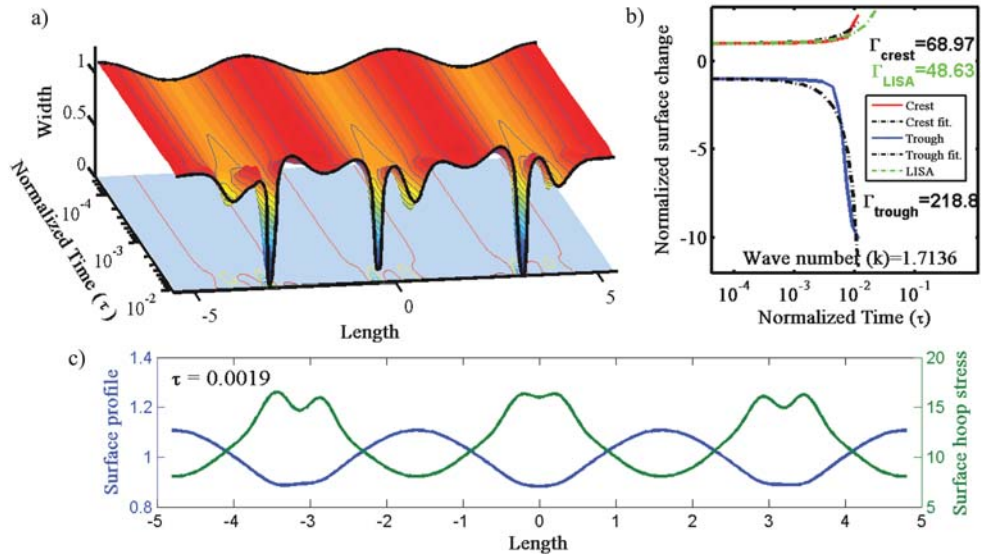


Figure 4.10: Side wall morphological evolution of single crystal copper thin film with isotropic diffusivity, wave number $k = 1.7$ and amplitude of $Amp = 0.1$, which is subjected to misfit tensile $\Xi = -5.58$ along the longitudinal axis. (a) Morphological evolution in 3D plot. (b) Normalized the displacement of trough and crest tips as a function of normalized time in logarithmic scale. (c) Instantaneous hoop stress and surface profile along the thin film at the on set of trough tip splitting ($\tau = 0.0019$).

of stress give rise to instability of trough so multiple crack formation observed.

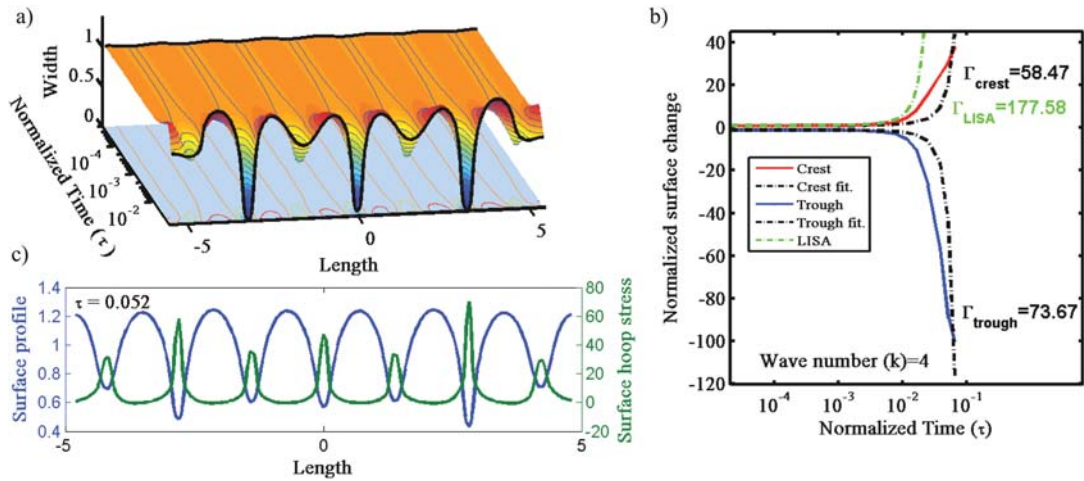


Figure 4.11: Side wall morphological evolution of single crystal copper thin film with isotropic diffusivity, wave number $k = 3.99$ and amplitude of $Amp = 0.01$, which is subjected to misfit tensile $\Xi = -3.35$ along the longitudinal axis. (a) Morphological evolution in 3D plot. (b) Normalized displacement of trough and crest tips as a function of normalized time in logarithmic scale. (c) Instantaneous hoop stress and surface profile along the thin film at the on set of trough tip splitting ($\tau = 0.052$).

Fig. 4.11 illustrate the transition regime experiment which has $\sigma_0 = -300 \text{ MPa}$ ($\Xi = -3.35$), $k = 3.99$ and $Amp = 0.01$ as a experiment parameter, here some troughs try to decay on the other hand other troughs transform into the crack like shape. This tendency can be summarized as surface perturbation with large wave numbers under low compressive stress values tends to decay off.

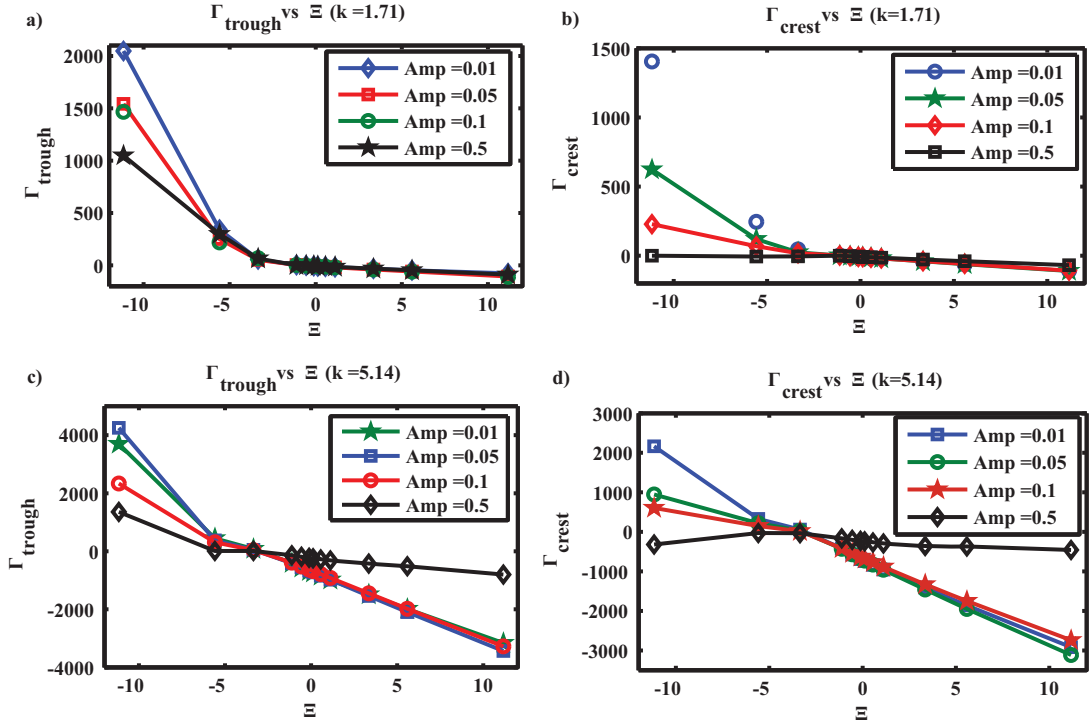


Figure 4.12: Growth rate Γ versus EDTI (Ξ) values represented for different values of amplitude and wave numbers. (a) Trough growth rate for wave number $k = 1.71$. (b) Crest growth rate for wave number $k = 1.71$. (c) Trough growth rate for wave number $k = 5.14$. (d) Crest growth rate for wave number $k = 5.14$.

At low wave number $k = 1.71$ growth rate values of different amplitude surfaces shows almost identical growth rate at EDTI values over $\Xi \geq -1.116$ and it shows linear dependency to the applied misfit stress at both crest and trough (Fig. 4.12(a)-(b)). On the other hand, at high compressive stress growth rate changes quadratically with applied misfit stress. Same nonlinear respond to applied high compressive misfit stress is seen at experiments with wave number $k = 5.14$ (Fig. 4.12(c)-(d)). At EDTI values higher than $\Xi \geq -1.116$ experiments with amplitude value $Amp = 0.5$ deviates from the linear behaviors, rest of the growth rate change with respect to Ξ values behaves similar with small slope change. Crest behavior at amplitude values $Amp = 0.5$ deviates from the general behavior at all experiments and LISA

predictions. LISA assume that Angle of the surface tangent with substrate surface is about 0, so at Amp = 0.5 this angle greater then the assumption. Deviation from general behavior is due to the high $\frac{Amp}{\lambda}$ ratio, at which capillary forces increase due to the increased curvature of surface.

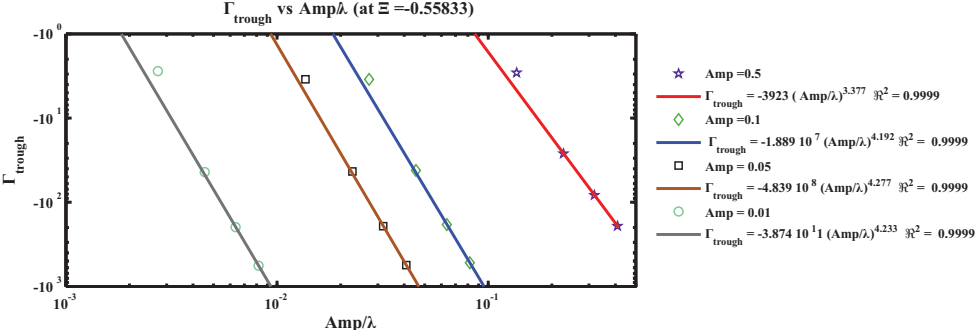


Figure 4.13: Growth rate Γ versus Amp/λ plot for $\Xi = -0.5558$ for different amplitudes and their power series fittings.

Amplitude dependency of growth rate is obeying power law at EDTI values $\Xi > -3.35$. At lower $\Xi \leq -3.35$ values growth rate does not change with amplitude because after the crack formation growth rate represents the crack propagation at trough which is mainly driven by crack tip stress concentration.

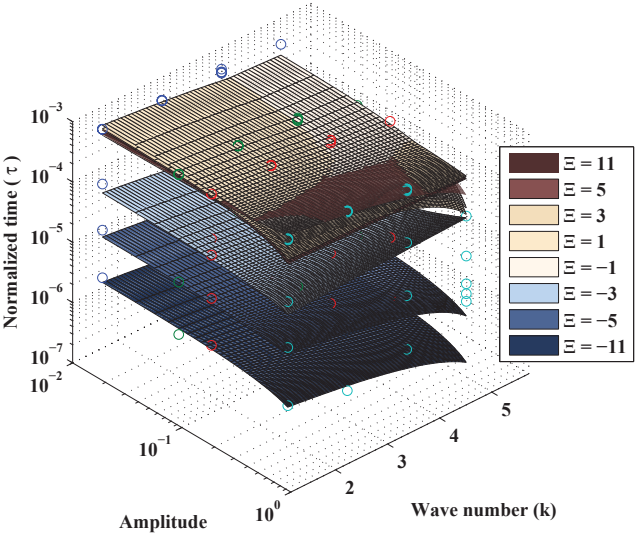


Figure 4.14: Experiment normalized failure and equilibrium reach time plot with respect to amplitude and surface wave number for different misfit stress values Ξ .

Fig. 4.14 shows final time at which case surface became flat with decaying of perturbation or perturbation reach to the substrate with growing cracking. Large distinction of final time between stress values $\Xi \leq -3.35$ and $\Xi > -3.35$ is observed. at $\Xi \leq -3.35$ high compressive stress values crack formation observed due to the instability of the surface, so thin films crack and divided into smaller pieces in a short time. On the other hand, under tensile stresses and low compressive stresses ($\Xi \geq -1.12$) surface perturbation tends to stable by decaying off.

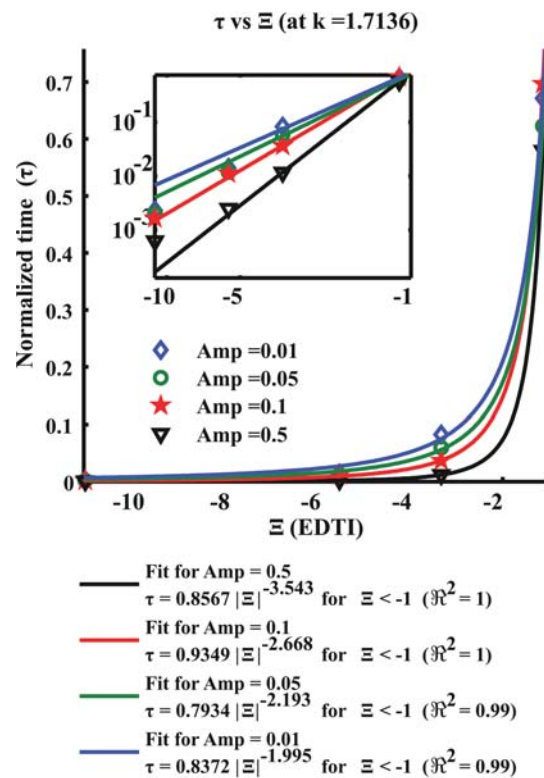


Figure 4.15: Normalized time plot with respect to misfit stress values $\Xi < -1$ (EDTI) for different amplitudes and their power series fittings at wave number $k = 1.7136$.

Fig. 4.15 represents the normalized time vs. EDTI graph and their regression analysis for EDTI values in the range $-12 < \Xi < -1$. As a result of analysis following set of equations obtained.

$$\tau_{Amp=0.5} = 0.8567|\Xi|^{-3.543} \quad \forall -12 < \Xi < -1 \quad (\mathcal{R}^2 = 1) \quad (4.18)$$

$$\tau_{Amp=0.1} = 0.9349|\Xi|^{-2.668} \quad \forall -12 < \Xi < -1 \quad (\mathcal{R}^2 = 1) \quad (4.19)$$

$$\tau_{Amp=0.05} = 0.7934|\Xi|^{-2.193} \quad \forall -12 < \Xi < -1 \quad (\mathcal{R}^2 = 0.99) \quad (4.20)$$

$$\tau_{Amp=0.01} = 0.8372|\Xi|^{-1.995} \quad \forall -12 < \Xi < -1 \quad (\mathcal{R}^2 = 0.99) \quad (4.21)$$

For the compression values in the range of $11.16 < \Xi < -3.35$, these functions predict the failure time of the thin film by cracking. As the thin film perturbation amplitude increase exponent of $\frac{1}{\Xi}$ increase. This shows that as the amplitude increase time to reach substrate decrease.

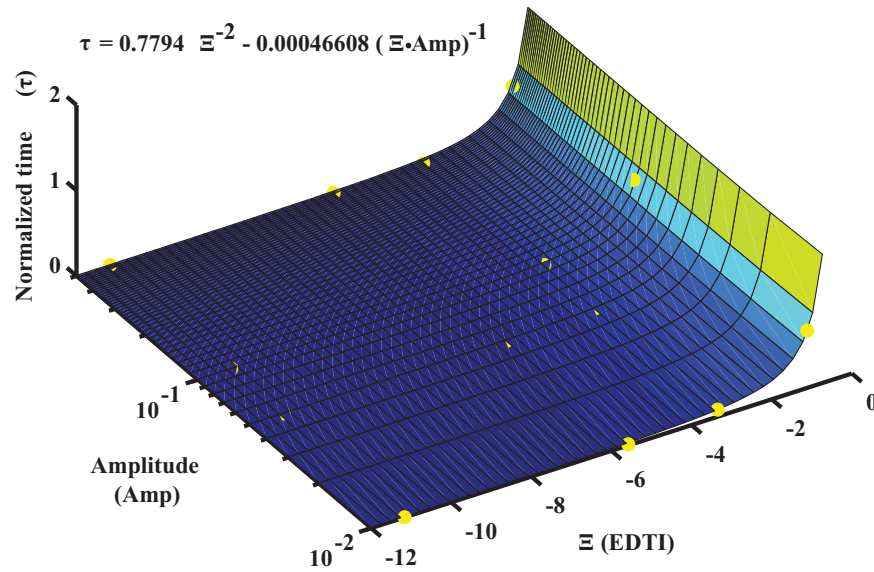


Figure 4.16: Experiment normalized failure time plot with respect to amplitude and surface wave number for $11.16 \geq \Xi \geq -3.35$ misfit stress values and its fitting surface.

General form might be defined as $\tau = 0.7794\Xi^{-2} - 4.6610^{-5}(\Xi \text{ Amp})^{-1}$.

For the tensile stress, Fig. 4.17 shows the normalized time vs. Ξ values.

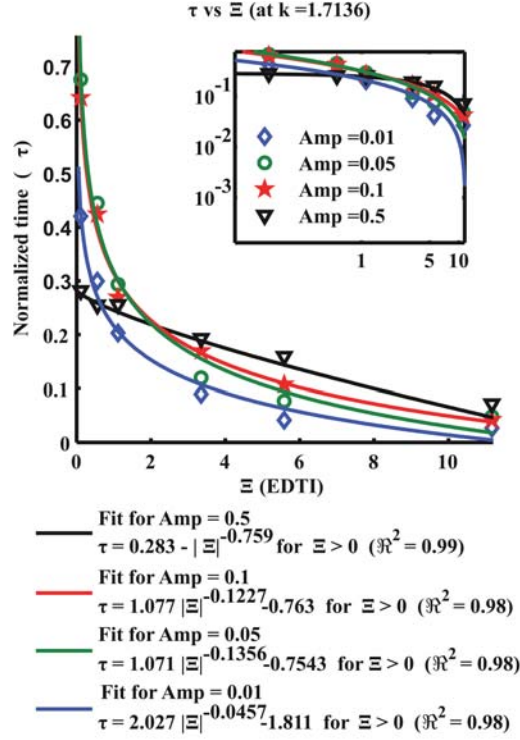


Figure 4.17: Normalized time plot with respect to misfit stress values $\Xi > 0$ (EDTI) for different amplitudes and their power series fittings.

Analysis gave following set of functions:

$$\tau_{Amp=0.5} = 0.283 - |\Xi|^{-0.759} \quad \forall 0 < \Xi < 12 \quad (\mathcal{R}^2 = 0.99) \quad (4.22)$$

$$\tau_{Amp=0.1} = 1.077 |\Xi|^{-0.1227} - 0.763 \quad \forall 0 < \Xi < 12 \quad (\mathcal{R}^2 = 0.98) \quad (4.23)$$

$$\tau_{Amp=0.05} = 1.071 |\Xi|^{-0.1356} - 0.7543 \quad \forall 0 < \Xi < 12 \quad (\mathcal{R}^2 = 0.98) \quad (4.24)$$

$$\tau_{Amp=0.01} = 2.027 |\Xi|^{-0.0457} - 1.811 \quad \forall 0 < \Xi < 12 \quad (\mathcal{R}^2 = 0.98) \quad (4.25)$$

In this case, normalized time gives the time to reach flat surface. Same increase in the exponent of $\frac{1}{\Xi}$ is observed but here exponent values under unity. This shows that in this case lower amplitude perturbation has faster decay.

In between described two regime there is third transition regime where $-1.116 \leq \Xi \leq 0.1116$ (Fig. 4.18). In which normalized decay time change with EDTI value linearly.

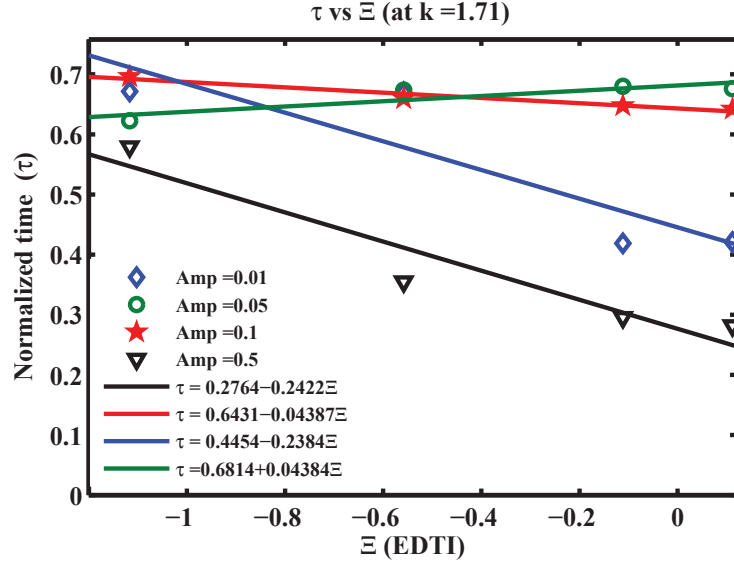


Figure 4.18: Normalized time plot with respect to misfit stress values $-1.116 \geq \Xi \leq 0$ (EDTI) for different amplitudes and their power series fittings.

4.3.2 Epitaxially strained thin film with anisotropic texture on rigid substrates

In this section, isochoric system is considered such that no external traction applied to the evolving surface, surface diffusivity is defined as anisotropic. System evolution is investigated under only applied misfit strain.

Evolution of the boundary is described in terms of displacement velocities with following formula:

$$\bar{V}_{ord} = \frac{\partial}{\partial \bar{\ell}} \left[\bar{D}(\theta, \phi, m) \frac{\partial}{\partial \bar{\ell}} (\Xi \bar{\sigma}_h - \Sigma \bar{\sigma}_h^2 + \bar{k} + \chi \bar{\theta}) \right] \quad (\text{Ordinary points}) \quad (4.26)$$

Where $\bar{D}(\theta, \phi, m)$ is the anisotropic surface diffusion.

4.3.2.1 Two-fold rotational symmetry in cubic structures: Zone axis $\langle 1\bar{1}0 \rangle$

In this section, single crystal thin film attached to the substrate is described by the zone axis $\langle 1\bar{1}0 \rangle$ which is associated with the set of vicinal (singular) planes such as $(111) \cup (110) \cup (001) \cup (11\bar{2})$ in FCC structure. In this plane, change in diffusion constant calculated by Eq. 3.41 with

parameter $m = 1$. In two fold symmetry Eq. 3.41 defines lowest diffusion direction as $[001]$ direction, and highest diffusion direction as $[\bar{1}10]$. Difference between highest and lowest diffusion constants defined by parameter A which is called diffusion anisotropy intensity.

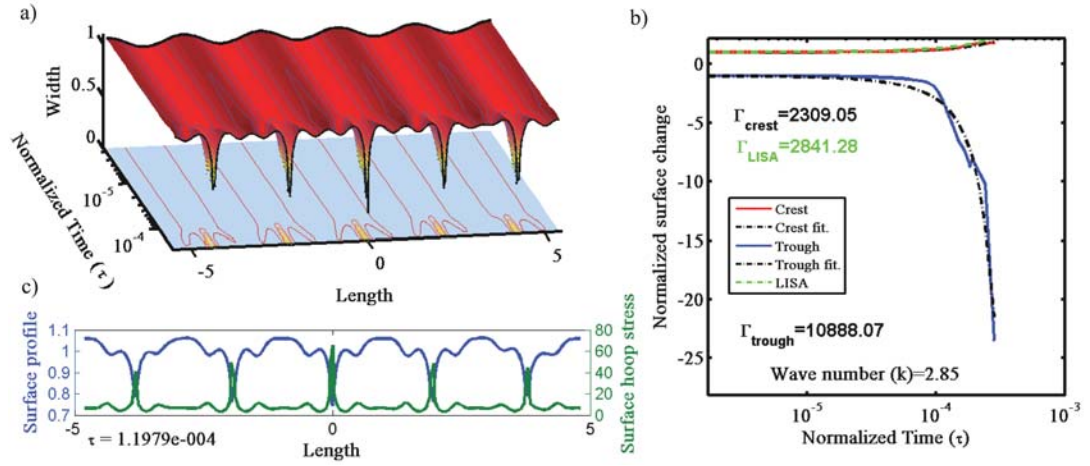


Figure 4.19: The evolution of side wall surface of thin film with (110) plane as a top plane with a tilt angle $\phi = 0^\circ$ and $A = 5$, subjected to a compression $\Xi = -5.58$ misfit, without electromigration ($\chi = 0$, $Amp = 0.05$, $k = 2.85$). (a) Morphological evolution in 3D plot. (b) Normalized displacement of trough and crest tips as a function of normalized time in logarithmic scale. (c) Hoop stress and surface profile on the evolving surface.

Fig. 4.19 demonstrate the sharp crack like formation for experiment parameters: $\phi = 0^\circ$, $A = 5$, $k = 2.85$, $\Xi = -5.58$, $Amp = 0.05$. Diffusion anisotropy effect can be seen as a high surface roughness and sharp crack like formation at stress value $\sigma_0 = 500$ MPa. Experimental trough growth rate is calculated as $\Gamma_{trough} = 10888$, this value far beyond the calculated theoretical trough growth rate $\Gamma_{LISA} = 2841$. This observation is the general consequence of crack formation and resultant stress concentration at the crack tip. Here, crack surface has low diffusion constant and there is high driving force due to misfit stress caused stress concentration at trough therefore there is no time to release energy with smoothing crack tip by diffusion.

Here, Same amount misfit stress is applied to the thin film with $\phi = 90^\circ$ tilt angle (Fig. 4.20). In this case, trough growth rate shows negative deviation. LISA predicts faster growth rate $\Gamma_{LISA} = 847.52$ but for $\phi = 90^\circ$ tilt angle trough and crest growth rates ($\Gamma_{crest} = 712$ and $\Gamma_{trough} = 1048$) are lower than the calculated value. Height increase mainly due to the grooving at side of crack like formation. even though same amount misfit stress applied

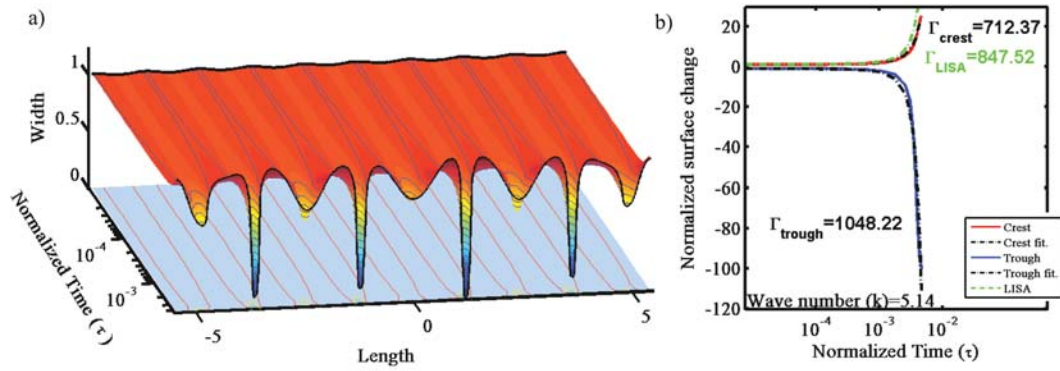


Figure 4.20: The evolution of side wall surface of thin film with (110) plane as a top plane with a tilt angle $\phi = 90^\circ$ and $A = 5$, subjected to a compression $\Xi = -5.58$ misfit, without electromigration ($\chi = 0$, $Amp = 0.01$, $k = 5.1$). (a) Morphological evolution in 3D plot. (b) Normalized displacement of trough and crest tips as a function of normalized time in logarithmic scale.

with previous experiment, here there is no sharp crack formation due to relatively easy mass transport at crack surface. So the rather crack tip formed to release stress concentration at crack tip and escaping mass form rather high grooving at the sides of crack.

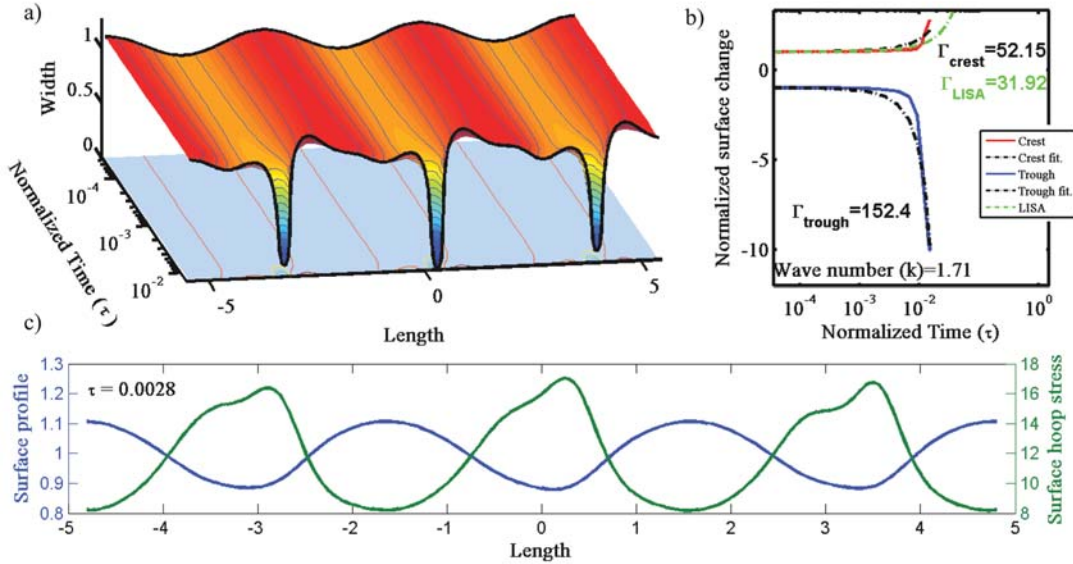


Figure 4.21: The evolution of side wall surface of thin film with (110) plane as a top plane with a tilt angle $\phi = 77^\circ$ and $A = 5$, subjected to a compression $\Xi = -3.35$ misfit, without electromigration ($\chi = 0$, $Amp = 0.1$, $k = 1.71$). (a) Morphological evolution in 3D plot. (b) Normalized displacement of trough and crest tips as a function of normalized time in logarithmic scale. (c) Hoop stress and surface profile on the evolving surface.

Fig. 4.21 utilizes $\phi = 77^\circ$ as a tilt angle. Again crack formation is observed but this time grooving at the side of the crack grows with different rate so the upper surface of thin film for an angled plateau which has $(\bar{1}10)$ plane. Right side of the crack wall form by (001) plane which has the highest transverse diffusion constant on the other hand left side of the crack formed on $(\bar{1}\bar{1}\bar{2})$ plane which has relatively lower transverse diffusion constant. This diffusion constant difference explain the formation of different grooving height.

4.3.2.2 Four-fold rotational symmetry in cubic structures: Zone axis $\langle 001 \rangle$

In this section, four fold rotational symmetrical investigated by thin film having top surface as $(100) \cup (2\bar{1}0) \cup (1\bar{1}0)$ which are belong to the $[001]$ zone axis.

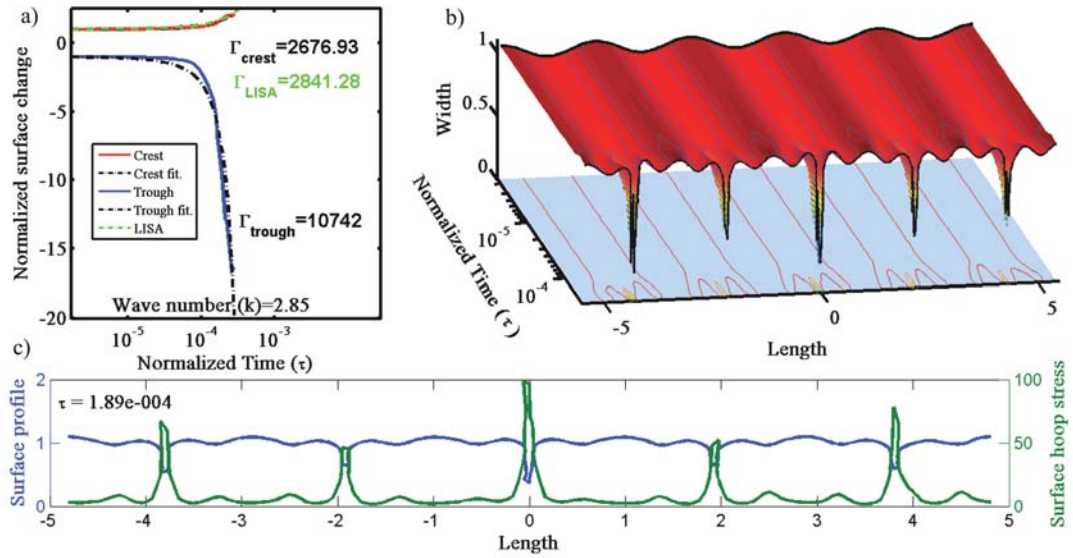


Figure 4.22: The evolution of side wall surface of thin film with (001) plane as a top plane with a tilt angle $\phi = 0^\circ$ and $A = 5$, subjected to a compression $\Xi = -11.16$ misfit, without electromigration ($\chi = 0$, $Amp = 0.05$, $k = 2.85$). (a) Normalized displacement of trough and crest tips as a function of normalized time in logarithmic scale. (b) Morphological evolution in 3D plot. (c) Hoop stress and surface profile on the evolving surface.

At the zero tilt angle case (Fig. 4.22), high misfit stress ($\Xi = -11.16 \cong \sigma = 1000 \text{ MPa}$) is applied, as a result again increased surface waviness is observed because both the crest and the cracking induced grooving are tend to grow with time. Morphologically almost identical to the 2-fold symmetry with zero tilt angle. Fig. 4.22(c) shows the hoop stress concentration at the crack tip and at the side of the tips tendency to create grooving. Growth rate of crest

($\Gamma_{crest} = 2676.93$) is good agreement with LISA value ($\Gamma_{LISA} = 2841.28$). Trough has much more faster with $\Gamma_{trough} = 10742$ due to the crack propagation.

Fig. 4.23 illustrate the dome like formations at the compressive stress value $\Xi = -1.116$. In this case, mass flow from the trough to the crest gradually and system evolve into the dome like formation due to the low wave number and diffusion anisotropy coupling.

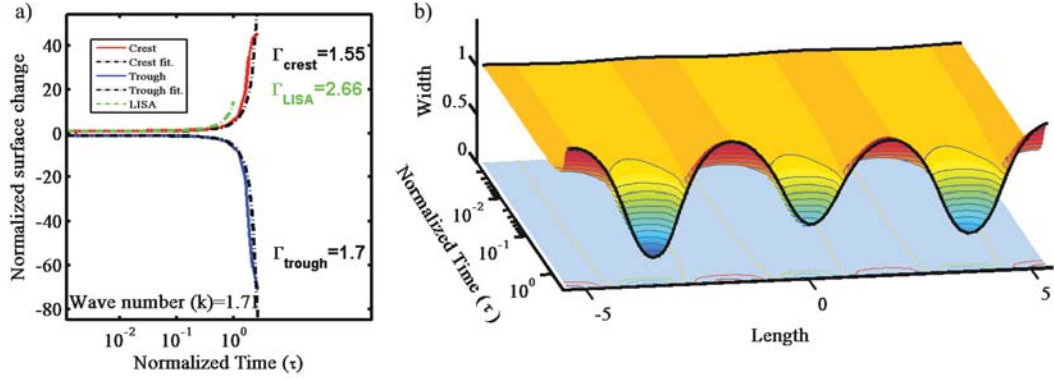


Figure 4.23: The evolution of side wall surface of thin film with (001) plane as a top plane with a tilt angle $\phi = 45^\circ$ and $A = 5$, subjected to a compression $\Xi = -1.116$ misfit, without electromigration ($\chi = 0$, $Amp = 0.01$, $k = 1.71$). (a) Morphological evolution in 3D plot. (b) Normalized displacement of trough and crest tips as a function of normalized time in logarithmic scale.

4.3.2.3 Six-fold rotational symmetry in cubic structures: Zone axis $\langle 111 \rangle$

In this case top plane has the highest symmetry elements $\{1\bar{1}0\} \cup \{\bar{1}\bar{1}2\}$, thin film attached to the substrate with surface normal of $\{111\}$ top plane.

High surface roughness of thin film with $\phi = 0^\circ$ tilt angle six fold symmetry surface is illustrated at Fig. 4.24. Due to high misfit stress value $\Xi = -11.16$, formation and annihilation of troughs are observed. Eventually some of them transform into the crack like form and grow very fast. Growth rate predicted value is $\Gamma_{LISA} = 648.2$, but crest and trough growth rates observed as $\Gamma_{crest} = 1817$ and $\Gamma_{trough} = 2439.28$, respectively.

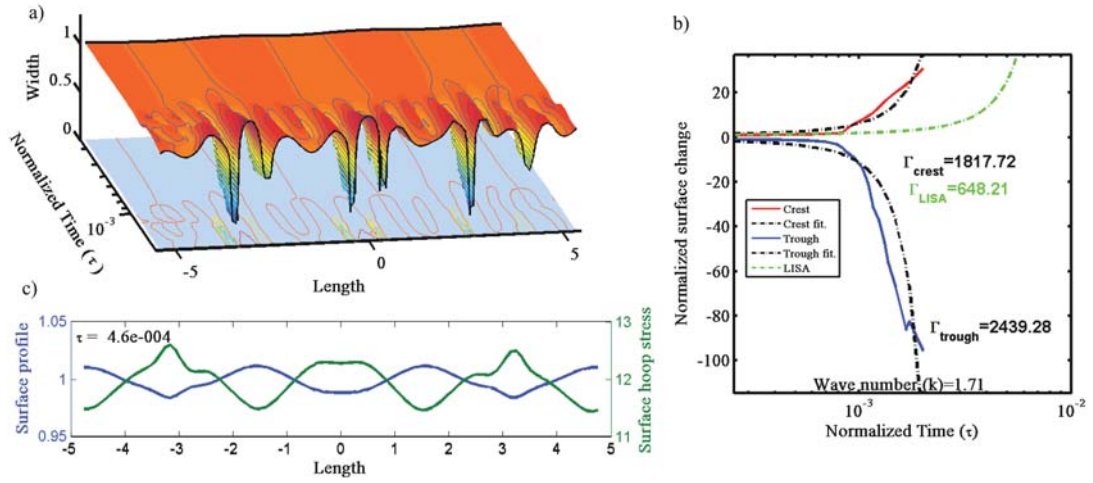


Figure 4.24: The evolution of side wall surface of thin film with (111) plane as a top plane with a tilt angle $\phi = 0^\circ$ and $A = 5$, subjected to a compression $\Xi = -11.16$ misfit, without electromigration ($\chi = 0$, $Amp = 0.01$, $k = 1.71$). (a) Morphological evolution in 3D plot. (b) Normalized displacement of trough and crest tips as a function of normalized time in logarithmic scale. (c) Surface profile and hoop stress along the thin film surface.

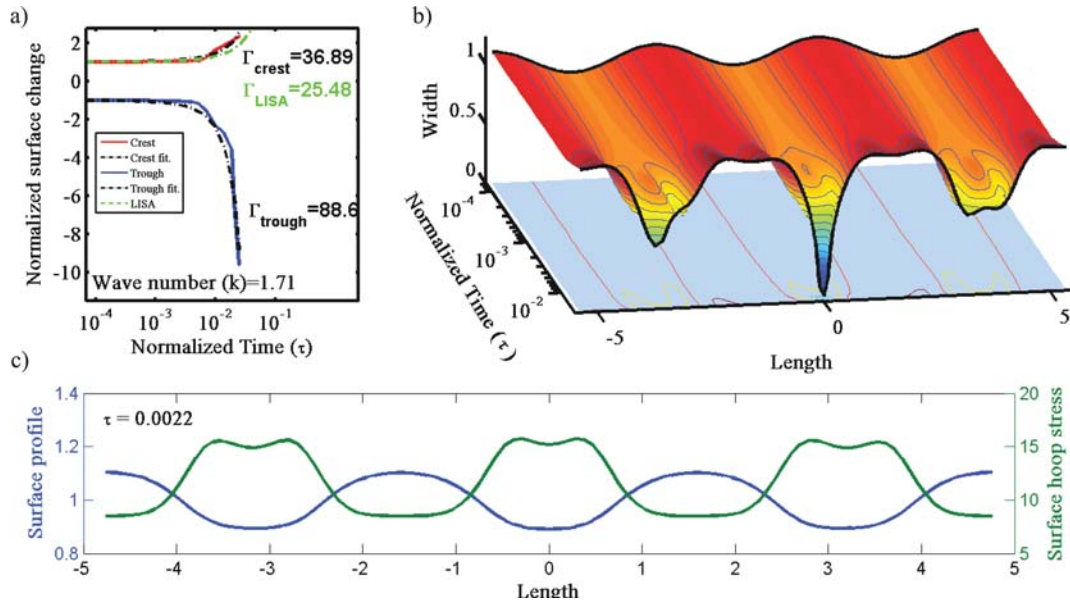


Figure 4.25: The evolution of side wall surface of thin film with (111) plane as a top plane with a tilt angle $\phi = 30^\circ$ and $A = 5$, subjected to a compression $\Xi = -3.35$ misfit, without electromigration ($\chi = 0$, $Amp = 0.01$, $k = 1.71$). (a) Morphological evolution in 3D plot. (b) Normalized displacement of trough and crest tips as a function of normalized time in logarithmic scale. (c) Instantaneous hoop stress and surface profile along the thin film at the onset of trough tip splitting ($\tau = 0.003$).

Fig. 4.25(c) shows the trough and crest splitting tendency at early stages of evolution for the $\phi = 30^\circ$ angled thin film under the $\Xi = -3.35$ compressive stress, but at the later stage formed double trough transform back into one and increase the growth rate of trough. these transformation stages can be observed as a change in slope at Fig. 4.25(a).

4.3.3 Epitaxially strained thin film with anisotropic texture under electromigration on rigid substrates

In previous sections thin film under only the misfit stress is considered, in this section observations on electromigration and its coupling with stress under anisotropic diffusion are presented.

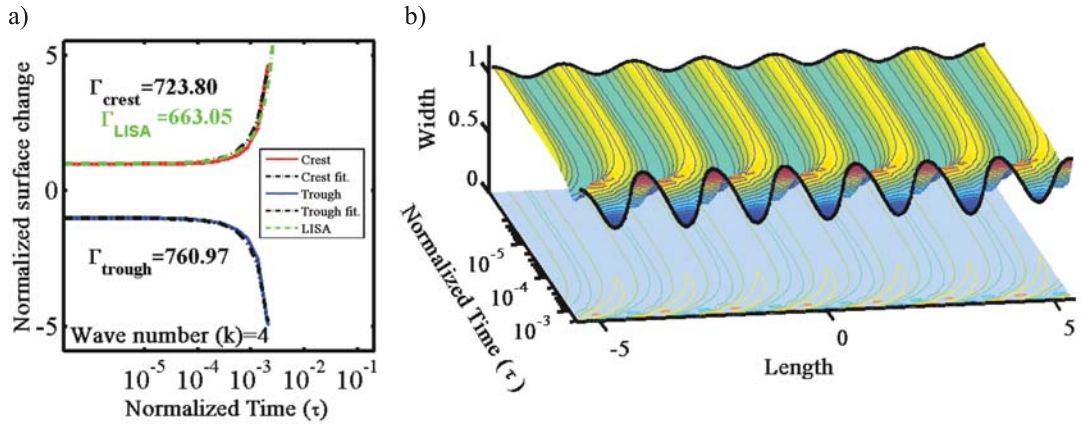


Figure 4.26: The evolution of side wall surface of thin film with (110) plane as a top plane with a tilt angle $\phi = -10^\circ$ and $A = 10$, subjected to a compression $\Xi = -1.11$ due to misfit, with electromigration $\chi = 20$. ($Amp = 0.05$, $k = 4$). (a) Normalized displacement of trough and crest tips as a function of normalized time in logarithmic scale. (b) Morphological evolution in 3D plot.

In Fig. 4.26 (110) plane of thin film is tilted by $\phi = -10^\circ (\equiv 170^\circ)$ to get the same surface configuration with experiment done by Muller et al. (Fig. 1.20) [77]. And then $\sigma = 100 \text{ MPa}$ compression and electron wind intensity $\chi = 20$ is applied to the thin film, similar morphological facets are observed. Both crest and trough growth rates ($\Gamma_{crest} = 723.8$ and $\Gamma_{trough} = 760.97$) are predicted with small deviation from the calculated by LISA ($\Gamma_{LISA} = 663.05$).

When tilt angle changed to the $\phi = 50^\circ$, edges of the facets gets sharper and pyramid like structure formed (Fig. 4.27). When tilt angle of texture get close to the 90° , after some

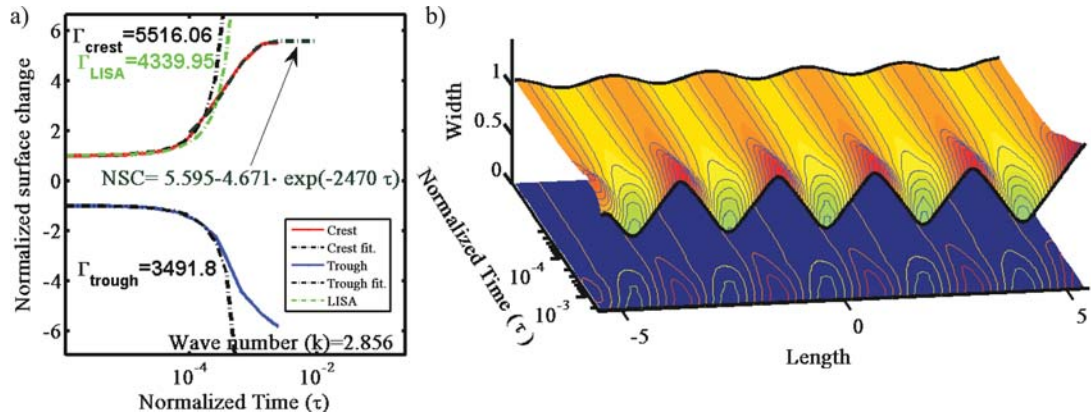


Figure 4.27: The evolution of side wall surface of thin film with (110) plane as a top plane with a tilt angle $\phi = 50^\circ$ and $A = 10$, subjected to a compression $\Xi = -1.11$ due to misfit, with electromigration $\chi = 20$. ($Amp = 0.05$, $k = 4$). (a) Normalized displacement of trough and crest tips as a function of normalized time in logarithmic scale. (b) Morphological evolution in 3D plot.

shape transformation of surface wave (Fig. 4.27(a)), which might involve one or more among growth, decay and tilting, shape change stops and resultant shape starts to drift without any change in its shape.

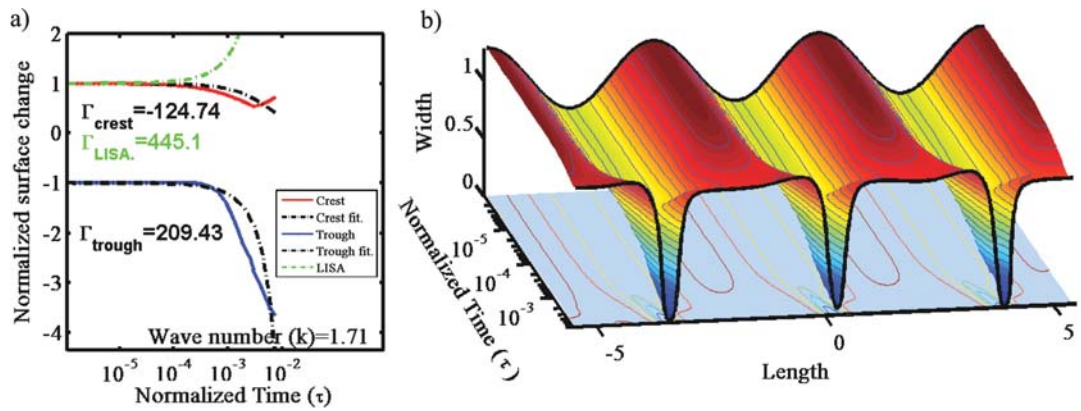


Figure 4.28: The evolution of side wall surface of thin film with (100) plane as a top plane with a tilt angle $\phi = 62^\circ$ and $A = 10$, subjected to a compression $\Xi = -3.35$ due to misfit, with electromigration $\chi = 6$. ($Amp = 0.27$, $k = 1.71$). (a) Normalized displacement of trough and crest tips as a function of normalized time in logarithmic scale. (b) Morphological evolution in 3D plot.

Fig. 4.28 illustrates the film evolution which has four fold symmetry plane (100) with $\phi = 62^\circ$ tilt angle under $\Xi = -3.35$ and $\chi = 6$. Trough growth rate $\Gamma_{trough} = 209.43$ shows large

deviation from the LISA predicted value $\Gamma_{LISA} = 445.1$ due to the crack like formation. But crest instead of showing growing behavior starts to decay until the crack formation, and then make sharp elbow due to the grooving created by crack formation. At the same time applied electrostatic potential difference keeps the surface flat by restraining the grooving from further growth.

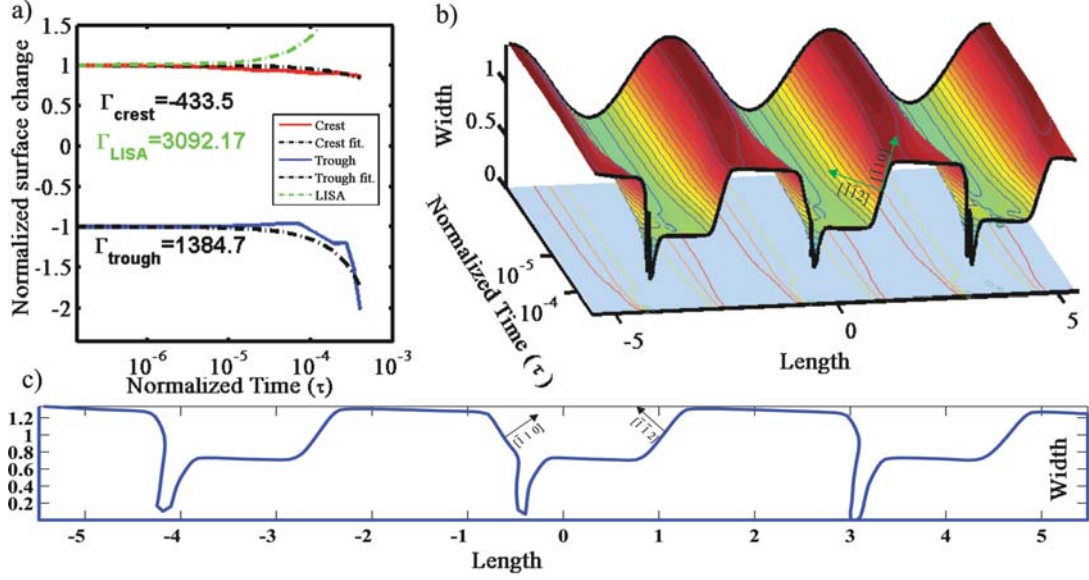


Figure 4.29: The evolution of side wall surface of thin film with (111) plane as a top plane with a tilt angle $\phi = 37.8^\circ$ and $A = 10$, subjected to a compression $\Xi = -5.58$ due to misfit, with electromigration $\chi = 46$ ($Amp = 0.37$, $k = 1.71$). (a) Normalized displacement of trough and crest tips as a function of normalized time in logarithmic scale. (b) Morphological evolution in 3D plot. (c) Final configuration.

Fig. 4.29 shows evolution of thin film with the six fold symmetry and $\phi = -46^\circ$ under high electrostatic potential $\chi = 46$ and compressive misfit stress $\Xi = -5.58$. Here, surface wave transforms into the sharp cornered trapezoid shape with flat surfaces, and from the left side of the lower surface crack emanates. Left side of the trapezoid with $[\bar{1}\bar{1}2]$ surface normal has highest possible transverse diffusion constant, on the other hand upper surface of trapezoid and the flat trough surface are almost parallel to the substrate surface and have nearly lowest possible transverse diffusion constant. These quantum dot like structures has roughly 150 nm length and 50 nanometer height in real space.

In addition to the drastic surface shape formation due to the electromigration, there is another important phenomena is healing effect of it. Fig. 4.30 shows two experiment, first one with

two fold symmetry system with $\phi = 120^\circ$ tilted with respect to substrate undergo shape change due to the applied compressive misfit stress $\Xi = -1.16$ (Fig. 4.30(a-b)). In this situation surface perturbation tends to grow and form dome like shape till the trough reach to the substrate. On the other hand, when electrostatic potential applied $\chi = 20$ to the same system surface perturbation starts to decay instead of growing (Fig. 4.30(c-d)).

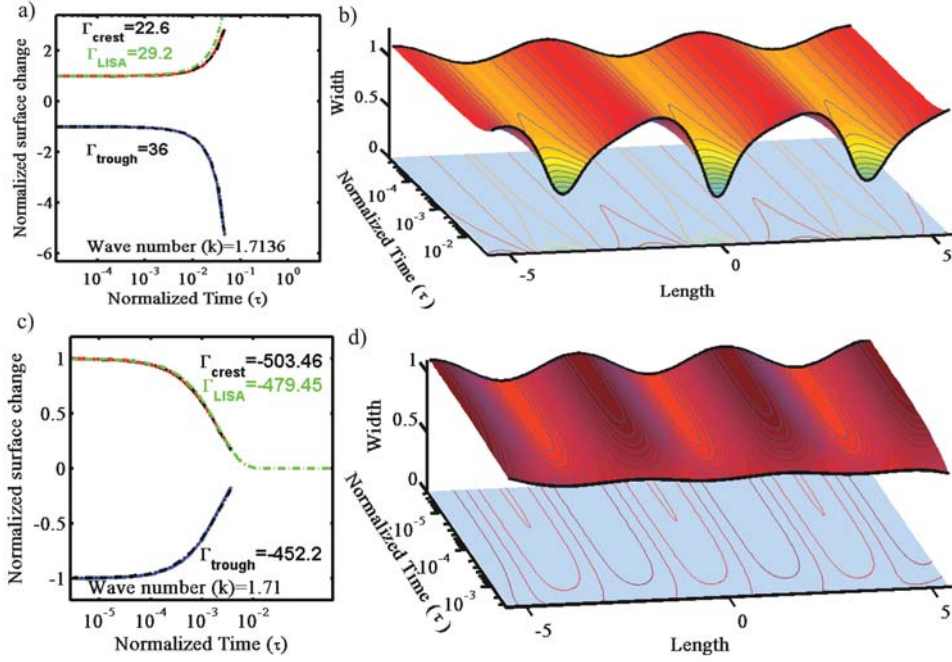


Figure 4.30: The evolution of side wall surface of thin film with (111) plane as a top plane with a tilt angle $\phi = 37.8^\circ$ and $A = 10$, subjected to a compression $\Xi = -5.58$ due to misfit, with electromigration $\chi = 46$ ($Amp = 0.37$, $k = 1.71$). (a) Normalized displacement of trough and crest tips as a function of normalized time in logarithmic scale. (b) Morphological evolution in 3D plot. (c) Final configuration. (d) Final configuration.

In the light of listed experiments, one can design an experiment to get surface structure with desired dimensional parameters. For example; in a micrometer 3 quantum dot like structures desired so desired width of QD is about 330 nm length then one can calculate the stress value by taking 300 nm as a λ_m . So the needed stress value calculated as $\sigma \cong -100 \text{ MPa}$ by the λ_m Eq. (4.16). For determining the height one must use the growth rate equation (4.13). After calculating time $\tau = 0.37$ for the desired height $h = 80 \text{ nm}$, electrostatic potential application should be started at that time. For the case of 4 QDs, parameters can be calculates as $\sigma \cong -140 \text{ MPa}$ and $\tau = 0.1$. For these two experiments (Fig. 4.31), Diffusion anisotropy intensity is taken as $A = 10$, surface of thin film with (111) plane as a top plane with a tilt

angle $\phi = 40^\circ$ is defined with random noise as a perturbation.

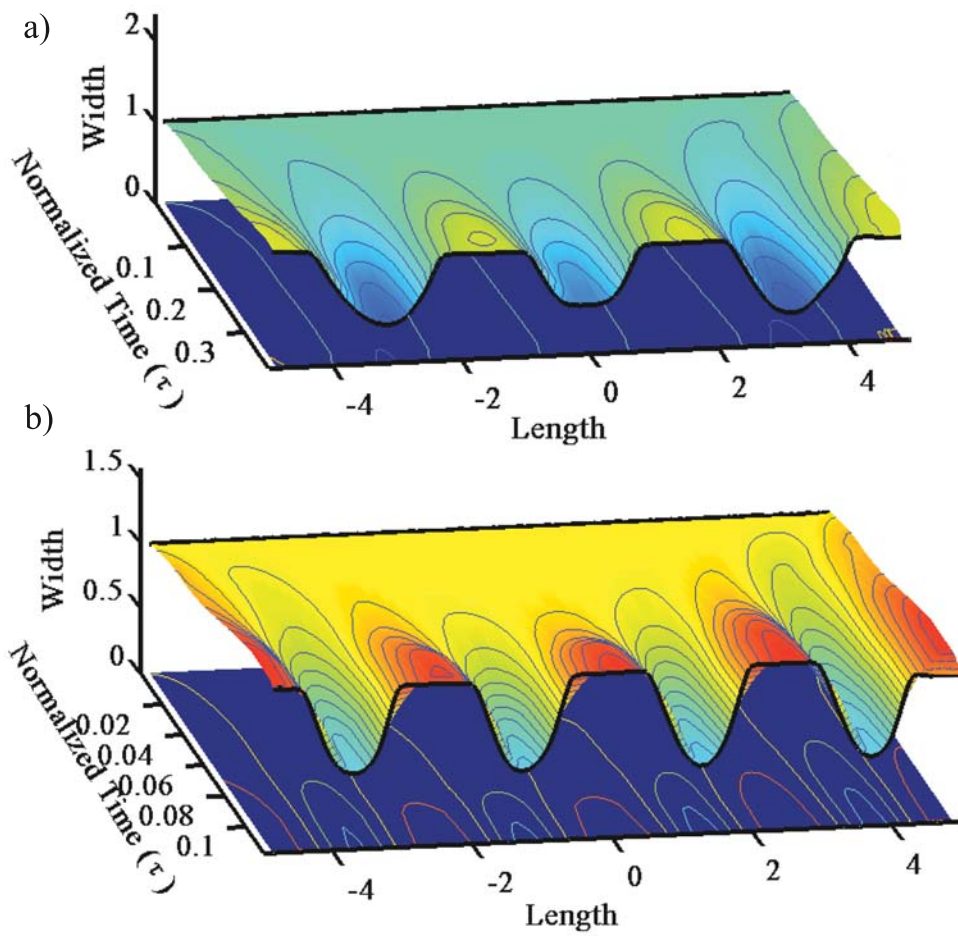


Figure 4.31: The evolution of side wall surface of thin film with (111) plane as a top plane with a tilt angle $\phi = 40^\circ$ and $A = 10$, (a) subjected to a compression $\Xi = -1.165$ due to misfit, with electromigration $\chi = 50$ which is applied from $\tau = 0.37$. (b) subjected to a compression $\Xi = -1.56$ due to misfit, with electromigration $\chi = 50$ which is applied from $\tau = 0.1$.

metrically disposed, half-wave length Cosine-function having a wave length and a height (i.e., amplitude) denoted by $2L$ and h_p , respectively. The droplet aspect ratio may be defined by: $\beta = L/h_p$, which prescribes a finite contact angle $\theta = \arctan(\pi/\beta)$ between film and the substrate at the onset of the simulation run. Therefore, in the normalized and scaled time-length space, the initial shape of a droplet is uniquely described by one single parameter, namely the aspect ratio β , since $\bar{h}_p = 1$ according to the scheme adopted in this study. Similarly, a close inspection of the normalized governing equation without the growth term shows that there is only one more additional parameter left for the complete predetermination of the morphological evolution process as an initial data, which is the ESED parameter denoted by $\Sigma = \ell_o/\ell^* \rightarrow h_p/\ell^*$. In real space, the size of the droplet may be described by $h_p = \ell_o$ for a given value of the aspect ratio, but now it is solely determined by Σ keeping the shape invariant (i.e., zooming) due to the fact that the characteristic length ℓ^* is an internal variable for the isochoric systems, and it depends only on the material properties of the film and the substrate including the misfit strain. Therefore, this unitless parameter Σ completely dictates the possible size effects of the droplet on the evolution process in real space; where one has: $h_p \leftarrow \ell_o = \Sigma\ell^*$. Hence, in the absence of the growth term, the aspect ratio β (i.e., shape) and the strain energy density parameter Σ (i.e., size) are two basic numbers capable to dictate the topographic features of the final stationary states.

5.2 Results and discussion

5.2.1 Island formation in epitaxially strained flat droplets with isotropic texture on rigid substrates

In this section, isochoric system is considered such that no external traction applied to the evolving surface, surface diffusivity is defined as isotropic. System evolution is investigated under the wetting effect potential, the potential related with the film/substrate interface misfit and curvature with or without condensation/evaporation.

Evolution of the boundary is described in terms of displacement velocities with following formula:

$$\begin{aligned} \bar{V}_{ord} = \frac{\partial}{\partial \bar{\ell}} \left[\frac{\partial}{\partial \bar{\ell}} \left(-\Sigma \bar{\sigma}_h^2 + \chi \bar{\vartheta} + \bar{\gamma}_{f \leftrightarrow s}(\bar{y}) \bar{\kappa} + \bar{\omega}(\bar{y}) \right) \right] \\ - M_{fv} \left(\Delta \bar{\gamma}_{fv}^o - \Sigma \bar{\sigma}_h^2 + \bar{\gamma}_{f \leftrightarrow s}(\bar{y}) \bar{\kappa} + \bar{\omega}(\bar{y}) \right) \quad (\text{Ordinary points}) \end{aligned} \quad (5.1)$$

$$\bar{V}_{long} = -\bar{M}_{long} \bar{\Omega}^{-1} \{ \lambda_{TJ} - \cos(\theta_W) \} \quad \forall \quad \lambda_{TJ} \geq 1 \quad (\text{Triple junction contour line}) \quad (5.2)$$

In Eq. 5.1, $\bar{\ell}$ is the arc length in $2\mathbf{D}$ space which is scaled with respect to ℓ_o . First part of the equation describes the evolution behavior of strained thin films by surface diffusion which is driven by the gradient of ESED $\Sigma(\bar{\sigma}_h)^2$ and capillary potential $\bar{\gamma}_{f \leftrightarrow s}(\bar{y}) \bar{\kappa}$. And second part defines the local phase change which is called growth term, Physically this term describes the evaporation or condensation of vapor phase. $\Delta \bar{\gamma}_{fv}^o(T) = (\bar{\gamma}_v^o - \bar{\gamma}_f^o)_T$ represents the thermal part of the helmholz free energy density related with the evaporation/condensation process. The positive value favors the condensation so growth of the film.

5.2.1.1 Morphological evolution of droplet without growth:

In this section, the results obtained from a set of special computer experiments done on the specimens having large aspect ratios (i.e., in the range of $\beta = (10 - 28)$), and subjected to the misfit strain at the interface between the thin film and the stiff substrate will be presented. Different elastic strain energy density parameters (ESED) that represents different parts of the spectrum of morphologies will be discussed; (i.e., $\Sigma = 0.075, 0.175, ||0.250||, 0.300, 0.350, 0.400, ||0.413||, 0.425, 0.450, \dots, 0.70$). The doubled vertical lines roughly indicate the transient states found. The lowest ESED value presented here is $\Sigma = 0.075$, which destabilize the initial droplet configuration by activating the TJ towards the Frank-van der Merwe layer structure by spreading over the substrate surface before switching to the island formation. Also transition to double islands (i.e., twins, etc) are observed. During our simulations, besides film morphologies, also the kinetics of the peak height development, the displacement of the TJ singularity during wetting layer extension, and the strain energy release during the evolution process are monitored. In order to relate simulations with the actual physical size of the islands, following parameters are considered, which are the parameters of Ge film grown epitaxially on a stiff silicon substrate. Namely: $\varepsilon_o = -0.042$, $E_{Ge} = 103\text{GPa}$,

$\nu_{\text{Ge}} = 0.273$, $f_{\text{Ge}} = 1.927 \text{ Jm}^{-2}$, and $f_{\text{Si}} = 2.513 \text{ Jm}^{-2}$. These numbers imply a characteristic length of $\ell^* = 12.11 \text{ nm}$, which may be used to calculate the heights and the base lengths of the droplets that are corresponding to the range of the strain energy intensity parameters for a given aspect ratio (i.e., $\beta = 28$), namely; for the singlet islands one has: $\{\Sigma : 0.25 - 0.40\} \Rightarrow \{h_o = 1.91 \text{ nm} - 3.08 \text{ nm}\} \cap \{L : 84 \text{ nm} - 134 \text{ nm}\}$.

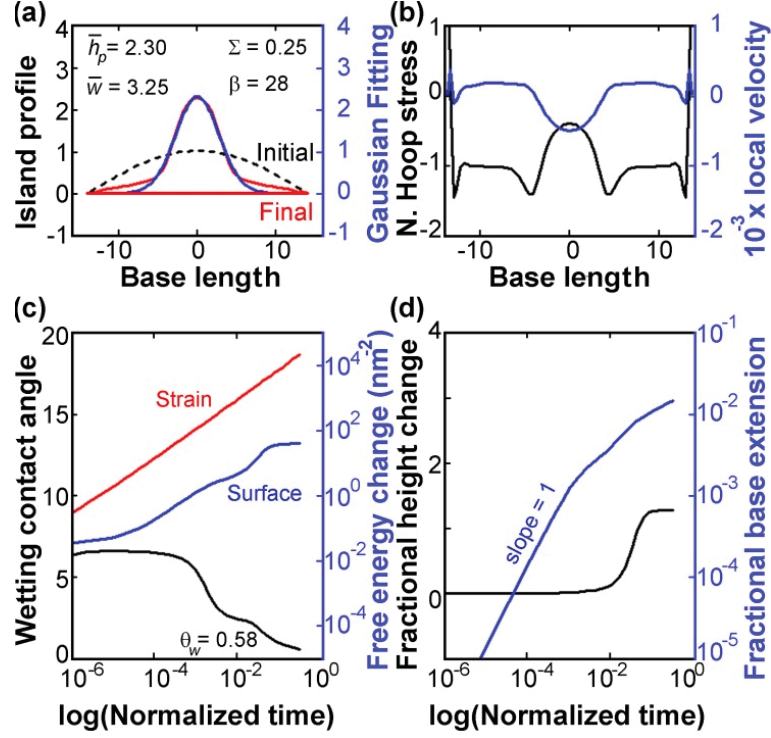


Figure 5.2: (a) The island profile change with transition stage just before the onset of the SK islands formation regime. The final profile is fitted by a Gaussian bell-shape curve having following parameters: $\bar{h}_p = 2.30$, $\bar{w} = 3.25$, which corresponds to the peak height-to-peak width ratio of $\xi = 0.354$. (b) Instantaneous velocity and the hoop stress distributions along the final droplet profile. (c) Evolution of the contact angle is shown on the left y-axis. On the right y-axis, the strain energy and surface free energy changes are given for Ge/Si(100) system, and scaled by $\text{nm}^2 \rightarrow 10^{-18}$. (d) Time evolution of peak height and TJ displacement. Simulation Data: $\Sigma = 0.25$, $\bar{h}_p = 1$, $\beta = 28$, $\nu = 0.273$, $\bar{M}_{TJ} = 2$, $\lambda_{TJ} = 1$, $\bar{\delta} = 0.005$, $\gamma_s = 1.2$ and $\gamma_f = 1$.

The results of a computer simulation, which is done on a hypothetical sample by assigning a critical value for the elastic strain energy density parameter (ESED) such as are presented in Fig.5.2. Fig.5.2(a) shows development of a premature or transient island profile without having any indication of the wetting layer formation even after $2^{46} \approx 7 \times 10^{13}$ runs. This profile, which was obtained by performing numerous experiments in the vicinity of the

stability-instability turn-over point for the linearized systems, corresponds to the transient stage between the SK islands and the FM type layers structures. This final profile as demonstrated in Fig.5.2. (a) may be described by a Gaussian curve (i.e., second degree) given by $G(x; \bar{h}_p, \bar{w}) = \bar{h}_p \cdot \exp(-\ln(2)x^2/\bar{w}^2)$, having a halve-width of $\bar{w} = 3.25$, and a peak height of $\bar{h}_p = 2.30$, in normalized space. These two value, corresponds to the peak height to peak width ratio of $\xi = 0.354$. According to the Prigogine description, this is a genuine stationary non-equilibrium state since even though the height of droplet reached a plateau region (Fig. 5.2(d)), the TJ contour line is still active with a temporal wetting angle of $\theta_W \approx 0.58^\circ$ (Fig. 5.2(c)). This TJ activity is the main indicator that the system is in the non-equilibrium state. To reveal the real physical system parameters, the data given above are employed for the Ge/Si(100) system to the normalized and scaled parameters and obtained $h_p \approx 6.9 \text{ nm}$ for the peak height, $2W = 18.98 \text{ nm}$ for the peak width of and $L \equiv \lambda \approx 86.5 \text{ nm}$ for the base (or the wave length that describes the spacing between islands) length with the help of Fig. 5.2(b). These values are in the range of numbers reported by Kukta and Freund, who were defining the base of the island as its width, which may create some confusion if there is no sharp turning point at the corners that separate island from the wetting layer. As seen in Fig. 5.2(d), the peak height showed logarithmic time dependence during the intermediate regime before the onset of the plateau region, namely; $\bar{h}_p(\bar{t}) \cong 2 \log(\bar{t}) + 3.6$. In Fig. 5.2 (c), the negative cumulative strain energy release, $-(\Delta F_f/w_o) \text{ nm}^2$, and the surface free energy variation $(\Delta F_s/w_o) \text{ nm}^2$, both scaled with respect to w_o . This plot shows almost perfectly linear decrease for the cumulative strain energy release with time compared to the surface free energy variation that indicates a leveling off in the early stages of the development followed by a positive change due to the surface layer extension during the evolution process. The free energies are plotted by considering the critical length of Ge/Si (100) system, which is about 12.11 nm for the present case. At the end of the test run the total strain energy release is calculated to be about $\Delta F_f \cong -3.203 \times 10^{-5} J$, which is very large compared to the total surface energy gain that amounts to $\Delta F_s \cong 3.36 \times 10^{-9} J$. This figure also shows that the global Helmholtz free energy is negative all the way through the natural change as one should expect from the thermodynamic considerations.

In Fig.5.3, a typical morphological evolution behavior of the SK island is presented in terms of the final droplet profile, the peak height, the base extension, and the TJ contact angle with respect to the normalized logarithmic scale. In this experiment, an elastic strain energy density

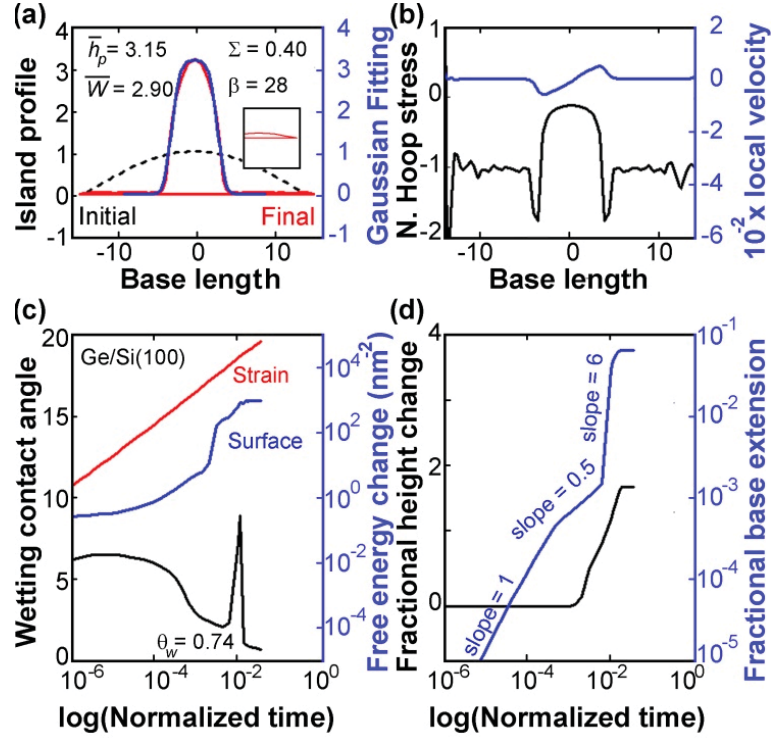


Figure 5.3: (a) Spontaneous formation of the SK island with an almost perfect flat wetting layer from a single crystal droplet on a stiff substrate by the isotropic surface drift diffusion driven by the combined actions of the misfit strain (isochoric) and the capillary forces. The inset details the structure of the wetting layer at the TJ. Gaussian bell-shape curve representing the final profile has the following parameters: $\bar{h}_p = 3.15$, $\bar{w} = 2.90$ and thus the peak height-to-peak width ratio of $\xi = 0.543$. (b) Instantaneous velocity and the hoop stress distributions along the final droplet profile. (c) Evolution of the contact angle is shown on the left y-axis. On the right y-axis, the strain energy and surface free energy changes are given for Ge/Si(100) system. (d) Time evolution of peak height and TJ displacement. Simulation Data: $\Sigma = 0.40$, $\bar{h}_p = 1$, $\beta = 28$, $\nu = 0.273$, $\bar{M}_{TJ} = 2$, $\lambda_{TJ} = 1$, $\bar{\delta} = 0.005$, $\gamma_s = 1.2$ and $\gamma_f = 1$.

parameter of $\Sigma = 0.40$ is used that was picked out from the upper edge of the stable singlet SK island formation range $\{\Sigma : 0.30, 0.35, 0.40\}$. The SK profile reported in this figure shows a very thin simultaneously-formed wetting layer having a normalized thickness of $\Delta\bar{h} \simeq 0.026$. This wetting layer thickness is about a factor of 5 greater than the adopted boundary layer thickness in our computer simulations. In real space, the wetting layer thickness for the Ge/Si(100) system may be computed as follows: $\Delta h \simeq 0.026\ell_o \rightarrow 0.026\Sigma\ell^* \simeq 0.12 \text{ nm}$, which may be easily improved by taking the boundary layer thickness 5 times smaller than the desired effective wetting layer thickness, namely that is about one atomic spacing, 0.6 nm . That means one should rather take $\bar{\delta} \rightarrow 0.025$.

The insert in Fig. 5.3(a) demonstrates the structure of the wetting layer at the TJ contour line, which has a temporal contact angle of $\theta \approx 0.74^\circ$ instead of zero degree, which indicates that the TJ is still active. A close inspection of Fig. 5.3(d) shows that the TJ displacement motion indicates three different time exponent stages, $\bar{L}(\bar{t}) = A\bar{t}^n$ where $n = 1; 1/2; 6$, before it enters to the plateau region. Similarly, the peak height shows a logarithmic time dependence during the intermediate regime before the onset of the plateau region, namely; $\bar{h}_p(\bar{t}) \sim 2 \log(\bar{t}) + 5.6$. Using the physicochemical data given for Ge/Si(100) system, one may calculate the critical film thickness as: $h_c^{Ge} = 0.56 \text{ nm}$, and the integrated thickness of the droplet as: $h_o^{Ge} = (2/\pi)\Sigma\ell^* \approx 3.08 \text{ nm}$. The critical parameter, which is given by $h_o^{Ge}/h_c^{Ge} \approx 5.546 \geq 5$ is in the range where the wetting parameter does not play any role. The normalized wave number $\underline{k} \equiv k\ell^*$, which corresponds to the maximum growth rate constant, may be calculated from the expression $\underline{k}_{\max} = \left\{3 + \sqrt{9 - 8(h_c/h_o)^{-3}}\right\}$, which yields $\underline{k}_{\max} \approx 2.996$. This result is very close to the theoretical value of 3. The perturbation wave length for the maximum growth rate constant now becomes about $\lambda_{\max} = 25.4 \text{ nm}$. This figure is about a factor of five smaller than the domain length of $L = 28\Sigma\ell^* \rightarrow 135.7 \text{ nm}$. According to the linear instability theory the system should be completely in the instability regime, therefore no stationary non-equilibrium state SK island formation would be possible. This is completely contrary to the findings demonstrated in this work, which implies that for the large amplitudes as well as for the certain initial configurations such as the flat droplets the linear instability theory is not reliable in predicting evolution behavior of the system.

In Fig. 5.3(c), the cumulative strain energy change, $-(\Delta F_f/w_o) \text{ nm}^2$ as well as the increase in the surface free energy, $(\Delta F_s/w_o) \text{ nm}^2$, of the droplet due to the island formation are presented. This figure clearly shows that there is a large increase in the surface free energy due to the island formation compared to Fig. 5.2(c) because of a factor of two peak height enhancement during the evolution process. Even though the surface free energy levels off after reaching the stationary non-equilibrium state, still the strain energy release continuous to increase due to the readjustment of the system through the TJ activities.

Fig. 5.4(a and b) illustrate a fully developed SK doublet at the stationary state separated by a thin wetting layer having a thickness of $\Delta\bar{h} \approx 0.0314 \rightarrow 0.17 \text{ nm}$. The wetting layer thickness between the peaks, and the peak tails are found to be almost same. In this case, an ESED parameter of $\Sigma = 0.45$, which is selected from a range $\{\Sigma : ||4.125||; 4.25; 0.45..\}$, where the doublet formation appears to be the stationary state instead of singlets is used. Above

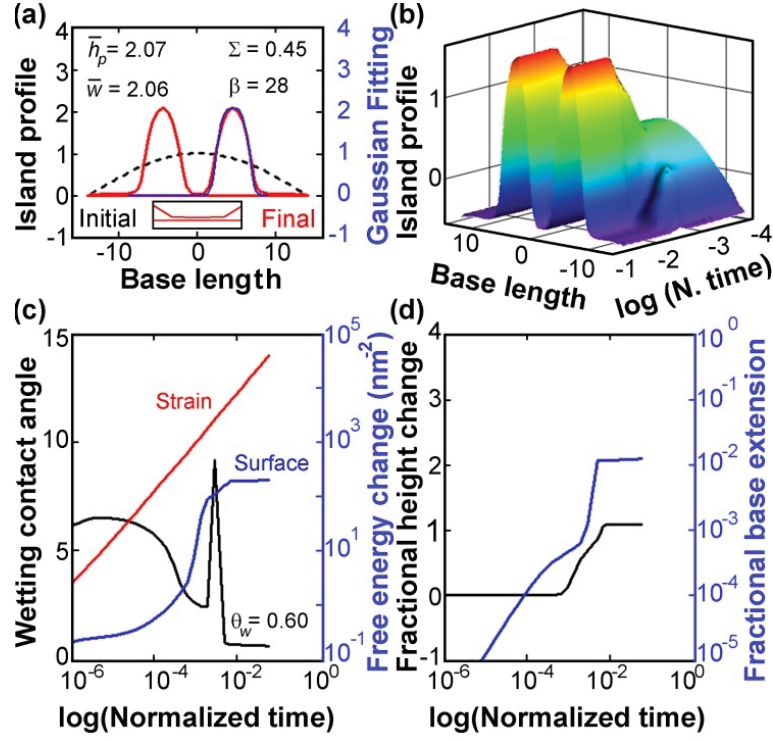


Figure 5.4: (a) Spontaneous formation of the SK doublets with an almost perfect flat wetting layer from a single crystal droplet. The inset details the structure of the wetting layer between the individual peaks. The fourth degree Gaussian fitting have the following parameters: $\bar{h}_p = 2.07$, $\bar{w} = 2.06$ and thus the peak height-to-peak width ratio of $\xi = 0.502$. (b) 3D time evolution of island profile. (c) Evolution of the contact angle is shown on the left y-axis. On the right y-axis, the strain energy and surface free energy changes are given for Ge/Si(100) system. (d) Time evolution of peak height and TJ displacement. Simulation Data: $\Sigma = 0.45$, $\bar{h}_p = 1$, $\beta = 28$, $\nu = 0.273$, $\bar{M}_{TJ} = 2$, $\lambda_{TJ} = 1$, $\bar{\delta} = 0.005$, $\gamma_s = 1.2$ and $\gamma_f = 1$.

this range not only the multiples but also the Volmer-Weber type island formation may be seen depending on the ESED value, which should be further investigated. The extended plateau in the TJ wetting angle plot in Fig. 5.4(c) indicates that at the stationary state equilibrium contact angle may not be necessarily realized, which should be otherwise zero degree. These doublet peaks may be represented by the fourth degree Gaussian type function $G(x; \bar{h}_p, \bar{w}) = \bar{h}_p \cdot \exp(-\ln(2)x^4/\bar{w}^4)$, where the peak height and the half width found to be $\bar{h}_{\max} = 2.07 \rightarrow 11.18 \text{ nm}$ and $\bar{w} = 2.06 \rightarrow 11.12 \text{ nm}$ respectively.

There is a strange peak on the wetting angle plot in Fig. 5.4(c), and the same phenomenon is also occurred in the formation of the singlet without the sign fluctuation in the global Helmholtz free energy. This event is strongly correlated with the TJ motion as may be seen from Fig. 5.4 (d), which shows drastic enhancement in the displacement velocity just at the onset

of the stationary non-equilibrium regime.

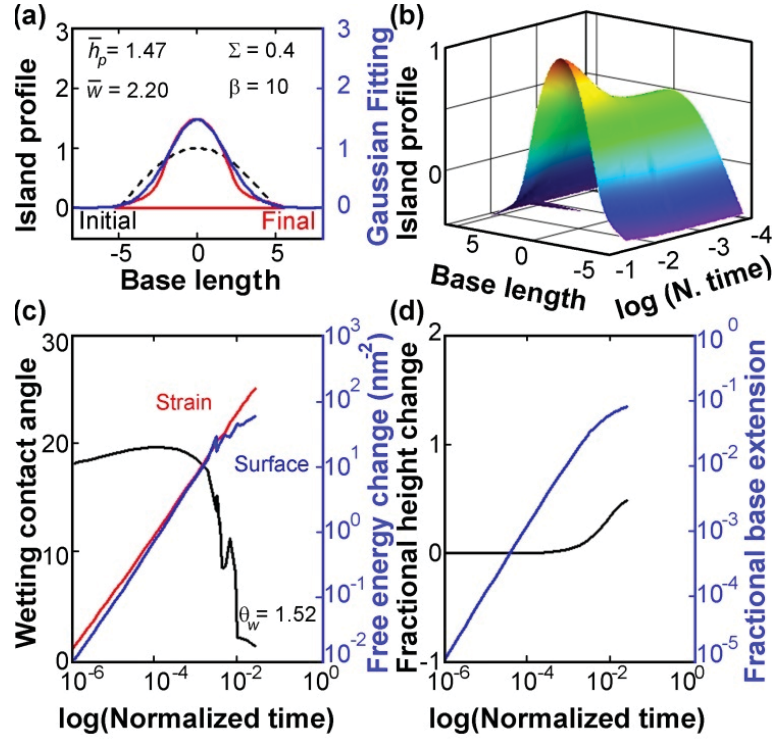


Figure 5.5: (a) The stationary island profile at the transient stage just before the onset of the SK island formation regime. Gaussian bell-shape curve representing the final profile has the following parameters: $\bar{h}_p = 1.47$, $\bar{w} = 2.20$ and thus the peak height-to-peak width ratio of $\xi = 0.334$. (b) 3D time evolution of island profile. (c) Evolution of the contact angle is shown on the left y-axis. On the right y-axis, the strain energy and surface free energy changes are given for Ge/Si(100) system. (d) Time evolution of peak height and TJ displacement. Simulation Data: $\Sigma = 0.4$, $\bar{h}_p = 1$, $\beta = 10$, $\nu = 0.273$, $\bar{M}_{TJ} = 2$, $\lambda_{TJ} = 1$, $\bar{\delta} = 0.005$, $\gamma_s = 1.2$ and $\gamma_f = 1$.

In Fig. 5.5, a new set of computer simulation studies are presented utilizing an aspect ratio of $\beta = 10$ which is 2.8 times smaller than the first set reported above. As expected, this modification pushed the onset of the SK island formation threshold described by the ESED parameter to higher values of $\Sigma \rightarrow 0.40$. This is a factor of 1.6 enhancement compared to the case presented in Fig. 5.2(a). As seen in Fig. 5.5, a bell shape profile extended all over the computation domain without the existence of any wetting layer. This is very typical for this transient regime as observed previously. Figure 5.5(a and b) shows that there is only a transformation of the Cosine-shape droplet into the second degree Gaussian shape profile with a minor increase in height and a very small stretching of the base line or the computation domain due to TJ motion. Fig. 5.5(c) indicates that the wetting contact angle reached

a value of $\theta_W \cong 1.52^\circ$, showing some sort of trend towards the plateau behavior. The most interesting event observed here is the sign of the global Helmholtz free energy change during the evolution process: In general it is negative indicating that the decrease in the strain energy is greater than the increase in the surface free energy of the system. However, only in one narrow region, one observes a sign inversion, which indicates the dynamical nature of the simulation experiment due to TJ displacement motion and may be interpreted as this abrupt change is unnatural. Nevertheless, this is a transient region mostly controlled by the TJ motions and involves additional positive entropy production, which is not accounted in the global Helmholtz free energy as presented above. A careful inspection of Fig. 5.5(c) may show that the surface free energy slowly deviates from linearity by making a turn towards the stationary non-equilibrium state region, and eventually it may be stabilized. This event is closely correlated with the behavior of the base line extension in Fig. 5.5(d). It is clear that this experiment prematurely terminated before the system reaches to the stationary non-equilibrium state, which is indicated by the plateau regions in the kinetic parameters such as the base extension, the TJ contact angle, and finally the peak height. The reason for this rather premature termination was the need for excessive computation time and memory, otherwise one may get a profile having little more flattened tails. In this experiment, the peak height and the peak halve-width are found to be, respectively, $h_p \cong 1.47 \rightarrow 7.12 \text{ nm}$, and $\bar{w} \cong 2.20 \rightarrow 10.65 \text{ nm}$ for Ge/Si(100) system.

In Fig. 5.6, the effect of decrease in the aspect ratio on the threshold level of ESED is presented for the formation of SK islands, which shows a substantial increase in ESED parameter from $\Sigma = 0.30$ for $\beta = 28$ to $\Sigma = 0.50$ for $\beta = 10$. Findings on the stationary values, which describes the morphology of SK in terms of a fourth degree Gaussian profile, may be summarized as: $\bar{h}_{\max} = 1.76$, $\bar{w} = 1.80$ and $\bar{L} = 10.784$. These parameters may be converted into the real space by employing the length scale, $\ell_o \equiv \Sigma \ell^* \rightarrow 6.06 \text{ nm}$, obtained for the Ge/Si(100) system. This conversion results a peak height of $h_{\max} = 10.49 \text{ nm}$, halve-peak width of $w = 10.82 \text{ nm}$ and the extended domain length of $L = \lambda \simeq 65.30 \text{ nm}$ for the SK island formed during the evolution of the droplet having integrated thickness of $h_o \simeq 3.85 \text{ nm}$, and the base length of $L = 60.55 \text{ nm}$ (i.e., the original area $A \cong 233.18 \text{ nm}^2$). At the stationary non-equilibrium state the stationary height-to-base length aspect ratio becomes $\beta_S = 5.93$ instead of $\beta = 10$.

A careful examination of Fig. 5.6(c and d) clearly shows that this experiment is also prema-

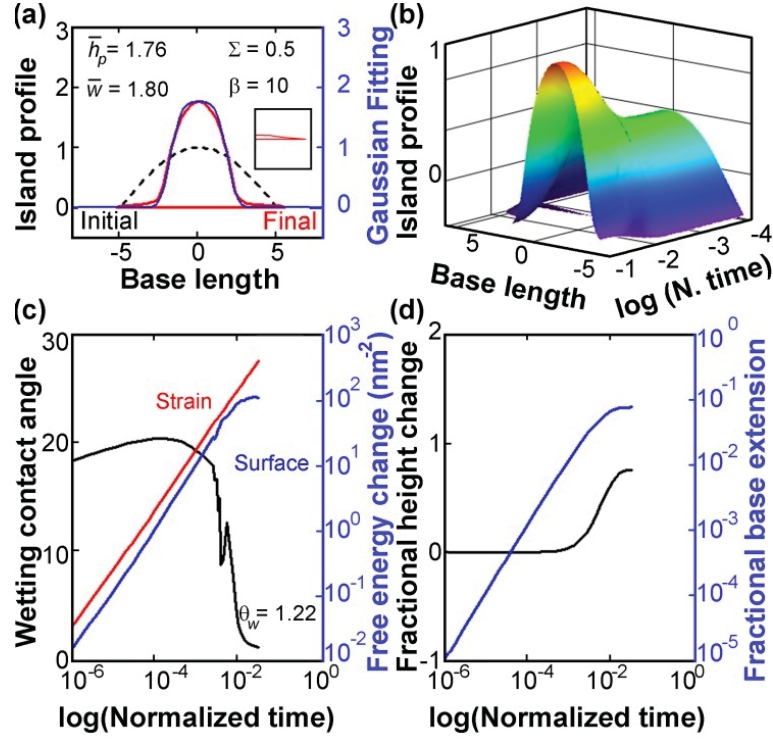


Figure 5.6: (a) Spontaneous formation of the SK island with an almost perfect flat wetting layer from a single crystal. The inset details the structure of the wetting layer at the TJ. The singlet has fourth degree Gaussian bell-shape curve having the following parameters: $\bar{h}_p = 1.76$, $\bar{w} = 1.80$ and thus the peak height-to-peak width ratio of $\xi = 0.489$. (b) 3D time evolution of island profile. (c) Evolution of the contact angle is shown on the left y-axis. On the right y-axis, the strain energy and surface free energy changes are given for Ge/Si(100) system. (d) Time evolution of peak height and TJ displacement. Simulation Data: $\Sigma = 0.50$, $\bar{h}_p = 1$, $\beta = 10$, $\nu = 0.273$, $\bar{M}_{TJ} = 2$, $\lambda_{TJ} = 1$, $\bar{\delta} = 0.005$, $\gamma_s = 1.2$ and $\gamma_f = 1$.

turely interrupted at the onset of the stationary non-equilibrium state due to the same computational requirements. Even though the kinetic parameters such as the base line extension and the wetting angle indicate that they have reached the stationary non-equilibrium state region, the global Helmholtz free energy change still does not show any sign reversal. This situation is closely correlated with Fig. 5.6(a), where one does not see any well developed flat wetting layer formation compared to its counterpart in Fig. 5.3(a). The case reported in Fig. 5.3(c) also shows different kinetic behavior even though topologically both SK islands appear to be very similar, with the exception of the depth and extend of the wetting layers.

In order to correlate two different SK states having exactly the same size in real space, a special test run is performed using an ESED parameter of $\Sigma = 0.30$, which corresponds to the onset of the SK island formation regime, where the droplet has an aspect ratio of $\beta = 28$,

and the normalized peak height of $\bar{h}_p = 1$. These figures in real space match up to a droplet having an initial integrated thickness of $h_o \simeq 2.31 \text{ nm}$, and base length of $L = 101.72 \text{ nm}$ (i.e., the original area $A \simeq 235.18 \text{ nm}^2$). This test run resulted following output data for the stationary state, which exhibits a fourth degree Gaussian profile: $\bar{h}_{\max} = 2.85$ (peak height) and $\bar{w} = 3.0$ (halve peak width), and $\bar{L} \simeq 10.784$ (extended domain size). In the real space, for the Ge/Si(100) system, these data amounts to: $h_{\max} = 10.35 \text{ nm}$, $w = 10.96 \text{ nm}$, and $L \equiv \lambda = 101.72 \text{ nm}$ with a stationary aspect ratio of $\beta_S = 9.82$.

This is a very interesting result, and clearly shows that two droplets having two different initial shapes, characterized by the two different aspect ratios in the normalized space, but having exactly the same sizes (i.e., area in $2\mathbf{D}$ space) in real space evolved into the SK islands having almost exactly the same shape and size. The only difference between these two systems is in the extensions of the wetting layer platforms, which are defined by the original domain sizes with slight enlargements due the TJ activities. This behavior may be summarized by an analytical expression for the adopted Cosine-shape droplet by writing:

$$A = \frac{2}{\pi}\beta\ell_o^2 \Rightarrow \frac{A}{\ell^{*2}} = \frac{2}{\pi}\beta\Sigma_\beta^2 \simeq 1.59$$

In above Equation, the subscript β attached to the ESED parameter, Σ , and the numeric value of 1.59 indicates the onset value for the appearance of the SK island formation regime (i.e., $\Sigma_{10} \rightarrow 0.50$; $\Sigma_{28} \rightarrow 0.30$), which may have well defined range or band structure for the singlet and doublet, etc. depending upon the height-to-base length aspect ratio of the droplet. Kukta and Freund found a parabolic connection between the aspect ratio, which defines the shape of the equilibrium island, and the normalized island area: A/ℓ^{*2} . Their aspect ratio is completely different than ours, and it relies on the ratio of the height-to-base width of the island, which is obtained by a numerical searching technique that is also based on the Cosine-shape initial film morphology, but it is nothing to do with self-evolution of the system towards the stationary non-equilibrium states.

In Fig. 5.7, the results of a computer experiment, which is executed by using a relatively low value for the ESED parameter (i.e., $\Sigma = 0.175$), are presented. In the case of Ge/Si(100) system, this value for the ESED represents a droplet having a peak height of $h_p = 2.12 \text{ nm}$ and the base length of $L = 59.34 \text{ nm}$, which may be described by a height-to-width aspect ratio of $\xi = 0.036$, and the normalized area of $A/\ell^{*2} = 0.546$. The profile of this island looks very similar to those described by Kukta and Freund in their remarkable work on the equilibrium

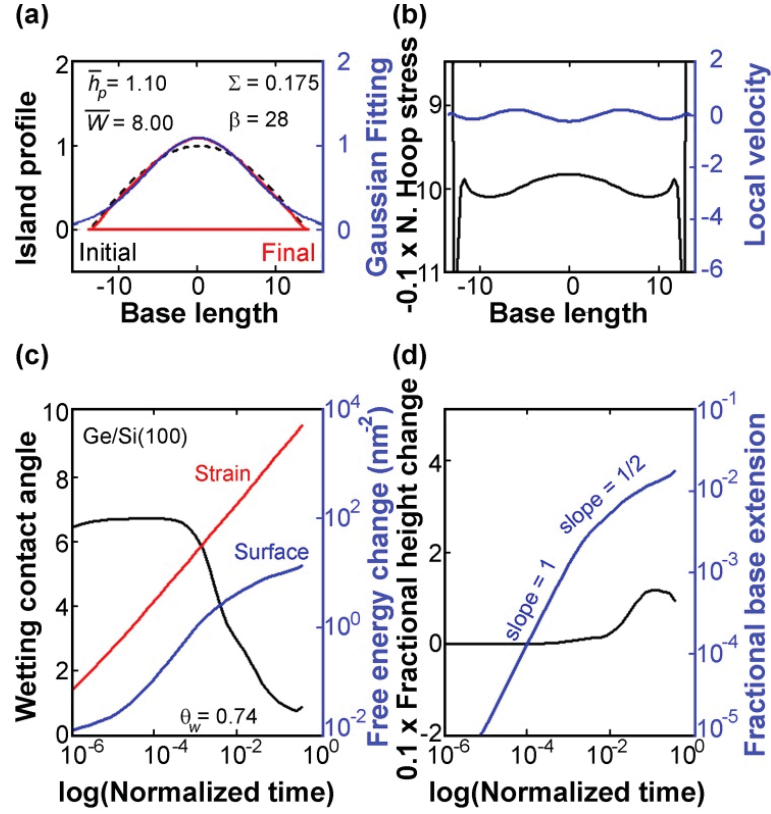


Figure 5.7: (a) Evolution of the Cosine-shape droplets towards the stationary equilibrium state by readjustment of the base length trough the TJ motion. Gaussian bell-shape curve representing the final profile has the following parameters: $\bar{h}_p = 1.10$, $\bar{w} = 8.00$ and thus the peak height-to-peak width ratio of $\xi = 0.069$. (b) Instantaneous velocity and the hoop stress distributions along the final droplet profile. (c) Evolution of the contact angle is shown on the left y-axis. On the right y-axis, the strain energy and surface free energy changes are given for Ge/Si(100) system. (d) Time evolution of peak height and TJ displacement. Simulation Data: $\Sigma = 0.175$, $\bar{h}_p = 1$, $\beta = 10$, $\nu = 0.273$, $\bar{M}_{TJ} = 2$, $\lambda_{TJ} = 1$, $\bar{\delta} = 0.005$, $\gamma_s = 1.2$ and $\gamma_f = 1$.

island shapes for very small size droplets. The wetting layers at the domain edges are very narrow and about 1.04 nm. This tiny droplet as may be deduced from Fig. 5.7(c and d) is stabilized spontaneously by small adjustments in the base length as well as in the wetting contact angle by the TJ motion. At the start, TJ displacement is linear with time and then turns to a new regime where it demonstrates a new slope of $\frac{1}{2}$ as may be seen from the double logarithmic plot in Fig. 5.7(d). The TJ has a constant velocity up to knee point then slows down by showing a connection such as $V_{TJ} \sim 1/\sqrt{t}$ up to the onset of the stationary state regime, then levels off. The calculated value of the integrated thickness is $h_o \cong 1.35 \text{ nm}$, which is greater than the critical film thickness calculated previously as $h_c^{Ge} = 0.56 \text{ nm}$. These values results $h_o/h_c^{Ge} \cong 2.428$, and the growth rate versus film thickness plot for this ratio

is given in Fig. 1 for demonstration. According to the linear theory presented previously, the droplet should be in the instability regime, on the other hand this experiment shows that the system is evolving towards the stationary non-equilibrium state with a large and negative global Helmholtz free energy release.

5.2.1.2 Morphological evolution of droplet with growth:

To show the effect of growth on the morphological evolution of droplet, an experiment using the same input data as it was employed previously to obtain Fig.5.3 is performed. But this time, the growth term is fully considered in the governing equation by employing the following values for the growth mobility and the Helmholtz free energy of condensation, respectively, $\bar{M}_b = 1$ and $\Delta\bar{F}_{vf}^o = 2$.

Fig. 5.8(a) illustrates two profiles with (red) and without (blue) the growth term. In fact, the no growth case was already discussed in the case presented in Fig. 5.3. In the growth case, a primary peak at the center accompanied by two subsidiary or satellite peaks in each side which altogether covers the computation domain is observed. By zooming this figure, one observes very narrow and thin wetting layers ($\delta\bar{h}_{Ge} \cong 0.0587 \rightarrow 0.28 \text{ nm}$) separating the satellites from the primary peak. This clearly indicates that system is still in the domain of the SK islands formation regime. As can be seen from the kinetics data presented in Fig. 5.8(c and d), this system shows some intermediate stationary non-equilibrium state for the time interval of $\bar{t} \approx \{0.05 - 0.1\}$, where the wetting contact angle $\theta_w \approx 0.998^\circ$ as well as the size of the computation domain $\delta L/L_o \approx 0.01$ seem to be stabilized as clearly indicated by the appearance of the plateau regions. Similarly, up to the onset of this rather short living intermediate regime, the height of the primary peak does not show any appreciable increase. Otherwise, the system there on evolving continually unless one turn-off the condensation process completely. In Fig. 5.8(b), the instantaneous velocity and the hoop stress distributions are plotted with respect to the position of the collocation points along the droplet surface. The normalized hoop stress is compressive in sign, since the Ge/Si(100) system is in the mind, which has a negative misfit strain of $\varepsilon_o = -0.042$. One observes very high tension stresses concentrated only at the edges of the interface, where the contact between droplet and the substrate takes place through the TJ, which goes up to the level of $\bar{\sigma} \cong 2.25 \rightarrow 13.389\text{GPa}$, and are not illustrated in this diagram. The velocity diagram (Fig. 5.8(b)) shows two positive

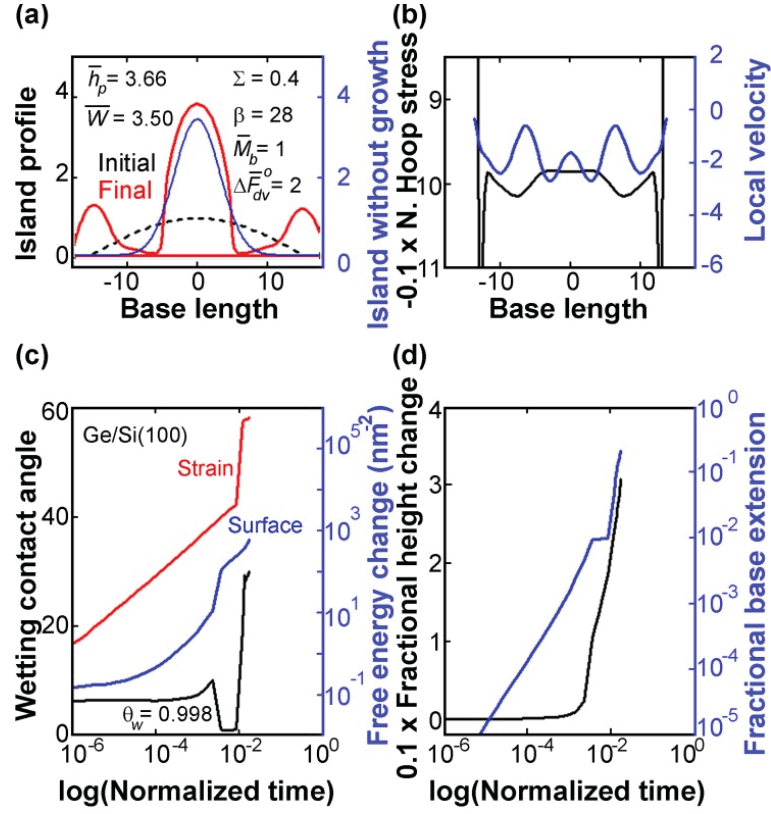


Figure 5.8: (a) The effect of the growth on the SK island morphology: formation of two satellites shouldering the primary pea, and separated by almost perfectly flat wetting layers. Gaussian bell-shape curve representing the final profile has the following parameters: $\bar{h}_p = 1.10$, $\bar{w} = 8.00$ and thus the peak height-to-peak width ratio of $\xi = 0.069$. (b) Instantaneous velocity and the hoop stress distributions along the final droplet profile. (c) Evolution of the contact angle is shown on the left y-axis. On the right y-axis, the strain energy and surface free energy changes are given for Ge/Si(100) system. (d) Time evolution of peak height and TJ displacement. Simulation Data: $\Sigma = 0.40$, $\bar{h}_p = 1$, $\beta = 28$, $\nu = 0.273$, $\bar{M}_{TJ} = 2$, $\lambda_{TJ} = 1$, $\bar{\delta} = 0.005$, $\gamma_s = 1.2$ and $\gamma_f = 1$ and the growth parameters $\bar{M}_b = 1$, $\Delta\bar{F}_{vf}^o = 2$.

maxima, which correspond to the shoulders of the satellites next to the primary peak sides. This indicates that there is a high rate of shrinkage or flattening taking place there, which causes not only the better development of the satellites by rounding off but also the enlargement of the wetting layers next to the primary peak. The velocity distribution shows plateau regions with zero growth rate at the wetting layers, which indicates the stabilization there.

5.2.2 Island formation in epitaxially strained flat droplets with anisotropic texture on rigid substrates

In this section, isochoric system is considered such that no external traction applied to the evolving surface. System evolution is investigated under the wetting effect potential, the potential related with the film/substrate interface misfit and curvature with or without condensation/evaporation.

Evolution of the boundary is described in terms of displacement velocities with following formula:

$$\bar{V}_{ord} = \frac{\partial}{\partial \bar{\ell}} \left[\frac{\partial}{\partial \bar{\ell}} \left(-\Sigma \bar{\sigma}_h^2 + \chi \bar{\vartheta} + \bar{\gamma}_{f \leftrightarrow s}(\bar{y}) \bar{\gamma}_f(\theta, \phi, m) \bar{k} + \bar{\omega}(\bar{y}) \right) \right] \quad (\text{Ordinary points}) \quad (5.3)$$

$$\begin{aligned} \bar{V}_{long} = & -\bar{M}_{long} \bar{\Omega}^{-1} \{ \lambda_{TJ} - \bar{\gamma}_{f \leftrightarrow s}(\bar{y}) \bar{\gamma}_f(\theta, \phi, m) \cos(\theta_W) + \bar{\gamma}_{f \leftrightarrow s}(\bar{y}) \partial_\theta \bar{\gamma}_f(\theta, \phi, m) \cos(\theta_W) \} \\ & \forall \lambda_{TJ} \geq 1 \quad (\text{Triple junction contour line}) \end{aligned} \quad (5.4)$$

In Eq. 5.3, $\bar{\ell}$ is the arc length in $2\mathbf{D}$ space which is scaled with respect to ℓ_o . First part of the equation describes the evolution behavior of strained thin films by surface diffusion which is driven by the gradient of ESED $\Sigma(\bar{\sigma}_h)^2$ and capillary potential $\bar{\gamma}_{f \leftrightarrow s}(\bar{y}) \bar{\gamma}_f(\theta, \phi, m) \bar{k}$, where $\bar{\gamma}_f(\theta, \phi, m)$ is the anisotropic surface stiffness.

5.2.2.1 Two-fold rotational symmetry in cubic structures: Zone axis $\langle 1\bar{1}0 \rangle$

In this section, the results of the extensive computer simulation experiments performed on the single crystal thin film droplets attached to the substrate top surfaces described by two-fold rotational symmetry designated by the zone-axis $\langle 1\bar{1}0 \rangle$ are presented. This zone axis is associated with the set of vicinal (singular) planes such as $(111) \cup (110) \cup (001) \cup (11\bar{2})$ in cubic crystal structures. In the present study it is assumed that $\{111\}$ crystallographic planes have the lowest surface free energy as observed experimentally in fcc and bcc metals and alloys. Therefore zero tilt angle, which designates the orientation of the cusp in the surface

free energy map in 2D space is associated with the (111) plane in the present simulation studies. The tilt angles, ϕ , which are in the range of ($0^\circ - 180^\circ$) are specially selected for demonstration purposes.

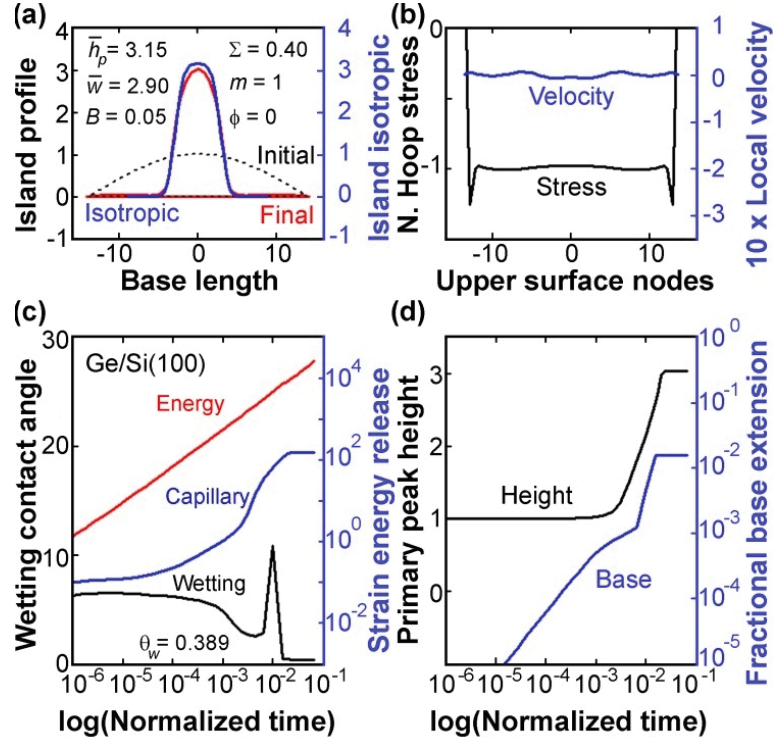


Figure 5.9: (a) Spontaneous formation of the SK island from a single crystal droplet on a stiff substrate via the surface drift diffusion driven by the combined actions of the misfit strain (isochoric) and the anisotropic capillary forces. (b) Instantaneous velocity and the hoop stress distributions along the final droplet profile. (c) Evolution of the contact angle is shown on the left y-axis. On the right y-axis, the strain energy and surface free energy changes are given for the Ge/Si(111) system. (d) Time evolution of peak height and TJ displacement. Data: $\Sigma = 0.40$, $B = 0.05$, $B = 0.05$, $\bar{h}_p = 1$, $\beta = 28$, $\nu = 0.273$, $\bar{M}_{TJ} = 2$, $\lambda_{TJ} = 1$, $\bar{\delta} = 0.005$, $\gamma_s = 1.2$ and $\gamma_f = 1$.

In Fig. 5.9, a typical morphological evolution behavior of the SK island deposited on the top of the Ge/Si vicinal plane is presented in terms of the final droplet profile. Here the peak height, the base extension, and the TJ contact angle are given with respect to the normalized logarithmic scale.

Fig.5.9(c) demonstrates evolution behavior of the wetting layer at the TJ contour line, which has a temporal contact angle of $\theta = 0.74^\circ$ instead of zero degree, which indicates that the TJ is still active. In Fig. 5.9(c), the cumulative strain energy change, $-(\Delta F_f/w_o) \text{ nm}^2$, as well as the increase in the surface free energy, $(\Delta F_s/w_o) \text{ nm}^2$, of the droplet due to the island

formation are also presented. Here the strain energy reduction shows a linear dependence on the normalized elapse time up to the onset of the stationary state regime. This fact may be easily anticipated by looking at the relevant plot, which with the exception of the initial transient stage has a slope of unity in the double logarithmic scale. A close inspection of Fig. 5.9(d) shows that the TJ displacement motion associated with the base extension has three different time exponent stages, $\bar{L}(\bar{t}) = A\bar{t}^n$ here $n = 1; 1/2; 6$, before it enters to the plateau region. Similarly, the peak height shows a logarithmic time dependence during the intermediate regime before the onset of the plateau region, namely; $\bar{h}_p(\bar{t}) = 2 \log(\bar{t}) + 5.6$.

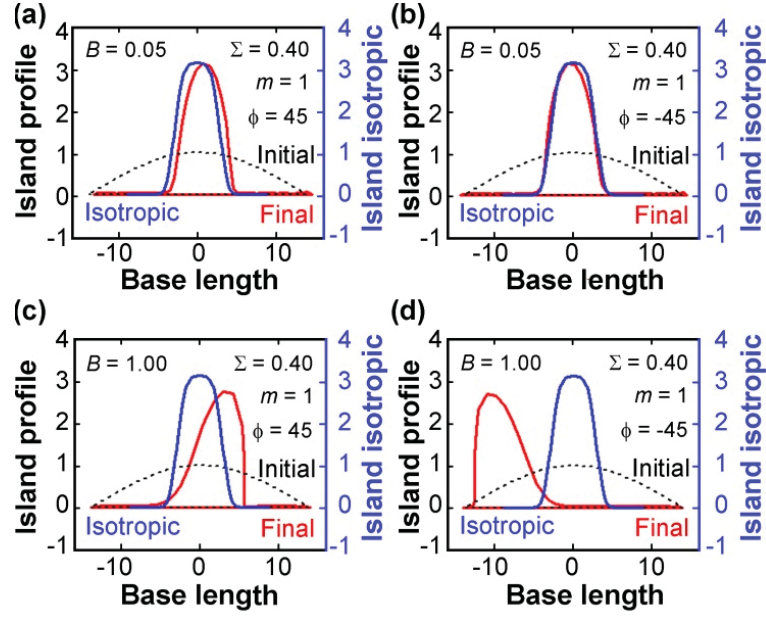


Figure 5.10: Spontaneous formations of the right- and left- shifted SK islands from single crystal droplets for (a and b) very low, $B = 0.05$, and (d and c) very high, $B = 1.0$, surface free energy anisotropy constants at $\pm 45^\circ$ tilt angles. At the threshold level of the anomalous instability regime, very sharp faceting at the right and left edges may be easily seen. Data: $\Sigma = 0.40$, $\bar{h}_p = 1$, $\beta = 28$, $\nu = 0.273$, $\bar{M}_{TJ} = 2$, $\lambda_{TJ} = 1$, $\bar{\delta} = 0.005$, $\gamma_s = 1.2$ and $\gamma_f = 1$.

Fig. 5.10(a-d) illustrate fully developed SK singlet islands, developed over those top substrate surfaces having $\phi = \pm 45^\circ$ tilt angles with respect to a member of the vicinal $\{111\}$ form of planes, which are assumed to be having smallest surface free energy.

The selected tilt angle $\phi = \pm 45^\circ$ is very close to the angle between (111) and (110) planes belonging to the $\langle 1\bar{1}0 \rangle$ zone axis, namely $\phi \cong 35.26^\circ$. Therefore, the results obtained here may easily be extrapolated to the SK islanding taking place in Ge/Si (110) system. Comparison between Fig. 5.10(a,b) and Fig. 5.10(c,d) shows that there is a substantial drop in the

final SK peak height, and the large shift in the peak position if one goes from very low value of $B = 0.05$ to the high anisotropy constants of $B = 1.0$ even though the system still stays in the normal Asaro-Tiller-Grinfeld (ATG) instability regime. From the SK profiles reported in Fig. 5.10(c,d), one may easily see that the very sharp faceting with 90° inclination to the platform is taking place on the right- and left-shoulders, respectively. The faceting planes may be identified as $(\bar{1}10)$ vicinal plane, which also belongs to the zone-axis $\langle 1\bar{1}0 \rangle$. At the stationary state regime, this faceted SK island is separated from the substrate by a thin wetting layer having a thickness of $\Delta\bar{h} = 0.030 \rightarrow 0.17 \text{ nm}$. In these last two cases, an ESED parameter of $\Sigma = 0.40$ is utilized, and a surface free energy anisotropy constant of $B = 1.0$, which is just at the onset of the anomalous instability regime. The peak height and the halve width for the low anisotropy constant $B = 1.0$ found to be about $\bar{h}_{SK} = 2.74 \rightarrow 13.27 \text{ nm}$ and $\bar{w} = 2.06 \rightarrow 9.8 \text{ nm}$, respectively, compared to the one obtained for $B = 0.05$, namely: $\bar{h}_{SK} \cong 3.03 \rightarrow 14.53 \text{ nm}$.

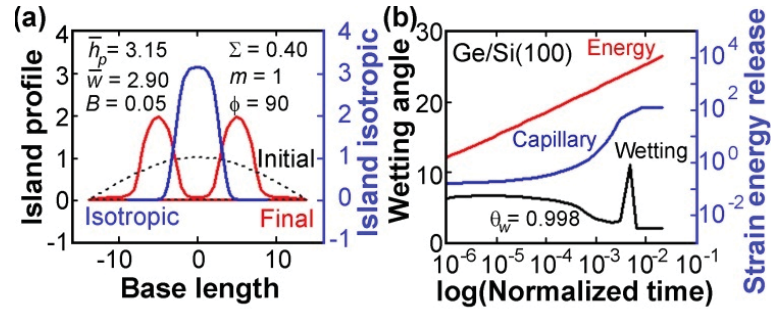


Figure 5.11: (a) Spontaneous formation of the SK doublets with an almost perfect flat wetting layer from a single crystal droplet having exposed to the anisotropic surface stiffness with a tilt angle of $\phi = 90^\circ$. (b) Evolution of the contact angle is shown on the left y-axis. On the right y-axis, the strain energy and surface free energy changes are given for Ge/Si $(11\bar{2})$ system. Data: $\Sigma = 0.40$, $B = 0.05$, $\phi = 90^\circ$, $\bar{h}_p = 1$, $\beta = 28$, $\nu = 0.273$, $\bar{M}_{TJ} = 2$, $\lambda_{TJ} = 1$, $\bar{\delta} = 0.005$, $\gamma_s = 1.2$ and $\gamma_f = 1$.

Fig. 5.11 illustrate a fully developed SK doublet at the stationary state separated by a thin wetting layer having a thickness of $\Delta\bar{h} = 0.0314 \rightarrow 0.17 \text{ nm}$. The wetting layer thickness between the peaks, and the peak tails are found to be almost same in magnitude. In this case, an ESED parameter of $\Sigma = 0.40$ is utilized, and a rather weak anisotropy constant of $B = 0.05$, with a tilt angle of $\phi = 90^\circ$. This tilt angle corresponds to $(11\bar{2})$ vicinal plane, which belongs to $\langle 1\bar{1}0 \rangle$ zone axis, and it is normal to the (111) plane.

The extended plateau in the TJ wetting angle plot in Fig. 5.11(b) indicates that the stationary

state equilibrium contact angle may not be necessarily realized, which should be otherwise equal to zero degree. These doublet peaks may be represented by the fourth degrees Gaussian type function $G(x; \bar{h}_p, \bar{w}) = \bar{h}_p \exp(-\ln(2)x^4/\bar{w}^4)$, where the peak height and the halve width found to be $\bar{h}_{SK} = 1.98 \rightarrow 9.59 \text{ nm}$ and $\bar{w} = 2.06 \rightarrow 11.12 \text{ nm}$, respectively.

5.2.2.2 Four-fold rotational symmetry in cubic structures: Zone axis $\langle 001 \rangle$

In this section, computer simulations are performed on single crystal thin film droplets having $(100) \cup (2\bar{1}0) \cup (1\bar{1}0)$ top substrate surfaces belonging to the $[001]$ zone axis, characterized by the four-fold rotational symmetry. In the first set of simulation experiments, a very low anisotropy constant such as $B = 0.05$ is selected in connection with the various tilt angles in the range of $\phi \supset (0^\circ - 90^\circ)$ to see the orientation effects on the morphological evolutions in the SK islanding. In the second set of experiments, the effects of the surface free energy anisotropy constant, which is chosen below and above the anomalous threshold level of $B_{th} = 1/7$ are examined in great details for the special tilt angle of $\phi = 0^\circ$. This orientation, which corresponds to the cusp in the Wulff free energy mapping is assumed to coincide with the top $(1\bar{1}0)$ surface of the substrate. This assumption as justified for fcc and bcc metals and alloys implies that $(1\bar{1}0)$ plane has the lowest surface free energy among the all vicinal surfaces belonging to the $[001]$ zone axis. A typical top plane of a substrate that has a practical interest in Ge/Si(100) system may be described by any member of the form of planes $\{100\}$ as illustrated in Fig. 5.12.

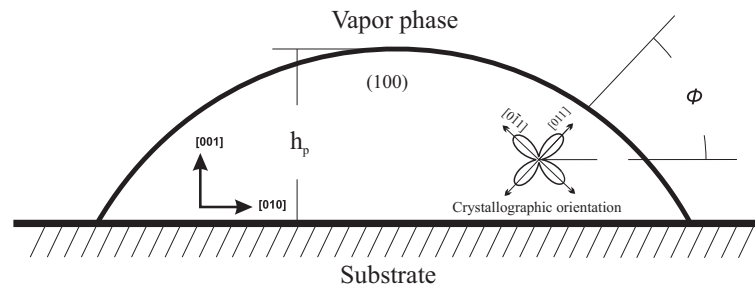


Figure 5.12: Side view of a metallic droplet. This configuration corresponds to the four-fold rotation symmetry designated by $[100]$ zone axis. Where $n = 2m = 4$ and the tilt angle $\phi = 45^\circ$ if one takes the $\{1\bar{1}0\}$ form has lower free energy than the form of planes $\{100\}$, as far as the diffusion and the specific surface Helmholtz free energy dyadics are concerned.

To investigate the effects of the tilt angle on the morphological evaluation of a droplet experi-

ments are performed where the test modulo is assumed to be exposed to an elastic strain energy density of $\Sigma = 0.4$, and the selected surface stiffness anisotropy constant $B = 0.05 \leq 1/7$ is below the threshold level of the anomalous regime. At the zero tilt angle case, these parameters result in a well-developed SK singlet islanding having exactly the same shape parameters as reported in Fig. 5.9(a).

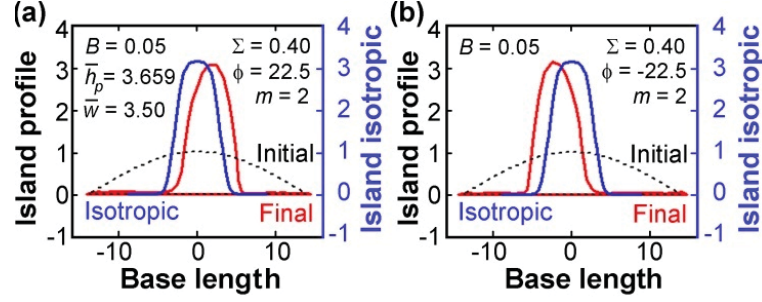


Figure 5.13: (a) Spontaneous formation of a tilted SK singlet towards the right edge with an almost perfect flat wetting layer from a single crystal droplet having exposed to the anisotropic surface stiffness with tilt angle of $\phi = 22.5^\circ$. (b) Where the same droplet is exposed to a tilt angle $\phi = -22.5^\circ$ by keeping all other system parameters same. Data: $\Sigma = 0.40$, $B = 0.05$, $\bar{h}_p = 1$, $\beta = 28$, $\nu = 0.273$, $\bar{M}_{TJ} = 2$, $\lambda_{TJ} = 1$, $\bar{\delta} = 0.005$, $\gamma_s = 1.2$ and $\gamma_f = 1$.

In Fig. 5.13, the results obtained from a simulation experiments performed on a sample oriented with two different tilt angles, namely $\phi = 22.5^\circ$ and $\phi = -22.5^\circ$, are presented. These orientations almost correspond to the set of vicinal planes $(\bar{1}20) \cup (2\bar{1}0)$ symmetrically disposed with respect to the $(\bar{1}10)$ plane with the tilt angles of $\phi \cong \pm 18.4^\circ$. Fig. 5.13(a-b) clearly show the asymmetric morphologies associated with the SK singlet islands, having slightly tilted towards the right and the left edge, respectively for the tilt angles of $\phi = 22.5^\circ$ and $\phi = -22.5^\circ$. The kinetics output data, which are not reported here, resembles those reported in Fig. 5.10(c-d), and indicates that the surface free energy has reached to a stationary state, and TJ-contact angle is almost zero. On the contrary, the elastic strain energy release shows linear increase having a slope of unity on a double-logarithmic scale. That means there is no saturation in the energy release rate rather than it is a constant of time up to the onset of the stationary non-equilibrium SK-state.

In Fig. 5.14(a,b) one can clearly see the morphology associated with the SK doublet islanding for the tilt angle of $\phi = 45^\circ$, which corresponds to the (100) top plane as illustrated in Fig. 5.12. The kinetics data, which is reported in Fig. 5.14(c) indicates that the surface free energy has reached to a stationary state, and TJ-contact angle is almost zero. Similarly, the

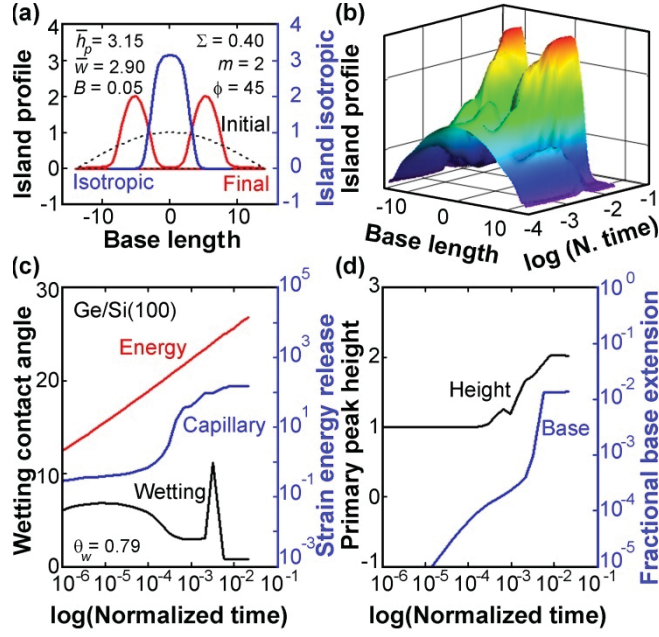


Figure 5.14: (a,b) Spontaneous formation of the SK doublets with an almost perfect flat wetting layer from a single crystal droplet having exposed to the anisotropic surface stiffness with tilt angle of $\phi = 45^\circ$. (c) Evolution of the contact angle is shown on the left y-axis. On the right y-axis, the strain energy and surface free energy changes are given for Ge/Si(100) system. (d) Time evolution of peak height and TJ displacement. Data: $\Sigma = 0.40$, $B = 0.05$, $\bar{h}_p = 1$, $\beta = 28$, $\nu = 0.273$, $\bar{M}_{TJ} = 2$, $\lambda_{TJ} = 1$, $\bar{\delta} = 0.005$, $\gamma_s = 1.2$ and $\gamma_f = 1$.

elastic strain energy released shows linear increase with the normalized elapse time on a semi-logarithmic scale, which means some sort of saturation in the energy release rate. Fig. 5.14(d) shows the behavior of TJ displacement motion associated with the base extension and the peak height.

In Fig. 5.15(a-d), the SK singlets at the stationary states are supported by the thin wetting layer having a thickness of about $\Delta\bar{h} = 0.0314 \rightarrow 0.17 \text{ nm}$. In these simulation experiments, an ESED parameter of $\Sigma = 0.40$ with a tilt angle of $\phi = 0^\circ$ are utilized. Fig. 5.15(c) corresponds to the case just below the threshold level, where one observes rather dome-shape island morphology having slight lower peak height, which is mostly takes places in isotropic systems and/or for the very low values of the surface free energy anisotropy constant as a typical example illustrated in Fig. 5.15(a,b).

In Fig. 5.16(a), a droplet is attached to the $(1\bar{1}0)$ top plane of a substrate for very high values of the surface free energy anisotropy constant in the anomalous regime such as $B \geq 1$. As

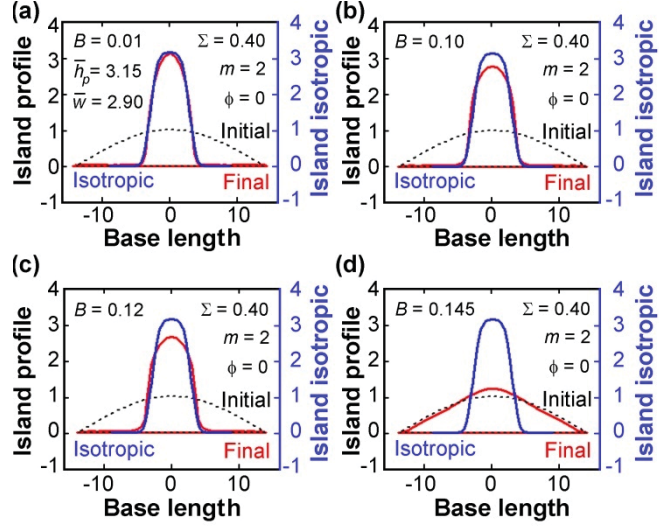


Figure 5.15: (a-c) Spontaneous formation of the SK singlets with an almost perfect flat wetting layer from a single crystal droplet having exposed to the anisotropic surface free energies having various intensities below the threshold level with the tilt angle of $\phi = 0^\circ \Rightarrow (1\bar{1}0)$. d) The formation of the pyramidal shape faceted islanding just above the onset of the anomalous instability regime without the wetting layer. Data: $\Sigma = 0.40$, $B = \{0.01 - 0.25\}$, $\bar{h}_p = 1$, $\beta = 28$, $\nu = 0.273$, $\bar{M}_{TJ} = 2$, $\lambda_{TJ} = 1$, $\bar{\delta} = 0.005$, $\gamma_s = 1.2$ and $\gamma_f = 1$.

one can see from Fig. 5.16(d), the overall system is in the transient nonequilibrium state. Namely, the droplet shows apparently no shape changes other than the monotonic decrease in the peak height, which is in cooperated by the simultaneous base length extension that is a linear function of time. The temporal value of this extension amounts to 10%. On the other hand, the wetting angles at the TJ's show practically no departure from the initial value of about $\phi \cong 6.4^\circ$ other than some erratic fluctuations at the edges.

In Fig. 5.16(c), there is another very interesting case, which is the behavior of the capillary surface free energy change during the evolution process. The capillary surface free energy shows a linear increase with the normalized time, and has a same slope with the strain energy release. The strain energy release exhibits some erratic oscillations at $\bar{t} \leq 10^{-3}$, and otherwise it is about two orders of magnitude larger than the capillary free energy. In Fig. 5.16(d) one also observes steady decrease in the peak height in contrast to the base length, which shows linear time dependent increase, which is somewhat a slow evolution process. Nevertheless, that gives us a strong clue for the existence of the Frank-van der Merwe mode of thin film formation by the flattening or the base extension mechanism operating in the anomalous surface stiffness regime.

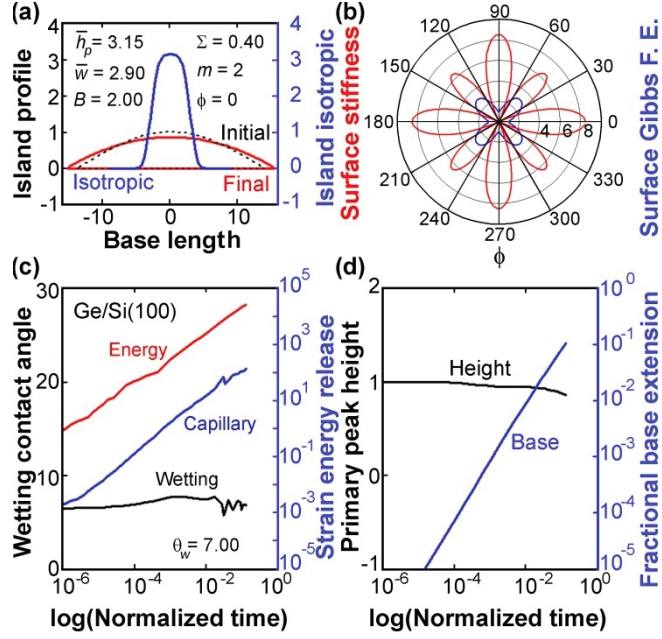


Figure 5.16: (a) The droplet at the zero tilt angle designated as $\phi = 0^\circ \Rightarrow_i \bar{1}\bar{1}0$ shows no shape change even for the very large values of the anisotropy constant other than the slight spreading. (b) Surface free energy and stiffness are illustrated in polar plot, which shows $\langle 100 \rangle$ spikes having rather strong negative intensities that indicates the anomalous regime. (c) Evolution of the contact angle is shown on the left y-axis. On the right y-axis, the strain energy and surface free energy changes are given for Ge/Si($\bar{1}\bar{1}0$) system. (d) Monotonic decrease in the peak height followed up by the substantial increase in the base length. Data: $\Sigma = 0.40$, $B = 2.0$, $\bar{h}_p = 1$, $\beta = 28$, $\nu = 0.273$, $\bar{M}_{TJ} = 2$, $\lambda_{TJ} = 1$, $\bar{\delta} = 0.005$, $\gamma_s = 1.2$ and $\gamma_f = 1$.

5.2.2.3 Six-fold rotational symmetry in cubic structures: Zone axis $\langle 111 \rangle$

In this final section, computer simulations are performed on a single crystal thin film droplet attached to one of those $\{1\bar{1}0\}$ form of planes as the top surface of a substrate described by the six-fold $[111]$ rotational symmetry axis in cubic crystal structures by using various tilt angles in the range of $\phi \supset (0^\circ - 60^\circ)$. Here zero tilt angle corresponds to any one of those six planes belong to the $\{1\bar{1}0\}$ form. From now on, only those experiments with an anisotropy constant of $B = 0.05 < 1/17$ will be reported. This anisotropy constant is specially chosen in order to amplify the effects since it is just below threshold level of the anomalous instability regime.

Similarly, to illustrate the role of the surface free energy anisotropy constant alone on the morphological evolution of droplets, a series of simulations experiments are executed by using values $\{B \subset 0.001 - 1.0\}$ well below and above the anomalous threshold level of $B_{th} = 1/17$,

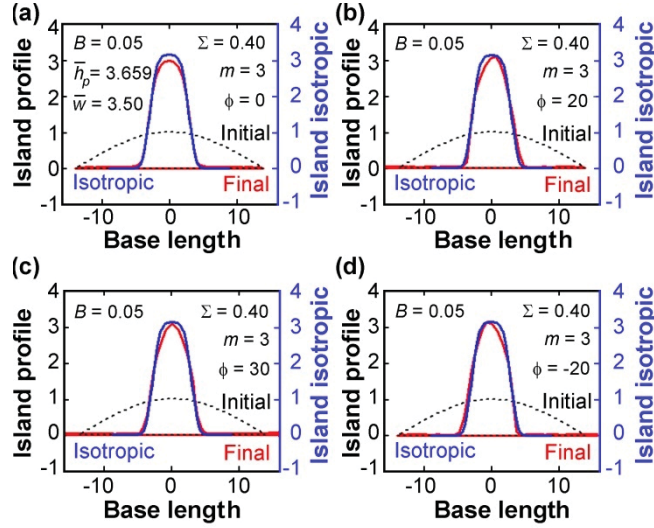


Figure 5.17: (a-d) Spontaneous formations of the SK singlets having different morphological appearances depending upon the tilt angles are presented for an anisotropy constant, B , which is just below the anomalous threshold level of $B_{th} = 1/17$. Data: $\Sigma = 0.40$, $\bar{h}_p = 1$, $\beta = 28$, $\nu = 0.273$, $\bar{M}_{TJ} = 2$, $\lambda_{TJ} = 1$, $\bar{\delta} = 0.005$, $\gamma_s = 1.2$ and $\gamma_f = 1$.

for the special tilt angle of $\phi = 0^\circ$ that is the most interested substrate configuration in practice, namely $\{1\bar{1}0\}$. Fig. 5.17 illustrate the non-equilibrium stationary states of the single crystal droplets for a surface anisotropy constant of $B = 0.05$ after the morphological evolutions taking place at the four different tilt angles, which are specially selected configurations having six-fold rotational symmetries. Fig. 5.17(a-d) clearly shows that the tilt angle $\phi = 30^\circ$, which corresponds to the form of planes $\{11\bar{2}\}$ that belongs to $[111]$ zone axis, plays a special role, and acts as a quasi-reflection-symmetry axis for the final shapes of SK-islanding. That means the shape modifications and distortions on the SK-island singlets are symmetrically disposed in terms of their respective tilt angles relative to this orientation. The morphology of the SK-island obtained for the zero tilt angle as illustrated in Fig. 5.17(a) is very similar to the isotropic case, and it has a dome shape rounded top contour, which may be represented by a fourth degrees Gaussian type curve. On the other hand the SK-island presented in Fig. 5.17(c), which is obtained for the tilt angle $\phi = 30^\circ$ has a sharply pointed top counter, and looks like a cross section of a rounded hoot-shape islanding at 3D space as observed numerically by Golovin et al. for (001) surface orientation in the literature.

Fig. 5.18 present the results of a simulation carried out with a very high value of the anisotropy constant, $B = 1$, and at the zero degree tilt angle. The applied anisotropy constant is well

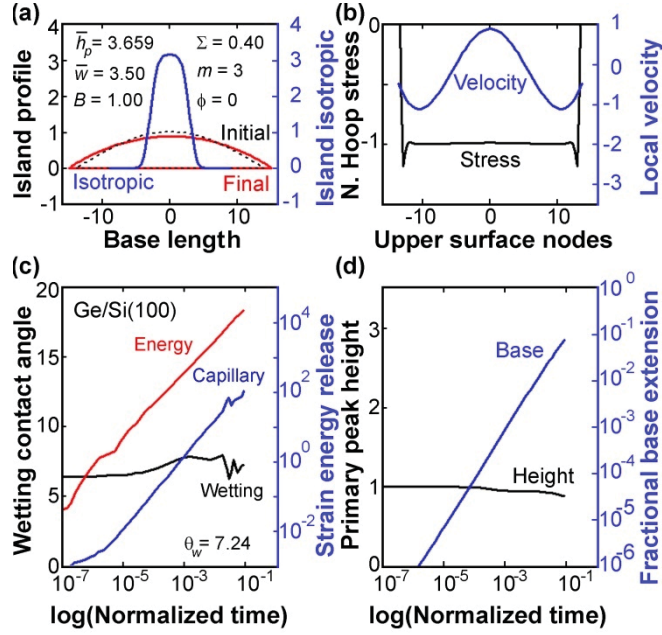


Figure 5.18: (a) The droplet at the zero tilt angle shows no shape change even for the very large values of the anisotropy constant in the anomalous regime. (b) Instantaneous velocity and the hoop stress distributions along the final droplet profile. (c) Evolution of the contact angle is shown on the left y-axis. On the right y-axis, the strain energy and surface free energy changes are given for the Ge/Si(100) system. (d) Time evolution of peak height and TJ displacement, which indicates the monotonic decrease in the peak height, and the steady increase in the base length, followed by some erratic variations in the wetting angles at the triple junctions.

above of the lower limit or the threshold level of the anomalous instability regime designated by $B \geq 1/17$. Even with such a high value of B , the crystalline droplet shows no indication of the morphological changes in the original Cosine-shape other than the adjustment of the triple junctions at the edges, and the substantial extension in the base length. This TJ adjustment as may be seen from Fig. 5.18(c) manifests itself by a major departure from the equilibrium configuration that is characterized by a wetting angle almost equal to zero degree. According to our observations, which are supported by our further simulation experiment that is not reported here, the base spreading increases with the anisotropy constant. Namely, the fractional changes in base length become: $\delta\ell/\ell = 0.01$ for $B = 0.01$ and $\delta\ell/\ell \geq 0.1$ for $B = 1.0$. That means no SK-islanding may be possible for the high anisotropy constants in the anomalous regime for the six-fold symmetries without having superimpose to the random undulations or white noise ripples over the droplet surfaces. In that case, one may talk about the Frank-van der Merwe mode of thin film formation by base-extension as a dominant morphological

scenario instead of the Volmer-Weber islanding and/or the Stranski-Krastanow growth modes.

CHAPTER 6

CONCLUSION

Irreversible thermodynamics treatment of thin film surface morphological evolution under elastostatic and electrostatic force fields with considering isotropic and anisotropic material properties are presented in this thesis. Results of this work is very useful to give guidance to understand thin film mechanics and growth under the applied forces and the control of surface morphologies.

Chapter 4 represents the investigations of dynamics of surface roughness on concurrent actions of the applied elasto- and electro- static fields clearly indicate that applied misfit stress level is highly important effect on resultant surface form which may be smooth wave like or crack like. Simulation experiments clearly presents the major role of the elastic dipole tensor interactions on crack like cavity formations. Surface diffusion anisotropy shows minor effect on the crack formation and growth rate under the elastostatic forces without the electrostatic forces. On the other hand, when electrostatic loads applied surface diffusion anisotropy became a major parameter which define the resultant surface formation.

Most important physical outcome of these experiments is the dominant role of the EDTI, which represents the mobile lattice defects contribution to the generalized driving force compared to the elastic strain energy density for the surface diffusion, in those thin film structures exposed to the surface tractions and body forces. The importance of the elastic dipole tensor interactions for the surface drift-diffusion by adatom hopping motion is also supported by the first principle calculations by Shu et al [88]. Due to the EDTI, crack like formation take place under the compressive forces, sharp crack tip creates high stress concentration zone as a result crack growth take place with high speed. As a result of this, surface roughness growth dynamics deviate from the predicted by LISA. LISA predict linear relation between growth rate

Γ and applied stress σ but at high compressive stresses $\sigma < -100 \text{ MPa}$ growth rate change becomes quadratically dependent on stress. Also surface roughness with high amplitude values deviate from LISA which assume the surface roughness is sine wave like with low angle surface tangent. When surface diffusion anisotropy taken into account in stress calculation, main difference from the isotropic one is that flux divergence caused by anisotropy of diffusion cause highest probability of observing crest and trough splitting phenomena. Texture tilt angle effects the surface perturbation by trying to minimize the surface area where the transverse diffusion constant is minimum.

Last section of chapter 4 represents the investigations of the actions of the applied electrostatic fields on the surface roughness clearly indicate that the proper selection of the tilt angle has vital importance; this fact is also demonstrated very recently by Tomar et al. and Ogurtani et al. [63]. On the other hand, the improper application of electron wind force direction in regards to the orientation of the texture of the single crystal film may generate adverse effects on the surface roughness rather than causing healing. Therefore, the healing effect of the electrostatic field is solely restricted to the properly oriented single crystal surfaces, and it may not be realized for the polycrystalline materials unless they have well controlled strong cubic sheet textures. In this respect, LISA gives very helpful clues on the proper selection of the rotational symmetry of the top surfaces of the thin film metallic lines exposed to the detrimental effects of compressive stresses, and then the direction of the applied electric field with respect to the tilt angle for the optimization of healing process. Through the interaction of stress and electric field there appear a very special type of structure called solitary wave, these structures are formed by transformation of surface perturbation to a new stable form at the transition regime between dissipation and regenerative regimes. This solitary structures are previously observed and reported in interconnect by TO Ogurtani and A Celik [89]. LISA predicts accurately according to the experiments done that at certain stress levels correspond to perturbations with the certain wavelength which has the highest growth rate. This phenomenon might be used as a pattern formation tool by combining the applied electric field.

In chapter 5, the physico-mathematical model, developed by Ogurtani based on the irreversible thermodynamics treatment of surfaces and interfaces with singularities, is applied to describe the dynamical and spontaneous evolution of flat solid droplets driven by the surface drift diffusion induced by capillary forces and mismatch stresses, during the development of the Stranski-Krastanow island morphology on a rigid substrate. The study showed great

potential to shade some more lights on the fundamental roles played by those parameters, which describe the shape β and the size Σ of epitaxially grown droplets, in SK island formation. These parameters, as demonstrated here, dictate selectively what type of SK island would be formed among a large pool of different possibilities (i.e., singlet, doublet, etc.), by the spontaneous evolutions of this isochoric system without having exposed to any external and/or internal perturbations. Work also demonstrated that for a given aspect number, β , defined as the height-to-length ratio of the droplet, any desired number of SK island multiples formation may be realized if the strain energy density parameter Σ belongs to the well defined closed (bonded) and continuous set of real numbers in the normalized and scaled length-time space. It is also revealed that the droplets (i.e., furnished by proper sets of shape and size parameters), having exactly the same size, regardless of their initial shapes may evolve spontaneously into the same SK island morphologies (i.e., same size and shape) in real space. The only difference is the extend of the wetting layer platform. The small aspect ratios result in narrow wetting layer platforms than the large aspect ratio constituents.

The non-equilibrium stationary state morphologies of isolated thin solid droplets are studied below and above the anomalous surface stiffness threshold level. It is assumed that the evolution process is initiated by the nucleation route and a self-consistent **2D** dynamical simulations having the free-moving boundary condition at the triple junction contour line were used. The anisotropic surface Helmholtz free energy, and the surface stiffness are all represented by the well accepted trigonometric functions. While various tilt angles and anisotropy constants are considered during simulation experiments, the main emphasis were given on the two-fold, four-fold and six-fold rotational symmetries associated with the surface Helmholtz free energy topography in **2D** space, to see their impacts on the final shapes of the SK islands. The following findings are observed as main features and/or characteristics of the morphological transitions taking place isothermally and spontaneously:

- i. Simulations in the two-fold and four-fold rotational symmetries revealed that for a given tilt angle, there are two well-defined domains in the surface free energy anisotropy constant. The first domain is below the threshold level of anomalous regime and characterized by the morphological transition of a droplet into the SK island formation embedded in a wetting layer platform. This transition may occur as both singlets and/or doublets depending upon the tilt angle. In the second domain (i.e., the anomalous regime), a partial stabilization of the initial shape of the droplet occurs if the anisotropy constant is just above the threshold

level. Otherwise the Frank-van der Merwe mode of thin film formation by base-extension takes place by following a linear kinetic law. Conversely, in the case of six-fold symmetry, the SK singlet islanding takes place regardless of the tilt angle as long as one stays in the normal stability regime.

ii. Six-fold rotational symmetry associated with the $\{1\bar{1}0\}$ form of planes as the top substrate planes with zero tilt angle in the anomalous regime has a unique property of showing absolute nonequilibrium stability of the original droplet even for very high values of the anisotropy constant, with the major base extension by almost keeping the original wetting angles at TJ-edges. This behavior implies the formation of Frank-van der Merwe mode of thin film as dominant scenario during the strain-heteroepitaxial growth if one have high anisotropies in the surface free energies.

iii. In general for a given anisotropy constant, the tilt angle may have profound effects on the morphology of the SK islanding. Arbitrarily selected tilt angle may cause distortion on the peaking shape rather than producing sharp faceting. Similarly, there are certain orientations exist, which may result doublet formation rather than the singlet islanding that is especially the typical case for the zero tilt angle.

iv. A careful examination of the simulation results also demonstrated that SK-singlet always prefers to those vicinal planes (i.e., cusps), which have the lowest surface free energy in a given set of planes associated with the rotational symmetry axis designated as the zone axis. On the other hand, the SK-doublets prefer to base on those substrate planes, which have higher surface free energies. This could be easily understood by looking at the surface stiffness map, which shows that the cusp corresponds to maxima in the stiffness plot, and the maxima in the surface free energy between cusps produces minima in the surface stiffness mapping. Since normalized curvature in the governing equation is augmented by the stiffness the capillary potential is totally controlled by the stiffness along the SK-profile but not by the surface free energy itself.

In conclusion, simulation experiment in this thesis presents the observations about what and how growth conditions of QD like structures from either SK islands or droplet are effected under the change of applied forces (electro- and elasto- static forces) and anisotropic physical properties (diffusivity, surface free energy). In addition to these, Stress effect on thin films and interconnect are investigated in large spectrum of stress values with anisotropic physical

properties, considering the reliability issues.

As a final point, in order to obtain more realistic morphological surface appearances one should have rather perform three dimensional simulations. This will provide geometrically realistic structures. In practice, physical experiments show very large variety of surface structures such as domes, huts, pyramids, pits, rings, and their complex variations due to the anisotropic nature of physical properties. Therefore one should assume for realistic simulations in mesoscopic level non-uniform athermal vacancy distributions, in addition to the orientation dependent specific surface gibbs free energies combined with the an anisotropic elasticity by taking into account discrete nature of the crystalline solids.

In addition to these, dislocation dynamics are very important in misfit stress relaxation process and play dominant role on quantum dot formation and their stability. For the sake of taking account these, coupled model of an atomistic model and current model can be designed.

REFERENCES

- [1] R Kern, G Le Lay and JJ Metois. *in Current Topics in Materials Science*. North-Holland, Amsterdam (1979), Vol. 3
- [2] JA Venables, GDT Spiller and M Hanbucken. *Nucleation and growth of thin films*. Rep. Prog. Phys. (1984) vol. 47 pp. 399-459
- [3] K Barnham and D Vvedensky. *Low-dimensional semiconductor structures: fundamentals and device applications*. Cambridge University Press (2001) pp. 393
- [4] DJ Eaglesham and M Cerullo. *Dislocation-free stranski-krastanow growth of Ge on Si(100)*. Phys. Rev. Lett. (1990) vol. 64 (16) pp. 1943-1946
- [5] Madhukar et al. *Realization of low defect density, ultrathick, strained InGaAs/GaAs multiple quantum-well structures via growth on patterned GaAs (100) substrates*. Appl. Phys. Lett. (1990) vol. 57 (19) pp. 2007-2009
- [6] PM Petroff and SP Denbaars. *MBE and MOCVD growth and properties of self-assembling quantum-dot arrays in III-V semiconductor structures*. Superlattices and microstructures vol. 15 (1) pp. 15-21
- [7] Seifert et al. *Microstructural instability in single-crystal thin films*. J. Mater. Res. (1996) vol. 11 (6) pp. 1470-1482
- [8] Georgsson et al. *Transmission electron-microscopy investigation of the morphology of in stranski-krastanow islands grown by metalorganic chemical-vapor-deposition*. Appl. Phys. Lett. (1995) vol. 67 (20) pp. 2981-2982
- [9] JG Belk. *Surface aspects of strain relaxation during InAs/GaAs heteroepitaxy*. open-sigle.inist.fr (1997)
- [10] Yamaguchi et al. *RHEED and STM study of the two-dimensional growth of InAs on GaAs (111)A*. Microelect. J. (1997) vol. 28 (8-10) pp. 825-831
- [11] J Tersoff and FK Legoues. *Competing relaxation mechanisms in strained layers*. Phys. Rev. Lett. (1994) vol. 72 (22) pp. 3570-3573
- [12] FK Legoues. *The effect of strain on the formation of dislocations at the SiGe/Si interface*. Mrs. Bull. (1996) vol. 21 (4) pp. 38-44
- [13] Leonard et al. *Direct formation of quantum-sized dots from uniform coherent islands of InGaAs on GaAs-surfaces*. Appl. Phys. Lett. (1993) vol. 63 (23) pp. 3203-3205
- [14] Moison et al. *Self-organized growth of regular nanometer-scale InAs dots on GaAs*. Appl. Phys. Lett. (1994) vol. 64 (2) pp. 196-198
- [15] Joyce et al. *Surface morphology during strain relaxation in the growth of InAs on GaAs(110)*. Surf. Sci. (1998) vol. 410 (1) pp. 82-98

- [16] Xie et al. *Realization of optically-active strained InAs island quantum boxes on GaAs(100) via molecular-beam epitaxy and the role of island induced strain fields*. J. Crys. Gro. vol. 150 (1-4) pp. 357-363
- [17] Voigtlander et al. *Formation of Si/Ge nanostructures at surfaces by self-organization*. J. Phys. Cond. Matt. (2004) vol. 16 (17) pp. S1535-S1551
- [18] Mo et al. *Kinetic pathway in stranski-krastanov growth of Gen on Si(001)*. Phys. Rev. Lett. (1990) vol. 65 (8) pp. 1020-1023
- [19] W Balluffi et al. *Kinetics of materials*. Wiley.com (2005) pp. 645
- [20] E Arzt, WD Nix. *A model for the effect of line width and mechanical strength on electromigration failure of interconnects with "near-bamboo" grain structures*. J. Mater. Res (1991) vol. 6 (4) pp. 731-736
- [21] HB Huntington, AR Grone. *Current-induced marker motion in gold wires*. J. Phys. Chem. Solids (1961) vol. 20 (1-2) pp. 76-87
- [22] JR Lloyd. *Electromigration in thin film conductors*. Sem. Sci. Tech. (1997) vol. 12 (10) pp. 1177-1185
- [23] WQ Wang, Z Suo. *A simulation of electromigration-induced transgranular slits*. J. Appl. Phys. (1996) vol. 79 (5) pp. 2394-2403
- [24] S Vaidya, TT Sheng, and AK Sinha. *Linewidth dependence of electromigration in evaporated al-0.5-percent cu*. Appl. Phys. Lett. (1980) vol. 36 (6) pp. 464-466
- [25] Marieb et al. *Observations of electromigration-induced void nucleation and growth in polycrystalline and near-bamboo passivated al lines*. J. Appl. Phys. (1995) vol. 78 (2) pp. 1026-1032
- [26] Sanchez et al. *Slit morphology of electromigration induced open circuit failures in fine line conductors*. J. Appl. Phys. (1992) vol. 72 (7) pp. 3201-3203
- [27] JH Rose. *Fatal electromigration voids in narrow aluminum-copper interconnect*. Appl. Phys. Lett. (1992) vol. 61 (18) pp. 2170-2172
- [28] Arzt et al. *Electromigration failure by shape change of voids in bamboo lines*. J. Appl. Phys. (1994) vol. 76 (3) pp. 1563-1571
- [29] Suo et al. *Electromigration instability - transgranular slits in interconnects*. Appl. Phys. Lett. (1994) vol. 64 (15) pp. 1944-1946
- [30] O Kraft, E Arzt. *Electromigration mechanisms in conductor lines: Void shape changes and slit-like failure*. Acta Mater. (1995) vol. 45 (4) pp. 1599-1611
- [31] MR Gungor and D Maroudas. *Electromigration-induced failure of metallic thin films due to transgranular void propagation*. Appl. Phys. Lett. (1998) vol. 72 (26) pp. 3452-3454
- [32] O Kraft, E Arzt. *Electromigration mechanisms in conductor lines: Void shape changes and slit-like failure*. Acta Mater. (1995) vol. 45 (4) pp. 1599-1611
- [33] TO Ogurtani, EE Oren. *Computer simulation of void growth dynamics under the action of electromigration and capillary forces in narrow thin interconnects*. J. Appl. Phys. (2001) vol. 90 (3) pp. 1564-1572

- [34] TO Ogurtani. *Thermal grain-boundary grooving in bicrystal thin solid films having strong anisotropic surface Gibbs free energy represented by the modified cycloid-curtate function*. Journal of Crystal Growth (2009) vol. 311 pp. 1584-1593
- [35] MR Gungor and D Maroudas. *Electromigration-induced failure of metallic thin films due to transgranular void propagation*. Appl. Phys. Lett. (1998) vol. 72 (26) pp. 3452-3454
- [36] D Maroudas and MR Gungor. *Continuum and atomistic modeling of electromechanically-induced failure of ductile metallic thin films*. Comp. Mater. Sci. (2002) vol. 23 (1-4) pp. 242-249
- [37] M Schimschak, J Krug. *Surface electromigration as a moving boundary value problem*. Phys. Rev. Lett. (1997) vol. 78 (2) pp. 278-281
- [38] M Schimschak, J Krug. *Electromigration-induced breakup of two-dimensional voids*. Phys. Rev. Lett. (1998) vol. 80 (8) pp. 1674-1677
- [39] M Schimschak, J Krug. *Electromigration-driven shape evolution of two-dimensional voids*. J. Appl. Phys. (2000) vol. 87 (2) pp. 695-703
- [40] M Mahadevan, RM Bradley and JM Debierre. *Simulations and theory of electromigration-induced slit formation in unpassivated single-crystal metal lines*. Phys. Rev. B (1999) vol. 59 (16) pp. 11037-11046
- [41] M Mahadevan, RM Bradley. *Phase field model of surface electromigration in single crystal metal thin films*. Physica D (1999) vol. 126 (3-4) pp. 201-213
- [42] RJ Asaro and WA Tiller. *Interface morphology development during stress-corrosion cracking .1. via surface diffusion*. Metall. Trans. (1972) vol. 3 (7) pp. 1789
- [43] DJ Srolovitz and SA Safran. *Capillary instabilities in thin-films .2. kinetics*. J. Appl. Phys. (1986) vol. 60 (1) pp. 255-260
- [44] DJ Srolovitz. *On the stability of surfaces of stressed solids*. Acta. Metall. Mater. (1989) vol. 37 (2) pp. 621-625
- [45] TJ Chuang, ER Fuller. *Extended charles-hillig theory for stress-corrosion cracking of glass*. Phys. Rev. B (2004) vol. 69 pp. 165413
- [46] GQ Lu, E Nygren, MJ Aziz. *Pressure-enhanced crystallization kinetics of amorphous si and ge - implications for point-defect mechanisms*. J. Appl. Phys. (1991) vol. 70 (10, Part 1) pp. 5323-5345
- [47] IA Blech. *Electromigration in thin aluminum films on titanium nitride*. J. Appl. Phys. (1976) vol. 47 (4) pp. 1203-1208
- [48] IA Blech, C Herring. *Stress generation by electromigration*. Appl. Phys. Lett. (1976) vol. 29 (3) pp. 131-133
- [49] Sun et al. *Emergence of cracks by mass-transport in elastic crystals stressed at high-temperatures*. J. Mech. Phys. Solids (1994) vol. 42 (11) pp. 1653
- [50] Sun et al. *A finite element method for simulating interface motion .1. Migration of phase and grain boundaries*. Acta Mater. (1997) vol. 45 (5) pp. 1907-1915

- [51] Z Suo. *Stable state of interconnect under temperature change and electric current*. Acta Mater. (1998) vol. 46 (11) pp. 3725-3732
- [52] XH Liu, Z Suo, Q Ma, H Fujimoto. *Developing design rules to avert cracking and debonding in integrated circuit structures*. Engineering Fracture Mechanics (2000) vol. 66 (4) pp. 387-402
- [53] E Liniger, L Gignacand, CK Hu, S Kaldor. *In situ study of void growth kinetics in electroplated Cu lines*. J. Appl. Phys. (2002) vol. 92 (4) pp. 1803-1810
- [54] Barvosa-Carter et al. *Kinetically driven growth instability in stressed solids*. Phys. Rev. Lett. (1998) vol. 81 (7) pp. 1445-1448
- [55] B Spencer and P Voorhees. *Morphological instability in epitaxially strained dislocation-free solid films*. Phys. Rev. Lett. (1991) vol. 67 (26) pp. 3696
- [56] CH Chiu and H Gao. *A numerical study of stress controlled surface diffusion during epitaxial film growth*. Thin films: Stresses and mechanical properties V (1995) pp. 33-44
- [57] YW Zhang, AF Bower, P Liu. *Morphological evolution driven by strain induced surface diffusion*. Thin Solid Films (2003) vol. 424 (1) pp. 9-14
- [58] R Krishnamurthy and DJ Srolovitz. *Film/substrate interface stability in thin films*. J. Appl. Phys. (2006) vol. 99 pp. 043504
- [59] N Medhekar. *Shape dynamics in anisotropically strained two-dimensional self-assembling systems*. J. Appl. Phys. (2008)
- [60] Golovin et al. *Faceting instability in the presence of wetting interactions: A mechanism for the formation of quantum dots*. Phys. Rev. B (2004) vol. 70 (23) pp. 235342
- [61] Levine et al. *Self-assembly of quantum dots in a thin epitaxial film wetting an elastic substrate*. Phys. Rev. B (2007) vol. 75 (20) pp. 205312
- [62] RV Kukta, LB Freund. *Minimum energy configuration of epitaxial material clusters on a lattice-mismatched substrate*. J. Mech. Phys. Solids (1997) vol. 45 pp.1835-1860
- [63] Tomar et al. *Current-Induced Stabilization of Surface Morphology in Stressed Solids*. Phys. Rev. Lett. (2008) vol. 100 (3) pp. 36106
- [64] Averbuch et al. *Computation for electromigration in interconnects of microelectronic devices*. J. Comp. Phys. (2001) vol. 167 (2) pp. 316-371
- [65] Averbuch et al. *Electromigration of intergranular voids in metal films for microelectronic interconnects*. J. Comp. Phys. (2003) vol. 186 (2) pp. 481-502
- [66] Berbezier et al. *SiGe nanostructures: new insights into growth processes*. J. Phys-Condens Mat. (2002) vol. 14 (35) pp. 8283-8331
- [67] Berbezier et al. *SiGe nanostructures: new insights into growth processes*. J. Phys-Condens Mat. (2002) vol. 14 (35) pp. 8283-8331
- [68] J Narayan. *New frontiers in thin film growth and nanomaterials*. Metall. Mater. Trans. B (2005) vol. 36 (1) pp. 5-22

- [69] Hull et al. *Precision placement of heteroepitaxial semiconductor quantum dots*. Mat. Sci. Eng. B-Solid (2003) vol. 101 (1-3) pp. 1-8
- [70] T Zhao and JD Weeks. *A two-region diffusion model for current-induced instabilities of step patterns on vicinal Si(111) surfaces*. Surf. Sci. (2005) vol. 580 (1-3) pp. 107-121
- [71] Zhao et al. *The challenges in guided self-assembly of Ge and InAs quantum dots on Si*. Thin Solid Films (2006) vol. 508 (1-2) pp. 195-199
- [72] G Bales and A Zangwill. *Morphological instability of a terrace edge during step-flow growth*. Phys. Rev. B (1990) vol.41 pp. 5500
- [73] L Schwenger and R Folkerts. *Bales-Zangwill meandering instability observed in homoepitaxial step-flow growth*. Phys. Rev. B (1997) vol. 55 (12) pp. 55
- [74] G Schulze Icking-Konert. *PhD Thesis, University of Aachen D82, Jüil-Report 3588*. Forschungszentrum Jülich (1998)
- [75] T Maroutian, L Douillard and HJ Ernst. *Wavelength selection in unstable homoepitaxial step flow growth*. Phys. Rev. Lett. (1999) vol. 83 (21) pp. 4353
- [76] T Maroutian, L Douillard and HJ Ernst. *Morphological instability of Cu vicinal surfaces during step-flow growth*. Phys. Rev. B (2001) vol. 64 pp. 165401
- [77] P Müller and J J Métois. *Anisotropy of the surface thermodynamic properties of silicon*. Thin Solid Films (2008) vol. 517 (1) pp. 65-68
- [78] TO Ogurtani, EE Oren. *Computer simulation of void growth dynamics under the action of electromigration and capillary forces in narrow thin interconnects*. J. Appl. Phys. (2001) vol. 90 (3) pp. 1564-1572
- [79] I Prigogine. *Thermodynamics of Irreversible Processes, 2nd ed.* Interscience, New York (1961) p. 75
- [80] A Guggenheim. *Thermodynamics, 4th edition*. North-Holland, Amsterdam (1959) p. 39
- [81] JD Van der Waals and G Bakker. *Handbuch der Experimentalphysik*. Springer-Verlag, Berlin (1928) Vol. 6, p. 22
- [82] P Glansdorff, I Prigogine. *Thermodynamic theory of structure, stability and fluctuations*. Wiley-Interscience (London and New York) (1971)
- [83] R Haase. *Thermodynamics of Irreversible Processes*. Reading, MA (1969) pp. 11-134
- [84] EE Oren. *Computer simulation of electromigration induced void grain boundary interactions with a special reference to the prediction of cathode failure times in bamboo structures* Ph.D. Thesis (2003), Department of Metallurgical and Materials Engineering, MIDDLE EAST TECHNICAL UNIVERSITY, Ankara, TURKEY
- [85] S. R. De Groot. *Thermodynamics of Irreversible Process* North-Holland, Amsterdam, (1961) pp. 208
- [86] G Beer, I Smith and C Duenser. *The boundary element method with programming: for engineers and scientists*. Springer (2008) pp. 500
- [87] LN Brush and EE Oren. *Private communication*.

- [88] Shu et al. *Simple generic method for predicting the effect of strain on surface diffusion*. Phys. Rev. B (2001) vol. 64 (24) pp. 245410
- [89] TO Ogurtani and A Celik. *Surface morphological evolution on single crystal films by strong anisotropic drift diffusion under capillary and electromigration forces*. J. Appl. Phys. (2006) vol. 100 (4) pp. 043504
- [90] J Aqua and T Frisch. *Influence of surface energy anisotropy on the dynamics of quantum dot growth*. Phys. Rev. B (2010) vol. 82 (8) pp. 085322
- [91] M Basham and F Montalenti and P Mulheran. *Multiscale modeling of island nucleation and growth during Cu(100) homoepitaxy*. Phys. Rev. B (2006) vol. 73 (4) pp. 045422
- [92] Berrehar et al. *Surface patterns on single-crystal films under uniaxial stress: Experimental evidence for the Grinfeld instability*. Phys. Rev. B (1992) vol. 46 (20) pp. 13487
- [93] AF Bower and S Shankar. *A finite element model of electromigration induced void nucleation, growth and evolution in interconnects*. Mod. Sim. Mat. Sci. Eng. (2007) vol. 15 (8) pp. 923-940
- [94] MA Biot. *Variational-Lagrangian irreversible thermodynamics of initially-stressed solids with thermomolecular diffusion and chemical reactions*. J. Mech. Phys. Solids (1977) vol. 25 (4) pp. 289-307
- [95] J Cahn. *Crystal shapes and phase equilibria: a common mathematical basis*. Met. Mat. Trans. A (1996) vol. 27A pp. 1431
- [96] A Celik. *Investigation of electromigration induced hillock and edge void dynamics on the interconnect surface by computer simulation* M.Sc. Thesis (2004), Department of Metallurgical and Materials Engineering, MIDDLE EAST TECHNICAL UNIVERSITY, Ankara, TURKEY
- [97] C Chiu. *Stable and uniform arrays of self-assembled nanocrystalline islands*. Phys. Rev. B (2004) vol. 69 pp. 165413
- [98] TJ Chuang, JR Rice. *Shape of intergranular creep cracks growing by surface diffusion*. Phys. Rev. B (2004) vol. 69 pp. 165413
- [99] P Colinet and A Nepomnyashchy. *Pattern Formation at Interfaces*. Springer (2010) pp. 304
- [100] M Cross and H Greenside. *Pattern formation and dynamics in nonequilibrium systems*. Cambridge University Press (2009) pp. 535
- [101] ME Gurtin. *Thermomechanics of evolving phase boundaries in the plane*. Oxford University Press (1993) pp. 148
- [102] Eaglesham et al. *Limiting thickness HEPI for epitaxial-growth and room-temperature Si growth on Si(100)*. Phys. Rev. Lett. (1990) vol. 65 (10) pp. 1227-1230
- [103] H Eisenberg. *Formation, ripening, and stability of epitaxially strained island arrays*. Phys. Rev. B (2005) vol. 71 pp. 115423
- [104] RF Tinder. *Tensor properties of solids: phenomenological development of the tensor properties of crystals*. Morgan & Claypool Publishers (2008) pp. 236

- [105] Floro et al. *Real-time stress evolution during Si 1-x Ge x heteroepitaxy: dislocations, islanding, and segregation*. Journal of Electronic Materials (1997) vol. 26 (9) pp. 969-979
- [106] LB Freund. *A surface chemical potential for elastic solids*. J. Mech. Phys. Solids (1998) vol. 46 (10) pp. 1835-1844
- [107] L Freund. *Instability of a biaxially stressed thin film on a substrate due to material diffusion over its free surface*. J. Mech. Phys. Solids (1993) vol. 41 (7) pp. 1245-1264
- [108] DR Fridline and AF Bower. *Influence of anisotropic surface diffusivity on electromigration induced void migration and evolution*. J. Appl. Phys. (1999) vol. 85 (6) pp. 3168-3174
- [109] H Gao. *Some general properties of stress-driven surface evolution in a heteroepitaxial thin film structure*. J. Mech. Phys. Solids (1994) vol. 42 (5) pp. 741-772
- [110] H Gao. *A boundary perturbation analysis for elastic inclusions and interfaces*. International Journal of Solids and Structures (1991) vol. 28 (6) pp. 703-725
- [111] Guha et al. *Onset of incoherency and defect introduction in the initial-stages of molecular-beam epitaxial-growth of highly strained InxGa1-xAs on GaAs(100)*. Appl. Phys. Lett. (1990) vol. 57 (20) pp. 2110-2112
- [112] MR Gungor and D Maroudas. *Modeling of electromechanically-induced failure of passivated metallic thin films used in device interconnections*. Int. J. Frac. (2001) vol. 109 (1) pp. 47-68
- [113] M Hanbücken and JP Deville. *Stress and strain in epitaxy: theoretical concepts, measurements, and applications*. Elsevier (2001) pp. 322
- [114] C Herring. in *The Physics of Powder Metallurgy*, edited by W. E. Kinston McGraw-Hill, New York, (1951) p. 147
- [115] Z Huang and K Elder. *Mesosopic and Microscopic Modeling of Island Formation in Strained Film Epitaxy*. Phys. Rev. Lett. (2008) vol. 101 (15) pp. 158701
- [116] H Ibach. *Physics of surfaces and interfaces*. Springer (2006) pp. 646
- [117] K Kondepudi and I Prigogine. *Modern thermodynamics: from heat engines to dissipative structures*. John Wiley (1998) pp. 486
- [118] J Kallunki and J Krug. *Competing mechanisms for step meandering in unstable growth*. Phys. Rev. B (2002) vol. 65 pp. 205411
- [119] Kim et al. *Three-stage nucleation and growth of Ge self-assembled quantum dots grown on partially relaxed SiGe buffer layers*. Phys. Rev. B (2003) vol. 68 (20) pp. 205312
- [120] Kraft et al. *Shape changes of voids in bamboo lines - a new electromigration failure-mechanism*. Qual. Reliab. Eng. Int. (1995) vol. 11 (4) pp. 279-283
- [121] M Krishnamurthy and J Drucker. *Microstructural evolution during the heteroepitaxy of Ge on vicinal Si (100)*. J. Appl. Phys. (2009) vol.69 (9) pp. 6461-6471

- [122] D Leonard and M Krishnamurthy. *Direct formation of quantum sized dots from uniform coherent islands of InGaAs on GaAs surfaces*. J. Appl. Phys. (2009) vol. 63 (23) pp. 3203-3205
- [123] P Liu and Y Zhang. *Coarsening kinetics of heteroepitaxial islands in nucleationless Stranski-Krastanov growth*. Phys. Rev. B (2003) vol. 68 (3) pp. 035402
- [124] Hans Lüth. *Solid Surfaces, Interfaces and Thin Films*. Springer (2010) pp. 577
- [125] J J Métois, A Saúl and P Müller. *Measuring the surface stress polar dependence*. Nature Materials (2005) vol. 4 (3) pp. 238-242
- [126] Misbah et al. *Crystal surfaces in and out of equilibrium: A modern view*. Rev. Mod. Phys. (2010) vol. 82 (1) pp. 981-1040
- [127] P Mulheran and M Basham. *Kinetic phase diagram for island nucleation and growth during homoepitaxy*. Phys. Rev. B (2008) vol. 77 (7) pp. 075427
- [128] WW Mullins. *Theory of thermal grooving*. J. Appl. Phys. (2009) vol. 28 (3) pp. 333-339
- [129] Nathan et al. *Electromigration-induced surface evolution in bamboo lines with transgranular and intergranular edge voids*. Thin Solid Films (2004) vol. 466 (1-2) pp. 347-350
- [130] Ngo et al. *Simulation model for self-ordering of strained islands in molecular-beam epitaxy*. Phys. Rev. B (1996) vol. 53 (15) pp. 9618-9621
- [131] G Nicolis and I Prigogine. *Self-organization in nonequilibrium systems: from dissipative structures to order through fluctuations*. A Wiley-Interscience publication (1977) pp. 491
- [132] F Nita and A Pimpinelli. *When smoothing makes it rough: Unhindered step-edge diffusion and the meandering instability on metal surfaces*. Phys. Rev. Lett. (2005) vol. 95 (10) pp. 106104
- [133] TO Ogurtani, A Celik and EE Oren *Morphological evolution of edge-hillocks on single-crystal films having anisotropic drift-diffusion under the capillary and electromigration forces*. Thin Solid Films (2007) vol. 515 (5) pp. 2974-2983
- [134] TO Ogurtani. *Mesosopic nonequilibrium thermodynamics of solid surfaces and interfaces with triple junction singularities under the capillary and electromigration forces in addition to the diffusional anisotropy*. The Journal of chemical physics (2006) vol. 124 (14) pp. 144706
- [135] TO Ogurtani. *Unified theory of linear instability of anisotropic surfaces and interfaces under capillary, electrostatic, and elastostatic forces: The regrowth of epitaxial amorphous*. Phys. Rev. B (2006) vol. 74 (15) pp. 155422
- [136] TO Ogurtani. *Variational formulation of irreversible thermodynamics of surfaces and interfaces with grain-boundary triple-junction singularities under the capillary and electromigration forces in anisotropic two-dimensional space*. Phys. Rev. B (2006) vol. 73 (23) pp. 235408

- [137] TO Ogurtani. *Thermal grain-boundary grooving in bicrystal thin solid films having strong anisotropic surface Gibbs free energy represented by the modified cycloid-curtate function*. Journal of Crystal Growth (2009) vol. 311 pp. 1584-1593
- [138] TO Ogurtani and O Akyildiz. *Morphological evolution of tilted grain-boundary thermal grooving by surface diffusion in bicrystal thin solid films having strong anisotropic surface Gibbs free energies*. J. Appl. Phys. (2009) vol. 104 (1) pp. 013518
- [139] TO Ogurtani. *The orientation dependent electromigration induced healing on the surface cracks and roughness caused by the uniaxial compressive stresses in single crystal*. J. Appl. Phys. (2009) vol. 106 (5) pp. 053503
- [140] TO Ogurtani, A Celik and EE Oren *Generic role of the anisotropic surface free energy on the morphological evolution in a strained-heteroepitaxial solid droplet on a rigid substrate*. J. Appl. Phys. (2010) vol. 108 (10) pp. 103516
- [141] TO Ogurtani, A Celik and EE Oren *Morphological evolution in a strained-heteroepitaxial solid droplet on a rigid substrate: Dynamical simulations*. J. Appl. Phys. (2010) vol. 108 (6) pp. 063527
- [142] TO Ogurtani. *Irreversible thermodynamics of triple junctions during the intergranular void motion under the electromigration forces*. International Journal of Solids and Structures (2005) vol. 42 (13) pp. 3918-3952
- [143] L Onsager. *Reciprocal Relations in Irreversible Processes. I*. Physical Review (1931) vol. 37 pp. 405
- [144] C Ozkan and W Nix. *Strain relaxation and defect formation in heteroepitaxial SiGe films via surface roughening induced by controlled annealing experiments*. Appl. Phys. Lett. (1997) vol. 70 (17) pp. 2247
- [145] J Pan. *A numerical technique for the analysis of coupled surface and grain-boundary diffusion*. Acta. Metall. Mater. (1995) vol. 43 (4) pp. 1395-1406
- [146] Y Pang and R Huang. *Nonlinear effect of stress and wetting on surface evolution of epitaxial thin films*. Phys. Rev. B (2006) vol. 74 (7) pp. 075413
- [147] P Peyla and A Vallat and C Misbah. *Elastic interaction between defects on a surface*. Journal of Crystal Growth (1999) vol. 201-202 (1) pp. 97 - 100
- [148] P Peyla and A Vallat and C Misbah. *Elastic interaction between surface defects in thin layers*. Phys. Rev. Lett. (1999) vol. 82 (4) pp. 787-790
- [149] Prieto et al. *A structural analysis of the Co(0001) surface and the early stages of the epitaxial growth of Cu on it*. Surf. Sci. (1998) vol. 401 (2) pp. 248-260
- [150] A Ramasubramaniam. *On the evolution of faceted grain-boundary grooves by surface diffusion*. Acta materialia (2005) vol. 53 (10) pp. 2943-2956
- [151] JR Rice. *Energy changes in stressed bodies due to void and crack growth*. International Journal of Fracture (1967) vol. 3 (1) pp. 19-27
- [152] JR Rice, TJ Chuang. *Energy variations in diffusive cavity growth*. Journal Of The American Ceramic Society (1981) vol. 64 (1) pp. 46-53

- [153] VB Shenoy and LB Freund. *A continuum description of the energetics and evolution of stepped surfaces in strained nanostructures*. J. Mech. Phys. Solids (2002) vol. 50 (9) pp. 1817-1841
- [154] Shilkrot et al. *Morphology evolution during the growth of strained-layer superlattices*. Phys. Rev. B (2000) vol. 62 (12) pp. 8397-8409
- [155] Signor et al. *Misfit-dislocation-mediated heteroepitaxial island diffusion*. Surface Science (2010) vol. 604 (21-22) pp. L67-L70
- [156] Snyder et al. *Effect of strain on surface morphology in highly strained InGaAs films*. Phys. Rev. Lett. (1991) vol. 66 (23) pp. 3032
- [157] B Spencer and S Davis. *Morphological instability in epitaxially strained dislocation-free solid films: Nonlinear evolution*. Phys. Rev. B (1993) vol. 47 (15) pp. 47
- [158] BJ Spencer and J Tersoff. *Equilibrium shapes and properties of epitaxially strained islands*. Phys. Rev. Lett. (1997) vol. 79 (24) pp. 4858-4861
- [159] BJ Spencer. *Asymptotic derivation of the glued-wetting-layer model and contact-angle condition for Stranski-Krastanow islands*. Phys. Rev. B (1999) vol. 59 (3) pp. 2011-2017
- [160] BJ Spencer and J Tersoff. *Asymmetry and shape transitions of epitaxially strained islands on vicinal surfaces*. Appl. Phys. Lett. (2010) vol. 96 (7) pp. 073114
- [161] DJ Srolovitz and SA Safran. *Capillary instabilities in thin-films .I. energetics*. J. Appl. Phys. (1986) vol. 60 (1) pp. 247-254
- [162] Switzer et al. *Electrochemical self-assembly of copper/cuprous oxide layered nanostructures*. J. Am. Chem. Soc (1998) vol. 120 (14) pp. 3530-3531
- [163] WT Tekalign and BJ Spencer. *Evolution equation for a thin epitaxial film on a deformable substrate*. J. Appl. Phys. (2009) vol. 96 (10) pp. 5505-5512
- [164] WT Tekalign and BJ Spencer. *Thin-film evolution equation for a strained solid film on a deformable substrate: Numerical steady states*. J. Appl. Phys. (2009) vol. 102 (7) pp. 073503
- [165] R Tromp and F Ross. *Instability-driven SiGe island growth*. Phys. Rev. Lett. (2000) vol. 84 (20) pp. 4641
- [166] Van Hecke et al. *Amplitude equations for pattern forming systems*. Fundamental Problems in Statistical Mechanics VIII, North-Holland, Amsterdam (1994)
- [167] Wang et al. *Time resolved optical characterization of InGaAs/GaAs quantum dots*. Appl. Phys. Lett. (2009) vol. 94 (21) pp. 2815-2817
- [168] W Wang. *Shape change of a pore in a stressed solid via surface diffusion motivated by surface and elastic energy variation*. J. Mech. Phys. Solids (1997) vol. 45 (5) pp. 709-729
- [169] YW Zhang. *Formation of epitaxially strained islands by controlled annealing*. Appl. Phys. Lett. (2009) vol. 94 (2) pp. 205-207
- [170] YW Zhang. *Numerical simulations of island formation in a coherent strained epitaxial thin film system*. J. Mech. Phys. Solids (1999) vol. 47 pp. 2273-2297

APPENDIX A

PROGRAM CODE

C++ code of thin film simulation

```
1 #include <stdlib.h>
2 #include <iostream>
3 #include <fstream>
4 #include <math.h>
5 #include <stdio.h>
6 #include <time.h>
7 #include <iomanip>
8 #include <string>
9 #include <dirent.h>
10 #include <sys/types.h>
11 #include <fcntl.h>
12 #include <unistd.h>
13 #include <process.h>
14 #include <windows.h>
15
16 #ifndef NULL
17 #define NULL '\0'
18 #endif
19
20 #include <stdio.h>
21 #ifndef __MSDOS__ // if we are not MS - DOS
22 #define __UNIX__ // then we are UNIX */
23 #endif __MSDOS__
24
25 #include <stdlib.h> /* ANSI Standard C file */
26
27 #ifdef __UNIX__
28 #include <sys/types.h> /* file defines for UNIX filesystem */
29 #include <sys/stat.h>
30 #include <fcntl.h>
31 #endif __UNIX__
32
33 #ifdef __MSDOS__
34 #include <fcntl.h> /* file defines for DOS filesystem */
35 #include <sys\stat.h>
36 #include <io.h>
37 #endif __MSDOS__
38
39 #ifdef __UNIX__
40 #define mkdir ( x ) mkdir ( ( x ) , 0755 )
41 #endif
42
43 #if defined ( __unix_ ) && defined ( __GNUC_ )
44
45 #endif
46
47 #define NMAX 2000
48 #define NRHMAX 1
49 const int lda = NMAX * 2, ldb = 2 * NMAX;
50 int info, n, nrhs = 1 /* means 1 dimention */;
51 double ibemMat [NMAX * NMAX * 4] , mu [NMAX * NRHMAX * 2] , ibemMat [NMAX * NMAX * 4] , muu←
52 [NMAX * NRHMAX * 2] ;
53 double ftt [NMAX * NMAX * 4] , tr [NMAX * NRHMAX * 2] , uuD [NMAX * NMAX * 4] , intMat [NMAX←
54 * NMAX * 4] ;
55 int ipiv [NMAX] , WORK [NMAX * NMAX * 4] ;
```

```

57 /* These macros allow access to 1 - d arrays as though
59 they are 2 - d arrays stored in column - major order,
as required by ACML C routines. */
61 #define A ( I, J ) ibemMat [ ( J ) * lda + ( I ) ]
#define B ( I, J ) mu [ ( J ) * lda + ( I ) ]
63 #define darray ( a, I, J ) a [ ( J ) * lda + ( I ) ]
#define Matdist ( a, i, j, k ) a [ ( 3 * j + k ) * lda + i ]
65
66 /* ***** */
67 /*
* Macros
*/
69 /* ***** */
71
72 #define E 1
73 #define nu 0.3
#define G E / ( 2 + 2 * nu )
75 #define pi 3.1415926535897932384626433832795
#define sqr ( x ) ( ( x ) * ( x ) )
77 #define cube ( x ) ( ( x ) * ( x ) * ( x ) )
#define minP ( a, b ) ( a < b ) ? a : ( b++ )
79 #define maxP ( a, b ) ( a > b ) ? a : ( b++ )
#define minR ( a, b ) ( a < b ) ? a : b
81 #define magnitude ( a ) sqrt ( ( a ) [ 0 ] * ( a ) [ 0 ] + ( a ) [ 1 ] * ( a ) [ 1 ] +
( a ) [ 2 ] * ( a ) [ 2 ] )
#define sqr_mag ( a ) ( ( a ) [ 0 ] * ( a ) [ 0 ] + ( a ) [ 1 ] * ( a ) [ 1 ] + ( a )
) [ 2 ] * ( a ) [ 2 ] )
83 #define dotPro ( a, b ) ( ( a ) [ 0 ] * ( b ) [ 0 ] + ( a ) [ 1 ] * ( b ) [ 1 ] + ( a )
) [ 2 ] * ( b ) [ 2 ] )
#define angle ( a, b ) ( dotPro ( a, b ) <= 0 ) ? ( pi - ( asin ( ( ( a ) [ 0 ] *
( b ) [ 1 ] - ( a ) [ 1 ] * ( b ) [ 0 ] ) / ( magnitude ( a ) * magnitude ( b ) ) )
) ) : ( asin ( ( ( a ) [ 0 ] * ( b ) [ 1 ] - ( a ) [ 1 ] * ( b ) [ 0 ]
) / ( magnitude ( a ) * magnitude ( b ) ) ) ) )
85 #define C0 ( 1 / ( 8 * pi * G * ( 1 - nu ) ) )
#define C1 ( 3 - 4 * nu )
87 #define C2 ( 1 / ( 4 * pi * ( 1 - nu ) ) )
#define C3 ( 1 - 2 * nu )
89 #define C ( 1 / ( 8 * pi * G * ( 1 - nu ) ) )
#define ex ( 1 - nu * nu )
91
92 #define uu ( rc ) { \
tempDouble [ 0 ] = magnitude ( rc ) ; \
95 tempDouble [ 1 ] = rc [ 0 ] / tempDouble [ 0 ] ; \
tempDouble [ 2 ] = rc [ 1 ] / tempDouble [ 0 ] ; \
97 tempDouble [ 3 ] = - 1 * C1 * SPEEDlog ( tempDouble [ 0 ] ) ; \
us [ 0][ 0 ] = C * ( tempDouble [ 3 ] + sqrt ( tempDouble [ 1 ] ) ) ; \
99 us [ 1][ 1 ] = C * ( tempDouble [ 3 ] + sqrt ( tempDouble [ 2 ] ) ) ; \
us [ 0][ 1 ] = C * ( tempDouble [ 1 ] * tempDouble [ 2 ] ) ; \
101 us [ 1][ 0 ] = us [ 0][ 1 ] ; \
103 #define TTSS ( rc, noc ) { \
tempDouble [ 0 ] = sqr_mag ( rc ) ; \
105 tempDouble [ 1 ] = magnitude ( rc ) ; \
tempDouble [ 2 ] = - 1 * ( dotPro ( rc, noc ) ) ; \
107 ts [ 0][ 0 ] = ( C3 + 2 * sqrt ( rc [ 0 ] ) / tempDouble [ 0 ] ) * tempDouble [ 2 ] /
tempDouble [ 0 ] ; \
ts [ 1][ 1 ] = ( C3 + 2 * sqrt ( rc [ 1 ] ) / tempDouble [ 0 ] ) * tempDouble [ 2 ] /
tempDouble [ 0 ] ; \
109 ts [ 0][ 1 ] = 2 * rc [ 0 ] * rc [ 1 ] * tempDouble [ 2 ] / sqrt ( tempDouble [ 0 ] ) ; \
ts [ 1][ 0 ] = ts [ 0][ 1 ] ; \
111 ta [ 0][ 1 ] = C3 * ( rc [ 0 ] * noc [ 1 ] - rc [ 1 ] * noc [ 0 ] ) / tempDouble [ 0 ] ; \
ta [ 1][ 0 ] = - ta [ 0][ 1 ] ; \
113 ta [ 1][ 1 ] = 0 ; \
ta [ 0][ 0 ] = 0 ; \
115 tt [ 0][ 0 ] = ( ts [ 0][ 0 ] + ta [ 0][ 0 ] ) * C2 ; \
tt [ 0][ 1 ] = ( ts [ 1][ 0 ] + ta [ 1][ 0 ] ) * C2 ; \
117 tt [ 1][ 0 ] = ( ts [ 0][ 1 ] + ta [ 0][ 1 ] ) * C2 ; \
tt [ 1][ 1 ] = ( ts [ 1][ 1 ] + ta [ 1][ 1 ] ) * C2 ; \
119 #define SSc ( rc ) { \
121 tempDouble [ 0 ] = magnitude ( rc ) ; \
rx = rc [ 0 ] / tempDouble [ 0 ] ; \
123 ry = rc [ 1 ] / tempDouble [ 0 ] ; \
tempDouble [ 0 ] = C2 / tempDouble [ 0 ] ; \
125 ss [ 0][ 0 ] = ( C3 * rx + 2 * cube ( rx ) ) * tempDouble [ 0 ] ; \
ss [ 0][ 1 ] = ( - C3 * ry + 2 * sqrt ( rx ) * ry ) * tempDouble [ 0 ] ; \

```

```

127 ss [1][0] = ( - C3 * rx + 2 * sqr ( ry ) * rx ) * tempDouble [0] ; \
ss [1][1] = ( C3 * ry + 2 * cube ( ry ) ) * tempDouble [0] ; \
129 ss [2][0] = ( C3 * ry + 2 * sqr ( rx ) * ry ) * tempDouble [0] ; \
ss [2][1] = ( C3 * rx + 2 * sqr ( ry ) * rx ) * tempDouble [0] ; \
131
132 /***** ***** */
133 /*
134  * Constants and variables
135  */
136 /***** ***** */
137
138 using namespace std;
139
140 ofstream out;
141 ifstream in;
142
143 typedef double Number;
144 typedef Number vect3 [3] ;
145 typedef Number vectn [NMAX] ;
146 typedef vect3 vectn3 [NMAX] ;
147 typedef vect3 matrix3 [3] ;
148 typedef Number matrix4 [NMAX][NMAX] ;
149
150 int tryme = 0, PRINT = 0, PrintName = 0, FINE = 1, voidBool, calcUpper, calcLower, ←
calcSides, remeshbool = 1, voidFound = 0, expState = 0, R, calcJumpBool = - 1, ←
sinwave = 0, periodic = 0, gibbsType = 0;
153
154 static int
155 numCathodeNodes, sideDivNum, numAnodeNodes, numSurfCentStack,
numVoidCentStack, calcJump = 50, calcR = 5000, i, j, k, m, l, ii, jj,
157 mm, ll, textNum, startNode, finishNode, integSegmentNumSt, ki, kj,
kk, numMatrix, newdata, control, initialLoopNum, dataRecNum,
159 numLoopNum, integSegmentNum, integSegmentNumStt, pertStartNode,
pertEndNode, stripDivNum, pertDivNum, foldSymNum, upperDivNum,
161 lowerDivNum, numUpperNodes, numLowerNodes, numVoidNodes,
numNodeStack, numCentStack, H, numLowerCent, numVoidCent,
163 numUpperCent, turnPoint [5] , tempInt [10] , remBool [600] , tStep = 1,
lastOutNum = 0, Msin, nsw, voidDivNum, numContData = 0, TYPE, intM, initialNodeNum ;
165
166 static int pertType;
167 static Number
168
169 nnn, dummy, interLength, interWidth, pertHeight, vMin, vMax, del_M,
phi, Mobility, fhi, chi, realTime, anisotIntensity, texTiltAngle,
171 bulkMobility, voidMobility, del_T, mpow = 1, tempv = 10000, vMaxx, minima = 0,
bulkGibbsEnergy, * apr, minSegLength, maxSegLength, scaleFactor,
173 tempDouble [10] , Loader [10][3] , timeStepCorrect = 1, maxSegLengthr,
minSegLengthr, rcos, rcms, eta, surfKntxT, voidKntxT, eps_T, insVoidArea,
175 initVoidArea, txtTilt, tempD, Bsurf, maxSegLengthhi, minSegLengthhi,
equilVel = 0.00001, normTime = 0, chiE, chiQ, vAvg, Asurf, epsTime, Wn, Beta,
177 Ln, LLamda, GammaSubstrate = 0, delAlpha, GammaFilm = 0, deltaW,
Amp, LamdaU = 10, Lamda, kv, scaleL, scaleW, gibbsBsurf, Sigma, Xi, eps,
179 delTime, delMean, powerT, MaxpowerGav = 0, Maxpowerav = 0, Maxpower,
Minpower, MaxpowerG, MinpowerG, voidX, voidY, ro, vsI, voidE, voidShape,
181 voidRadius, poisson, alfaI, maxY, minY, insAmp, eps_Ttemp, endTime = 100,
tempChi, kappaAv;
183
184 static vect3 anx = {1, 0, 0}, normKappa, rcij, surfKntx, voidKntx, voidCenter;
185 static vectn segLength, difTheta, difMag, surfEnergy, thetaAtNode, normEF,
alpha, kappa, ekap, trio, fieldI, fieldII, fieldT, fieldTII, fieldTI, fieldTN,
187 nodeVel, ddd, TN, fSigma, UB, epsc, qTarik, energy, traXS, gibbsGamma, gibbsGammaS,
gibbsGammaGamma, hoop, Trsig, sighoop, sigTrsig, tempSYS, WU, WUU;
189
190 static vectn3 anodeNodes, cathodeNodes, asig, asigXY, var, centers,
191 stackVector, del_R, upperNodes, lowerNodes, voidNodes, centStack, centNormal,
localLineNorm, tempVect, tempVectNew, trac, del_C, ubXS, traa, periodicNodes;
193
194 static matrix3 antiRot;
195 static matrix4 del_U, fttp;
196
197 static vect3 juu = {0, 1, 0}, iuu = {1, 0, 0};
198
199 typedef Number vect2x2 [3][3] ;
vect2x2 temp2x2, ttss, uuss, us, ts, ta, tt, ss;
201
202 Number rx, ry, sigx;
203

```

```

string textName, dirName, outName, PIDname, comand;
205 time_t rawtime;

207 DIR * dir_p;
FILE * fp;
209 char line [256] = "";
211 int mkdir ( const char * pathname, mode_t mode ) ;
213 double dclock ( void ) ;

215 /***** ***** */
/*
217 * Structure for remeshing and void creation
*/
219 /***** ***** */

221 typedef struct Node
223 {
Number radius ;
225 Number kappa ;
Number power;
227 Number powerG;
int boolr;
229 int rem ;
Number segLength;
231 Number segLengthF;
Number segLengthB;
233 Number Point [2] ;
Number Center [2] , CenterNorm [2] ;
235 int immortal ;
int periodic ;
237 int pro ;

239 struct Node * back, * forward;

241 void calcPoint ()
{
243 if ( ( * back ) .radius != 0 ) {

245 ( * this ) .Point [0] = ( ( * back ) .Center [0] + ( * back ) .radius * ( * ←
back ) .CenterNorm [0] ) ;
( * this ) .Point [1] = ( ( * back ) .Center [1] + ( * back ) .radius * ( * ←
back ) .CenterNorm [1] ) ;

247
249 if ( ( * forward ) .radius != 0 ) {

( * this ) .Point [0] = ( ( ( * back ) .Center [0] + ( * back ) .radius * ( ←
* back ) .CenterNorm [0] )
251 + ( ( * forward ) .Center [0] + ( * forward ) .radius * ( * back ) .CenterNorm ←
[0] ) ) * 0.5 ;
( * this ) .Point [1] = ( ( ( * back ) .Center [1] + ( * back ) .radius * ( ←
* back ) .CenterNorm [1] )
253 + ( ( * forward ) .Center [1] + ( * forward ) .radius * ( * back ) .CenterNorm ←
[1] ) ) * 0.5 ;

255 }

257 } else if ( ( * forward ) .radius != 0 ) {

259 ( * this ) .Point [0] = ( ( * forward ) .Center [0] + ( * forward ) .radius * ←
( * back ) .CenterNorm [0] ) ;
( * this ) .Point [1] = ( ( * forward ) .Center [1] + ( * forward ) .radius * ←
( * back ) .CenterNorm [1] ) ;

261 }
else {
263 ( * this ) .Point [0] = ( ( * back ) .Point [0] + ( * forward ) .Point [0] ) * ←
0.5;
( * this ) .Point [1] = ( ( * back ) .Point [1] + ( * forward ) .Point [1] ) * ←
0.5;

265 }

267 ( * this ) .immortal = 0;
};

269 void calcPointn ()
271 {
( * this ) .Point [0] = ( ( * back ) .Point [0] + ( * forward ) .Point [0] ) * ←

```

```

273     0.5;
    ( * this ) .Point [1] = ( ( * back ) .Point [1] + ( * forward ) .Point [1] ) * ←
    0.5;
    ( * this ) .immortal = 0;
275 };

277 void calcSegLength ()
    {
279     tempVect [0][0] = ( ( * forward ) .Point [0] - ( * this ) .Point [0] ) ;
    tempVect [0][1] = ( ( * forward ) .Point [1] - ( * this ) .Point [1] ) ;
281     segLength = magnitude ( tempVect [0] ) ;
    segLengthF = segLength;
283
    tempVect [0][0] = ( ( * back ) .Point [0] - ( * this ) .Point [0] ) ;
285     tempVect [0][1] = ( ( * back ) .Point [1] - ( * this ) .Point [1] ) ;
    segLengthB = magnitude ( tempVect [0] ) ;
287
    };
289
    Number calcDistance ( struct Node * n ) {
291     tempVect [0][0] = ( ( * n ) .Point [0] - ( * this ) .Point [0] ) ;
    tempVect [0][1] = ( ( * n ) .Point [1] - ( * this ) .Point [1] ) ;
293     return magnitude ( tempVect [0] ) ;
    };
295
    void addNode ( struct Node * p )
297     {
    ( * p ) .back = this;
299     ( * p ) .forward = ( * this ) .forward;
    ( * ( ( * p ) .forward ) ) .back = p;
301     ( * this ) .forward = p;
    ( * p ) .CenterNorm [0] = ( * this ) .CenterNorm [0] ;
303     ( * p ) .CenterNorm [1] = ( * this ) .CenterNorm [1] ;
    ( * p ) .Center [0] = ( * this ) .Center [0] ;
305     ( * p ) .Center [1] = ( * this ) .Center [1] ;
    ( * p ) .radius = ( * this ) .radius ;
307
    ( * p ) .calcPoint () ;
309     ( * p ) .calcSegLength () ;
    ( * ( * p ) .back ) .calcSegLength () ;
311 };

313 void addNoden ( struct Node * p )
    {
315     ( * p ) .back = this;
    ( * p ) .forward = ( * this ) .forward;
317     ( * ( ( * p ) .forward ) ) .back = p;
    ( * this ) .forward = p;
319
    ( * p ) .calcPointn () ;
321     ( * p ) .calcSegLength () ;
    ( * ( * p ) .back ) .calcSegLength () ;
323 };

325 void addBack ( struct Node * p )
    {
327     ( * p ) .forward = this;
    ( * p ) .back = ( * this ) .back;
329     ( * ( ( * p ) .back ) ) .forward = p;
    ( * this ) .back = p;
331
    ( * p ) .calcPoint () ;
333     ( * p ) .calcSegLength () ;
    ( * ( * p ) .back ) .calcSegLength () ;
335 };

337 struct Node * nodeShift ( int i ) {
    if ( i<0 ) return ( * ( nodeShift ( i + 1 ) ) ) .back;
339     if ( i>0 ) return ( * ( nodeShift ( i - 1 ) ) ) .forward;
    if ( i == 0 ) return this;
341 };

343 void remNode () {
    if ( !immortal ) {
345     ( * ( ( * this ) .forward ) ) .Point [0] = ( * this ) .Center [0] ;
    ( * ( ( * this ) .forward ) ) .Point [1] = ( * this ) .Center [1] ;
347
    ( * back ) .forward = ( * this ) .forward;
349     ( * ( * this ) .back ) .calcSegLength () ;

```

```

351     ( * forward ) .back = ( * this ) .back;
352 }
353 };
354 } Node_type;
355
356 /******
357  * CPU and OS parameters
358 */
359 /******
360
361 #define LINUX 0
362 #define BITS 32
363
364
365 #if ( LINUX == 1 )
366 #define mkdir ( x ) mkdir ( ( x ) , 0755 )
367 #else
368 #define mkdir ( x ) mkdir ( ( x ) )
369 #endif
370
371 #if ( BITS == 64 )
372 #include <acml.h>
373 #include <acml_mv.h>
374 #define SPEEDsin(x) fastsin ( x )
375 #define SPEEDcos(x) fastcos ( x )
376 #define SPEEDlog(x) fastlog ( x )
377
378 #else
379 #define SPEEDsin( x ) sin( x )
380 #define SPEEDcos( x ) cos( x )
381 #define SPEEDlog( x ) log( x )
382 #endif
383
384 /******
385  * Creation of experiment folder and priority procedures
386 */
387 /******
388
389 string convert ( char * buffer , int decimal , int sign , int precision ) {
390 string out;
391 if ( decimal<0 ) {
392     if ( sign ) out = " - " ;
393     out += ".";
394     for ( k = decimal; k<decimal + precision; k++ ) {
395         if ( k<0 ) out += "0" ;
396         else out += buffer [k] ;
397     }
398 }
399 else {
400     if ( sign ) out = " - " ;
401     for ( k = 0; k<precision; k++ ) {
402         if ( k == decimal ) k = precision ;
403         else out += buffer [k] ;
404     }
405 }
406 return out;
407 }
408
409 void print_elapsed_time ()
410 {
411     double elapsed ;
412     double resolution ;
413
414     // Obtain and display elapsed execution time
415     elapsed = ( double ) clock () / CLK.TCK ;
416     resolution = 1.0 / CLK.TCK ;
417
418     printf ( "Elapsed time: %8.4f sec ( %6.4f sec resolution ) \n" ,
419             elapsed , resolution ) ;
420 }
421
422 void priorityDeamon ()
423 {
424     int decimal , sign;
425     char * buffer;

```

```

429 int precision = 5;
printf ( "Process id: %d\n", _getpid () );
431 // DWORD MainThreadId = GetCurrentThreadId ();
// SetThreadPriority ( GetCurrentThread () , THREAD_PRIORITY_ABOVE_NORMAL );
433 comand = "process - p ";
buffer = _ecvt ( _getpid () , precision , &decimal , &sign );
435 PIDname = convert ( buffer , decimal , sign , precision );
comand += PIDname ;
437 comand += " AboveNormal" ;//BelowNormal
system ( comand.c_str () );
439 system ( "cls" );
}
441
442 void afinityDeamon ( int argc , char * argv [] )
443 {
444     int decimal , sign;
445     char * buffer;
446     int precision = 5;
447
448     printf ( "Process id: %d\n", _getpid () );
449     DWORD MainThreadId = GetCurrentThreadId ();
450     SetThreadPriority ( GetCurrentThread () , THREAD_PRIORITY_ABOVE_NORMAL );
451     if ( argc == 2 ) {
452         comand = "process - a ";
453         comand += PIDname;
454         comand += " " + ( string ) argv [1] ;
455         system ( comand.c_str () );
456     }
457     system ( "cls" );
458 }
459
460 void int2str ( int i ) {
461     char index [10][2] = {"0", "1", "2", "3", "4", "5", "6", "7", "8", "9"};
462     textName = ( string ) index [i/100];
463     i -= ( i/100 ) * 100;
464     textName += ( string ) index [i/10];
465     i -= ( i/10 ) * 10;
466     textName += ( string ) index [i];
467     textName += ".txt";
468 }
469
470
471
472 void directoryName () {
473
474     char index [10][2] = {"0", "1", "2", "3", "4", "5", "6", "7", "8", "9"};
475
476     dir_p = opendir ( textName.c_str () );
477     int dirPar ;
478     i = 1;
479     j = 0;
480     while ( j == 0 ) {
481         dirPar = i;
482         if ( sinwave == 1 ) dirName = "./SinWave" ;
483         else if ( pertType == 0 ) dirName = "./Line";
484         else if ( pertType == 1 ) dirName = "./Hillock";
485         else if ( pertType == -1 ) dirName = "./EdgeVoid" ;
486         if ( voidBool == 1 ) dirName += " + InnerVoid" ;
487         dirName += " - " ;
488
489         dirName += ( string ) index [dirPar/100] ;
490         dirPar -= ( dirPar/100 ) * 100;
491         dirName += ( string ) index [dirPar/10] ;
492         dirPar -= ( dirPar/10 ) * 10;
493         dirName += ( string ) index [dirPar] ;
494         dirName += "/";
495         dir_p = opendir ( dirName.c_str () );
496         if ( dir_p == NULL ) {
497             mkdir ( dirName.c_str () );
498             j = 1;
499         }
500         else i++;
501     }
502 }
503
504
505
506 /* ***** */
507 /*

```

```

509  * Usefull procedures
510  */
511  /***** *****/
512  void createAntiRotMat ( Number * w ) {
513  antiRot [0][0] = SPEEDcos ( w [0] );
514  antiRot [0][1] = - SPEEDsin ( w [0] );
515  antiRot [0][2] = 0.0;
516  antiRot [1][0] = - antiRot [0][1] ;
517  antiRot [1][1] = antiRot [0][0] ;
518  antiRot [1][2] = 0.0;
519  antiRot [2][0] = 0.0;
520  antiRot [2][1] = 0.0;
521  antiRot [2][2] = 1.0;
522  }

523  void extremumAtSurf () {
524  tempDouble [0] = stackVector [0][1] ;
525  tempInt [0] = 0;
526  for ( i = 0; i < numUpperNodes ; i++ ) {
527  if ( pertType == 1 ) {
528  if ( stackVector [i][1] > tempDouble [0] ) {
529  tempDouble [0] = stackVector [i][1] ;
530  tempInt [0] = i;
531  }
532  }
533  if ( pertType == - 1 ) {
534  if ( stackVector [i][1] < tempDouble [0] ) {
535  tempDouble [0] = stackVector [i][1] ;
536  tempInt [0] = i;
537  }
538  }
539  }
540  }

541  void calcVoidCenter () {
542  voidCenter [0] = 0;
543  voidCenter [1] = 0;
544  voidCenter [2] = 0;
545  tempInt [0] = numUpperNodes + numLowerNodes;
546  for ( i = 0; i < numVoidNodes; i++ ) {
547  voidCenter [0] += stackVector [i + tempInt [0] ][0] ;
548  voidCenter [1] += stackVector [i + tempInt [0] ][1] ;
549  }
550  voidCenter [0] /= Number ( numVoidNodes ) ;
551  voidCenter [1] /= Number ( numVoidNodes ) ;
552  voidCenter [2] /= Number ( numVoidNodes ) ;
553  }

554  inline void vectorpro ( Number * a, Number * b ) {
555  tempVect [0][0] = a [1] * b [2] - a [2] * b [1] ;
556  tempVect [0][1] = - a [0] * b [2] + a [2] * b [0] ;
557  tempVect [0][2] = a [0] * b [1] - a [1] * b [0] ;
558  }

559  inline Number voidArea () {
560  tempDouble [0] = 0.0;
561  for ( i = 0; i < numVoidNodes - 1; i++ ) {
562  tempVect [0][0] = stackVector [i + turnPoint [3] ][0] - voidCenter [0] ;
563  tempVect [0][1] = stackVector [i + turnPoint [3] ][1] - voidCenter [1] ;
564  tempVect [1][0] = stackVector [turnPoint [3] + i + 1][0] - voidCenter [0] ;
565  tempVect [1][1] = stackVector [turnPoint [3] + i + 1][1] - voidCenter [1] ;
566  vectorpro ( tempVect [0] , tempVect [1] ) ;
567  tempDouble [0] += fabs ( tempVect [0][2] ) ;
568  }
569  tempVect [0][0] = stackVector [numVoidNodes + turnPoint [3] ][0] - voidCenter [0] ;
570  tempVect [0][1] = stackVector [numVoidNodes + turnPoint [3] ][1] - voidCenter [1] ;
571  tempVect [1][0] = stackVector [turnPoint [3] ][0] - voidCenter [0] ;
572  tempVect [1][1] = stackVector [turnPoint [3] ][1] - voidCenter [1] ;
573  vectorpro ( tempVect [0] , tempVect [1] ) ;
574  tempDouble [0] = ( tempDouble [0] + fabs ( tempVect [0][2] ) ) * 0.5;
575  }

576  return tempDouble [0] ;
577  }
578  /***** *****/

```

```

587 /*
588  * Write methods
589  */
590 /***** *****/
591 void printScreen ( vectn3 a, int b ) {
592     for ( i = 0; i<b; i++ )
593         cout << a [i][0] <<" "<< a [i][1] <<" " << a [i][2] << endl;
594 }
595
596 void printScreen ( vectn a, int b ) {
597     for ( i = 0; i<b; i++ ) cout << a [i] << endl;
598 }
599
600 void printFile ( vectn3 a, int b, string name ) {
601     out.open ( name.c_str () );
602     out << setiosflags ( ios::showpoint ) ;
603     for ( i = 0; i<b; i++ ) {
604         out << setprecision ( 20 ) << a [i][0] <<" "<< a [i][1] <<" " << a [i][2] << endl;
605         out.close () ;
606     }
607 }
608
609 void printFile ( Number * * a, int b, string name ) {
610     out.open ( name.c_str () );
611     out << setiosflags ( ios::showpoint ) ;
612     for ( i = 0; i<b; i++ ) {
613         for ( j = 0; j<b; j++ ) out << setprecision ( 20 ) << a [i][j] <<" " ;
614         out << endl;
615     }
616     out.close () ;
617 }
618
619 void printFile ( matrix4 a, int b, string name ) {
620     out.open ( name.c_str () );
621     out << setiosflags ( ios::showpoint ) ;
622     for ( i = 0; i<b; i++ ) {
623         for ( j = 0; j<b; j++ ) out << setprecision ( 20 ) << a [i][j] <<" " ;
624         out << endl;
625     }
626     out.close () ;
627 }
628
629 void printFile ( vectn a, int b, string name ) {
630     out.open ( name.c_str () );
631     for ( i = 0; i<b; i++ ) out << a [i] << endl;
632     out.close () ;
633 }
634
635 /***** *****/
636 /*
637  * Read input parameters
638  */
639 /***** *****/
640
641 void getInputPar () {
642     fp = fopen ( "input.txt", "r" ) ;
643
644     fgets ( line, sizeof ( line ), fp ) ;
645     sscanf ( line, "%Lg", &Wn ) ; //double
646     fgets ( line, sizeof ( line ), fp ) ;
647     sscanf ( line, "%Lg", &Beta ) ; //double
648     fgets ( line, sizeof ( line ), fp ) ;
649     sscanf ( line, "%d", &calcLower ) ; //int
650     fgets ( line, sizeof ( line ), fp ) ;
651     sscanf ( line, "%d", &upperDivNum ) ; //int
652     fgets ( line, sizeof ( line ), fp ) ;
653     sscanf ( line, "%d", &lowerDivNum ) ; //int
654     fgets ( line, sizeof ( line ), fp ) ;
655     sscanf ( line, "%d", &sideDivNum ) ; //double
656     //fgets ( line, sizeof ( line ), fp ) ;
657     fgets ( line, sizeof ( line ), fp ) ;
658     sscanf ( line, "%Lg", &delTime ) ; //double
659     fgets ( line, sizeof ( line ), fp ) ;
660     sscanf ( line, "%Lg", &epsTime ) ; //double
661     fgets ( line, sizeof ( line ), fp ) ;
662     sscanf ( line, "%d", &H ) ; //int
663     fgets ( line, sizeof ( line ), fp ) ;
664     sscanf ( line, "%Lg", &minSegLengthr ) ; //double
665     fgets ( line, sizeof ( line ), fp ) ;

```

```

sscanf ( line , "%Lg" , &maxSegLengthr ) ; //double
667 fgets ( line , sizeof ( line ) , fp ) ;
sscanf ( line , "%Lg" , &Amp ) ; //double
669 fgets ( line , sizeof ( line ) , fp ) ;
sscanf ( line , "%d" , &nsw ) ; //int
671 //fgets ( line , sizeof ( line ) , fp ) ;
fgets ( line , sizeof ( line ) , fp ) ;
673 sscanf ( line , "%Lg" , &poisson ) ; //double
fgets ( line , sizeof ( line ) , fp ) ;
675 sscanf ( line , "%Lg" , &alfal ) ; //double
fgets ( line , sizeof ( line ) , fp ) ;
677 sscanf ( line , "%d" , &foldSymNum ) ; //int
fgets ( line , sizeof ( line ) , fp ) ;
679 sscanf ( line , "%Lg" , &anisotIntensity ) ; //double
fgets ( line , sizeof ( line ) , fp ) ;
681 sscanf ( line , "%Lg" , &texTiltAngle ) ; //double
fgets ( line , sizeof ( line ) , fp ) ;
683 sscanf ( line , "%Lg" , &bulkMobility ) ; //double
fgets ( line , sizeof ( line ) , fp ) ;
685 sscanf ( line , "%Lg" , &bulkGibbsEnergy ) ; //double
fgets ( line , sizeof ( line ) , fp ) ;
687 sscanf ( line , "%d" , &gibbsType ) ; //int
fgets ( line , sizeof ( line ) , fp ) ;
689 sscanf ( line , "%Lg" , &gibbsBsurf ) ; //double
fgets ( line , sizeof ( line ) , fp ) ;
691 sscanf ( line , "%Lg" , &Bsurf ) ; //double
//fgets ( line , sizeof ( line ) , fp ) ;
693 fgets ( line , sizeof ( line ) , fp ) ;
sscanf ( line , "%d" , &integSegmentNum ) ; //int
695 fgets ( line , sizeof ( line ) , fp ) ;
sscanf ( line , "%d" , &integSegmentNumSt ) ; //int
697 fgets ( line , sizeof ( line ) , fp ) ;
sscanf ( line , "%d" , &integSegmentNumStt ) ; //int
699 fgets ( line , sizeof ( line ) , fp ) ;
sscanf ( line , "%Lg" , &chi ) ; //double
701 fgets ( line , sizeof ( line ) , fp ) ;
sscanf ( line , "%Lg" , &Xi ) ; //double
703 fgets ( line , sizeof ( line ) , fp ) ;
sscanf ( line , "%Lg" , &Sigma ) ; //double
705 fgets ( line , sizeof ( line ) , fp ) ;
sscanf ( line , "%Lg" , &GammaSubstrate ) ; //double
707 fgets ( line , sizeof ( line ) , fp ) ;
sscanf ( line , "%Lg" , &GammaFilm ) ; //double
709 fgets ( line , sizeof ( line ) , fp ) ;
sscanf ( line , "%Lg" , &deltaW ) ; //double
711 fgets ( line , sizeof ( line ) , fp ) ;
sscanf ( line , "%d" , &newdata ) ; //int
713 integSegmentNum++ ;
integSegmentNumSt++ ;
715 integSegmentNumStt++ ;
}
717
/***** *****/
719 /*
* Write input parameters to experiment folder
*/
/***** *****/
723
void writeInputParameters () {
725 outName = dirName + "input.txt" ;
fp = fopen ( outName.c_str () , "w" ) ;
727 fprintf ( fp , "%- 10Lg interconnect width - interWidth ( interconnect width ) \n" , Wn ) ←
;
fprintf ( fp , "%- 10Lg aspect ratio - beta \n" , Beta ) ;
729 fprintf ( fp , "%- 10d boolean for calculation of lower surface - ALT \n" , calcLower ) ;
fprintf ( fp , "%- 10d interconnect upper division number - upperDivNum \n" , upperDivNum )←
;
731 fprintf ( fp , "%- 10d interconnect lower division number - lowerDivNum \n" , lowerDivNum ) ←
;
fprintf ( fp , "%- 10d interconnect side division number - sideDivNum \n" , sideDivNum ) ;
733 fprintf ( fp , "%- 10Lg initial time interval - del_T \n" , delTime ) ;
fprintf ( fp , "%- 10Lg time step correction - eps_T \n" , epsTime ) ;
735 fprintf ( fp , "%- 10d Maximum H Loop Number - H \n" , H ) ;
fprintf ( fp , "%- 10Lg minimum segment length for remeshing - rmin SegLength \n" , ←
minSegLengthi ) ;
737 fprintf ( fp , "%- 10Lg maximum segment length for remeshing - rmax SegLength \n" , ←
maxSegLengthi ) ;
fprintf ( fp , "%- 10Lg sinewave amplitude - Amp \n" , Amp/scaleFactor ) ;
739 fprintf ( fp , "%- 10d number of sinewave - nsw \n" , nsw ) ;

```

```

741 fprintf ( fp, "% - 10Lg Poisson's ratio - poisson \n", poisson ) ;
fprintf ( fp, "% - 10Lg Wulff surface topography index - alfa ( bu programda curtate yok ←
dolayisiyla calismiyor ) \n", alfa ) ;
fprintf ( fp, "% - 10d diffusion anisotropy:0 for isotropic , 1 for 2 foldsym , 2 for 4 ←
foldsym , 3 for 6 foldsym - foldSymNum \n", foldSymNum ) ;
743 fprintf ( fp, "% - 10Lg diffusion anisotropy intensity - anisotIntensity \n", ←
anisotIntensity ) ;
fprintf ( fp, "% - 10Lg grain tilt angle to the applied electric field - texTiltAngle \n", ←
texTiltAngle/pi * 180 ) ;
745 fprintf ( fp, "% - 10Lg normalized bulk mobility coefficient - bulkMobility \n", ←
bulkMobility ) ;
fprintf ( fp, "% - 10Lg normalized bulk gibbs free energy - bulkGibbsEnergy \n", ←
bulkGibbsEnergy ) ;
747 fprintf ( fp, "% - 10d boolean for gibbs free surface energy calculation ( TOO = 0 , SHE ←
= 1 ) - gibbsType \n", gibbsType ) ;
fprintf ( fp, "% - 10Lg Gibbs Free Energy Anisotropy constant ( <1, <1/7 and <1/17 for 110←
( 1 ) , 100 ( 2 ) and 111 ( 3 ) ) - gibbsBsurf \n", gibbsBsurf ) ;
749 fprintf ( fp, "% - 10Lg SurfStiffness OFF = 0 - ON = 1 \n", Bsurf ) ;
fprintf ( fp, "% - 10d integration segment number - integSegmentNum \n", integSegmentNum ←
- 1 ) ;
751 fprintf ( fp, "% - 10d integration segment number - integSegmentNum \n", ←
integSegmentNumSt - 1 ) ;
fprintf ( fp, "% - 10d integration segment number - integSegmentNum \n", ←
integSegmentNumStt - 1 ) ;
753 fprintf ( fp, "% - 10Lg electron wind intensity - chi \n", chi ) ;
fprintf ( fp, "% - 10Lg Elastic Dipole Intensity Parameter - Xi \n", Xi ) ;
755 fprintf ( fp, "% - 10Lg Elastic Strain Energy Intensity Parameter - Sigma \n", Sigma ) ;
fprintf ( fp, "% - 10Lg wetting parameter - GammaSubstrate \n", GammaSubstrate ) ;
757 fprintf ( fp, "% - 10Lg wetting parameter - GammaFilm \n", GammaFilm ) ;
fprintf ( fp, "% - 10Lg wetting parameter - deltaW \n", deltaW ) ;
759 fprintf ( fp, "% - 10d use cont.txt \n", 1 ) ;
fclose ( fp ) ;
761
outName = dirName + "inputt.txt" ;
763 fp = fopen ( outName.c_str ( ) , "w" ) ;
fprintf ( fp, "% - 10d \n", newdata ) ;
765 fprintf ( fp, "% - 10d \n", control ) ;
fprintf ( fp, "% - 10d \n", remeshbool ) ;
767 fprintf ( fp, "% - 10Lg \n", Wn ) ;
fprintf ( fp, "% - 10Lg \n", Beta ) ;
769 fprintf ( fp, "% - 10d \n", calcLower ) ;
fprintf ( fp, "% - 10d \n", upperDivNum ) ;
771 fprintf ( fp, "% - 10d \n", lowerDivNum ) ;
fprintf ( fp, "% - 10d \n", sideDivNum ) ;
773 fprintf ( fp, "% - 10Lg \n", delTime ) ;
fprintf ( fp, "% - 10Lg \n", epsTime ) ;
775 fprintf ( fp, "% - 10d \n", H ) ;
fprintf ( fp, "% - 10Lg \n", minSegLengthi ) ;
777 fprintf ( fp, "% - 10Lg \n", maxSegLengthi ) ;
fprintf ( fp, "% - 10Lg \n", Amp/scaleFactor ) ;
779 fprintf ( fp, "% - 10d \n", nsw ) ;
fprintf ( fp, "% - 10Lg \n", poisson ) ;
781 fprintf ( fp, "% - 10Lg \n", alfa ) ;
fprintf ( fp, "% - 10d \n", foldSymNum ) ;
783 fprintf ( fp, "% - 10Lg \n", anisotIntensity ) ;
fprintf ( fp, "% - 10Lg \n", texTiltAngle/pi * 180 ) ;
785 fprintf ( fp, "% - 10Lg \n", bulkMobility ) ;
fprintf ( fp, "% - 10Lg \n", bulkGibbsEnergy ) ;
787 fprintf ( fp, "% - 10d \n", gibbsType ) ;
fprintf ( fp, "% - 10Lg \n", gibbsBsurf ) ;
789 fprintf ( fp, "% - 10Lg \n", Bsurf ) ;
fprintf ( fp, "% - 10d \n", integSegmentNum - 1 ) ;
791 fprintf ( fp, "% - 10d \n", integSegmentNumSt - 1 ) ;
fprintf ( fp, "% - 10d \n", integSegmentNumStt - 1 ) ;
793 fprintf ( fp, "% - 10Lg \n", chi ) ;
fprintf ( fp, "% - 10Lg \n", Xi ) ;
795 fprintf ( fp, "% - 10Lg \n", Sigma ) ;
fprintf ( fp, "% - 10Lg \n", GammaSubstrate ) ;
797 fprintf ( fp, "% - 10Lg \n", GammaFilm ) ;
fprintf ( fp, "% - 10Lg \n", deltaW ) ;
799 fclose ( fp ) ;
}
801
/***** *****/
803 /*
* Interrupted experiment continue by this procedure
805 */
/***** *****/
807

```

```

void continues () {
809 int null1;
    Number null11;
811
    in.open ( "cont.txt" );
813 in >> stackVector [0][0] >> stackVector [0][1]
    >> numUpperNodes >> numCathodeNodes >> numLowerNodes
815 >> numAnodeNodes >> numVoidNodes >> tStep >> lastOutNum
    >> normTime >> numCentStack >> minSegLengthi >> maxSegLengthi;
817
    turnPoint [0] = numUpperNodes;
819 turnPoint [1] = turnPoint [0] + numCathodeNodes;
    turnPoint [2] = turnPoint [1] + numLowerNodes;
821 turnPoint [3] = turnPoint [2] + numAnodeNodes;
    numNodeStack = turnPoint [3] + numVoidNodes;
823
825 for ( i = 1; i<numNodeStack; i++ ) {
    in >> stackVector [i][0] >> stackVector [i][1] ;
827 }
829 in.close () ;
831
    numVoidCent = numVoidNodes;
833 numCentStack = numNodeStack;
    numSurfCentStack = turnPoint [3] ;
835 numVoidCentStack = numVoidNodes;
    mpow = int ( pow ( 1.2, ( Number ) lastOutNum ) ) ;
837
    expState = 0;
839 }
841 void initiateInterconnect () {
843 if ( sinwave ) {
845 numUpperNodes = 2 * Msin + 1 ;
    double jump = 1 - 2/ ( double ( numUpperNodes ) ) ;
847 for ( int i = 0; i< numUpperNodes; i++ ) {
        upperNodes [i][0] = - interLength * jump * SPEEDcos ( pi * 0.5 + pi * 0.125 * Number ( ←
            i - Msin ) /Number ( Msin ) ) /SPEEDcos ( pi * 0.5 + pi * 0.125 * Number ( - Msin ) /←
            Number ( Msin ) ) ;
849 upperNodes [i][1] = interWidth + Amp * SPEEDsin ( upperNodes [i][0] * pi * nsW/ ( ←
            interLength * jump ) + 3 * pi/2 ) ;
            upperNodes [i][2] = 0.0;
851 }
    } else if ( calcUpper && !voidBool && pertType ) {
853 // UpperStrip forming
        stripDivNum = upperDivNum ;
855 Number ups;
        vectn hx;
857 Number h = interLength/upperDivNum;
        Number hw = ( pertEndNode - pertStartNode ) * h/6;
859 Number hym = pertHeigth * pertType;
        Number delh = h/pertDivNum;
861 int si = pertStartNode + 1;
        int fi = pertStartNode + ( pertEndNode - pertStartNode ) * pertDivNum;
863
        for ( int i = 0; i<= 2 * upperDivNum; i++ ) hx [i] = i * h;
865 for ( int i = si; i<= fi; i++ ) hx [i] = hx [pertStartNode] + ( i - pertStartNode ←
            ) * delh;
            int i = fi;
867 while ( hx [i] <= 2 * interLength ) {
                hx [i + 1] = hx [fi] + ( i + 1 - fi ) * h;
869 i++ ;
            }
871
            int ifinal = i - 1;
            Number hxm = ( hx [fi] + hx [si] ) /2;
            for ( int i = 0; i<= ifinal; i++ ) {
875 if ( ( i >= pertStartNode - 10 ) && ( i<= fi + 10 ) ) {
                    upperNodes [i][0] = hx [i] - interLength;
877 ups = hx [i] - hxm ;
                    upperNodes [i][1] = interWidth + hym * exp ( ( - sqr ( ups ) ) /sqr ( hw ) ) ;
879 upperNodes [i][2] = 0.0;
                }
            } else {
881 upperNodes [i][0] = hx [i] - interLength;

```

```

883     upperNodes [i][1] = interWidth;
884     upperNodes [i][2] = 0.0;
885 }
886 }
887 numUpperNodes = ifinal + 1;
888 }
889 else {
890     numUpperNodes = 2 * upperDivNum + 1 ;
891     for ( int i = 0; i< numUpperNodes ; i++ ) {
892         upperNodes [i][0] = ( Number ( i - upperDivNum ) ) * interLength/ ( Number ( ←
893             upperDivNum ) ) ;
894         upperNodes [i][1] = interWidth;
895         upperNodes [i][2] = 0.0;
896     }
897 }
898 stripDivNum = lowerDivNum ;
899 numLowerNodes = 2 * lowerDivNum + 1 ;
900 }
901 for ( int i = 0; i< numLowerNodes ; i++ ) {
902     lowerNodes [i][0] = interLength * SPEEDcos ( pi * i/ ( numLowerNodes - 1 ) ) ;
903     lowerNodes [i][1] = - interWidth;
904     lowerNodes [i][2] = 0.0;
905 }
906 numCathodeNodes = 2 * sideDivNum + 1 ;
907 for ( int i = 0; i< numCathodeNodes + 2 ; i++ ) {
908     cathodeNodes [i][0] = interLength;
909     cathodeNodes [i][1] = interWidth * SPEEDcos ( pi * Number ( i + 1 ) /Number ( ←
910         numCathodeNodes + 1 ) ) ;
911     cathodeNodes [i][2] = 0.0;
912 }
913 numAnodeNodes = 2 * sideDivNum + 1 ;
914 for ( int i = 0; i< numAnodeNodes + 2 ; i++ ) {
915     anodeNodes [i][0] = - interLength;
916     anodeNodes [i][1] = - interWidth * SPEEDcos ( pi * Number ( i + 1 ) /Number ( ←
917         numAnodeNodes + 1 ) ) ;
918     anodeNodes [i][2] = 0.0;
919 }
920 initialNodeNum = numUpperNodes;
921 }
922
923 /* ***** System nodes augmented ***** */
924
925 void constrStack () {
926     if ( PrintName ) cout<< "constrStack" << endl;
927     turnPoint [0] = numUpperNodes;
928     turnPoint [1] = turnPoint [0] + numCathodeNodes;
929     turnPoint [2] = turnPoint [1] + numLowerNodes;
930     turnPoint [3] = turnPoint [2] + numAnodeNodes;
931     numNodeStack = turnPoint [3] + numVoidNodes;
932 }
933
934 for ( i = 0; i<numNodeStack; i++ ) {
935     if ( i<turnPoint [0] ) {
936         stackVector [i][0] = upperNodes [i][0] ;
937         stackVector [i][1] = upperNodes [i][1] ;
938         stackVector [i][2] = upperNodes [i][2] ;
939     }
940     else if ( i>= turnPoint [0] && i<turnPoint [1] ) {
941         tempInt [0] = i - turnPoint [0] ;
942         stackVector [i][0] = cathodeNodes [tempInt [0] ][0] ;
943         stackVector [i][1] = cathodeNodes [tempInt [0] ][1] ;
944         stackVector [i][2] = cathodeNodes [tempInt [0] ][2] ;
945     }
946     else if ( i>= turnPoint [1] && i<turnPoint [2] ) {
947         tempInt [0] = i - turnPoint [1] ;
948         stackVector [i][0] = lowerNodes [tempInt [0] ][0] ;
949         stackVector [i][1] = lowerNodes [tempInt [0] ][1] ;
950         stackVector [i][2] = lowerNodes [tempInt [0] ][2] ;
951     }
952     else if ( i>= turnPoint [2] && i<turnPoint [3] ) {
953         tempInt [0] = i - turnPoint [2] ;
954         stackVector [i][0] = anodeNodes [tempInt [0] ][0] ;
955         stackVector [i][1] = anodeNodes [tempInt [0] ][1] ;
956         stackVector [i][2] = anodeNodes [tempInt [0] ][2] ;
957     }
958 }

```

```

959     else if ( voidBool == 1 && i >= turnPoint [3] ) {
          tempInt [0] = i - turnPoint [3] ;
961     stackVector [i][0] = voidNodes [tempInt [0] ][0] ;
          stackVector [i][1] = voidNodes [tempInt [0] ][1] ;
963     stackVector [i][2] = voidNodes [tempInt [0] ][2] ;
          }
965 }

967 stackVector [turnPoint [0] ][1] = stackVector [turnPoint [0] - 1][1] ;
stackVector [turnPoint [3] - 1][1] = stackVector [0][1] ;
969 stackVector [turnPoint [0] + 1][1] = ( stackVector [turnPoint [0] ][1] + stackVector[
[turnPoint [0] + 1][1] ) * 0.5 ;
stackVector [turnPoint [3] - 2][1] = ( stackVector [turnPoint [3] - 2][1] + ↵
stackVector [turnPoint [3] - 1][1] ) * 0.5 ;
971 if ( PRINT ) printFile ( stackVector , numNodeStack , "stack.txt" ) ;
}

973
975 /*
          * Centroid positions calculation
          */
977 /*
          *
          */
979 void calcCentroid () {
981     if ( PrintName ) cout << "calcCentroid" << endl;

983     numSurfCentStack = turnPoint [3] ;
numVoidCentStack = numVoidNodes;
985     numCentStack = numSurfCentStack + numVoidCentStack ;

987     for ( i = 0; i < numCentStack; i++ ) {
          if ( i < turnPoint [3] - 1 ) {
989             centStack [i][0] = ( stackVector [i][0] + stackVector [i + 1][0] ) * 0.5;
centStack [i][1] = ( stackVector [i][1] + stackVector [i + 1][1] ) * 0.5;
991         }
          else if ( i == ( turnPoint [3] - 1 ) ) {
993             centStack [i][0] = ( stackVector [0][0] + stackVector [i][0] ) * 0.5;
centStack [i][1] = ( stackVector [0][1] + stackVector [i][1] ) * 0.5;
995         }
          else if ( voidBool == 1 && i == numCentStack - 1 ) {
997             centStack [i][0] = ( stackVector [i][0] + stackVector [turnPoint [3] ][0] ) * 0.5;
centStack [i][1] = ( stackVector [i][1] + stackVector [turnPoint [3] ][1] ) * 0.5;
999         }
          else if ( voidBool == 1 && i >= turnPoint [3] ) {
1001             centStack [i][0] = ( stackVector [i][0] + stackVector [i + 1][0] ) * 0.5;
centStack [i][1] = ( stackVector [i][1] + stackVector [i + 1][1] ) * 0.5;
1003         }
          //Field calculation
1005         if ( chi != 0 ) fieldI [i] = 1 * centStack [i][0] ;
          }
1007     if ( PRINT ) printFile ( centStack , numCentStack , "center.txt" ) ;
1009 }

1011 void calcInterMatrix () {
          if ( PrintName ) cout << "calcInterMatrix" << endl;
1013         for ( i = 0; i < numCentStack; i++ )
          for ( j = 0; j < numCentStack; j++ ) {
1015             Matdist ( intMat , i , j , 0 ) = ( stackVector [j][0] - centStack [i][0] ) ;
Matdist ( intMat , i , j , 1 ) = ( stackVector [j][1] - centStack [i][1] ) ;
1017         }

1019         if ( PRINT ) {
          out.open ( "intMat.txt" ) ;
1021         for ( i = 0; i < numCentStack; i++ ) {
          for ( j = 0; j < numCentStack; j++ )
1023         for ( k = 0; k < 3; k++ ) out << Matdist ( intMat , i , j , k ) << " " ;
          out << endl ;
1025         }
          out.close () ;
1027         }
          }
1029

1031 /*
          * Segmenth vector and its length calculations
          */
1033 /*
          *
          */
1035

```

```

1037 void calcDelR_segLength () {
1038     if ( PrintName ) cout<< "calcDelR_segLength" << endl;
1039     for ( i = 0; i<numCentStack; i++ ) {
1040         if ( i<turnPoint [3] - 1 ) {
1041             del_R [i][0] = ( stackVector [i + 1][0] - stackVector [i][0] );
1042             del_R [i][1] = ( stackVector [i + 1][1] - stackVector [i][1] );
1043         }
1044         else if ( i == ( turnPoint [3] - 1 ) ) {
1045             del_R [i][0] = ( stackVector [0][0] - stackVector [i][0] );
1046             del_R [i][1] = ( stackVector [0][1] - stackVector [i][1] );
1047         }
1048         else if ( voidBool == 1 && i == numCentStack - 1 ) {
1049             del_R [i][0] = ( stackVector [numSurfCentStack][0] - stackVector [i][0] );
1050             del_R [i][1] = ( stackVector [numSurfCentStack][1] - stackVector [i][1] );
1051         }
1052         else if ( voidBool == 1 && i >= turnPoint [3] ) {
1053             del_R [i][0] = ( stackVector [i + 1][0] - stackVector [i][0] );
1054             del_R [i][1] = ( stackVector [i + 1][1] - stackVector [i][1] );
1055         }
1056         if ( i == turnPoint [0] - 1 ) {
1057             del_R [i][0] = del_R [0][0];
1058             del_R [i][1] = del_R [0][1];
1059         }
1060         segLength [i] = magnitude ( del_R [i] );
1061     }
1062     if ( PRINT ) {
1063         printFile ( del_R, numCentStack, "delr.txt" );
1064         printFile ( segLength, numCentStack, "s.txt" );
1065     }
1066 }
1067 /***** ***** */
1068 /*
1069  * Segmenth normal vector calculations
1070  */
1071 /***** ***** */
1072 void calcNormOfCent () {
1073     if ( PrintName ) cout<< "calcNormOfCent" << endl;
1074     for ( i = 0; i<numCentStack; i++ ) {
1075         centNormal [i][0] = ( del_R [i][1] ) /segLength [i];
1076         centNormal [i][1] = ( - del_R [i][0] ) /segLength [i];
1077     }
1078     if ( i == turnPoint [0] - 1 ) {
1079         centNormal [i][0] = ( del_R [0][1] ) /segLength [0];
1080         centNormal [i][1] = ( - del_R [0][0] ) /segLength [0];
1081     }
1082 }
1083 if ( PRINT ) printFile ( centNormal, numCentStack, "centNormal.txt" );
1084 }
1085 /***** ***** */
1086 /*
1087  * Crystallographic texture calculations
1088  */
1089 /***** ***** */
1090 void calcDiffusivity () {
1091     if ( PrintName ) cout<< "calcDiffusivity" << endl;
1092     for ( i = 0; i<numCentStack; i++ ) {
1093         if ( foldSymNum == 0 ) {
1094             difMag [i] = anisotIntensity + 1;
1095             gibbsGamma [i] = 1;
1096             gibbsGammaS [i] = 1;
1097             surfEnergy [i] = 1;
1098         } else {
1099             difTheta [i] = angle ( anx, del_R [i] );
1100
1101             if ( difTheta [i] > pi ) difTheta [i] -= 2 * pi;
1102             if ( difTheta [i] < 0.0 ) difTheta [i] += 2 * pi;
1103
1104             difMag [i] = 1.0 + anisotIntensity * sqr ( SPEEDcos ( foldSymNum * ( difTheta [i] - ←
1105                 texTiltAngle ) ) );
1106             surfEnergy [i] = ( 1 + Bsurf/2 ) * ( 1 + pow ( - 1, Number ( foldSymNum ) ) * ←
1107                 Bsurf * ( 1 - 4 * sqr ( foldSymNum ) )
1108                 / ( Bsurf + 2 ) * ( SPEEDcos ( 2 * foldSymNum * ( difTheta [i] + texTiltAngle ) ) ) ←
1109                 );
1110             if ( gibbsType == 0 ) {
1111                 gibbsGammaGamma [i] = gibbsBsurf * foldSymNum * ( SPEEDsin ( 2 * foldSymNum * ( ←

```

```

        difTheta [i] - texTiltAngle ) ) ) ;
gibbsGamma [i] = 1 + gibbsBsurf * sqrt ( SPEEDsin ( foldSymNum * ( difTheta [i] - ↵
texTiltAngle ) ) ) ) ;
1113 gibbsGammaS [i] = ( 1 + gibbsBsurf/2 ) * ( 1 - ( gibbsBsurf * ( 1 - 4 * sqrt ( ↵
foldSymNum ) ) / ( gibbsBsurf + 2 ) ) * ( SPEEDcos ( 2 * foldSymNum * ( difTheta [↵
i] - texTiltAngle ) ) ) ) ) ;
}
1115 else if ( gibbsType == 1 ) {
gibbsGammaGamma [i] = 0.5 * gibbsBsurf * foldSymNum * ( SPEEDsin ( 0.5 * foldSymNum * ↵
( difTheta [i] - texTiltAngle ) ) ) * ( SPEEDcos ( 0.5 * foldSymNum * ( difTheta↵
[i] - texTiltAngle ) ) ) * ( 1/
1117 ( fabs ( SPEEDsin ( 0.5 * foldSymNum * ( difTheta [i] - texTiltAngle ) ) ) ) - 1/↵
( fabs ( SPEEDcos ( 0.5 * foldSymNum * ( difTheta [i] - texTiltAngle ) ) ) ) ) ↵
) ) ;
gibbsGamma [i] = 1 - gibbsBsurf + gibbsBsurf * ( fabs ( SPEEDsin ( 0.5 * ↵
foldSymNum * ( difTheta [i] - texTiltAngle ) ) ) + fabs ( SPEEDcos ( 0.5 * ↵
foldSymNum * ( difTheta [i] - texTiltAngle ) ) ) ) ) ;
1119 gibbsGammaS [i] = 1 - gibbsBsurf + gibbsBsurf * ( 1 - 0.25 * sqrt ( foldSymNum ) ↵
) * ( fabs ( SPEEDsin ( 0.5 * foldSymNum * ( difTheta [i] - texTiltAngle ) ) ) ) ↵
+ fabs ( SPEEDcos ( 0.5 * foldSymNum * ( difTheta [i] - texTiltAngle ) ) ) ) ) ↵
;
}
}
1121 }
}
1123
for ( i = 0; i < numNodeStack; i++ ) {
1125 if ( i < turnPoint [3] || i > turnPoint [3] )
tempSYS [i] = ( surfEnergy [i - 1] * segLength [i] + surfEnergy [i] * segLength [i - ↵
1] ) / ( segLength [i] + segLength [i - 1] ) ;
1127 if ( i == 0 )
tempSYS [i] = ( surfEnergy [turnPoint [0] - 2] * segLength [i] + surfEnergy [i] * ↵
segLength [turnPoint [0] - 2] ) / ( segLength [i] + segLength [turnPoint [0] - 2] ) ↵
;
1129 if ( i == turnPoint [3] )
tempSYS [i] = ( surfEnergy [numNodeStack - 1] * segLength [i] + surfEnergy [i] * ↵
segLength [numNodeStack - 1] ) / ( segLength [i] + segLength [numNodeStack - 1] ) ;
1131 }
tempSYS [turnPoint [0] - 1] = tempSYS [0] ;
1133 for ( i = 0; i < numNodeStack; i++ ) surfEnergy [i] = tempSYS [i] ;
1135
for ( i = 0; i < numNodeStack; i++ ) {
1137 if ( i < turnPoint [3] || i > turnPoint [3] )
tempSYS [i] = ( gibbsGammaS [i - 1] * segLength [i] + gibbsGammaS [i] * segLength [i ↵
1] ) / ( segLength [i] + segLength [i - 1] ) ;
1139 if ( i == 0 )
tempSYS [i] = ( gibbsGammaS [turnPoint [0] - 2] * segLength [i] + gibbsGammaS [i] * ↵
segLength [turnPoint [0] - 2] ) / ( segLength [i] + segLength [turnPoint [0] - 2] ) ↵
;
1141 if ( i == turnPoint [3] )
tempSYS [i] = ( gibbsGammaS [numNodeStack - 1] * segLength [i] + gibbsGammaS [i] * ↵
segLength [numNodeStack - 1] ) / ( segLength [i] + segLength [numNodeStack - 1] ) ;
1143 }
tempSYS [turnPoint [0] - 1] = tempSYS [0] ;
1145 for ( i = 0; i < numNodeStack; i++ ) gibbsGammaS [i] = tempSYS [i] ;
1147
for ( i = 0; i < numNodeStack; i++ ) {
1149 if ( i < turnPoint [1] )
tempSYS [i] = ( gibbsGammaGamma [i - 1] * segLength [i] + gibbsGammaGamma [i] * ↵
segLength [i - 1] ) / ( segLength [i] + segLength [i - 1] ) ;
1151 if ( i == 0 )
tempSYS [i] = ( gibbsGammaGamma [turnPoint [1] - 1] * segLength [i] + gibbsGammaGamma ↵
[i] * segLength [turnPoint [1] - 1] ) / ( segLength [i] + segLength [turnPoint [1] ↵
1] ) ;
1153 if ( i == turnPoint [1] )
tempSYS [i] = ( gibbsGammaGamma [numNodeStack - 1] * segLength [i] + gibbsGammaGamma [i ↵
] * segLength [numNodeStack - 1] ) / ( segLength [i] + segLength [numNodeStack - 1] ) ↵
;
1155 }
}
1157 for ( i = 0; i < numNodeStack; i++ ) gibbsGammaGamma [i] = tempSYS [i] ;
if ( PRINT ) {
1159 printFile ( difTheta, numCentStack, "difTheta.txt" ) ;
printFile ( gibbsGammaS, numCentStack, "gibbsGammaS.txt" ) ;
1161 printFile ( gibbsGamma, numCentStack, "gibbsGamma.txt" ) ;
printFile ( surfEnergy, numCentStack, "surfEnergy.txt" ) ;
1163 printFile ( gibbsGammaGamma, numCentStack, "gibbsGammaGamma.txt" ) ;
}

```

```

1165 }
1167 /***** ***** */
1169 /* Angle calculations at nodes
1171 */
1173 void calcPsir () {
1175 if ( PrintName ) cout<< "calcPsir" << endl;
1176 for ( i = 0; i<numNodeStack; i++ ) {
1177 if ( i == 0 ) thetaAtNode [i] = angle ( del_R [turnPoint [0] - 2] , del_R [i] );
1178 else if ( i<turnPoint [3] || i>turnPoint [3] ) thetaAtNode [i] = angle ( del_R [i - 1] ←
1179 , del_R [i] );
1180 else if ( i == turnPoint [3] ) thetaAtNode [i] = angle ( del_R [numCentStack - 1] , ←
1181 del_R [i] );
1182 if ( i == turnPoint [0] - 1 ) thetaAtNode [i] = thetaAtNode [0] ;
1183 if ( thetaAtNode [i] < 0.0 ) thetaAtNode [i] += 2 * pi;
1184 if ( thetaAtNode [i] > pi ) thetaAtNode [i] -= 2 * pi;
1185 }
1186 if ( PRINT ) printFile ( thetaAtNode , numCentStack , "thetaAtNode.txt" );
1187 }
1188 /***** ***** */
1189 /* Boundary conditions for electromigration
1191 */
1193 void calcNormEF () {
1195 if ( PrintName ) cout<< "calcNormEF" << endl;
1196 for ( i = 0; i<numCentStack; i++ ) {
1197 B ( i , 0 ) = - 1 * centNormal [i][0] ;
1198 if ( i >= turnPoint [0] - 1 && i < turnPoint [1] ) B ( i , 0 ) = 0 ;
1199 if ( i >= turnPoint [2] - 1 && i < turnPoint [3] ) B ( i , 0 ) = 0 ;
1200 }
1201 if ( PRINT ) printFile ( mu , numCentStack , "B.txt" );
1202 }
1203 /***** ***** */
1205 /* Curvature Calculation
1207 */
1209 void calcKappa () {
1210 if ( PrintName ) cout<< "calcKappa" << endl;
1211 for ( i = 0; i<numNodeStack; i++ ) {
1212 if ( i == 0 ) {
1213 alpha [i] = atan ( SPEEDsin ( thetaAtNode [i] ) / ( segLength [turnPoint [3] - 1] / ←
1214 segLength [i] + SPEEDcos ( thetaAtNode [i] ) ) ) ;
1215 kappa [i] = 2.0 * SPEEDsin ( alpha [i] ) / segLength [i] ;
1216 tempDouble [0] = ( alpha [i] - pi * 0.5 ) ;
1217 createAntiRotMat ( tempDouble ) ;
1218 normKappa [0] = dotPro ( antiRot [0] , del_R [turnPoint [3] - 1] ) ;
1219 normKappa [1] = dotPro ( antiRot [1] , del_R [turnPoint [3] - 1] ) ;
1220 normKappa [2] = dotPro ( antiRot [2] , del_R [turnPoint [3] - 1] ) ;
1221 tempDouble [0] = magnitude ( normKappa ) ;
1222 localLineNorm [i][0] = normKappa [0] / tempDouble [0] ;
1223 localLineNorm [i][1] = normKappa [1] / tempDouble [0] ;
1224 localLineNorm [i][2] = normKappa [2] / tempDouble [0] ;
1225 }
1226 else if ( i == turnPoint [3] ) {
1227 alpha [i] = atan ( SPEEDsin ( thetaAtNode [i] ) / ( segLength [numCentStack - 1] / ←
1228 segLength [i] + SPEEDcos ( thetaAtNode [i] ) ) ) ;
1229 kappa [i] = 2.0 * SPEEDsin ( alpha [i] ) / segLength [i] ;
1230 tempDouble [0] = ( alpha [i] - pi * 0.5 ) ;
1231 createAntiRotMat ( tempDouble ) ;
1232 normKappa [0] = dotPro ( antiRot [0] , del_R [numCentStack - 1] ) ;
1233 normKappa [1] = dotPro ( antiRot [1] , del_R [numCentStack - 1] ) ;
1234 normKappa [2] = dotPro ( antiRot [2] , del_R [numCentStack - 1] ) ;
1235 tempDouble [0] = magnitude ( normKappa ) ;
1236 localLineNorm [i][0] = normKappa [0] / tempDouble [0] ;
1237 localLineNorm [i][1] = normKappa [1] / tempDouble [0] ;
1238 localLineNorm [i][2] = normKappa [2] / tempDouble [0] ;
1239 }
1240 else {

```

```

1241     alpha [i] = atan ( SPEEDsin ( thetaAtNode [i] ) ) / ( segLength [i - 1] /segLength [i]↵
        + SPEEDcos ( thetaAtNode [i] ) ) );
1242     if ( i >= turnPoint [0] ) alpha [i] = 0 ;
        kappa [i] = 2.0 * SPEEDsin ( alpha [i] ) /segLength [i] ;
1243     tempDouble [0] = ( alpha [i] - pi * 0.5 ) ;
        createAntiRotMat ( tempDouble ) ;
1245     normKappa [0] = dotPro ( antiRot [0] , del_R [i - 1] ) ;
        normKappa [1] = dotPro ( antiRot [1] , del_R [i - 1] ) ;
1247     normKappa [2] = dotPro ( antiRot [2] , del_R [i - 1] ) ;
        tempDouble [0] = magnitude ( normKappa ) ;
1249     localLineNorm [i][0] = normKappa [0] / tempDouble [0] ;
        localLineNorm [i][1] = normKappa [1] / tempDouble [0] ;
1251     localLineNorm [i][2] = normKappa [2] / tempDouble [0] ;
    }
1253 }
    if ( 1 ) {
1255     difMag [turnPoint [0] - 1] = difMag [0] ;
        surfEnergy [turnPoint [0] - 1] = surfEnergy [0] ;
1257     thetaAtNode [0] = angle ( del_R [turnPoint [0] - 2] , del_R [0] ) ;
        if ( thetaAtNode [0] < 0.0 ) thetaAtNode [0] += 2 * pi ;
1259     if ( thetaAtNode [0] > pi ) thetaAtNode [0] -= 2 * pi ;
        thetaAtNode [turnPoint [0] - 1] = thetaAtNode [0] ;
1261
        alpha [0] = atan ( SPEEDsin ( thetaAtNode [0] ) ) / ( segLength [turnPoint [0] - 2]
1263 /segLength [0] + SPEEDcos ( thetaAtNode [0] ) ) ) ;
        kappa [0] = 2.0 * SPEEDsin ( alpha [0] ) /segLength [0] ;
1265     tempDouble [0] = ( alpha [0] - pi * 0.5 ) ;
        createAntiRotMat ( tempDouble ) ;
1267     normKappa [0] = dotPro ( antiRot [0] , del_R [turnPoint [0] - 2] ) ;
        normKappa [1] = dotPro ( antiRot [1] , del_R [turnPoint [0] - 2] ) ;
1269     normKappa [2] = dotPro ( antiRot [2] , del_R [turnPoint [0] - 2] ) ;
        tempDouble [0] = magnitude ( normKappa ) ;
1271     localLineNorm [0][0] = normKappa [0] / tempDouble [0] ;
        localLineNorm [0][1] = normKappa [1] / tempDouble [0] ;
1273     localLineNorm [0][2] = normKappa [2] / tempDouble [0] ;
        alpha [turnPoint [0] - 1] = alpha [0] ;
1275     kappa [turnPoint [0] - 1] = kappa [0] ;
        localLineNorm [turnPoint [0] - 1][0] = localLineNorm [0][0] ;
1277     localLineNorm [turnPoint [0] - 1][1] = localLineNorm [0][1] ;
        localLineNorm [turnPoint [0] - 1][2] = localLineNorm [0][2] ;
1279 }
    kappaAv = 0;
1281     for ( i = 0; i < numNodeStack ; i++ ) {
        if ( i < turnPoint [0] ) {
1283     WU [i] = ( GammaSubstrate + GammaFilm ) /GammaFilm * 0.5 + ( GammaFilm - ↵
        GammaSubstrate ) / ( pi * GammaFilm ) * atan ( ( stackVector [i][1] + ↵
        interWidth ) / ( deltaW * scaleFactor * 1 ) ) ) ;
        WUU [i] = localLineNorm [i][1] * ( GammaFilm - GammaSubstrate ) / ( pi * GammaFilm ) ↵
        * ( deltaW * scaleFactor ) / ( sqr ( deltaW * scaleFactor ) + sqr ( stackVector [i]↵
        ][1] + interWidth ) ) * gibbsGamma [i] - localLineNorm [i][0] * ( GammaFilm - ↵
        GammaSubstrate ) / ( pi * GammaFilm ) * ( deltaW * scaleFactor ) / ( sqr ( deltaW * ↵
        scaleFactor ) + sqr ( stackVector [i][1] + interWidth ) ) * gibbsGammaGamma [i] ;
1285     } else {
        WU [i] = 0;
1287     WUU [i] = 0;
        }
1289     kappaAv += fabs ( kappa [i] ) ;
    }
1291     kappaAv /= numNodeStack;
    if ( PRINT ) {
1293     printFile ( centers , numNodeStack , "centers.txt" ) ;
        printFile ( localLineNorm , numNodeStack , "localLineNorm.txt" ) ;
1295     printFile ( tempVectNew , 1 , "ss.txt" ) ;
        printFile ( kappa , numNodeStack , "kappa.txt" ) ;
1297     printFile ( WU , numNodeStack , "WU.txt" ) ;
        printFile ( WUU , numNodeStack , "WUU.txt" ) ;
1299     printFile ( alpha , numNodeStack , "alpha.txt" ) ;
        printFile ( stackVector , numNodeStack , "stack.txt" ) ;
1301 }
1303
1305 /* ***** */
        * Electromigration Calculations
1307 */
1309 /* ***** */
    void formingIBEMmatrix () {
1311     if ( PrintName ) cout << "formingIBEMmatrix" << endl;

```

```

tempInt [3] = integSegmentNum - 1;
1313 tempDouble [1] = 0.5/ ( pi * tempInt [3] ) ;
    for ( i = 0; i<numCentStack; i++ ) {
1315     for ( j = 0; j<numCentStack; j++ ) {
        // Matrixin kosegeninne deger atiyor.
1317     if ( i == j )
        A ( i, j ) = 0.5;
1319     else {
        for ( m = 0; m<integSegmentNum; m++ ) {
1321         tempVect [m][0] = Matdist ( intMat, i, j, 0 ) + m * del_R [j][0] /tempInt [3] ;
        tempVect [m][1] = Matdist ( intMat, i, j, 1 ) + m * del_R [j][1] /tempInt [3] ;
1323     }

1325     for ( k = 0; k<2; k++ ) {
        tempDouble [0] = 0.0;
1327     for ( m = 1; m<tempInt [3] ; m++ )
        tempDouble [0] += tempVect [m][k] /sqr_mag ( tempVect [m] ) ;

1329     rcij [k] = tempDouble [0] ;
        rcos = sqr_mag ( tempVect [0] ) ;
1331     rcms = sqr_mag ( tempVect [tempInt [3] ] ) ;
        rcij [k] += 0.5 * ( tempVect [0][k] /rcos + tempVect [tempInt [3] ][k] /rcms ) ;
1333     //burda degisiklik yapildi 18.02.2008
1335     }
        A ( i, j ) = - segLength [j] * tempDouble [1] * ( dotPro ( centNormal [i] , rcij ) ←
        ) ;
1337     if ( i>= turnPoint [1] &&i<turnPoint [2] - 1 ) A ( i, j ) * = - 1;
        if ( i>= turnPoint [0] - 1&&i<turnPoint [1] ) A ( i, j ) = 0;
1339     if ( i>= turnPoint [2] - 1&&i<turnPoint [3] ) A ( i, j ) = 0;
    }
1341 }
1343
1345 if ( PRINT ) {
    out.open ( "IBEM.txt" ) ;
    out << setiosflags ( ios::showpoint ) ;
1347     for ( i = 0; i<numCentStack; i++ ) {
        for ( j = 0; j<numCentStack; j++ ) {
1349         out << setprecision ( 20 ) << darray ( ibemMat, i, j ) <<" " ;
        }
        out << endl ;
    }
1353     out.close () ;
1355 }
1357
void calcEField () {
1359     if ( PrintName ) cout<< "calcEField" << endl;

1361     nrhs = 1;
    /* Factorize ftt */
1363     dgetrf ( numCentStack, numCentStack, ibemMat, lda, ipiv, &info ) ;
    /* Solve ftt */
1365     dgetrs ( 'N', numCentStack, nrhs, ibemMat, lda, ipiv, mu, ldb, &info ) ;

1367     tempInt [0] = integSegmentNum - 1;

1369     for ( i = 0; i< numCentStack; i++ ) {
        for ( j = 0; j< numCentStack; j++ ) {
1371         tempVect [1][0] = stackVector [j + 1][0] - centStack [i][0] ;
        tempVect [1][1] = stackVector [j + 1][1] - centStack [i][1] ;
1373
        tempVect [0][0] = Matdist ( intMat, i, j, 0 ) ;
1375         tempVect [0][1] = Matdist ( intMat, i, j, 1 ) ;
        tempDouble [0] = 0.5 * ( log ( magnitude ( tempVect [0] ) ) + log ( magnitude ( ←
        tempVect [1] ) ) ) ;
1377         for ( m = 1; m<tempInt [0] ; m++ ) {
            tempVect [3][0] = tempVect [0][0] + m * del_R [j][0] /tempInt [0] ;
1379             tempVect [3][1] = tempVect [0][1] + m * del_R [j][1] /tempInt [0] ;
            tempDouble [0] += log ( magnitude ( tempVect [3] ) ) ;
1381         }
        del_U [i][j] = - 0.5/ ( pi * ( tempInt [0] ) ) * ( segLength [j] ) * ( ←
        tempDouble [0] ) ;
1383     }
        fieldII [i] = 0.0;
1385     for ( k = 0; k<numCentStack; k++ )
        fieldII [i] += ( del_U [i][k] ) * mu [k] ;
1387     fieldT [i] = fieldI [i] + fieldII [i] ;

```

```

1389 }
1391 for ( i = 0; i<numNodeStack; i++ ) {
1392     if ( i<turnPoint [3] || i>turnPoint [3] )
1393         fieldTN [i] = ( fieldT [i - 1] * segLength [i] + fieldT [i] * segLength [i - 1] ) / ( ←
1394             segLength [i] + segLength [i - 1] );
1395     if ( i == 0 )
1396         fieldTN [i] = ( fieldT [turnPoint [3] - 1] * segLength [i] + fieldT [i] * segLength [ ←
1397             turnPoint [3] - 1] ) / ( segLength [i] + segLength [turnPoint [3] - 1] );
1398     if ( i == turnPoint [3] )
1399         fieldTN [i] = ( fieldT [numNodeStack - 1] * segLength [i] + fieldT [i] * segLength [ ←
1400             numNodeStack - 1] ) / ( segLength [i] + segLength [numNodeStack - 1] );
1401 }
1402
1403 if ( PRINT ) {
1404     printFile ( fieldTN, numNodeStack, "fieldTN.txt" );
1405     printFile ( del_U, numNodeStack, "del_U.txt" );
1406     printFile ( fieldI, numNodeStack, "fieldI.txt" );
1407     printFile ( fieldII, numNodeStack, "fieldII.txt" );
1408     printFile ( mu, numNodeStack, "mu.txt" );
1409 }
1410
1411 /****** ***** */
1412 /*
1413 * Stress Calculations
1414 */
1415 /****** ***** */
1416 void formingStressIBEMmatrix () {
1417     if ( PrintName ) cout<< "formingStressIBEMmatrix" << endl;
1418
1419     tempInt [1] = integSegmentNumSt - 1;
1420
1421     for ( i = 0; i<numCentStack; i++ ) {
1422         for ( j = 0; j<numCentStack; j++ ) {
1423             if ( i<turnPoint [0] || i == numCentStack - 1 ) {
1424                 if ( i == j ) {
1425                     darray ( ftt, i * 2, j * 2 ) = 0.5 ; // ftt [i * 2][j * 2]
1426                     darray ( ftt, i * 2 + 1, j * 2 + 1 ) = 0.5; // ftt [i * 2 + 1][j * 2 + 1]
1427                     darray ( ftt, i * 2 + 1, j * 2 ) = 0 ; // ftt [i * 2 + 1][j * 2]
1428                     darray ( ftt, i * 2, j * 2 + 1 ) = 0; // ftt [i * 2][j * 2 + 1]
1429                 }
1430                 else {
1431                     for ( m = 0; m<integSegmentNumSt; m++ ) {
1432                         tempVect [m][0] = Matdist ( intMat, i, j, 0 ) + m * del_R [j][0] /tempInt [1] ;
1433                         tempVect [m][1] = Matdist ( intMat, i, j, 1 ) + m * del_R [j][1] /tempInt [1] ;
1434                     }
1435
1436                     TTSS ( tempVect [0] , centNormal [i] ) ;
1437
1438                     temp2x2 [0][0] = tt [0][0] ;
1439                     temp2x2 [0][1] = tt [0][1] ;
1440                     temp2x2 [1][0] = tt [1][0] ;
1441                     temp2x2 [1][1] = tt [1][1] ;
1442
1443
1444                     TTSS ( tempVect [tempInt [1] ] , centNormal [i] ) ;
1445
1446                     temp2x2 [0][0] += tt [0][0] ;
1447                     temp2x2 [0][1] += tt [0][1] ;
1448                     temp2x2 [1][0] += tt [1][0] ;
1449                     temp2x2 [1][1] += tt [1][1] ;
1450
1451                     ttss [0][0] = temp2x2 [0][0] * 0.5;
1452                     ttss [0][1] = temp2x2 [0][1] * 0.5;
1453                     ttss [1][0] = temp2x2 [1][0] * 0.5;
1454                     ttss [1][1] = temp2x2 [1][1] * 0.5;
1455                     for ( k = 1; k<tempInt [1] ; k++ ) {
1456                         TTSS ( tempVect [k] , centNormal [i] ) ;
1457                         ttss [0][0] += tt [0][0] ;
1458                         ttss [0][1] += tt [0][1] ;
1459                         ttss [1][0] += tt [1][0] ;
1460                         ttss [1][1] += tt [1][1] ;
1461                     }
1462
1463                     tempDouble [0] = segLength [j] /tempInt [1] ;

```

```

1465 darray ( ftt , i * 2, j * 2 ) = ttss [0][0] * tempDouble [0] ;
darray ( ftt , i * 2, j * 2 + 1 ) = ttss [0][1] * tempDouble [0] ;
1466 darray ( ftt , i * 2 + 1, j * 2 ) = ttss [1][0] * tempDouble [0] ;
1467 darray ( ftt , i * 2 + 1, j * 2 + 1 ) = ttss [1][1] * tempDouble [0] ;
}
1469 } else {
for ( m = 0; m<integSegmentNumSt; m++ ) {
1471 tempVect [m][0] = Matdist ( intMat, i, j, 0 ) + m * del_R [j][0] /tempInt [1] ;
tempVect [m][1] = Matdist ( intMat, i, j, 1 ) + m * del_R [j][1] /tempInt [1] ;
1473 }
1475 uu ( tempVect [0] ) ;
1477 temp2x2 [0][0] = us [0][0] ;
temp2x2 [0][1] = us [0][1] ;
1479 temp2x2 [1][0] = us [1][0] ;
temp2x2 [1][1] = us [1][1] ;
1481 uu ( tempVect [tempInt [1] ] ) ;
1483 temp2x2 [0][0] += us [0][0] ;
temp2x2 [0][1] += us [0][1] ;
1485 temp2x2 [1][0] += us [1][0] ;
temp2x2 [1][1] += us [1][1] ;
1487
1489 uuss [0][0] = temp2x2 [0][0] * 0.5;
uuss [0][1] = temp2x2 [0][1] * 0.5;
1491 uuss [1][0] = temp2x2 [1][0] * 0.5;
uuss [1][1] = temp2x2 [1][1] * 0.5;
1493
for ( k = 1; k<tempInt [1] ; k++ ) {
1495 uu ( tempVect [k] ) ;
uuss [0][0] += us [0][0] ;
1497 uuss [0][1] += us [0][1] ;
uuss [1][0] += us [1][0] ;
1499 uuss [1][1] += us [1][1] ;
}
1501 tempDouble [0] = segLength [j] /tempInt [1] ;
1503
darray ( ftt , i * 2, j * 2 ) = uuss [0][0] * tempDouble [0] ;
1505 darray ( ftt , i * 2, j * 2 + 1 ) = uuss [0][1] * tempDouble [0] ;
darray ( ftt , i * 2 + 1, j * 2 ) = uuss [1][0] * tempDouble [0] ;
1507 darray ( ftt , i * 2 + 1, j * 2 + 1 ) = uuss [1][1] * tempDouble [0] ;
}
1509 }
1511 }
1513 if ( PRINT ) {
out.open ( "fttp.txt" ) ;
1515 out << setiosflags ( ios::showpoint ) ;
for ( i = 0; i<2 * numCentStack; i++ ) {
1517 for ( j = 0; j<2 * numCentStack; j++ ) {
out << setprecision ( 20 ) << darray ( ftt , i, j ) <<" " ;
1519 }
out << endl ;
1521 }
out.close () ;
1523 }
1525 }
1527 void ASYM () {
if ( PrintName ) cout<< "ASYM" << endl;
1529 Number nm = int ( ( numLowerNodes - 1 ) /2 ) ;
Number nnn = interLength/nm * ex;
1531
for ( i = 0; i<numCentStack; i++ ) {
1533 if ( i<turnPoint [0] ) {
trac [i][0] = 0;
1535 trac [i][1] = 0;
trac [i][2] = 1;
1537 }
else if ( i<turnPoint [1] ) {
1539 trac [i][0] = 0;
trac [i][1] = 0;
1541 trac [i][2] = 1;
}
}

```

```

1543 else if ( i<turnPoint [2] - 1 ) {
1544     trac [i][0] = nnn * ( turnPoint [1] + nm - i + 0.5 ) ;
1545     trac [i][1] = 0;
1546     trac [i][2] = nnn;
1547 }
1548 else if ( i<turnPoint [3] ) {
1549     trac [i][0] = 0;
1550     trac [i][1] = 0;
1551     trac [i][2] = 1;
1552 }
1553 else {
1554     trac [i][0] = 0;
1555     trac [i][1] = 0;
1556     trac [i][2] = 1;
1557 }
1558
1559 TN [i] = - 1 * ( dotPro ( trac [i] , centNormal [i] ) ) ;
1560 }
1561 if ( 1 ) {
1562     printFile ( trac , numNodeStack , "trac.txt" ) ;
1563     printFile ( TN , numNodeStack , "TN.txt" ) ;
1564 }
1565 }
1566
1567 void AAASYM () {
1568     if ( PrintName ) cout<< "AASYM" << endl;
1569     nnn = interLength/int ( ( numLowerNodes - 1 ) /2 ) * ex;
1570
1571     for ( i = 0; i<numCentStack; i++ ) {
1572         if ( i<turnPoint [0] - 1 ) {
1573             trac [i][0] = 0; /* R;
1574             trac [i][1] = 0; /* 1 * R;
1575             trac [i][2] = 1; /* R;
1576         }
1577         else if ( i<turnPoint [1] ) {
1578             trac [i][0] = ex * 0.5 * ( centStack [i][0] /interLength ) ;
1579             trac [i][1] = 0;
1580             trac [i][2] = nnn;
1581         }
1582         else if ( i<turnPoint [2] - 1 ) {
1583             trac [i][0] = ex * 0.5 * ( centStack [i][0] /interLength ) ;
1584             trac [i][1] = 0;
1585             trac [i][2] = nnn;
1586         }
1587         else if ( i<turnPoint [3] ) {
1588             trac [i][0] = ex * 0.5 * ( centStack [i][0] /interLength ) ;
1589             trac [i][1] = 0;
1590             trac [i][2] = nnn;
1591         }
1592         else {
1593             trac [i][0] = 0;
1594             trac [i][1] = 0;
1595             trac [i][2] = 1;
1596         }
1597     }
1598     TN [i] = - 1 * ( dotPro ( trac [i] , centNormal [i] ) ) ;
1599 }
1600
1601 if ( PRINT ) {
1602     printFile ( trac , numNodeStack , "tracn.txt" ) ;
1603     printFile ( TN , numNodeStack , "TNn.txt" ) ;
1604 }
1605 }
1606
1607 void AASYM () {
1608     if ( PrintName ) cout<< "AASYM" << endl;
1609     nnn = interLength/int ( ( numLowerNodes - 1 ) /2 ) * ex;
1610
1611     for ( i = 0; i<numCentStack; i++ ) {
1612         if ( i<turnPoint [0] || i == numCentStack - 1 ) {
1613             trac [i][0] = 0;
1614             trac [i][1] = 0;
1615             trac [i][2] = 1;
1616         }
1617         else {
1618             trac [i][0] = ex * 0.5 * ( centStack [i][0] /interLength ) ;
1619             trac [i][1] = 0;
1620             trac [i][2] = nnn;
1621         }
1622     }

```

```

1623     }
1624     TN [i] = - 1 * ( dotPro ( trac [i] , centNormal [i] ) ) ;
1625 }
1627 if ( PRINT ) {
1628     printFile ( trac , numNodeStack , "tracn.txt" ) ;
1629     printFile ( TN , numNodeStack , "TNn.txt" ) ;
1630 }
1631 }
1632 }
1633 void boundary () {
1634     if ( PrintName ) cout<< "boundary" << endl;
1635     for ( i = 0; i<numCentStack; i++ ) {
1636         darray ( fSigma , i * 2 , 0 ) = trac [i][0] ;
1637         darray ( fSigma , i * 2 + 1 , 0 ) = trac [i][1] ;
1638     }
1639     n = 2 * numCentStack ;
1640     if ( PRINT ) printFile ( fSigma , n , "fsigc.txt" ) ;
1641 }
1642 }
1643 void fsig () {
1644     if ( PrintName ) cout<< "fsig" << endl;
1645     n = 2 * numCentStack ;
1646     nrhs = 1;
1647     /* Factorize ftt */
1648     dgetrf ( n , n , ftt , lda , ipiv , &info ) ;
1649     /* Solve ftt */
1650     dgetrs ( 'N' , n , nrhs , ftt , lda , ipiv , fSigma , ldb , &info ) ;
1651     if ( PRINT ) printFile ( fSigma , n , "fsigp.txt" ) ;
1652 }
1653 }
1654 }
1655 void delSgrand () {
1656     if ( PrintName ) cout<< "delSgrand" << endl;
1657     tempInt [1] = integSegmentNumStt - 1;
1658     for ( i = 0; i<numCentStack; i++ )
1659         for ( j = 0; j<numCentStack; j++ ) {
1660             if ( i == j ) {
1661                 darray ( uuD , i * 3 , j * 2 ) = 0 ;
1662                 darray ( uuD , i * 3 , j * 2 + 1 ) = 0 ;
1663                 darray ( uuD , i * 3 + 1 , j * 2 ) = 0 ;
1664                 darray ( uuD , i * 3 + 1 , j * 2 + 1 ) = 0 ;
1665                 darray ( uuD , i * 3 + 2 , j * 2 ) = 0 ;
1666                 darray ( uuD , i * 3 + 2 , j * 2 + 1 ) = 0 ;
1667             }
1668             else {
1669                 for ( m = 0; m<integSegmentNumStt; m++ ) {
1670                     tempVect [m][0] = ( Matdist ( intMat , i , j , 0 ) + m * del_R [j][0] /tempInt [1] ) ;
1671                     tempVect [m][1] = ( Matdist ( intMat , i , j , 1 ) + m * del_R [j][1] /tempInt [1] ) ;
1672                 }
1673                 SSc ( tempVect [0] ) ;
1674                 temp2x2 [0][0] = ss [0][0] ;
1675                 temp2x2 [0][1] = ss [0][1] ;
1676                 temp2x2 [1][0] = ss [1][0] ;
1677                 temp2x2 [1][1] = ss [1][1] ;
1678                 temp2x2 [2][0] = ss [2][0] ;
1679                 temp2x2 [2][1] = ss [2][1] ;
1680                 SSc ( tempVect [tempInt [1] ] ) ;
1681                 temp2x2 [0][0] += ss [0][0] ;
1682                 temp2x2 [0][1] += ss [0][1] ;
1683                 temp2x2 [1][0] += ss [1][0] ;
1684                 temp2x2 [1][1] += ss [1][1] ;
1685                 temp2x2 [2][0] += ss [2][0] ;
1686                 temp2x2 [2][1] += ss [2][1] ;
1687                 uuss [0][0] = temp2x2 [0][0] * 0.5;
1688                 uuss [0][1] = temp2x2 [0][1] * 0.5;
1689                 uuss [1][0] = temp2x2 [1][0] * 0.5;

```

```

1701 uuss [1][1] = temp2x2 [1][1] * 0.5;
uuss [2][0] = temp2x2 [2][0] * 0.5;
1703 uuss [2][1] = temp2x2 [2][1] * 0.5;

1705 for ( k = 1; k<tempInt [1] ; k++ ) {
  SSc ( tempVect [k] ) ;
1707 uuss [0][0] += ss [0][0] ;
uuss [0][1] += ss [0][1] ;
1709 uuss [1][0] += ss [1][0] ;
uuss [1][1] += ss [1][1] ;
1711 uuss [2][0] += ss [2][0] ;
uuss [2][1] += ss [2][1] ;
1713 }

1715 tempDouble [0] = segLength [j] /tempInt [1] ;

1717 darray ( uuD, i * 3, j * 2 ) = uuss [0][0] * tempDouble [0] ;
darray ( uuD, i * 3, j * 2 + 1 ) = uuss [0][1] * tempDouble [0] ;
1719 darray ( uuD, i * 3 + 1, j * 2 ) = uuss [1][0] * tempDouble [0] ;
darray ( uuD, i * 3 + 1, j * 2 + 1 ) = uuss [1][1] * tempDouble [0] ;
1721 darray ( uuD, i * 3 + 2, j * 2 ) = uuss [2][0] * tempDouble [0] ;
darray ( uuD, i * 3 + 2, j * 2 + 1 ) = uuss [2][1] * tempDouble [0] ;
1723 }
1725 }

1727 for ( i = 0 ; i < 3 * numCentStack ; i++ ) {
  UB [i] = 0;
1729 for ( k = 0 ; k < 2 * numCentStack ; k++ )
  UB [i] += darray ( uuD, i, k ) * fSigma [k] ;
1731 }

1733 if ( PRINT ) {
  out.open ( "delq.txt" ) ;
1735 out << setiosflags ( ios::showpoint ) ;
  for ( i = 0; i<3 * numCentStack; i++ ) {
1737 for ( j = 0; j<2 * numCentStack; j++ ) out << setprecision ( 20 ) << darray ( uuD, i, j ) <<
    <<" " ;
  out << endl;
1739 }
  out.close () ;

1741 printFile ( UB, 3 * numCentStack, "UB.txt" ) ;
1743 }
1745 void SigmaStress () {
1747 if ( PrintName ) cout<< "SigmaStress" << endl;
1749 for ( i = 0; i < numCentStack; i++ ) {
  asig [i][0] = UB [i * 3] ;
1751 asig [i][1] = UB [3 * i + 1] ;
  asigXY [i][0] = UB [3 * i + 2] ;
1753 asig [i][2] = nu * ( asig [i][0] + asig [i][1] ) ;
  Trsig [i] = ( 1 + nu ) * ( asig [i][0] + asig [i][1] ) ;
1755 var [i][0] = del_R [i][0] * del_R [i][0] ;
  var [i][1] = del_R [i][1] * del_R [i][1] ;
1757 var [i][2] = del_R [i][1] * del_R [i][0] ;
  hoop [i] = ( asig [i][0] * var [i][0] + 2 * asigXY [i][0] * var [i][2] + asig [i][1] * var [i][1] ) / magnitude ( var [i] ) ;
1759 }

1761 for ( i = 0; i < numNodeStack; i++ ) {
  if ( i < turnPoint [0] )
1763 sighoop [i] = ( hoop [i - 1] * segLength [i] + hoop [i] * segLength [i - 1] ) / ( segLength [i] + segLength [i - 1] ) ;

1765 if ( i == 0 ) sighoop [i] = ( hoop [turnPoint [0] - 2] * segLength [i] + hoop [i] * segLength [turnPoint [0] - 2] ) / ( segLength [i] + segLength [turnPoint [0] - 2] ) ;
  if ( i >= turnPoint [0] ) sighoop [i] = 0;
1767 }
1769 sighoop [turnPoint [0] - 1] = sighoop [0] ;

1771 for ( i = 0; i < numNodeStack; i++ ) {
  if ( i < turnPoint [3] || i > turnPoint [3] )
1773 sigTrsig [i] = ( Trsig [i - 1] * segLength [i] + Trsig [i] * segLength [i - 1] ) / ( segLength [i] + segLength [i - 1] ) ;

```

```

1775 if ( i == 0 )
sigTrsig [i] = ( Trsig [turnPoint [0] - 2] * segLength [i] + Trsig [i] * segLength [↔
turnPoint [0] - 2] ) / ( segLength [i] + segLength [turnPoint [0] - 2] ) ;
1777 if ( i == turnPoint [3] )
sigTrsig [i] = ( Trsig [numNodeStack - 1] * segLength [i] + Trsig [i] * segLength [↔
numNodeStack - 1] ) / ( segLength [i] + segLength [numNodeStack - 1] ) ;
}
1779 if ( PRINT ) {
printFile ( sighoop , numNodeStack , "sighoop.txt" ) ;
1781 printFile ( sigTrsig , numNodeStack , "sigTrsig.txt" ) ;
}
1783 }
1785 }
1787
void stress () {
1789 if ( PrintName ) cout<< "STRESS" << endl;
formingStressIBEMmatrix () ;
1791 AASYM () ;
boundary () ;
1793 fsig () ;
delSgrand () ;
1795 SigmaStress () ;
}
1797
/***** *****/
1799 /*
*
1801 */
/***** *****/
1803
void calcEkap () {
1805 if ( PrintName ) cout<< "calcEkap" << endl;
1807 for ( i = 0; i<numNodeStack; i++ ) {
if ( Bsurf ) kappa [i] = ( kappa [i] * gibbsGammaS [i] ) ;
1809 if ( GammaSubstrate == 0 && GammaFilm == 0 )
ekap [i] = kappa [i] * scaleFactor * 1 ;
1811 else ekap [i] = ( kappa [i] * WU [i] + WU [i] ) * scaleFactor * 1 ;
1813 if ( chi != 0 ) ekap [i] += chi/scaleFactor * fieldTN [i] ;//
if ( Xi != 0 || Sigma != 0 ) ekap [i] += Xi * sighoop [i] - Sigma * sighoop [i] *↔
sighoop [i] ;
1815 if ( i>= turnPoint [0] ) ekap [i] = 0;
}
1817
if ( PRINT ) {
1819 printFile ( ekap , numNodeStack , "ekap.txt" ) ;
printFile ( kappa , numNodeStack , "kappa.txt" ) ;
1821 printFile ( fieldTN , numNodeStack , "fieldTN.txt" ) ;
printFile ( sighoop , numNodeStack , "sighoop.txt" ) ;
1823 }
1825 }
1827
/***** *****/
1829 /*
* Velocity calculations at nodes
*/
1831 /***** *****/
void calcVelocities () {
1833
if ( PrintName ) cout<< "calcVelocities" << endl;
1835 ekap [turnPoint [0] - 1] = ekap [0] ;
1837 nodeVel [0] = ( difMag [0] * ( ekap [1] - ekap [0] ) /segLength [0] ) - ( difMag [↔
turnPoint [0] - 2] * ( ekap [0] - ekap [turnPoint [0] - 2] ) /segLength [turnPoint
[0] - 2] ) ;
nodeVel [0] * = 2/ ( segLength [0] + segLength [turnPoint [0] - 2] ) ;
1839 nodeVel [0] -= bulkMobility * ( bulkGibbsEnergy + kappa [0] * gibbsGammaS [0] * ↔
surfEnergy [0] ) /sqr ( scaleFactor ) ;
1841
for ( j = 1; j<turnPoint [0] - 1; j++ ) {
nodeVel [j] = ( difMag [j] * ( ekap [j + 1] - ekap [j] ) /segLength [j] ) - ( ↔
difMag [j - 1] * ( ekap [j] - ekap [j - 1] ) /segLength [j - 1] ) ;
1843 nodeVel [j] * = 2/ ( segLength [j] + segLength [j - 1] ) ;
nodeVel [j] -= bulkMobility * ( bulkGibbsEnergy + kappa [j] * gibbsGammaS [j] * ↔
surfEnergy [j] ) /sqr ( scaleFactor ) ;
}
}

```

```

1845 }
1847 nodeVel [turnPoint [0] - 1] = nodeVel [0] ;
1849 vMax = 1;
1849 vMin = 1000;
1851 tempDouble [0] = 0;
1853 for ( i = 0; i<turnPoint [0] ; i++ ) {
1855     if ( fabs ( nodeVel [i] ) > vMax )
1855         vMax = fabs ( nodeVel [i] ) ;
1857     if ( fabs ( nodeVel [i] ) < vMin )
1857         vMin = fabs ( nodeVel [i] ) ;
1859     tempDouble [0] += nodeVel [i] ;
1859 }
1861 tempDouble [0] /= turnPoint [0] ;
1863 if ( PRINT ) printFile ( nodeVel , numNodeStack , "nodeVel.txt" ) ;
1865 }
1867 /****** ***** ***** ***** ***** ***** */
1869 /*
1869  * New position calculations at nodes
1871 */
1871 /****** ***** ***** ***** ***** ***** */
1873 void moveToNewPositions () {
1875
1877     if ( PrintName ) cout<< "moveToNewPositions" << endl;
1877     for ( j = 0; j<turnPoint [0] ; j++ ) {
1879         if ( j == 0 || j == turnPoint [0] - 1 ) {
1881             stackVector [j][0] = stackVector [j][0] + delTime * nodeVel [j] * localLineNorm [j][0] ;
1881             stackVector [j][1] = stackVector [j][1] + delTime * nodeVel [j] * localLineNorm [j][1] ;
1883         } else {
1883             stackVector [j][0] = stackVector [j][0] + delTime * nodeVel [j] * localLineNorm [j][0] ;
1885             stackVector [j][1] = stackVector [j][1] + delTime * nodeVel [j] * localLineNorm [j][1] ;
1885         }
1887         if ( stackVector [j][1] < - interWidth ) {
1889             tStep = maxLoopNum ;
1889             cout<< "substrate" ;
1891             outName = dirName + "substrate";//
1891             out.open ( outName.c_str () , ios::trunc ) ;
1893             out.close () ;
1893         }
1895         if ( stackVector [turnPoint [0] ][1] > - interWidth ) stackVector [turnPoint [0] ][1] = ←
1895             stackVector [0][1] ;
1897         if ( stackVector [turnPoint [3] - 1][1] > - interWidth ) stackVector [turnPoint [3] - ←
1897             1][1] = stackVector [turnPoint [0] - 1][1] ;
1899         if ( PRINT ) printFile ( stackVector , numNodeStack , "stackVectorNew.txt" ) ;
1901         delTime = epsTime * delMean/vMax;
1901         normTime += delTime;
1903     }
1905     /****** ***** ***** ***** ***** ***** */
1907     /*
1907     * Recording new state
1909     */
1909     /****** ***** ***** ***** ***** ***** */
1911     void record () {
1913         if ( PrintName ) cout<< "record" << endl;
1915         if ( tStep == mpow || tStep == maxLoopNum ) {
1917             time ( &rawtime ) ;
1917             int2str ( lastOutNum ) ;
1919             textName = dirName + textName;//
1921             out << setiosflags ( ios::showpoint ) ;

```

```

out.open ( textName.c_str () , ios::trunc ) ;
1923 outName = ctime ( &rawtime ) ;
out << setprecision ( 20 )
1925 << stackVector [0][0] <<" "<< stackVector [0][1] <<" "
<< segLength [0] <<" "
1927 << thetaAtNode [0] <<" "<< kappa [0] <<" "
<< gibbsGammaS [0] <<" "<< surfEnergy [0] <<" "
1929 << difMag [0] <<" "<< difTheta [0] <<" "
<< fieldI [0] <<" "<< fieldII [0] <<" "
1931 << fieldTN [0] <<" "<< mu [0] <<" "
<< fSigma [0] <<" "<< fSigma [1] <<" "
1933 << asig [0][0] <<" "<< asig [0][1] <<" "
<< asigXY [0][0] <<" "<< hoop [0] <<" "
1935 << sigTrsig [0] <<" "<< sighoop [0] <<" "
<< ekap [0] <<" "<< nodeVel [0] <<" "
1937 << numUpperNodes <<" "
<< numCathodeNodes <<" "<< numLowerNodes<<" "
1939 << numAnodeNodes <<" "<< numVoidNodes <<" "
<< tStep <<" "<< lastOutNum <<" "
1941 << normTime <<" "<< numCentStack <<" "
<< del_M <<" "<< voidBool <<" "
1943 << voidCenter [0] <<" "<< voidCenter [1] <<" "
<< endl;
1945
for ( i = 1; i<numNodeStack; i++ ) {
1947 out << setprecision ( 20 )
<< stackVector [i][0] <<" "<< stackVector [i][1] <<" "
1949 << segLength [i] <<" "
<< thetaAtNode [i] <<" "<< kappa [i] <<" "
1951 << gibbsGammaS [i] <<" "<< surfEnergy [i] <<" "
<< difMag [i] <<" "<< difTheta [i] <<" "
1953 << fieldI [i] <<" "<< fieldII [i] <<" "
<< fieldTN [i] <<" "<< mu [i] <<" "
1955 << fSigma [2 * i] <<" "<< fSigma [2 * i + 1] <<" "
<< asig [i][0] <<" "<< asig [i][1] <<" "
1957 << asigXY [i][0] <<" "<< hoop [i] <<" "
<< sigTrsig [i] <<" "<< sighoop [i] <<" "
1959 << ekap [i] <<" "<< nodeVel [i] <<" " << endl ;
}
1961 out << endl ;
1963 out.close () ;
1965 lastOutNum++ ;
1967 mpow = lastOutNum + ( int ) pow ( 1.2, ( double ) lastOutNum ) ;
}
1969
if ( numContData == 20000 || tStep == maxLoopNum ) {
1971 time ( &rawtime ) ;
1973 int2str ( lastOutNum ) ;
1975
textName = dirName + "cont.txt";//
1977 out << setiosflags ( ios::showpoint ) ;
out.open ( textName.c_str () , ios::trunc ) ;
1979 outName = ctime ( &rawtime ) ;

1981 out << setprecision ( 20 ) << stackVector [0][0] <<" "<< stackVector [0][1] <<" "
<< numUpperNodes <<" "<< numCathodeNodes <<" " << numLowerNodes <<" "
1983 << numAnodeNodes <<" "<< numVoidNodes <<" "
<< tStep <<" "<< lastOutNum <<" "<< normTime <<" "
1985 << numCentStack <<" "<< minSegLengthi <<" "<< maxSegLengthi << endl;

1987 for ( i = 1; i<numNodeStack; i++ ) {
out << setprecision ( 20 )
1989 << stackVector [i][0] <<" "<< stackVector [i][1] << endl;
}
1991 out << endl ;
out.close () ;
1993 numContData = 0;
}
1995
numContData++ ;
1997
}
1999
void findMinSeg () {

```

```

2001  aptr = segLength;
maxSegLength = * aptr;
2003  for ( i = 0; i<numUpperNodes - 1; i++ )    maxSegLength = maxP ( maxSegLength, aptr ) ;
aptr = segLength;
2005  minSegLength = * aptr;
for ( i = 0; i<numUpperNodes - 1; i++ )    minSegLength = minP ( minSegLength, aptr ) ;
2007  delMean = minSegLength ;
}
2009  void searchVoiding () {
2011      Node_type interNodes [ 2 * turnPoint [ 3] + 1 ] ;
2013      Node_type * firstK = &interNodes [ 0 ] ;
2015      Node_type * secK = &interNodes [ turnPoint [ 0] - 1 ] ;
Node_type * thirdK = &interNodes [ turnPoint [ 1] ] ;
2017      Node_type * fourK = &interNodes [ turnPoint [ 2] - 1 ] ;
2019      for ( i = 0; i<turnPoint [ 3] ; i++ ) {
2021          interNodes [ i ] .Point [ 0] = stackVector [ i][ 0 ] ;
interNodes [ i ] .Point [ 1] = stackVector [ i][ 1 ] ;
2023          interNodes [ i ] .segLength = segLength [ i ] ;
2025          if ( i == 0 || i == turnPoint [ 0] - 1 || i == turnPoint [ 1] || i == turnPoint [ 2] - 1 ←
)
{
2027              interNodes [ i ] .immortal = 1;
}
2029          else interNodes [ i ] .immortal = 0;
2031          if ( i == 0 ) {
interNodes [ i ] .back = &interNodes [ turnPoint [ 3] - 1 ] ;
2033          interNodes [ i ] .forward = &interNodes [ i + 1 ] ;
}
2035          else if ( i != turnPoint [ 3] - 1 ) {
interNodes [ i ] .back = &interNodes [ i - 1 ] ;
2037          interNodes [ i ] .forward = &interNodes [ i + 1 ] ;
}
2039          else {
interNodes [ turnPoint [ 3] - 1 ] .back = &interNodes [ turnPoint [ 3] - 2 ] ;
2041          interNodes [ turnPoint [ 3] - 1 ] .forward = &interNodes [ 0 ] ;
}
2043      }
2045      Node_type * secK1 = ( * secK ) .nodeShift ( - 8 ) ;
2047
Node_type * ptr;
2049      Node_type * pp;
Node_type * point1;
2051      Node_type * point2;
Node_type * point3;
2053      Node_type * point4;
Node_type * head;
2055      ptr = firstK;
2057      tempDouble [ 1] = 10.0;
2059      do {
pp = ( * ptr ) .nodeShift ( 7 ) ;
2061      do {
tempDouble [ 0] = ( * ptr ) .calcDistance ( pp ) ;
2063      if ( tempDouble [ 0] <minSegLength * 2 && tempDouble [ 0] < tempDouble [ 1] )
{
2065          tempDouble [ 1] = tempDouble [ 0] ;
point1 = ptr;
2067          point2 = pp;
point3 = ( * ptr ) .back;
2069          point4 = ( * pp ) .forward;
voidBool = 1;
2071          voidFound = 1;
}
2073          pp = ( * pp ) .forward;
} while ( pp != secK ) ;
2075          ptr = ( * ptr ) .forward;
} while ( ptr != secK1 ) ;
2077

```

```

2079     if ( voidBool ) {
2081         ( * point3 ) .forward = point4;
2083         ( * point4 ) .back = point3;

2085         head = point1;
2087         ( * point1 ) .back = point2;
2087         ( * point2 ) .forward = point1;

2089
2091         ptr = point1 ;
2091         do {
2093             pp = ( * ptr ) .forward;
2093             ptr = pp;
2095         } while ( ptr != point1 ) ;

2097     }

2099     i = 0;
2099     ptr = firstK;
2101     do {
2103         stackVector [i][0] = ( * ptr ) .Point [0] ;
2103         stackVector [i][1] = ( * ptr ) .Point [1] ;
2103         if ( ptr == secK ) turnPoint [0] = i + 1;
2105         else if ( ptr == thirdK ) turnPoint [1] = i;
2105         else if ( ptr == fourK ) turnPoint [2] = i + 1;
2107         i++;
2107         ptr = ( * ptr ) .forward ;
2109     } while ( ptr != firstK ) ;

2111     turnPoint [3] = i;

2113
2115     if ( voidBool ) {
2115
2117         ptr = head;
2117         do {
2119             stackVector [i][0] = ( * ptr ) .Point [0] ;
2119             stackVector [i][1] = ( * ptr ) .Point [1] ;
2121             i++;
2121             ptr = ( * ptr ) .forward ;
2123         } while ( ptr != head ) ;
2123     }
2125     numNodeStack = i;

2127     numUpperNodes = turnPoint [0] ;
2127     numCathodeNodes = turnPoint [1] - turnPoint [0] ;
2129     numLowerNodes = turnPoint [2] - turnPoint [1] ;
2129     numAnodeNodes = turnPoint [3] - turnPoint [2] ;
2131     numVoidNodes = numNodeStack - turnPoint [3] ;

2133     numVoidCent = numVoidNodes;
2133     numCentStack = numNodeStack;
2135     numSurfCentStack = turnPoint [3] ;
2135     numVoidCentStack = numVoidNodes;

2137     if ( voidBool ) {
2139         calcVoidCenter () ;
2139         initVoidArea = voidArea () ;
2141         insVoidArea = initVoidArea;
2143     }

2145     void checkArea () {
2147         if ( insVoidArea < 0.01 ) {
2149             tStep = maxLoopNum;
2149             outName = dirName + "state.txt"; //
2149             out.open ( outName.c_str () , ios::trunc ) ;
2151             out << "Too much void area decrease" ;
2151             cout << "Too much void area decrease" ;
2153             out.close () ;
2155         }
2155     }
2157     void voidTouch () {

```

```

2159 for ( i = 0; i<turnPoint [0] ; i++ )
for ( j = turnPoint [3] ; j<numNodeStack; j++ ) {
tempVect [0][0] = stackVector [i][0] - stackVector [j][0] ;
2161 tempVect [0][1] = stackVector [i][1] - stackVector [j][1] ;
if ( tempVect [0][1] <0 && magnitude ( tempVect [0] ) <minSegLength ) {
2163 tStep = maxLoopNum;
outName = dirName + "state.txt";//
2165 out.open ( outName.c_str () , ios::trunc ) ;
out << "Void reach to upper surface" ;
2167 cout << "Void reach to upper surface" ;
out.close () ;
2169 }
}
2171
for ( i = turnPoint [0] ; i<turnPoint [3] ; i++ )
2173 for ( j = turnPoint [3] ; j<numNodeStack; j++ ) {
tempVect [0][0] = stackVector [i][0] - stackVector [j][0] ;
2175 tempVect [0][1] = stackVector [i][1] - stackVector [j][1] ;
if ( tempVect [0][1] >0 && magnitude ( tempVect [0] ) <minSegLength ) {
2177 tStep = maxLoopNum;
outName = dirName + "state.txt";//
2179 out.open ( outName.c_str () , ios::trunc ) ;
out << "Void reach to lower surface" ;
2181 cout << "Void reach to lower surface" ;
out.close () ;
2183 }
}
2185
2187 }

2189 void shortCircuit ( int mm ) {
if ( mm )
2191 for ( i = 0; i<turnPoint [0] ; i++ )
for ( j = turnPoint [0] ; j<turnPoint [3] ; j++ ) {
2193 if ( ( j - i ) > 5 ) {
tempVect [0][0] = stackVector [i][0] - stackVector [j][0] ;
2195 tempVect [0][1] = stackVector [i][1] - stackVector [j][1] ;
if ( tempVect [0][1] <0 && magnitude ( tempVect [0] ) <minSegLength ) {
2197 tStep = maxLoopNum;
outName = dirName + "state.txt";//
2199 out.open ( outName.c_str () , ios::trunc ) ;
cout << "Short circuit" ;
2201 out << "Short circuit" ;
out.close () ;
2203 }
}
2205 }
}
2207

void controls () {
2209 if ( calcUpper && !voidBool ) searchVoiding () ;
if ( voidBool ) {
2211 checkArea () ;
voidTouch () ;
2213 if ( calcUpper ) searchSecVoiding () ;
}
2215 shortCircuit ( control ) ;
checkEquilibrium () ;
2217 }

2219 /***** *****/
2221 /* Remeshing
*/
2223 /***** *****/

2225 void powerMeshAdd () {
if ( PrintName ) cout << "powerMeshX" << endl;
2227 if ( PRINT ) printFile ( stackVector , numCentStack , "stackVector1.txt" ) ;
calcDelR_segLength () ;
2229
Node_type interNodes [2 * turnPoint [3] + 1] ;
2231
Node_type * firstK = &interNodes [0] ;
2233 Node_type * secK = &interNodes [turnPoint [0] - 1] ;
Node_type * thirdK = &interNodes [turnPoint [1] ] ;
2235 Node_type * fourK = &interNodes [turnPoint [2] - 1] ;
Node_type * endK = &interNodes [turnPoint [3] - 1] ;

```

```

2237 for ( i = 0; i < turnPoint [3] ; i++ ) {
2239
2241     interNodes [i] .Point [0] = stackVector [i][0] ;
2241     interNodes [i] .Point [1] = stackVector [i][1] ;
2241     interNodes [i] .segLength = segLength [i] ;
2243     interNodes [i] .power = fabs ( segLength [i] * segLength [i] * ekap [i] ) ;
2245
2245     interNodes [i] .CenterNorm [0] = centNormal [i][0] ;
2245     interNodes [i] .CenterNorm [1] = centNormal [i][1] ;
2247
2247     interNodes [i] .radius = 1/kappa [i] ;
2249     interNodes [i] .Center [0] = centers [i][0] ;
2249     interNodes [i] .Center [1] = centers [i][1] ;
2251
2253     if ( i == 0 || i == turnPoint [0] - 1 || i == turnPoint [1] || i == turnPoint [2] - 1↔
2253         )
2253     {
2255         interNodes [i] .immortal = 1;
2255     }
2257     else interNodes [i] .immortal = 0;
2259
2259     if ( i == 0 ) {
2259         interNodes [i] .back = &interNodes [turnPoint [3] - 1] ;
2261         interNodes [i] .forward = &interNodes [i + 1] ;
2263     }
2263     else if ( i != turnPoint [3] - 1 ) {
2265         interNodes [i] .back = &interNodes [i - 1] ;
2265         interNodes [i] .forward = &interNodes [i + 1] ;
2267     }
2269     else {
2269         interNodes [turnPoint [3] - 1] .back = &interNodes [turnPoint [3] - 2] ;
2271         interNodes [turnPoint [3] - 1] .forward = &interNodes [0] ;
2273     }
2275 }
2277 Node_type * ptr;
2277 i = turnPoint [3] ;
2279
2279 Node_type * pp;
2281
2281 ptr = firstK;
2283 do {
2283     ( * ptr ) .calcSegLength () ;
2285     pp = ( * ptr ) .forward;
2285     if ( ( ( * ptr ) .segLengthF + ( * ptr ) .segLengthB ) * 0.5 > maxSegLengthr ) {
2287     if ( ( * ptr ) .segLengthF > ( * ptr ) .segLengthB ) {
2287         ( * ptr ) .addNoden ( &interNodes [i] ) ;
2289     }
2289     else {
2291         ( * ( * ptr ) .back ) .addNoden ( &interNodes [i] ) ;
2291         if ( ptr == firstK ) firstK = &interNodes [i] ;
2293     }
2293     i++ ;
2295 }
2295 ptr = pp ;
2297 } while ( ptr != secK ) ;
2299
2299 ptr = ( * firstK ) .nodeShift ( - 2 ) ;
2299 if ( ( * ptr ) .segLength > maxSegLengthr ) {
2301     ( * ptr ) .addNoden ( &interNodes [i] ) ;
2301     i++ ;
2303 }
2305
2305 ptr = ( * secK ) .nodeShift ( 1 ) ;
2305 if ( ( * ptr ) .segLength > maxSegLengthr ) {
2307     ( * ptr ) .addNoden ( &interNodes [i] ) ;
2307     i++ ;
2309 }
2311
2311 i = 0;
2311 ptr = firstK;
2313 do {

```

```

2315 stackVector [i][0] = ( * ptr ) .Point [0] ;
stackVector [i][1] = ( * ptr ) .Point [1] ;
2317 if ( ptr == secK ) turnPoint [0] = i + 1;
else if ( ptr == thirdK ) turnPoint [1] = i;
2319 else if ( ptr == fourK ) turnPoint [2] = i + 1;
i++;
2321 ptr = ( * ptr ) .forward ;

2323 } while ( ptr != firstK ) ;

2325 turnPoint [3] = i;

2327 numNodeStack = i;

2329 numUpperNodes = turnPoint [0] ;
numCathodeNodes = turnPoint [1] - turnPoint [0] ;
2331 numLowerNodes = turnPoint [2] - turnPoint [1] ;
numAnodeNodes = turnPoint [3] - turnPoint [2] ;
2333 numVoidNodes = numNodeStack - turnPoint [3] ;

2335 numVoidCent = numVoidNodes;
numCentStack = numNodeStack;
2337 numSurfCentStack = turnPoint [3] ;
numVoidCentStack = numVoidNodes;

2339 if ( PRINT ) printFile ( stackVector , numCentStack , "stackVector2.txt" ) ;
2341 }
2343 void powerMeshRemove () {
2345 if ( PrintName ) {
cout<< "powerMeshXX" << endl;
2347 }

2349 calcDeIR_segLength () ;

2351 Node_type interNodes [2 * turnPoint [3] + 1] ;

2353 Node_type * firstK = &interNodes [0] ;
Node_type * secK = &interNodes [turnPoint [0] - 1] ;
2355 Node_type * thirdK = &interNodes [turnPoint [1] ] ;
Node_type * fourK = &interNodes [turnPoint [2] - 1] ;
2357 Node_type * endK = &interNodes [turnPoint [3] - 1] ;

2359 for ( i = 0; i<turnPoint [3] ; i++ ) {

2361 interNodes [i] .Point [0] = stackVector [i][0] ;
interNodes [i] .Point [1] = stackVector [i][1] ;
2363 interNodes [i] .segLength = segLength [i] ;

2365 if ( i == 1 ) interNodes [i] .segLength = segLength [0] ;
if ( i == 0 || i == turnPoint [3] - 1 || i == turnPoint [0] || i == turnPoint [0] - ←
1 || ( i>= turnPoint [1] && i<turnPoint [2] ) ) //
2367 {
interNodes [i] .immortal = 1;
2369 }
else interNodes [i] .immortal = 0;

2371 if ( i == 0 ) {
2373 interNodes [i] .back = &interNodes [turnPoint [3] - 1] ;
interNodes [i] .forward = &interNodes [i + 1] ;
2375 }
else if ( i!= turnPoint [3] - 1 ) {
2377 interNodes [i] .back = &interNodes [i - 1] ;
interNodes [i] .forward = &interNodes [i + 1] ;
2379 }
else {
2381 interNodes [turnPoint [3] - 1] .back = &interNodes [turnPoint [3] - 2] ;
interNodes [turnPoint [3] - 1] .forward = &interNodes [0] ;
2383 }

2385 }

2387 Node_type * pp;
2389 Node_type * ptr;
i = turnPoint [3] ;
2391 i = 0;

```

```

2393 ptr = firstK;
2394 if ( ( * firstK ) .segLength < ( * ( ( * firstK ) .forward ) ) .segLength )
2395 ( * ( ( * firstK ) .forward ) ) .segLength = ( * firstK ) .segLength;
2397 do {
2399 if ( ( * ptr ) .immortal == 0 && ( ( * ptr ) .segLength < minSegLengthi * 0.8 || ( ←
      * ( ( * ptr ) .back ) ) .segLength < minSegLengthi * 0.8 ) ) ptr = ( * ptr ) ←
      .forward;
2400 stackVector [i][0] = ( * ptr ) .Point [0] ;
2401 stackVector [i][1] = ( * ptr ) .Point [1] ;
2403 if ( ptr == secK ) {
      turnPoint [0] = i + 1;
2405 if ( ( * ptr ) .segLength < minSegLengthi * 0.5 ) ptr = ( * ptr ) .forward ;
      }
2407 else if ( ptr == thirdK ) turnPoint [1] = i;
2409 else if ( ptr == fourK ) turnPoint [2] = i + 1;
      i++;
2411 ptr = ( * ptr ) .forward ;
2413 if ( ( * ptr ) .immortal == 0 && ptr == ( ( * endK ) .back ) ) if ( ( * ptr ) ←
      .segLength < minSegLengthi * 0.5 ) ptr = ( * ptr ) .forward ;
2415 } while ( ptr != firstK ) ;
2417 turnPoint [3] = i;
2419 numNodeStack = i;
2421 numUpperNodes = turnPoint [0] ;
      numCathodeNodes = turnPoint [1] - turnPoint [0] ;
2423 numLowerNodes = turnPoint [2] - turnPoint [1] ;
      numAnodeNodes = turnPoint [3] - turnPoint [2] ;
2425 numVoidNodes = numNodeStack - turnPoint [3] ;
2427 numVoidCent = numVoidNodes;
      numCentStack = numNodeStack;
2429 numSurfCentStack = turnPoint [3] ;
      numVoidCentStack = numVoidNodes;
2431 if ( PRINT ) printFile ( stackVector , numCentStack , "stackVector2.txt" ) ;
2433 }
2435
2437 void calcMinima () {
      tempDouble [0] = 110;
2439
      for ( i = 0; i < ( numNodeStack/nsw ) ; i++ ) {
2441 if (tempDouble [0] > stackVector [i][1])
          tempDouble [0] = stackVector [i][1];
2443 else break;
      }
2445 minima = i;
      }
2447
2449 void simulate () {
      directoryName () ;
2451 if ( PRINT ) cout << dirName << endl;
2453 if ( expState == 0 ) {
      writeInputParameters () ;
2455
      while ( tStep <= maxLoopNum ) {
2457 if ( tStep != 1 ) PRINT = 0;
2459
      calcCentroid () ;
2461 if ( Xi != 0 || Sigma != 0 || chi != 0 ) calcInterMatrix () ;
      calcDelR_segLength () ;
2463 calcNormOfCent () ;
      calcDiffusivity () ;
2465 calcPsiR () ;
      calcKappa () ;
2467
      if ( chi != 0 && ( tStep%calcJump == 1 || tStep%calcJump == 0 || tStep < 18 ) ) ←

```

```

    calcNormEF () ;
2469 if ( chi != 0 && ( tStep%calcJump == 1 || tStep%calcJump == 0 || tStep<18 ) ) {
    formingIBEMmatrix () ;
2471    calcEField () ;
    }
2473
if ( ( Xi != 0 || Sigma != 0 ) && ( tStep%calcJump == 1 || tStep%calcJump == 0 <←
    || tStep<18 ) ) stress () ;
2475
calcEkap () ;
2477 calcVelocities () ;
findMinSeg () ;
2479 moveToNewPositions () ;

record () ;
if ( tStep% ( calcJump * 2 ) == 0 ) {
2483    powerMeshAdd () ;
    powerMeshRemove () ;
2485 }

tStep++ ;
if ( maxLoopNum>tStep ) {
2489    if ( ( numNodeStack > NMAX ) || ( initialNodeNum > numNodeStack * 3 ) ) && !←
        newdata ) tStep = maxLoopNum;
    if ( tStep% ( calcJump * 2 ) == 1 ) {
2491        if ( ( maxSegLength/maxSegLengthi ) >3 ) {
2493            cout<< "maxseglength" ;
                outName = dirName + "maxseglength";//
                out.open ( outName.c_str () , ios::trunc ) ;
2495            out.close () ;
        }
2497        if ( ( numUpperNodes >initialNodeNum * 3 ) ) {
                outName = dirName + "MAX numUpperNodes";//
2499            out.open ( outName.c_str () , ios::trunc ) ;
                out.close () ;
2501            cout<< "numUpperNodes" ;
        }
    }
2503    if ( ( numNodeStack > NMAX ) ) {
2505        cout<< "NMAX" ;
                outName = dirName + "NMAX";//
2507            out.open ( outName.c_str () , ios::trunc ) ;
                out.close () ;
2509        }
    }
2511 }
}
2513
outName = dirName + "ok";//
2515 dir_p = opendir ( outName.c_str () ) ;
if ( dir_p == NULL ) mkdir ( outName.c_str () ) ;
2517 }

2519 int main ( int argc , char * argv [] )
{
2521    cout << argc << " " << argv [1] ;

2523    double start , finish , duration ;
    priorityDeamon () ;
2525    afinityDeamon ( argc , argv ) ;

2527    start = clock () ;
    getInputPar () ;
2529
if ( !newdata ) {
2531    normTime = delTime;
    // cont () ;
2533    initiateInterconnect () ;
    constrStack () ;
2535    calcCentroid () ;
    calcDelR_segLength () ;
2537    calcMinima () ;
    apr = segLength;
2539    maxSegLengthi = * apr;
    for ( i = 0; i< numUpperNodes - 10; i++ ) maxSegLengthi = maxP ( maxSegLengthi , apr ) ;
2541    apr = segLength;
    minSegLengthi = * apr;
2543    for ( i = 0; i<numUpperNodes - 10; i++ ) minSegLengthi = minP ( minSegLengthi , apr ) ;
    delMean = maxSegLengthi ;

```

```
2545 }
2546     else {
2547         continues () ;
2548         calcCentroid () ;
2549         calcDelR.segLength () ;
2550         delMean = maxSegLengthi;
2551     }
2552
2553 simulate () ;
2554
2555 finish = clock () ;
2556 duration = ( finish - start ) ;
2557 print_elapsed_time () ;
2558 cout<< duration << endl;
2559 return EXIT.SUCCESS;
2560 }
```

CURRICULUM VITAE

Name : Aytaç Çelik
Date of Birth/Place : March 15, 1978 / Sinop, TURKEY
Nationality : Turkish
E-mail : aytacelik@gmail.com

EDUCATION

Ph.D. (2004-2011)

Metallurgical and Materials Engineering Department,
Middle East Technical University, Ankara, TURKEY

M.Sc. (2001-2004)

Metallurgical and Materials Engineering Department,
Middle East Technical University, Ankara, TURKEY

B.S. (1997-2001)

Metallurgical and Materials Engineering Department,
Middle East Technical University, Ankara, TURKEY

WORK EXPERIENCE

Project Assistant (2005-2010)

Metallurgical and Materials Engineering Department,
Middle East Technical University, Ankara, TURKEY

Student Assistant (2002-2005)

Metallurgical and Materials Engineering Department,
Middle East Technical University, Ankara, TURKEY

AWARDS AND ACHIEVEMENTS

Transfer from Chemistry Department to Metallurgical And Materials Engineering Department
by high grade performance

METU Graduate School of Natural and Applied Sciences:

The Best Thesis Award, 2004 September

PUBLICATIONS

A Celik

Investigation of electromigration induced hillock and edge void dynamics on the interconnect
surface by computer simulation

M.Sc. Thesis (2004)

TO Ogurtani, A Celik

Surface morphological evolution on single crystal films by strong anisotropic drift diffusion
under capillary and electromigration forces

J. Appl. Phys. 100, 043504 (2006)

TO Ogurtani, A Celik, EE Oren

Morphological evolution of edge-hillocks on single-crystal films having anisotropic drift-
diffusion under the capillary and electromigration forces

Thin Solid Films, 515 (2007) 2974-2983

TO Ogurtani, A Celik, EE Oren

Morphological evolution in a strained-heteroepitaxial solid droplet on a rigid substrate: Dy-
namical simulations

J. Appl. Phys. 108, 063527 (2010)

TO Ogurtani, A Celik, EE Oren

Generic role of the anisotropic surface free energy on the morphological evolution in a strained-
heteroepitaxial solid droplet on a rigid substrates

J. Appl. Phys. 108, 103516 (2010)